

Fabrication of bismuth-based photocatalytic heterojunctions for hydrogen generation

Von der Naturwissenschaftlichen Fakultät
der Gottfried Wilhelm Leibniz Universität Hannover

zur Erlangung des Grades

**Doktorin der Naturwissenschaften
(Dr. rer. nat.)**

genehmigte Dissertation von

**María Teresa Ayala Ayala, Maestra en Ciencias
(Mexiko)**

2022

Referent: Prof. Dr. rer. nat. habil. Detlef W. Bahnemann

Korreferentin: Prof. Dr. rer. nat. Nadja-Carola Bigall

Korreferent: Prof. Dr. rer. nat. Sascha Beutel

gutachterliche Stellungnahme: Dr.-Ing. Juan Muñoz Saldaña

Tag der Promotion: 24.05.2022

**TO THE LOVE OF MY LIFE, MY BESTFRIEND,
AND MY HUSBAND
JAIME**

Kurzzusammenfassung

Das schnelle Bevölkerungswachstum und die Industrialisierung der letzten Jahrzehnte haben zu einer zunehmenden Umweltverschmutzung und einer hohen Nachfrage nach nicht erneuerbaren Energiequellen aus fossilen Brennstoffen geführt. Wasserstoff ist ein sauberer Energieträger, der aus der Dissoziation von Wasser und Sonnenenergie, einer erneuerbaren Quelle, gewonnen werden kann. Seit der Entdeckung der Wasserstoffentwicklung durch photoelektrochemische Wasserspaltung an n-Typ-TiO₂-Elektroden wird die auf Halbleitern basierende photokatalytische Wasserspaltungstechnologie zur Erzeugung von Wasserstoff mit Hilfe von Sonnenenergie als einer der wichtigsten Ansätze zur Lösung der globalen Energiekrise angesehen. Die Entwicklung von Halbleiter-Photokatalysatoren ist daher in letzter Zeit Gegenstand erheblicher Forschungsanstrengungen gewesen. Die Synthese neuer, im sichtbaren Licht aktiver Photokatalysatoren mit hoher photokatalytischer Effizienz ist eine der größten Herausforderungen, bei der das Hauptproblem die schnelle Elektron-Loch-Rekombination ist. Das Design und die Herstellung von halbleitenden Heteroübergängen stellen eine Lösung für den Ladungsträgertransfer und die Trennung dar, um Reduktions- und Oxidationsreaktionen für die H₂-Produktion zu erreichen. In der vorliegenden Arbeit wurden mit sichtbarem Licht betriebene Wismut-Heteroübergänge, die durch mechanisches Fräsen und thermisches Flammenspritzen hergestellt wurden, für die photokatalytische Entwicklung von H₂ in Gegenwart von Opferstoffen eingesetzt. Die Wirkung der Verarbeitungsparameter führte zu strukturellen Veränderungen, z.B. Gitterparameter, Kristallitgröße und Bindungsenergie, und damit zu Veränderungen ihrer optischen Eigenschaften, z.B. des Photolumineszenzsignals und der Bandlückenenergie, um die Oberflächenmodifikation und die Kopplung zwischen Halbleitern zu verstehen. Die Analyse der physikalisch-chemischen Eigenschaften dient dazu, den gewünschten Weg zur Synthese von Bi-basierten Heteroübergängen zu finden, die eine niedrige photogenerierte Elektron-Loch-Paar-Rekombination und eine hohe Absorption im sichtbaren Bereich des Sonnenspektrums nachahmen. In dieser Arbeit schlagen wir photokatalytische Reaktionsmechanismen für die H₂-Evolution vor, die auf dem Bandkantenpotential jedes Halbleiters, der Bestimmung der photogenerierten Ladungsträger und der Erzeugung freier Radikale, gemessen durch paramagnetische Elektronenspektroskopie, basieren. Die Ergebnisse zeigen, dass der Aufbau eines Heteroübergangs in einer gestaffelten Technik wünschenswert ist, um den Ladungsträgertransfer und die Trennung zu verbessern. Die Stabilität des Halbleiters und einige physikochemische Eigenschaften wie Partikelgröße und Oberfläche dienen dazu, die Aktivität des Materials zu verbessern.

Stichworte: Wismut, H₂, Methanol-oxidation, Reaktionsmechanismus, Flammenspray

Abstract

Rapid population growth and industrialization in recent decades has led to increased environmental pollution and a high demand for non-renewable energy sources from fossil fuels. Hydrogen is a clean energy fuel that can be obtained from the dissociation of water and solar energy, a renewable source. Since the discovery of hydrogen evolution through photoelectrochemical water splitting on n-type TiO₂ electrodes, semiconductor-based photocatalytic water splitting technology to produce hydrogen using solar energy has been considered as one of the most important approaches to solve the global energy crisis. Therefore, the development of semiconductor photocatalysts has recently been the subject of considerable research efforts. The synthesis of new visible-light active photocatalysts with high photocatalytic efficiencies is one of the main challenges in which the major problem is the fast electron-hole recombination. The design and fabrication of semiconducting heterojunctions represent a solution to address charge carrier transfer and separation to achieve reduction and oxidation reactions for H₂ production. In the present work, visible light driven bismuth heterojunctions synthesized by mechanical milling and flame thermal spraying process were employed for the photocatalytic evolution of H₂ in the presence of sacrificial agents. The effect of processing parameters induced structural modifications, for instance, lattice parameter, crystallite size, binding energy and thus led to changes in their optical properties, for instance, photoluminescence signal and band gap energy, to understand the surface modification and coupling between semiconductors. The analysis of physicochemical properties serves to achieve a desired route to synthesize Bi-based heterojunctions that lead to low photogenerated electron-hole pair recombination and high absorbance in the visible range of the solar spectrum. In this work, we propose photocatalytic reaction mechanisms for H₂ evolution based on the band edge potential of each semiconductor, the determination of photogenerated charge carriers and free radical generation measured by electron paramagnetic spectroscopy. The results show that the construction of a heterojunction in a staggered engineering is desirable to improve charge carrier transfer and separation. The stability of the semiconductor and some physicochemical properties such as particle size and surface area serve to enhance the activity of the material.

Keywords: bismuth, H₂, methanol oxidation, reaction mechanism, flame spray

Resumen

El rápido aumento de la población e industrialización en las últimas décadas ha generado un incremento en la contaminación ambiental y en la demanda de fuentes de energía no renovables provenientes de combustibles fósiles. El hidrogeno es un combustible limpio que se puede obtener a partir de agua y energía solar (fuente inagotable de energía). Desde el descubrimiento de la evolución de H_2 por la separación fotoelectroquímica del agua en un electrodo tipo-n de TiO_2 , la tecnología de semiconductores basada en la separación fotocatalítica del agua para producir H_2 usando energía solar ha sido considerada uno de los logros más importantes para resolver la crisis energética mundial. Por lo tanto, el desarrollo de semiconductores fotocatalizadores ha generado una investigación considerable. La síntesis de nuevos fotocatalizadores activos en luz visible es uno de los mayores desafíos, el principal problema es la rápida recombinación de los pares electrón-hueco. Los semiconductores heterounión presentan una solución para mejorar la separación y transferencia de los portadores de carga y lograr las reacciones de oxido/reducción en la producción de H_2 . En el presente trabajo, heterouniones base-Bi activas en luz visible sintetizadas por molienda mecánica y rociado por flama se emplearon para la evolución fotocatalítica de H_2 en presencia de agentes de sacrificio. El efecto de los parámetros de procesamiento mostro modificaciones i) estructurales; parámetro de red, tamaño de cristalita, energía de enlace y ii) cambios en las propiedades ópticas; fotoluminiscencia y energía del ancho de banda, que elucidaron modificaciones superficiales lo cual prueba el acoplamiento entre los semiconductores. El análisis de las propiedades fisicoquímicas conllevo a establecer una ruta de síntesis deseada de las heterouniones base-Bi buscando obtener una baja recombinación de los pares electrón-hueco y alta absorbancia de luz visible. El mecanismo de reacciones fotocatalíticas para evolución de H_2 se propone basada en el potencial de bandas de cada semiconductor, la detección de portadores de carga y radicales libres determinados por espectroscopía paramagnética de electrones. La construcción de heterouniones en ingeniería escalonada es deseable para aumentar la transferencia y separación de portadores de carga. La estabilidad del semiconductor y las propiedades fisicoquímicas como tamaño de partícula y área superficial mejoran la actividad del material.

Palabras clave: bismuto, H_2 , oxidación de metanol, mecanismo de reacción, rociado por flama

Acknowledgments

I would like to sincerely express my utmost gratitude to all who had supported, encouraged, and accompanied me during my PhD research journey to completion. Without your wise assistance and help in each step of my study and stay in Germany, it would have been impossible for me to achieve my goal and cross the finish line.

To begin with, special and heartfelt thanks to my supervisor **Prof. Detlef W. Bahnemann** for giving me the opportunity to be a member of such a great research group where I could learn to do real science and have the freedom to perform my project. The extensive discussions were so helpful to make me develop my skills as researcher. Although, your kindness and respectful is such admirable from a person that is so recognized in all over the world from his scientific career.

To my supervisor **Dr. Juan Muñoz Saldaña** for his encouragement and helpful in all these years. The guidance, motivation and professional and personal support was unbelievably valuable.

To **Dr. Ralf Dillert** who support me in all the experimental stage and analysis of my research project and who behaves as a co-supervisor during my stay in Germany. The discussion and scientific questions that always ask. Although I would thank for his attention and worries during my stay in Germany.

To **Dr. Gerardo Torres Delgado** for the further discussion, helpful guidance, and accessibility to equipment during all the PhD and for being my examiner.

To **Dr. Jesús González Hernández** and **Dra. Astrid Lorena Giraldo Betancur** for his valuable helpful, discussion and supportive comments as examiners.

To **Prof. Nadja Bigall** and **Prof. Sascha Beutel** to be part of the examination board as reviewer and chair.

To the laboratory managers **Adair Jimenez, Guillermo Valencia, Francisco Melgarejo, Joaquin Raboño, Agustin Galindo** and **Ariel Estrada** for their disposal in helping me in the characterization and experimental stage.

To **CONACYT** for the financial support in the development of the doctoral thesis. To my institution **CINVESTAV** and the laboratory **CENAPROT** for let me develop part of my research in the laboratory. I would also want to thank **CIDESI** for the use of the equipment. Thanks to my institution **Leibniz Universität Hannover** and the **Institut für Technische Chemie**. It was an honor for me to belong to such recognized institution.

To my colleagues from ITC **Barbara Nunes, Carsten Günemann, Osama Al-Madanat, Narmina Balayeva, Haoran Wang** for helping me in the laboratory always with the best disposition and kindness and for become my friends and the best colleagues. All the discussions were so worthy and richness I learn a lot from all of you.

To **Solenne Shwanemann** from the International office for helping me even before I arrived in Germany, to guide me in all the enrollment process with her distinguished kindness and make me feel part of the students.

To my colleagues and friends from Cinvestav **Paola Forero, Aixa Gutierrez, Paola Cardenas, Natalia Brizuela, Carolina Hernandez,** and **Jaime Patiño.**

To my family: my mother **Rita** and my father **Salvador**, my siblings **Pablo** and **Miriam** and of course my lovely **Leo**. All of you are the most valuable thing of my life and my motivation to keep going and do not quit. Thank you for all your love and support even more during my stay in Germany.

And finally, and most important to the love of my life: **Jaime**. I do not have the words to thank you all the love, support, and encouragement you have always gave it to me. I have the best husband, friend, colleague, and partner on you. Thank you for always telling me that I can do it and when I cannot you push me. For your love and care, for all the late nights and early mornings, for all the sacrifices that you made during the past four years. Thank you for listening to me when I could not support more the pressure, for see me crying and then tell me: Ok, this is what we are going to do... Thank you for taking your time for helping me in the lab even until midnight and in weekends, and for picking me up at night after an exhausting day at lab and bring me tacos. Thank you for all the sacrifices you made and even put my things first from yours.

Acronyms

GHG	greenhouse gas
PWS	photocatalytic water splitting
PC	photocatalyst
SC	semiconductor
UV	ultraviolet
OER	oxygen evolution reaction
SBR	surface back reaction
CBM	conduction band minimum
VBM	valence band maximum
VB	valence band
CB	conduction band
EDM	electric dipole moments
LEPs	lone electron pairs
NHE	normal hydrogen electrode
PEC	Photoelectrochemical
SOD	stand-off distance
BSE	back scattering electron
EDS	energy dispersive spectroscopy
DSC	differential scanning calorimeter
TGA	transient gravimetric analysis
NIR	near infrared
SE	secondary electrons
FS	flame spray
FESEM	field emission scanning electron microscopy
DRS	diffused reflectance spectroscopy
DDL	3:5-diacetyl-1:4-dihydrolutidine
XRD	X-ray diffraction
BET	Brunauer–Emmett–Teller

FTO	fluoride-doped tin oxide
CLV	Cyclic light voltammetry
PL	Photoluminescence
CIF	Crystallographic information file
LED	Light emitting diode
GC	Gas chromatography
EPR	Electron paramagnetic resonance
DMPO	5,5-dimethyl-1-pyrroline N -oxide

Formula sign

ΔG	Gibbs free energy (kJmol^{-1})
ΔE°	photon energy (eV)
E_g	band gap energy (eV)
E_{CB}	conduction band edge (V vs NHE)
E_{VB}	valence band edge (V vs NHE)
E°	electrochemical potential (V vs NHE)
$F(R)$	function of reflectance
ν	photon frequency (s^{-1})
R	reflectance (a.u.)
n	optical transition
q^3	distribution particle density
$Q^3\%$	cumulative particle distribution
2θ	scanning range angle ($^\circ$)
a, b, c	lattice parameter (\AA)
d_{10}, d_{50}, d_{90}	particle size diameter
χ^2	goodness coefficient
R_f	structural factor
Q	net heat transfer between hot gas and particles
d_p	diameter of the particle

T	temperature $T(^{\circ}\text{C}) = T(\text{K}) - 273.15$
T_s	surface temperature of the particle (K)
T_{∞}	temperature of hot gas (K)
T_a	temperature of the environment (K)
ε	emissivity of the particle
h	heat transfer coefficient between the hot gas and the particle
Nu	Nusselt number
κ	thermal conductivity of a gas
T_g	temperature of the gas
T_p	temperature of the particle
Bi	biot number
ϕ	equivalence ratio
dC/dt	reaction rate
Φ	quantum yield
I_o	observed powder diffraction data
I_c	simulated powder diffraction data
R_{wb}	weighted residual error
R_{exp}	expected error
w_i	weight factors
N	number of experimental observations
P	number of refined parameters
GoF	goodness of fit factor
C_{SC}	capacitance of the space charge layer
ε	dielectric constant of the semiconductor
A	interfacial area
N_D	donor density
q	electronic charge
E_{appl}	applied potential (V)
I_0	Photon flux density
I	Light irradiance (Wm^{-2})

ξ	photonic efficiency
V	volume (L)
s	spin quantum number
m_s	electron's magnetic moment
B_0	magnetic field

Physical constant

h	plank's constant (4.135×10^{-15} eVs)
ϵ_0	permittivity of the vacuum ($8,854187817$ Fm ⁻¹)
σ_s	Stefan-Boltzmann constant (5.67×10^{-8} Wm ⁻² K ⁻⁴)
c	speed of the light ($3E8$ ms ⁻¹)
N_A	Avogadro number ($6.022E23$ mol ⁻¹)
g_e	electron's g-factor for the free electron (2.0023)
m_B	Bohr magneton ($5.7883E-5$ eVT ⁻¹)
k	proportional constant

Table of contents

Dedication	I
Kurzzusammenfassung	III
Abstract	V
Resumen	VII
Acknowledgments	IX
Acronyms	XI
Formula sign	XII
Physical constant	XIV
Table of contents	XV
Chapter 1:General introduction	1
1.1.Photocatalysis: A promise to environmental remediation	1
1.2.Photocatalytic water splitting.....	3
1.2.1.Main processes on photocatalytic H ₂ production	6
1.2.2.Approaches to enhance the PWS reaction	7
1.3.Desired properties in a photocatalysts for H ₂ evolution	11
1.3.1.Heterojunction photocatalysts.....	13
1.4.Bismuth based photocatalysts	16
1.4.1.Bismuth oxide	17
1.4.2.Bi-based heterojunctions.....	21
1.5.Objectives and thesis outline	24
Chapter 2:Synthesis and characterization of photoactive β-bismuth oxide by flame spray	27
2.1.Introduction.....	27
2.2.Materials and methods	30
2.2.1. Powder synthesis.....	30
2.2.2. Structure and microstructure.....	31
2.2.3. Thermal transformation analysis	32
2.2.4. Optical properties.....	32
2.3. Results and discussion	32
2.3.1. Characterization of precursor bismuth powder.....	32
2.3.2. Phase transitions of Bi ₂ O ₃ by DSC	34

2.3.3. Characterization of nanometric-sized bismuth oxide powder	35
2.3.4. Characterization of micrometric-sized bismuth oxidized powder	39
2.3.5. Influence of flame spray parameters on oxidation characteristics of bismuth.	44
2.3.6. Oxidation mechanisms by electron microscopy	45
2.4. Conclusion	48
Chapter 3:Photocatalytic H₂ evolution and methanol photooxidation of visible-light driven bismuth-based heterojunctions synthesized by flame spray	49
3.1. Introduction.....	49
3.2. Materials and methods	54
3.2.1. Powder feeder calibration	54
3.2.2. Pulverization of bismuth pellets	54
3.2.3. Thermal spray and collection.....	55
3.2.4. Structural and optical characterization.....	56
3.2.5. Photocatalytic activity.....	57
3.3. Results and discussion	58
3.3.1. Characterization of precursor metallic powder.....	58
3.3.2. Experimental set-up and thermal spray conditions.....	59
3.3.3. Effect of flame sprayed parameters on the physicochemical properties of the obtained powder.....	60
3.3.4. Photocatalytic activity for methanol oxidation and hydrogen generation	71
3.4. Conclusion	76
3.5. Appendix.....	77
Chapter 4:Bi-based heterojunctions synthesized by mechanical milling: Effect of the structural parameters in the optical properties.....	85
4.1. Introduction.....	85
4.2. Materials and methods	87
4.2.1. Synthesis of heterojunctions	87
4.2.2. Structural and microstructural characterization.....	88
4.2.3. Optical properties.....	89
4.2.4. Electrochemical measurements.....	90
4.3. Results and discussion	91
4.3.1. Characterization of precursor catalyst powders.....	91
4.3.2. Optical properties of heterojunctions.....	94

4.3.3. Structural and microstructural properties of heterojunctions.....	97
4.3.4. Electrochemical measurements of heterojunctions.....	104
4.4. Conclusion	109
4.5. Appendix.....	110
Chapter 5:Photocatalytic activity of Bi-based heterojunction for methanol oxidation using a black-body like reactor	115
5.1. Introduction.....	115
5.2. Materials and methods	118
5.2.1. Synthesis of photocatalyst	118
5.2.2. Catalysts characterization	119
5.2.3. Photocatalytic methanol oxidation.....	120
5.2.4. Determination of quantum yields	122
5.3. Results and discussion	122
5.4. Conclusion	138
5.5. Appendix.....	138
Chapter 6:Photoinduced H₂ evolution of Bi-based heterojunctions: Fate of photogenerated charge carriers	147
6.1. Introduction.....	147
6.2. Materials and methods	149
6.3. Results and discussion	150
6.4. Conclusion	160
Chapter 7:Summary and outlook	161
Chapter 8:References	165
Curriculum vitae	182
Publications	184
Journal publications	184
Oral presentations	185
Poster presentations	186
Courses.....	186

Chapter 1:General introduction

1.1. Photocatalysis: A promise to environmental remediation

The rapid increase in population over the last decades and as consequence the industrialization generates an increase in environmental pollution and a high demand of energy sources such as coal, petroleum, natural gas and hydrocarbons. These sources came from fossil fuels a non-renewable energy source that also causes several damages to the environment and then to human health in its extraction, transportation, production, and use. The increase in demand and the decrease of available sources generates the searching of new clean energy sources to replace fossil fuels¹.

Because of its high energy capacity, recycling potential and environmental friendliness, hydrogen has been identified as a potential energy carrier in many low greenhouse gas (GHG) energy scenarios². In a proposed hydrogen energy system, hydrogen containing compounds such as fossil fuels, biomass or even water are potential sources of hydrogen. When hydrogen is derived from hydrocarbons such as fossil fuels or biomass, CO₂ capture, and sequestration are requirements in a low GHG scenario. The greenhouse effect is one of the most serious global problems. The increase in CO₂ concentration in the atmosphere due to the continuous burning of fossil fuels may lead to irreversible disastrous changes in our planet's climate³.

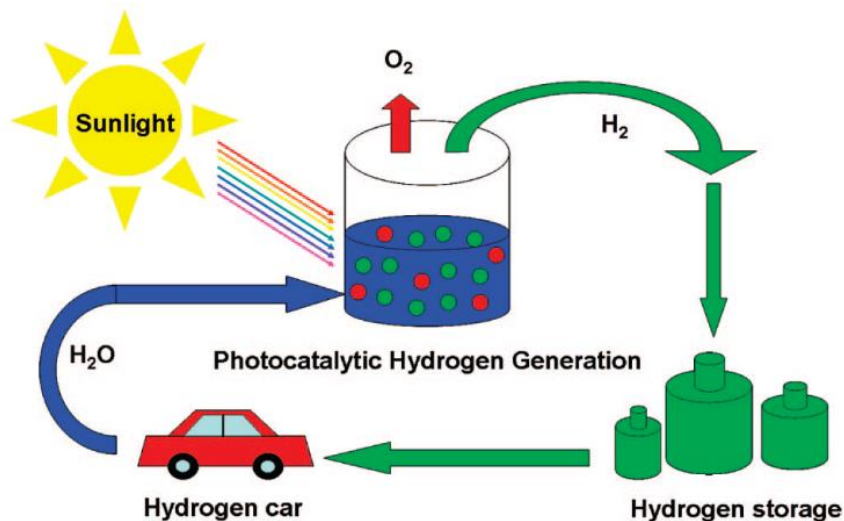


Figure 1.1 Schematic diagram of photocatalytic hydrogen generation in the hydrogen energy system⁴.

However, known modern processes of hydrogen production using fossil fuels and water (including electrolysis of water combined with thermal power stations) are accompanied by the emission of large quantities of CO₂ into the atmosphere. All these processes are highly endothermic and consume additional fossil fuels as energy sources. On the other hand, hydrogen produced from water does not present the challenge of unwanted emissions at the point of conversion, but it does require that energy be supplied from an external resource. If this energy can be obtained from a renewable energy source such as solar energy, hydrogen can be considered a green energy alternative capable of powering everything from laptop to submarines⁴. However, at present, renewable energy only contributes about 5% of commercial hydrogen production through electrolysis of water, while the other 95% of hydrogen is obtained mainly from fossil fuels⁵.

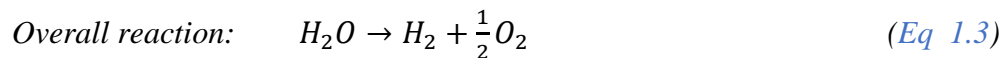
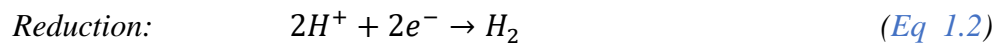
The motivation of this project entails to solve the problem of the acquisition of new energy sources as solar energy. Photocatalytic water splitting (PWS) is an innovative technology for the purpose, since H₂ could be obtained directly from abundant and renewable water and solar light from the process (Fig. 1.1). If successfully developed with

economic viability, this could be the ultimate technology that could solve both energy and environmental problems altogether in the future⁶.

Since the discovery of hydrogen evolution through the photoelectrochemical (PEC) splitting of water on n-type TiO₂ electrodes, the technology of semiconductor (SC) based photocatalytic water splitting to produce hydrogen using solar energy has been considered as one of the most important approaches to solving the world energy crisis. Hence, the development of the necessary semiconductor photocatalysts (PC) has undergone considerable research⁷.

1.2. Photocatalytic water splitting

Since the Fujishima and Honda report on water splitting using TiO₂ as a photocatalyst, numerous attempts have been made towards the development of new semiconductor photocatalysts for efficient water splitting⁸. Photocatalytic water splitting, like other photocatalytic processes, starts when a semiconductor photocatalyst absorbs photons with energies greater than the energy of the band gap (E_g). This absorption creates excited photoelectrons in the conduction band (CB) and holes in the valence band (VB) of the semiconductor. Photoelectrons and holes reduce and oxidize water to produce the 2:1 stoichiometric mixture of H₂ and O₂ by the following reactions⁹ (Eq 1.1-1.3):



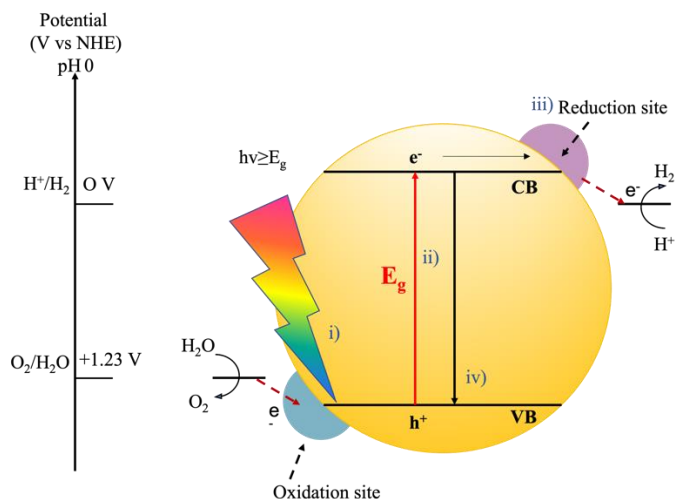


Figure 1.2. Schematic illustration of water splitting over semiconductor photocatalyst¹⁰.

Generally, photocatalytic reaction over a photocatalyst involves four steps, including i) photogeneration of electron–hole pairs under light irradiation, ii) charge carrier separation and migration to the surface, iii) participation of electrons/holes in reduction/oxidation reaction, and iv) recombination of charge carriers in the bulk or on the photocatalyst surface (Figure 1.2). These four steps are complementary, and the thermodynamics and kinetics of these processes determine the efficiency of a given photocatalyst¹¹.

The free energy change for the conversion of a molecule from H₂O to H₂ and 1/2O₂ under standard conditions is $\Delta G = 237.2$ kJ/mol, which, according to the Nernst equation, corresponds to $\Delta E^\circ = 1.23$ eV by electron transferred. To use a semiconductor to drive this reaction with light, the semiconductor must absorb radiant light with photon energies of 1.23 eV (equal to wavelengths of ~ 1000 nm or less) and convert the energy into H₂ and O₂. This process should generate two electron-hole pairs per H₂ molecule (2×1.23 eV = 2.46 eV) or four electron-hole pairs per O₂ molecule (4×1.23 eV = 4.92 eV). In the ideal case, a single semiconductor material having a band gap energy large enough to divide the water, a conduction band edge energy (E_{CB}) and a valence band edge energy (E_{VB}) that extends to the electrochemical potentials $E^\circ(\text{H}^+/\text{H}_2)$ and $E^\circ(\text{O}_2/\text{H}_2\text{O})$, can drive the hydrogen evolution

reaction (HER) and the oxygen evolution reaction (OER) using generated electrons/holes under lighting^{4,9,12}.

In a simple description, when a photocatalyst is used for water splitting, the energetic position of the bottom of the conduction band must be more negative than the reduction potential of water to produce H₂, and that of the top of the valence band must be more positive than the oxidation potential of water to produce O₂. Based on these parameters, a theoretical semiconductor band gap energy of ~1.23 eV is required to drive the water splitting reaction. The band edge potential of some common and highly active photocatalyst reported so far is shown in Figure 1.3 respect to the Normal Hydrogen Electrode (NHE). Furthermore, the photocatalyst must be stable in aqueous solutions under photoirradiation. It is intrinsically difficult to develop an oxide semiconductor photocatalyst that has both characteristics¹³.

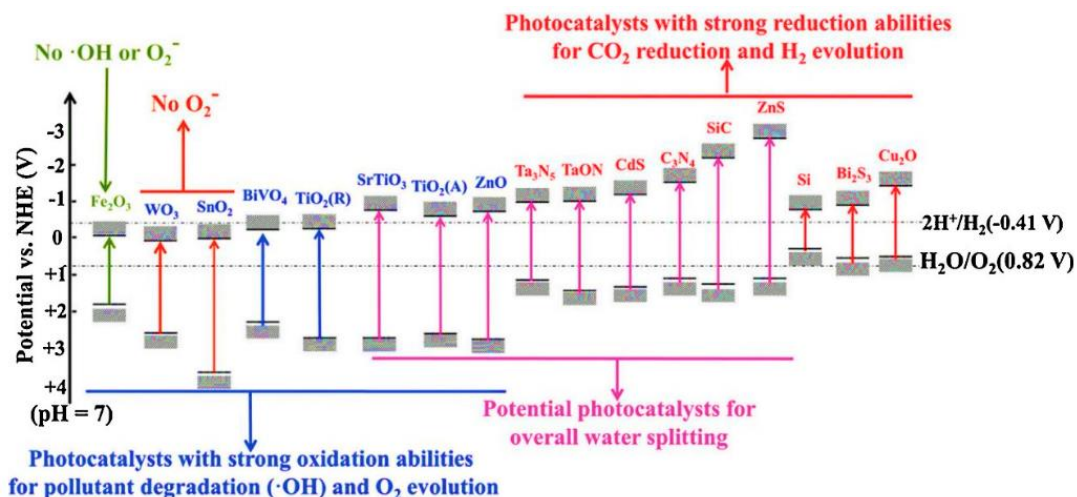


Figure 1.3. Band edge positions of different semiconductors at pH 0. The compounds that possess a E_{CB} more negative than the formation of H₂ (0 V vs NHE) are possible candidates for PWS¹⁴.

Semiconductors with smaller band gaps or lower flat band potentials require a bias voltage or external redox reagents to drive the reaction. Alternatively, two or more small band gap semiconductors can be combined to drive water oxidation/reduction processes

separately via multiphoton processes. It is well known that flat band potentials strongly depend on ion absorption (protonation of surface hydroxyl groups), crystallographic orientation of the exposed surface, surface defects, and surface oxidation processes. These factors are rarely considered in the preparation and testing of photochemical water splitting catalysts⁴.

The approach to solving the water splitting problem has focused on evaluating new materials for anodic/cathodic processes and integrating configurations using photovoltaic cell junctions, to increase the voltage obtainable for a single band gap device. or double. The final objective of these efforts is an efficient design of photoelectrolysis cells that can conduct simultaneously, in an unassisted way, both for the evolution of hydrogen and for the oxidation reactions of water. Water splitting cells require semiconductor materials that can address rapid charge transfer at a semiconductor/aqueous interface, which exhibit long term stability, and that can efficiently collect a large portion of the solar spectrum. To achieve these functions, multifunction configurations using p-type and n-type semiconductors with different band gaps and surface bound electrocatalysts have been the predominant approach for the development of efficient photoelectrolysis cells⁹.

1.2.1. Main processes on photocatalytic H₂ production

The total amount of H₂ generated is determined by the number of excited electrons at the water/photocatalyst interface capable of reducing water. After the electron-hole pairs are created, charge recombination and separation/migration processes are two important competitive processes inside the semiconductor photocatalyst that largely affect the efficiency of the photocatalytic reaction for water splitting¹³. Charge recombination reduces the number of e⁻/h⁺ pairs by emitting light or generating phonons. This includes both, surface and bulk recombination, and is classified as a deactivation process, and it is ineffective for water splitting. The reaction of photogenerated H₂ and O₂ to form H₂O on the photocatalyst surface is normally called “surface back-reaction (SBR)”⁴.

There are two main approaches to suppress the SBR: one involves the addition of sacrificial reagents into the photocatalytic reaction environment and the second creates a

separation of the photoactive sites on the surface of the photocatalysts. Sacrificial reagents act as electron donor or acceptors, respectively, drive the reaction into alternative pathways as they are reduced or oxidized, respectively¹⁰.

Various organic compounds such as alcohols, organic acids, and hydrocarbons have been and are being employed as hole scavengers (i.e., as electron donors) for photocatalytic H₂ generation. In particular, methanol is frequently used as a sacrificial reagent. For practical applications, the utilization of methanol will only be environmentally sensible if it is derived from biomass or from toxic residues that must be disposed of. Adding methanol as an electron donor to react irreversibly with the photogenerated valence band (VB) holes can enhance the photocatalytic electron-hole separation efficiency, resulting in higher quantum efficiencies. Because electron donors are consumed in the photocatalytic reaction, their continuous addition is required to sustain H₂ production¹⁵.

1.2.2. Approaches to enhance the PWS reaction

Photocatalytic Water Splitting has made remarkable progress in the last decade under ultraviolet (UV) light, but many technical challenges remain for PWS under visible light. Various approaches are taken in search of efficient photocatalysts for PWS under visible light: to find new monophasic materials to decorate UV-activated photocatalysts with a photosensitizer that absorbs visible light to adjust band gap energy by modifying the cations or anions of the photocatalysts UV actives with substitution doping manufacture multicomponent photocatalysts forming compounds or solid solutions⁵.

Taking into consideration the basic mechanism and the individual processes of photocatalytic water splitting, there are two keys for the development of a suitable high efficiency semiconductor for the visible light driven photocatalytic splitting of water into H₂ and/or O₂: (1) a photocatalyst should have a sufficiently narrow band gap (1.23 eV - E_g - 3.0 eV) to both harvest visible light and possess the correct band structure; and (2) photoinduced charges in the photocatalyst should be separated efficiently in order to avoid bulk/surface electron-hole recombination¹⁶. In addition, both charge carriers must migrate to the photocatalyst surface for H₂ and/or O₂ evolution at the respective photocatalytic

active sites. It is important that economical, highly efficient photocatalytic systems for light to H₂ energy conversion, in which aqueous solutions containing sacrificial reagents can be used to minimize the back-ward reaction of H₂ and O₂ to water on the surface of photocatalysts, can be constructed¹⁷.

The energy band configuration of a semiconductor plays a significant role in the absorption of light and in determining the redox potentials. In order to narrow the band gap of semiconductors to extend the absorption of light into the visible region, three approaches have been widely used: (I) modification of the VB, (II) adjustment of the CB, and (III) continuous modulation of the VB and/or CB¹⁸.

Suppression of charge recombination can be attempted in a number of ways⁴:

- (i) the use of scavengers (sacrificial solutions), which can remove either holes or electrons in the system so that only one half of the water splitting reaction can be studied in isolation (either reduction or oxidation).
- (ii) variation of the morphology of the photocatalyst, which has been shown to improve photocatalytic activity due to the increase in surface area and the shortening of charge carrier diffusion pathways to the surface; and
- (iii) the creation of a heterojunction, whereby charge carriers are generated in one photocatalyst and subsequently vectorially transferred to the other material, allowing for long-lived electron–hole pairs, mimicking the mechanism exhibited in Photosystem II during artificial photosynthesis.

- Z-scheme

One approach for achieving water splitting using visible light is to apply a two-step photoexcitation mechanism between two photocatalysts (a two-step system shown in [Figure 1.4](#)). In two-step systems, the water splitting reaction is broken up into two stages: one for H₂ evolution and the other for O₂ evolution; these are combined by using a shuttle redox couple (Red/Ox) in the solution. At the H₂ evolution photocatalyst, the photoexcited electrons reduce water to H₂ while the holes in the valence band oxidize the reductant (Red) to its oxidized form (Ox). This system lowers the energy required for photocatalysis,

allowing visible light to be utilized more efficiently than in conventional water splitting systems¹⁹.

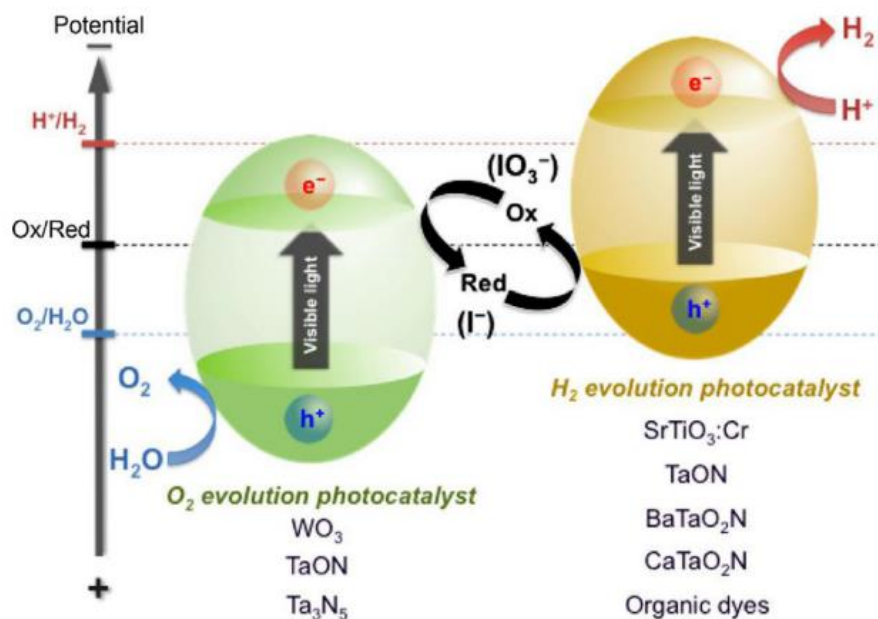


Figure 1.4. Schematic energy diagrams of Z-scheme photocatalytic water splitting system (two step photoexcitation system) using a redox couple¹¹.

Water splitting under visible light illumination was demonstrated for the first time in 2001 using a Z-scheme photocatalytic system consisting of SrTiO₃ doped with Cr and Ta (denoted as SrTiO₃:Cr/Ta) for H₂ evolution, WO₃ for O₂ evolution, and an iodate/iodide (IO₃⁻/I⁻) redox couple as electron mediator²⁰. Prior to that, Z-scheme photocatalytic water splitting had been demonstrated using a combination of Pt-loaded anatase TiO₂ and rutile TiO₂ photocatalysts in the presence of an iodate/iodide (IO₃⁻/I⁻) shuttle redox mediator²¹. Although this system operates only upon UV light irradiation ($\lambda < 400$ nm) due to the large band gap of the TiO₂ photocatalysts, it eventually opened the way to achieve water splitting under visible light. The key was controlling the reactivity of electrons and holes with the redox mediator (IO₃⁻/I⁻ anions) and the water molecules, respectively. It is quite difficult to achieve the simultaneous evolution of H₂ and O₂ in two-step water splitting systems (Z-

scheme) because the back-ward reactions of the redox mediator usually proceed readily over both photocatalysts thus suppressing the forward reactions (H_2 and O_2 evolutions)¹¹.

- Semiconductor heterojunctions

The other approach is based in photocatalyst engineering: Coupling of two or more semiconductors with appropriate band positions and having two different energy levels, is an efficient route to effectively improve photocatalytic activity of the semiconductor photocatalysts, because it can considerably enhance the separation of photogenerated electron-hole pairs and interfacial charge transfer efficiency. Therefore, substantial efforts have been put into solving these problems. In particular, the loading of co-catalysts or secondary semiconductors that can act as either electron or hole acceptors for improved charge separation is a promising strategy, leading to the adaptation of a junction architecture²².

- Cocatalyst loading

Transition metals, especially noble metals, are widely used as effective cocatalysts for photocatalytic reactions. When the noble metal is loaded onto the surface of the photocatalyst, the photogenerated electrons migrating to the surface of the host photocatalyst are entrapped by the noble metal cocatalyst (Figure 1.5), because the Fermi energy level of noble metal is always lower than that of the semiconductor photocatalyst. The most widely used co-catalysts are noble metals (Pt, Ru, Rh, Pd) and metal oxides (NiO, RuO, MoS₂ as a co-catalyst has been reported to be even more effective than Pt for CdS water splitting systems¹¹.

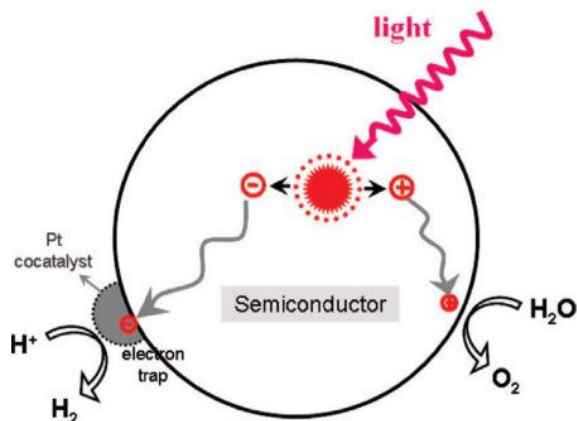


Figure 1.5 Processes of charge transfer between host photocatalyst and cocatalyst¹¹.

1.3. Desired properties in a photocatalysts for H₂ evolution

Great efforts have been made to fabricate a novel catalyst with optimal physical and chemical properties with high activity. The most used materials are semiconductors for its charge carrier transport and its feasible fabrication, nontoxicity, and chemical inertness. The use of new photocatalyst to achieve H₂ production is one of the major challenges in which the desired characteristics are: a narrow band gap energy, a band edge potential of the CB and VB to overcome photocatalytic water splitting reactions (Figure 1.3) and to decrease the rapid electron-hole recombination process that decrease the activity of the semiconductor²³.

TiO₂ was the first material described as a photochemical water splitting catalyst. It crystallizes in three structure types: Rutile, Anatase, and Brookite. All modifications contain TiO₆ octahedra that are interconnected via two (Rutile), three (Brookite), or four (Anatase) common edges and via shared corners, and as a result, the band gaps (3.0 eV for Rutile and 3.15 eV for Anatase) differs lightly²⁴. In their 1971/72 papers, Fujishima and Honda described an electrochemical cell consisting of an-type TiO₂ (Rutile) anode and a Pt black cathode. When the cell was irradiated with UV light ($\lambda < 415$ nm) from a 500 W Xe lamp, O₂ evolution was observed at the anode with a current flowing to the Pt counter electrode. Based on the current, a photoelectrochemical efficiency of approx. 10% was estimated^{7,23}.

A wide range of semiconducting materials have been developed as photocatalysts under UV irradiation. On the basis of their electronic configuration properties, these UV-active photocatalysts can be typically classified into four groups: (1) d^0 metal (Ti^{4+} , Zr^{4+} , Nb^{5+} , Ta^{5+} , W^{6+} , and Mo^{6+}) oxide photocatalysts, (2) d^{10} metal (In^{3+} , Ga^{3+} , Ge^{4+} , Sn^{4+} , and Sb^{5+}) oxide photocatalysts, (3) f^0 metal (Ce^{4+}) oxide photocatalysts, and (4) a small group of non-oxide photocatalysts¹¹.

Since nearly half of the solar energy incident to the earth's surface lies in the visible region ($400\text{ nm} < \lambda < 800\text{ nm}$), it is essential to use visible light efficiently to realize H_2 production on a large scale by photocatalytic water splitting. A maximum solar conversion efficiency for photocatalytic water splitting with a quantum efficiency of 100% can be calculated using the standard solar spectrum. Even if all UV light up to 400 nm were utilized, the solar conversion efficiency would be only 2% (Figure 1.6).

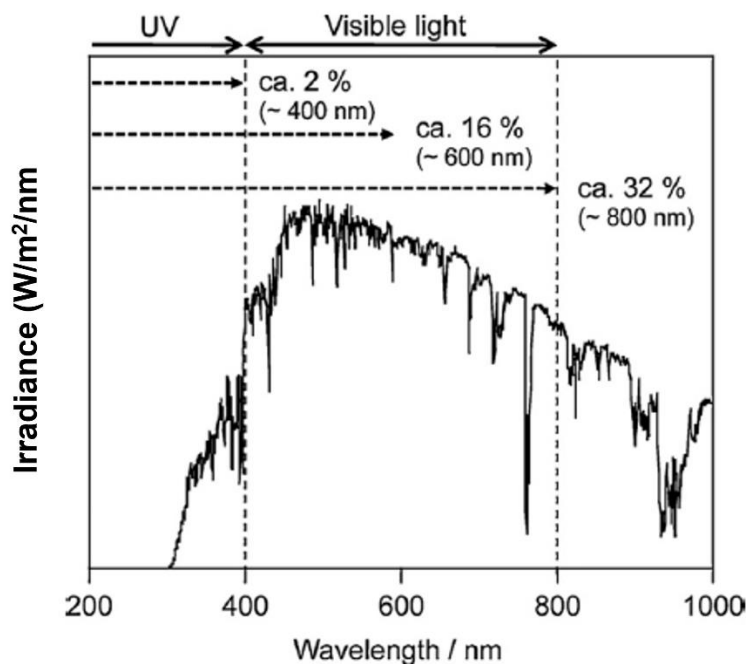


Figure 1.6. Solar spectrum and maximum solar light conversion efficiencies for water splitting with 100% of quantum efficiency¹¹.

If it were possible to utilize visible light up to 600 nm, the efficiency would drastically improve to 16%; a further extension up to 800 nm would give a conversion efficiency of 32%. Therefore, achieving water splitting under visible light has been a challenging goal since the discovery of the Honda–Fujishima effect in 1972.

Numerous attempts have been made to develop photocatalysts that work not only under UV light but also under visible-light illumination to efficiently utilize solar energy⁶. While visible light driven photocatalysts with proper band structures are currently being developed using some modification technologies or band engineering approaches, the issue of photogenerated charge carrier separation is another key factor strongly affecting the efficiency of the photocatalytic water splitting process⁵.

Besides this, a photocatalyst should possess biological and chemical inertness, stability under photocorrosion, low cost and non-toxicity. The reported research in the synthesis of new visible light active photocatalyst or the modification of existent ones, the tuned of the physicochemical properties has generated significant interest. These modifications include to increase the surface area, the active sites, and the absorption of photons and to reduce the energy of the band gap. In a real-scale application scenario, the photocatalyst should overcome high activity, poisoning resistance, stability to prolonged exposure in elevated temperatures, mechanical stability, wear resistance and physical and chemical stability.

1.3.1. Heterojunction photocatalysts

In recent years, great efforts have been put into manufacturing semiconductor materials to improve the performance of existing photocatalysts, and to understand the fundamental factors that mediate photocatalytic efficiency. One of the effective methods for photostimulated electron-hole separation is semiconductor combining as it is of increasing interest. The method constructs a heterojunction interface between semiconductors with coincident band potentials. In this way, the electric field-assisted transport of charge from one particle to another through the interfaces is positive for the electron-hole separations in

the coupled materials, and for the consequent abundance of electrons and/or holes on the surfaces of two combined semiconductors, respectively^{25,26}.

Typically, the S–S heterojunctions can be divided into three types: conventional heterojunction, p–n heterojunction and direct Z-scheme heterojunction. According to the different CB and VB level of two semiconductors, there are three types of conventional heterojunction (Figure 1.7): straddling band gap type (type-I), staggered band gap type (type-II), and broken band gap type (type-III), where the most suitable for photocatalysis is the type-II.

In type-II heterojunction (Figure 1.7b), the CB and VB levels of semiconductor A are higher than the corresponding level of semiconductor B. Thus, under light irradiation, electrons in the CB of semiconductor A can be transferred to that of semiconductor B, while holes in the VB of semiconductor B can be transferred to that of semiconductor A. As a result, the spatial separation of electron–hole pairs can be realized. Whereas electron–hole pairs cannot be separated so effectively in type-I heterojunction since both electrons and holes accumulate on the same semiconductor.

Besides, the separation of electron–hole pairs cannot occur in type-III heterojunction (Figure 1.7c) because the band gaps do not overlap. When two semiconductors are p-type and n-type, respectively, a p–n heterojunction can be obtained. Before light irradiation, a space-charge region can be formed at the interface due to the diffusion of majority carriers, resulting in a built-in electric field that can direct the photogenerated electrons and holes to flow in the opposite direction. Compared with type-II heterojunction, the charge separation of p–n heterojunction is faster due to the synergy between the internal field and the band alignment.

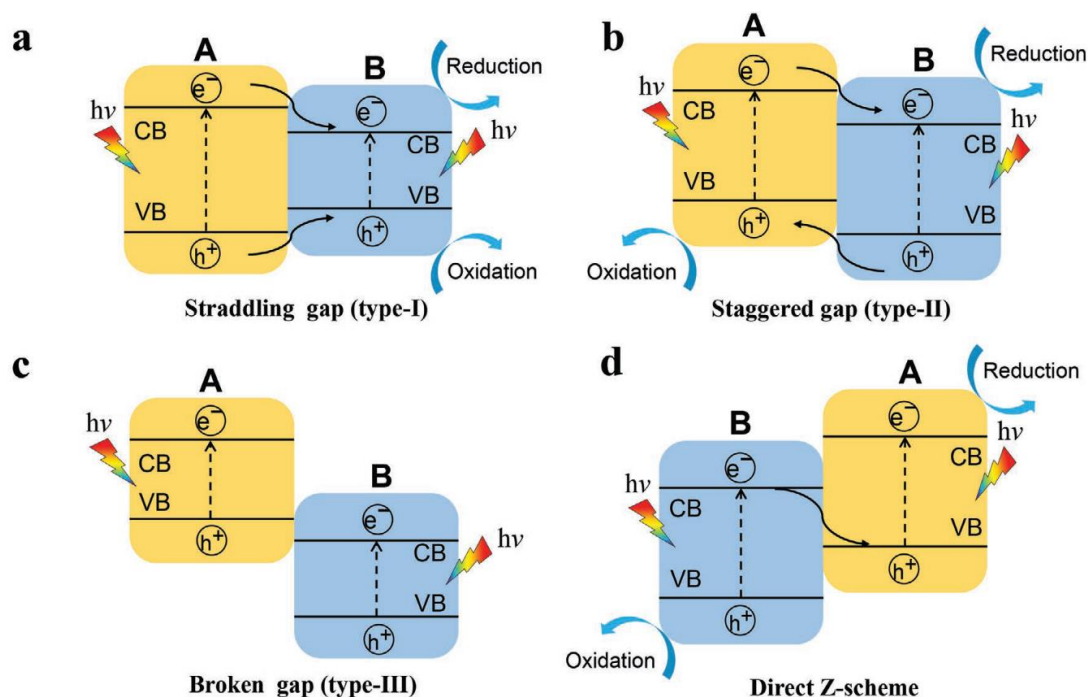


Figure 1.7 Migration of electron–hole pairs under irradiation in different type of heterojunction photocatalysts: a) type-I, b) type-II, c) type-III, and d) direct Z-scheme²⁷.

However, the redox ability of the heterojunction mentioned above is sacrificed because the reduction and oxidation processes occur on the semiconductor with the lower reduction and oxidation potentials. The direct Z-scheme heterojunction (Figure 1.7d) can solve this problem. In the direct Z-scheme heterojunction, the band structure is quite similar to that of type-II heterojunction, but the direction of charge transfer is opposite. Under light irradiation, the electrons in the CB of semiconductor B recombine with the holes in the VB of semiconductor A, while the strongly oxidative holes in the VB of semiconductor B and strongly reductive electrons in the CB of semiconductor A participate in the redox reaction. As a result, the heterojunction not only can improve the charge separation efficiency but also can retain strong redox ability.

Light harvesting, charge separation, charge transport, charge utilization and surface adsorption capacity are the steps that influence the photocatalytic quantum efficiency.

Thus, design of photocatalyst to engineer the desired properties has been the current research focus.

1.4. Bismuth based photocatalysts

Among visible-light photocatalysts, the bismuth-based composite oxides have received much attention as potential promising photocatalysts for water oxidation since Kudo et al. firstly reported photocatalytic oxygen generation under visible light by Bi_2WO_6 and BiVO_4 ²⁸. Related references have well studied about bismuth-based composite oxides, such as mediating the morphology and structure, constructing heterojunction, and doping with different elements. During the past decades, bismuth-related materials have stimulated extensive research on the preparation, modification and application of photodegradation of organic pollutants, splitting of photoinduced water, photocatalytic removal of hazardous gases and heavy metal ions²⁹.

A variety of bismuth-based composite oxides have been proved as photocatalysts such as Bi_2O_3 , Bi_2MO_6 ($M = \text{Cr}, \text{Mo}$ and W), BiMO_4 ($M = \text{P}, \text{V}, \text{Nb}$ and Ta), BiOX ($X = \text{Cl}, \text{Br}$ and I), BiFeO_3 , BiYO_3 , $(\text{BiO})_2\text{CO}_3$, and pentavalent bismuthates³⁰. These compounds present efficient photocatalytic activity, high stability, low cost, and non-toxicity. However, they are failed to photocatalytic reduce the hydrogen from water, due to their lower conduction band not satisfying the reduction potential of H^+ to H_2 as shown in [Figure 1.8](#)³¹. Thus, it may be exciting if these bismuth-based composite oxides can also be able to photocatalytic hydrogen generation. If so, more and more new visible light materials for photocatalytic hydrogen generation would be discovered.

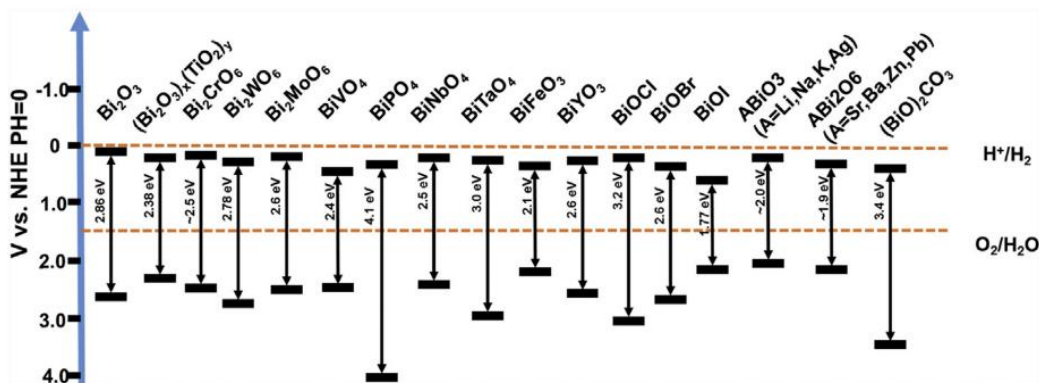


Figure 1.8 Band positions of bismuth based composite oxides³¹.

In recent years, some modified bismuth-based composite oxides have been reported to achieve photocatalytic hydrogen production. To modulate their levels of the conduction and valence bands, meeting the potential requirements of reduction and oxidation of H₂O at the same time, is significant. On the other hand, building Z-scheme system with another H₂ evolution photocatalyst is also an important way to achieve water splitting by bismuth-based composite oxides. Several preparation methods were proposed to control conduction band minimum (CBM) and valence band maximum (VBM) of particle material, such as doping, quantum size effect, and solid solution. To realize photocatalytic hydrogen production by bismuth-based composite oxides, it needs to improve their conduction band. These modification will lead to the synthesis and application of photocatalytic hydrogen generation³².

1.4.1. Bismuth oxide

Among active photocatalysts, Bi₂O₃ has proven to be a valuable alternative photocatalyst to TiO₂ as it has an adequate energy band gap (less than 3.0 eV). Bi₂O₃ is a p-type oxide semiconductor (monoclinic phase) with many excellent physical and chemical properties, such as thermal stability, non-toxicity, chemically inertness in neutral water, dielectric permittivity, high refractive index, ion conductivity and remarkable photoconductivity. This makes Bi₂O₃ an attractive material for gas sensors, optical coatings and photocatalysis^{25,26}. Some of the novel reported research probe that Bi₂O₃ behave as a

photosensitizer which act by absorbing ultraviolet or visible region of electromagnetic radiation and transferring it to an adjacent co-catalyst. This process enhances the transfer of the electrons and holes photogenerated due to a band bending between semiconductors increasing thus the photocatalytic activity.

Additionally, Bi_2O_3 photocatalyst is considered safe, non-toxic, and non-carcinogenic. Bi_2O_3 has six main crystallographic polymorphs denoted by the phases α - (monoclinic), β - (tetragonal), γ - (cubic, bcc), δ - (cubic, fcc), ϵ - (orthorhombic), and ω - (triclinic). The room temperature and high temperature stable phases are α - Bi_2O_3 and δ - Bi_2O_3 , respectively while the others are metastable phases at high temperature. α - Bi_2O_3 is thermodynamically the most stable phase in the range of 25 °C to 730 °C. At 730 °C, α - Bi_2O_3 transforms into the δ phase and remains stable until reaching its melting point at 825 °C. At high rates of cooling of the δ phase, the β phase can be observed near 650 °C and then it can return to the α phase (Figure 1.9)^{25,26}.

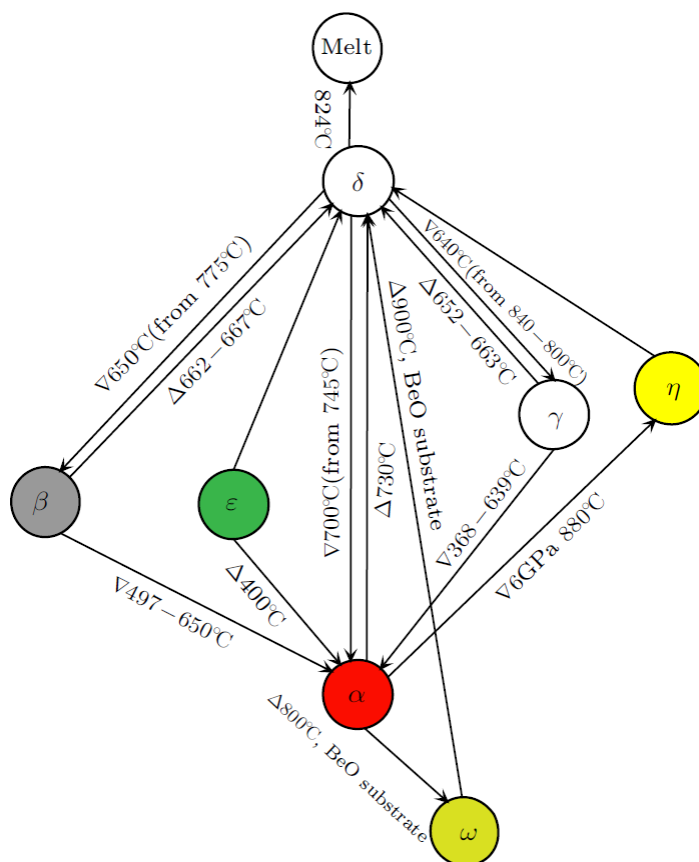


Figure 1.9 Phase transformations of bismuth oxide³³.

Furthermore, α - Bi_2O_3 has a deeper maximum valence band (E_{VB}) ($\sim + 3.13$ V vs. NHE), which infers a suitably high oxidation power from valence holes. However, α - Bi_2O_3 exhibits poor photocatalytic performance due to the inability of its conduction band electrons (E_{CB}) ($\sim + 0.33$ V vs. NHE) to scavenge surface oxygen molecules through a process in the reduction reaction of one electron ($E^0(\text{O}_2/\text{O}_2^{\bullet-}) = -0.33$ V vs. NHE), which results in the rapid recombination of photogenerated electron-hole pairs³⁴.

In all polymorphs of Bi_2O_3 , the valence band is composed of O2p and Bi6s orbitals, while the conduction band is comprised of Bi6p levels. Compared to other polymorphs, the valence band of β - Bi_2O_3 is shifted to higher energy, yielding a smaller band gap value. This phase exhibits enhanced electron transport arising from its c -axis oriented tetragonal structure. The electron mobility under irradiation is also enhanced by the lone-pair

electrons (Bi6s) present in the valence band³⁵. The high photoconductivity of β -Bi₂O₃ is attributed to its intrinsic polarizability and tetragonal structure, both of which favor the separation of photogenerated electron-hole pairs³⁶. Moreover, the lone pair in Bi provides a channel for photoexcited electron transport and reduces electron-hole recombination.

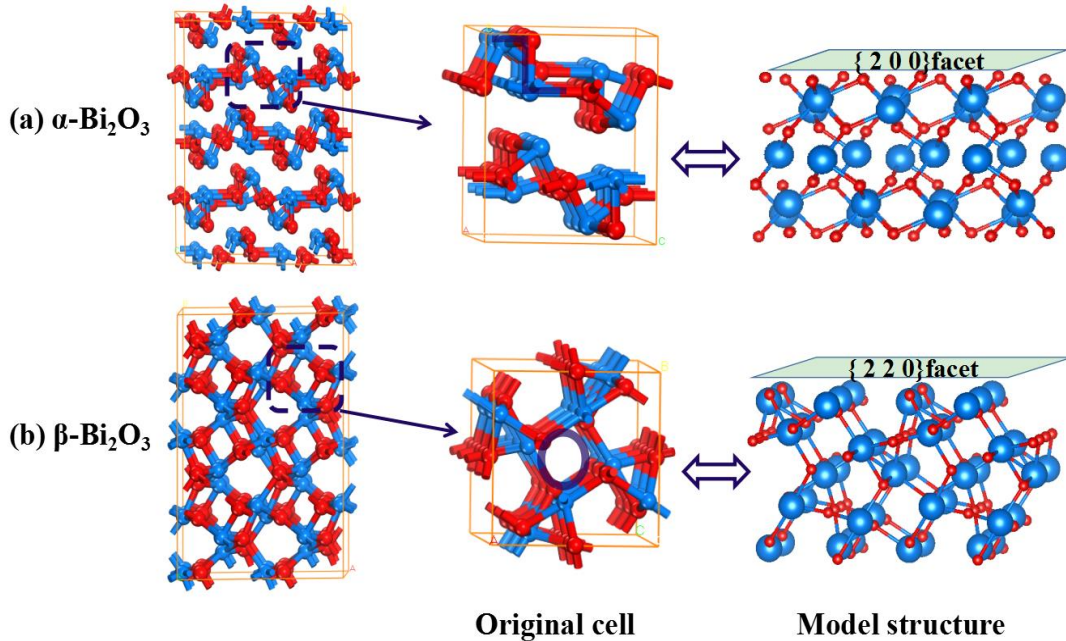


Figure 1.10 Crystal structure of α -Bi₂O₃ and β -Bi₂O₃ layers of bismuth and oxygen atoms of α -Bi₂O₃ are alternately arranged in a zigzag manner, while large tunnels penetrate the crystal structure of β -Bi₂O₃ along the Z-direction³⁵.

The unequal bond lengths cause the formation of irregular BiO₄ tetrahedrons, which share corners to form large-size straight tunnels throughout the entire crystal (Figure 1.10). This unique crystal structure results in free charge and mass transportation and hence induces high photocatalytic activity³⁵. Since there exists displacement between the centers of bismuth and oxygen atoms, every BiO₄ tetrahedron causes the formation of electric dipole moments (EDM). EDM of the four BiO₄ tetrahedrons are offset along the *c* axis, i.e., the tunnel direction. The components perpendicular to the *c* axis oppositely point to the tunnel wall, which will benefit the separation of the electron-hole pairs and induce the charge-carriers accumulation on the tunnel wall to react with the mass incoming from the

environments³⁷. Along with the many advantages of β - Bi_2O_3 as a semiconducting photoelectrochemical material, the β - Bi_2O_3 phase has one key disadvantage. The β - Bi_2O_3 is metastable at ambient conditions and thus may not be maintained over long periods of use³⁸.

Bismuth oxides have been studied as semiconductors for photocatalytic applications for the degradation of organic pollutants³⁹⁻⁴⁴, gas phase pollutants⁴⁵, and only some research has been carried out for their use in hydrogen generation^{8,46-49}. These studies show that bismuth oxides are potential candidates for hydrogen generation and their activity can be enhanced by coupling with other semiconductors or by grafting metal ions to the surface. Several approaches have been successfully developed to improve the photocatalytic performance of Bi_2O_3 , including control of the microstructure⁵⁰, fluorination and surface modification^{26,51,52} and the coupling with other semiconductors^{44,50,53-58}.

1.4.2. Bi-based heterojunctions

In reported literature several bismuth-based heterojunctions coupling Bi_2O_3 with other semiconductor has been probed to have high efficiency for photocatalytic hydrogen evolution. The synthesis of these heterojunctions shown an efficient coupling. Some of these processes include mechanical milling with post annealing³¹.

Bismuth-based heterojunctions has been synthesized by several chemical and physical process as sol-gel, impregnation method, mechanical milling followed by annealing at high temperatures, solid state reaction, among others. $\text{Bi}_2\text{O}_3/\text{Bi}-\text{NaTaO}_3$ ⁸, $\text{Bi}-\text{Bi}_2\text{O}_3-\text{TiO}_2$ ^{46,59}, $\text{Bi}_2\text{O}_3-\text{ZnO}$ ⁶⁰, $\text{Bi}_2\text{O}_3-\text{Cu}_2\text{O}$ ⁶¹⁻⁶⁴, $\text{Cu}_2\text{O}-\text{Bi}_2\text{O}_3-\text{TiO}_2$ ⁶⁵, $\text{Bi}_2\text{O}_3-\text{BiOCl}$ ⁶⁶, $\text{Bi}_2\text{O}_3-\text{SnO}_2$ ⁶⁷, $\text{Bi}_2\text{O}_3-\text{BiOI}$ ⁶⁸, $\text{Bi}_2\text{O}_3-\text{BiOBr}$ ⁶⁹, $\text{Bi}_2\text{O}_3-\text{Bi}_2\text{WO}_6$ ⁷⁰, $\text{Bi}_2\text{O}_3-\text{BaTiO}_3$ ⁵⁴ are some of the heterojunctions (Figure 1.11) that exhibits and enhancement on the photocatalytic activity for degradation of organic and inorganic compounds and hydrogen evolution under UV and visible light⁷¹. A study of the photoluminescence (PL) confirms the optimal amount of each catalyst, suppress the velocity of photorecombination of the photogenerated charge carriers. The higher heterojunction yield is mainly attributed to the separation of the electron-hole driven by the electric field as in the interface as in the semiconductors.

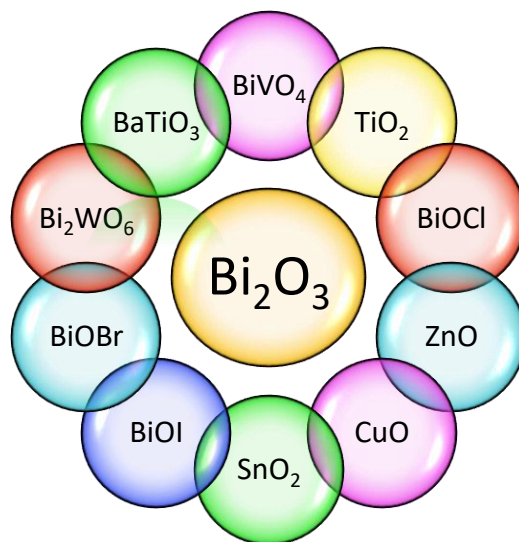


Figure 1.11 Visible light driven heterojunctions with $\beta\text{-Bi}_2\text{O}_3$ reported in the literature.

Between the heterojunctions reported in the literature, only few studies have probed the photocatalytic activity of Bi_2O_3 in a heterojunction assemble for hydrogen evolution. Some of this work is shown in [Table 1.1](#). The studies performed shown that Bi_2O_3 coupled to other semiconductor with a CB more negative than the potential of H_2 evolution is affordable to enhance the activity of both catalyst⁷². The H_2 evolution was performed even by water splitting or using some sacrificial agents as oxalic acid, methanol, methyl viologen among others^{8,73}. The photocatalytic efficiency reported in the table is the reaction rate as a function of moles of H_2 evolved per unit time. Even if reaction rates are not a standard value to compare the activity of different materials reported by different research groups. All of these studies reported an enhancement in the activity of the heterojunction compared with the single catalyst. Also, a red shifting in the absorbance spectra was observed which infers that Bi_2O_3 can serve as a photosensitizer and the heterojunction could be applied for visible light photocatalytic process⁷⁴.

Table 1.1 Photocatalytic efficiency of Bi₂O₃ based heterojunctions for hydrogen evolution.

	<i>Catalyst</i>	<i>Synthesis route</i>	<i>Photocatalytic H₂ production</i>	<i>Photocatalytic efficiency</i>	<i>Reference</i>
<i>Homo-junctions</i>	β/γ-Bi ₂ O ₃	Sol-gel method	Oxalic acid sacrificial agent	24.2 μmolg ⁻¹ h ⁻¹	49
<i>Hetero junctions</i>	Bi ₂ O ₃ /Bi–NaTaO ₃	Solid-state reaction	Methanol sacrificial agent	102.5 mmolh ⁻¹	8
	α- Bi ₂ O ₃ /TiO ₂ -xNx	Soft chemistry method- Homogeneous coprecipitation	Water splitting	198.4 μmolh ⁻¹	75
	Bi ₂ O ₃ /TiO ₂	Impregnation method	Water splitting	26.02 mmolh ⁻¹ g ⁻¹	46
	Bi /β-Bi ₂ O ₃ / anatase-rutile TiO ₂	Impregnation method and annealing	Water splitting	920 μmolh ⁻¹	47
	Pt/Bi ₂ O ₃ /RuO ₂	Platinization and high temperature synthesis in Ar atmosphere	Methyl viologen sacrificial agent	0.66 mLh ⁻¹	73
<i>Metal doping</i>	IIIA elements (Al, Ga, In and Tl) β-Bi ₂ O ₃	Polarized density function theory	Calculus of metal displacement	Co-doped N/In and N/Ti	76
	Doping of transition metal ions γ-Bi ₂ O ₃	High temperature synthesis	Water splitting	1 at % Pd (II)/γ-Bi ₂ O ₃ 35.23 μmolh ⁻¹	77
	Bi/β-Bi ₂ O ₃	Pulverization of magnetron method and electrolysis treatment	Water splitting	15.8 μmolh ⁻¹	48

1.5. Objectives and thesis outline

The development of a new visible light driven bismuth-based material to produce hydrogen from photocatalytic reactions represent a sustainable pathway to produce green energy fuel as well an eco-friendly method. However, the low photocatalytic activity of single semiconductors relies in the fast rate of recombination of the photogenerated electron-hole pairs. This leads to the design and engineering of coupling two semiconductors in a heterojunction assemble. This PhD thesis is devoted to fabricating bismuth-based heterojunctions by a simple, affordable, and green synthesis route and evaluate the photocatalytic activity for H₂ generation. The band gap energy, photoluminescence, particle size and morphology, surface area, structural parameters and flat band potential are some of the properties measured in the single catalyst and its heterojunctions that will elucidate the enhancement in performance of the synthesized heterojunction and to understand the photocatalytic reactions mechanism for H₂ evolution.

The tetragonal phase of bismuth oxide β -Bi₂O₃ that presents remarkable physicochemical properties was chose to synthesize the heterojunctions by coupling with three different metal oxides: Cu₂O, ZnO and Bi_{0.5}Na_{0.5}TiO₃. Since it is well reported that the synthesis method will have a significant influence in the coupling between both semiconductors, two different methods were performed and analyzed: mechanical milling and flame spray (FS) process. The specifics objectives to be achieved are:

- (i) Synthesize β -Bi₂O₃ by flame spray process with high purity and a narrow band gap energy and characterize its physical and chemical properties (Chapter 2).
- (ii) Synthesize bismuth base heterojunctions Bi₂O₃/Cu₂O, Bi₂O₃/ZnO and Bi₂O₃/Bi_{0.5}Na_{0.5}TiO₃ by mechanical milling and evaluate the structural and optical properties to enhance the transfer of the photogenerated charge carriers and study the heterojunction coupling (Chapter 4 and 5).
- (iii) Measure the flat band potential and the semiconducting type of each catalyst to determine the conduction band and valence band potential (Chapter 4 and 5).

- (iv) Evaluate the photocatalytic activity and the quantum yield for methanol oxidation and H₂ evolution in presence of sacrificial agents and propose a possible mechanism of the photocatalytic reactions (Chapter 3, 5 and 6).

Chapter 2: Synthesis and characterization of photoactive β -bismuth oxide by flame spray

This chapter contains the article *Manufacturing of photoactive β -bismuth oxide by flame spray oxidation* by María Teresa Ayala Ayala, Martha Yasmid Ferrer Pacheco and Juan Muñoz Saldaña, published in *Journal of thermal spray technology*, 2021, 30, 4, 1107-1119. “Reproduced with permission from *Springer Nature*”.

2.1. Introduction

During the past decades, bismuth-based oxides, such as perovskites, pyrochlores, Aurivillius, among others have stimulated extensive research related to the preparation, modification, and applications in alternative energies, biomedicine, and environmental remediation^{29,78-81}. Particularly, solutions for environmental remediation taking advantage of the photocatalytic properties of bismuth-based materials are nowadays of big interest.

Bismuth-based semiconducting materials can be excited by visible light irradiation due to their electronic structure and a narrow band gap energy, E_g , which is lower than 3 eV. For instance, bismuth oxide (Bi_2O_3) has received much attention as a potential visible light active photocatalyst for both solar energy conversion and environmental remediation because of its efficient photocatalytic activity, high stability, low cost, and nontoxicity³⁰. Its photocatalytic performance is itself closely related to the phase, morphology, structure, size, band gap, surface area, crystallinity, rate of the charge transfer, efficiency of charge separation, among others²⁹. The narrow band gap energy of Bi_2O_3 is dependent on its crystal structure (2.2-2.8 eV), which is found in seven polymorphs: low-temperature stable monoclinic α ⁸², high-temperature stable fcc δ , and the metastable tetragonal β , bcc γ ⁸³, orthorhombic ε ⁸⁴, triclinic ω ⁸⁵ and high-pressure hexagonal phases⁸⁶.

The tetragonal β phase has an E_g of ~ 2.3 eV and higher photocatalytic performance than the other Bi_2O_3 polymorphs. β -phase has a unique tunnel structure caused by the special orientation of Bi^{3+} lone electron pairs (LEPs). Its tunnel structure is ideal for the transfer of the photogenerated electrons and holes, preventing their excessive

recombination and enabling more free carriers to participate in the photocatalytic process^{36,87}.

It is well known that the physical and chemical and therefore photocatalytic behavior of bismuth-based materials are also strongly dependent on their synthesis method⁸⁸. The synthesis of β - Bi_2O_3 powder has been reported by several routes that include conventional chemical methods^{34,42,89–91} using bismuth nitrates and carbonates as precursors, and alternative physical methods based on the oxidation of granulated bismuth under air or vacuum atmospheres^{92–94}. For instance, liquid phase microwave irradiation allowed the synthesis of β - Bi_2O_3 nanoparticles with an E_g of 2.77 eV using $\text{Bi}(\text{NO}_3)_3 \cdot 5\text{H}_2\text{O}$ as a precursor. The obtention of yellowish precipitate has been reported to take place under irradiation with 500 W of power for 90 min and then centrifugated and washed several times before drying. This precipitate was finally calcined at 300 °C for 4 h to stabilize the β - Bi_2O_3 ⁹⁵.

The hydrothermal process has also been frequently reported for the synthesis of β - Bi_2O_3 powder with specific morphology e.g. flower-like⁹¹ or nano-sized sheets⁹⁶. Both methods use consistently $\text{Bi}(\text{NO}_3)_3 \cdot 5\text{H}_2\text{O}$ as a precursor. In the former method, a white suspension was formed by adding acetic acid and ethanol, which was cleared by stirring and adding N,N-dimethylformamide. The solution was transferred to a Teflon-lined autoclave and heated at 100 °C for 40 min. Thermal decomposition of the dried precursors was obtained by heating the previously washed solution (with deionized water and ethanol) at 350 °C for 4 h at a heating rate of 2 °C/min. The obtained powder showed an orange-yellow color with flower-like morphology having a E_g of 2.39 eV⁹¹. Upon similar hydrothermal process conditions, β - Bi_2O_3 sheets were synthesized following a hydrothermal procedure that requires a Teflon stainless autoclave. The precursor was dissolved in benzyl alcohol under stirring before being transferred to an autoclave and heated at 240 °C for 24 h. The obtained samples were collected, several times washed, vacuum-dried and post-heat treated at 300 °C for 5 h. The obtained β - Bi_2O_3 powder exhibited a sheet-like morphology and a band gap energy of 2.48 eV⁹⁶.

It is clear that methods of chemical synthesis of β - Bi_2O_3 powder with interesting morphological characteristics and a narrow band gap energy with high photocatalytic activity for organic pollutants degradation are available in the literature. However, the necessity of an alternative method to synthesize photoactive β - Bi_2O_3 powder in one-step and high volumes with desired physical and chemical properties still exists.

Flame spray is a low-cost, high performance thermal spray technique typically used to manufacture coatings⁹⁷. The process consists of atomizing particles in a compressed gas that have been melted or are in a semi-molten state thanks to the energy released by a heat source. Combustion between premixed oxygen and acetylene gas provides the energetic jet stream. Particles with velocities below 100 m/s are generally achieved. The lower speed experienced by the in-flight particles compared to other TS techniques can be exploited to increase the particle's dwell time inside the jet, thus improving their temperature⁹⁸. The flame temperature is in the range between 2727-3077 °C, where particles only reach however 70% of this temperature depending on their residence time in the flame⁹⁷.

Therefore, flame spray oxidation of bismuth seems to be promising to control oxidation characteristics of semi-metallic bismuth, the phase transformation of the formed oxides as well on their physicochemical properties. However, the synthesis of highly pure tetragonal bismuth oxide with controlled physical and chemical properties by flame spray is still challenging since the process is highly chaotic. The analysis of process parameters by design of experiments is required seeking to obtain specific particle size distribution, morphology, and phase transformations. Particularly, key factors to stabilize metastable β - Bi_2O_3 at room temperature are dependent on the residence time and intrinsic high cooling rates^{99,100}.

In this work, flame spray oxidation was used to synthesize β - Bi_2O_3 by using bismuth pellets obtained from mineral compounds from Mexico¹⁰¹. The structural and microstructural properties of the oxidation products were studied by varying feedstock particle size, and stand-off distance (SOD) by a 2²-factorial design of experiments. Oxidation characteristics of bismuth particles are presented and discussed.

2.2. Materials and methods

2.2.1. Powder synthesis

Bismuth needle-shaped pellets obtained from mining beneficiation of 1-2 cm in size (Industrias Peñoles SA, Mexico) were used as precursor material and milled in a planetary mill (PM400 Retsch, Hann, Germany) for 30 min using a 10:1 ball to powder ratio at 250 rpm. Milled bismuth powder was classified in fine and coarse particles by sieving, passing through 600, 325, and 140 mesh sieves.

The synthesis of β - Bi_2O_3 was carried out by flame spray oxidation using a 6PII gun (Oerlikon Metco, New York, USA) with a ceramic-type nozzle. 99.999% pure nitrogen gas (Atlas-Copco NPG+ SKID plant) was used for particle feeding with a Sulzer Metco 5MPE powder feeder (New York, USA). The combustion atmosphere was fixed for an oxygen/fuel ratio of 1:1.15 ($\text{lmin}^{-1}:\text{lmin}^{-1}$) (oxygen/acetylene) that corresponds to a neutral flame¹⁰².

The fed powder was heated and oxidized thanks to the energy released during the reaction in the flame spray process, in which the combustion of oxygen/acetylene mixture has an enthalpy of 8714 kJ/kg. Bismuth powder was fed at a rate of 18 g/min with high pure nitrogen flow to the flame spray gun that carries an oxygen/acetylene gas for the oxidation of bismuth varying the SOD and feedstock particle size.

The parameters used for the synthesis of Bi_2O_3 powder by flame spray (Table 1) were varied in a 2²-factorial design. The SOD measured from the nozzle to the surface of the water was set at 20 cm and 30 cm. The feedstock particle size of bismuth powder was fixed at 16-60 μm and 18-122 μm distributions. From the factorial experimental design, four experiments were performed labeled as *20P1*, *30P1*, *20P2*, and *30P2*, where *P1* and *P2* correspond to fine and coarse feedstock powder, respectively, and 20 and 30 are the used SOD (in cm). A home-made set-up able to collect either evaporated or quenched in-flight particles in water was used (Cinvestav-CENAPROT). The evaporated particles were collected by condensation and identified as “nanometric sized powder.” The water quenched powder was identified as “micrometric sized powder.”

2.2.2. Structure and microstructure

Phase identification was performed by X-ray diffraction XRD with a Rigaku TX, USA Dmax 2100 diffractometer with monochromatic radiation $\text{CuK}\alpha$ ($\lambda = 1.5406 \text{ \AA}$) operating at 30 kV and 20 mA. Diffraction patterns were collected in the range of 20° to 60° of 2θ scale with a 0.02 step size and a step time of 0.5 s with a fixed angle of 5° . Phase quantification was determined by Rietveld refinement using *GSAS*® software¹⁰³.

The size distribution of bismuth feedstock was measured using the laser diffractometer (HELOS/BR, Sympatec GmbH, Germany). The technique for measuring the dry powder was REDOS, where samples were placed in the powder feeder and air pressurized at 200 kPa.

Analysis of morphology and particle size distribution of synthesized powder was done by field emission scanning electron microscopy (FESEM) using a JEOL 7610F microscope (Tokyo, Japan) with secondary electron (SE) detector at 2 kV and backscattering electron (BSE) detector at 15 kV electron acceleration voltage. The cumulative size distribution of flame spray powder was determined by ImageJ®¹⁰⁴. For each sample, the average particle size was measured in at least 5 micrographs.

The oxidation mechanism of the obtained micrometric powder was analyzed by cross-sectional area of the as-synthesized powder. The powder was embedded in epoxy resin and polished until the particle cross section was observed in an optical microscope. These samples were analyzed with a scanning electron microscope XL30 ESEM-Philips (Massachusetts, USA) using energy dispersive spectroscopy (EDS) for semi-quantitative chemical composition characterization. The oxidation characteristics of bismuth were identified by tracking the oxygen distribution with EDS using a backscattering electron detector. The semi-quantitative chemical characterization was analyzed with an atomic and mass percentage on at least 3 zones of sample cross-sections.

2.2.3. Thermal transformation analysis

Phase transitions of commercially available α - Bi_2O_3 powder (Sigma-Aldrich S. de RL. de CV.) have been studied using differential scanning calorimeter/thermogravimeter DSC-TGA (SETSYS Setaram, Caluire-etCuire, France). DSC-TGA was run using 70 mg of the powder in platinum crucibles. The heating stage was performed from 400 °C up to 800 °C at a rate of 1 °C/min in air. The cooling stage was performed from 800 °C up to 25 °C varying the cooling rate up to 10 °C/min.

2.2.4. Optical properties

UV-Vis NIR spectrophotometry was used to determine the band gap energy of the prepared Bi_2O_3 powder with a Varian spectrophotometer (Cary 5000) coupled to a PTFE integration sphere (Malvern, UK). The band gap was determined by measuring reflectance spectra and using Tauc plot (Eq 2.1), of the intersection of the extrapolated tangent, which is based on the Kubelka-Munk theory¹⁰⁵.

$$F(R)hv = k(hv - E_g)^n \quad (\text{Eq 2.1})$$

where h is the Planck's constant (4.135E-15 eVs), ν is the frequency of light (s^{-1}), k is a proportional constant, E_g is the band gap energy (eV), and n is $\frac{1}{2}$ or 2 if it is a direct permitted or indirect permitted transition. $F(R)$ is a function of reflectance and is calculated with the following equation (Eq 2.2).

$$F(R) = \frac{(1-R)^2}{2R} \quad (\text{Eq 2.2})$$

The band gap energy value was obtained by plotting $(F(R)hv)^{1/2}$ vs hv and extrapolating a linear fit to the abscissa axis¹⁰⁶.

2.3. Results and discussion

2.3.1. Characterization of precursor bismuth powder

As mentioned in the experimental section, bismuth feedstock powder was classified in fine and coarse by milling and sieving with different mesh number. Figure 2.1a and 2.1b show the SEM micrographs of both milled powders. The powder

morphology is irregular with flat faces and pronounced corners at the edges, which is expected due to the milling process. [Figure 2.1c](#) shows the cumulative particle size distribution $Q3\%$ (black lines) and the distribution density $q3$ (blue lines) of both powder types. Fine powder presents a maximum frequency of 38.8 μm , while the maximum frequency for coarse powder is 78.7 μm . 90% of the cumulative distribution of fine particles has a maximum size of 60 and 122 μm for coarse particles. Geometry and particle size distribution are relevant characteristics of the fed powder because of its direct influence in energy and mass transfer with the gas flow during the oxidation process.

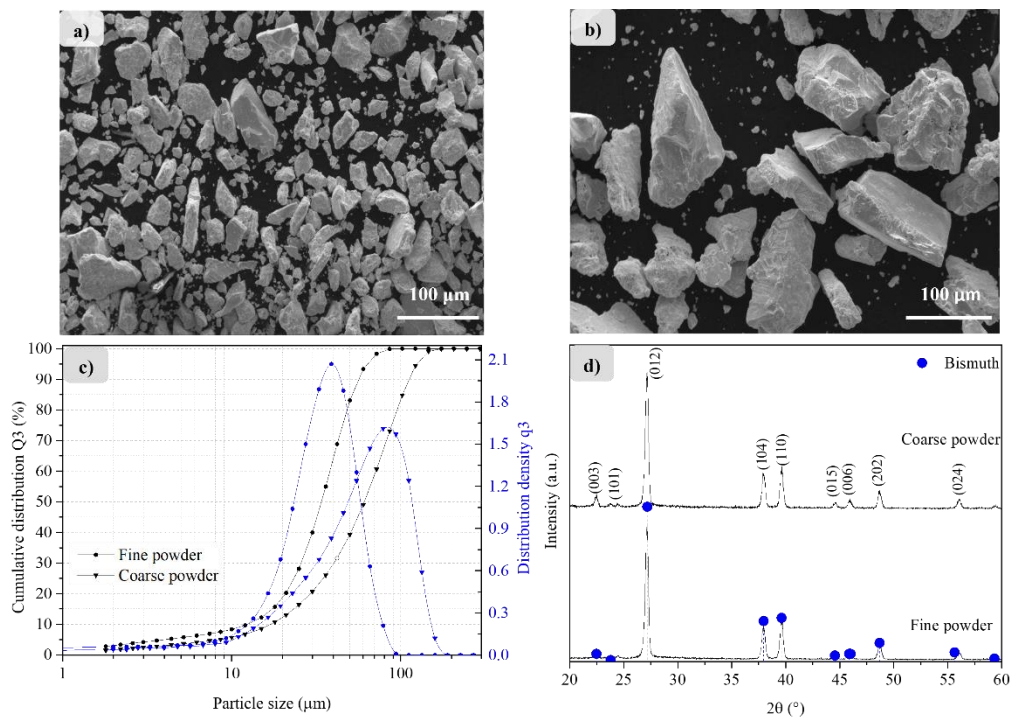


Figure 2.1 SEM micrographs of a) fine and b) coarse bismuth feedstock powder, c) cumulative particle size distribution and d) X-ray diffraction patterns.

X-ray diffraction patterns of milled bismuth powder are shown in [Figure 2.1d](#). In both samples, a single bismuth phase is identified according to the PDF 44-1246 with

the theoretical lattice parameters $a = b = 4.547 \text{ \AA}$, $c = 11.8616 \text{ \AA}$, hexagonal structure, and space group $R\text{-}3m$. XRD patterns evidence a pure semi-metallic bismuth phase.

2.3.2. Phase transitions of Bi_2O_3 by DSC

Phase transformations were analyzed in a commercial $\alpha\text{-Bi}_2\text{O}_3$ powder by DSC. Figure 2.2 shows the DSC plot, where positive or negative heat transfer is identified with up and down arrows, which respectively correspond to exothermic and endothermic reactions. According to previous data reported elsewhere, two intermediate metastable phases can be obtained by quenching the $\delta\text{-Bi}_2\text{O}_3$ phase from temperatures between 730 and 823 °C. β and γ are present in the range between 667-662 °C and 652-633 °C, respectively. The transformations $\delta \rightarrow \beta$ and $\delta \rightarrow \gamma$ depend not only on the chosen atmosphere but also on the used cooling rate³³.

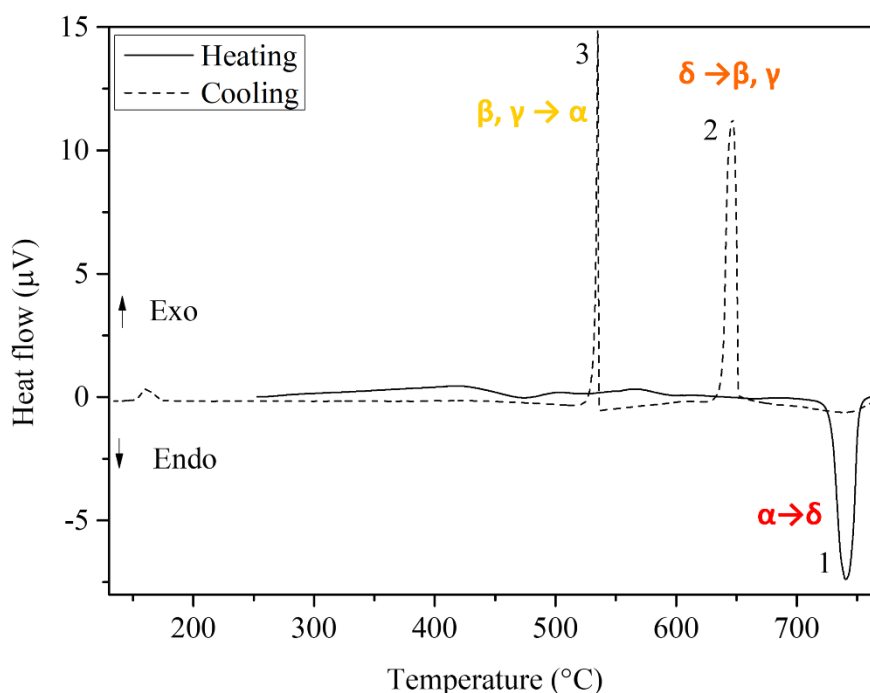


Figure 2.2 Thermal behavior of $\alpha\text{-Bi}_2\text{O}_3$ starting powder.

In the current results, a unique transition from α to δ (peak 1) is present on heating at 730 °C⁹⁹. During cooling from 800 °C to room temperature and a cooling rate of 10 °C/min, two endothermic phase transitions are observed at 660-630 °C (peak 2) and 538-518 °C (peak 3). In the case of peak 2, the $\delta \rightarrow \beta$ and $\delta \rightarrow \gamma$ transformations seem to be overlapped. The latter transition (peak 3) corresponds to the formation of α -Bi₂O₃, which remains stable at room temperature.

The analysis as a function of cooling rates (not shown here) allowed retaining both phases at room temperature in a metastable state if high cooling rates and oxidizing atmospheres are used. Based on these results, it is possible to envisage retaining the β -Bi₂O₃ by flame spray if abrupt cooling (high cooling rates) from temperatures above 650 °C is undertaken, which can be easily achieved by collecting evaporated or water quenched in-flight particles.

Thermally sprayed oxidized powder was collected in two ways, from evaporated particles and quenched in water inferring two mechanisms of bismuth oxidation. Bigger particles dropped into the water leading to partial oxidation, whereas a certain number of fine particles evaporated and were completely oxidized due to the high temperature of the flame.

2.3.3. Characterization of nanometric-sized bismuth oxide powder

The evaporated powder presents a characteristic bright yellowed color and nanometric particle size. This powder was labeled as “nanometric” and its physicochemical properties were as follows. [Figure 2.3](#) shows typical SEM micrographs recorded at high magnifications of the nanometric powder obtained by varying the SOD and particle size of feedstock powder.

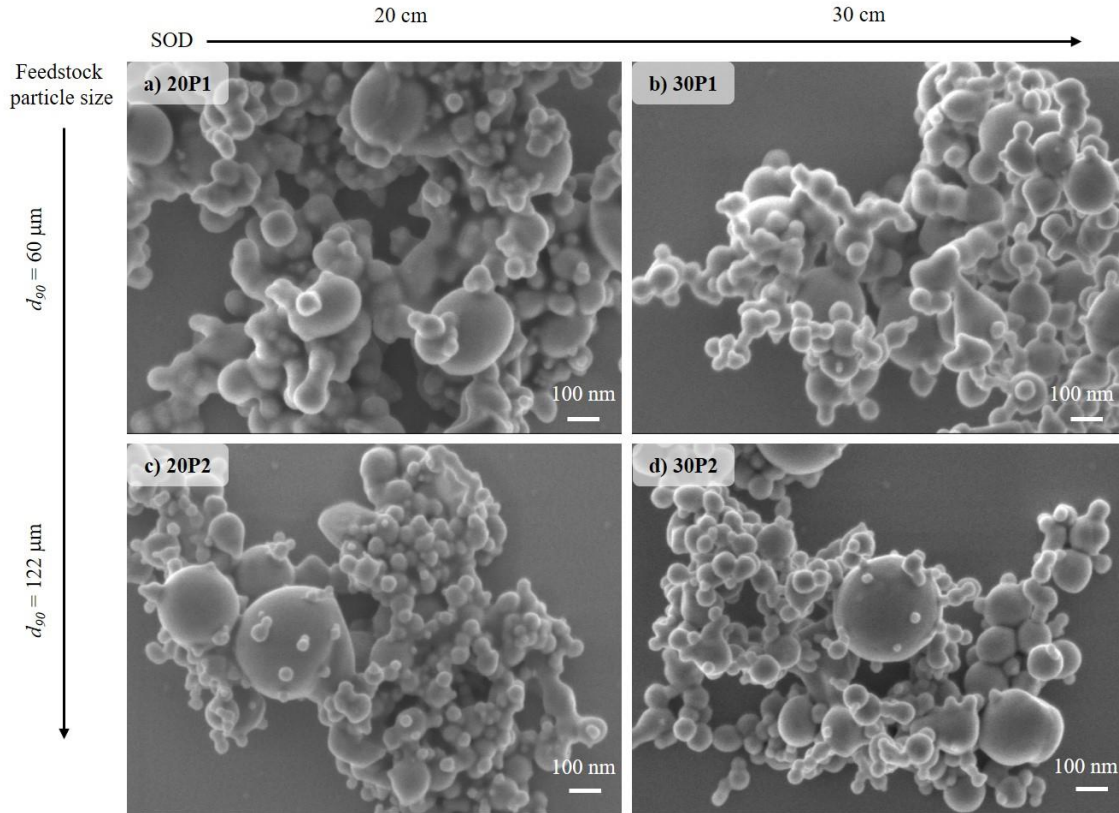


Figure 2.3 SEM micrographs for nanometric sized thermal sprayed β - Bi_2O_3 powder.

The synthesized powder showed agglomerated nanometric sized spherical particles. Most particles have sizes less than 100 nm and few bigger ones of around 200 nm, irrespective of the tested processing conditions. Agglomeration is observed in samples 20P1 and 30P1 (Figure 2.3a and 2.3b) when fine feedstock powder is used. The produced nanometric particles have a large effective contact surface, which causes friction and electrostatic forces between them promoting agglomeration. The cumulative size distribution of this powder is shown in Table 2.1. For each sample, at least 5 micrographs were measured reporting the average particle size. The 90% (d_{90}) of the cumulative distribution of nanometric particles has a maximum size between 227-163 nm for fine feedstock powder and 188-133 nm for coarse powder.

Table 2.1 Flame spray parameters and particle size distribution of thermal sprayed nanometric and micrometric sized powder.

Sample ID	Standoff distance (cm)	Cumulative particle size distribution			
		Precursor bismuth powder (μm)	Micrometric oxidized powder (μm)	Nanometric oxidized powder (nm)	
20P1	20	d_{10}	12	11 ± 1.41	49 ± 3.05
		d_{50}	36	26 ± 1.41	100 ± 2.04
		d_{90}	60	41 ± 5.65	227 ± 5.18
30P1	30	d_{10}	12	15 ± 7.07	56 ± 5.18
		d_{50}	36	26 ± 5.65	94 ± 1.19
		d_{90}	60	35 ± 2.82	163 ± 3.38
20P2	20	d_{10}	18	10 ± 0.10	25 ± 1.51
		d_{50}	60	38.5 ± 2.12	56 ± 2.29
		d_{90}	122	63.5 ± 2.12	188 ± 4.21
30P2	30	d_{10}	18	14.5 ± 0.70	28 ± 1.52
		d_{50}	60	36.5 ± 2.12	57 ± 2.43
		d_{90}	122	61.5 ± 9.19	133 ± 3.92

An increase in the SOD decreases the size of the nanometric oxidized powder (see d_{90} in Table 2.1). Additionally, an increase in the size of feedstock powder decreases the size of the nanometric oxidized powder. Specifically, fine P1 feedstock generated agglomerates of nanometric sized particles, which are larger than those obtained with coarse P2 feedstock.

X-ray diffraction and Rietveld refinement patterns of as-synthesized powder are shown in Figure 2.4. A typical XRD pattern of 20P1 sample is shown in Figure 2.4a. All

samples exhibit a high pure Bi_2O_3 phase with a tetragonal structure. No evidence of secondary phases or impurities was observed. All diffraction lines can be indexed to a tetragonal phase with $a = b = 7.742 \text{ \AA}$, $c = 5.631 \text{ \AA}$ unit cell parameters identified with PDF 27-0050 with a space group $P421-c$.

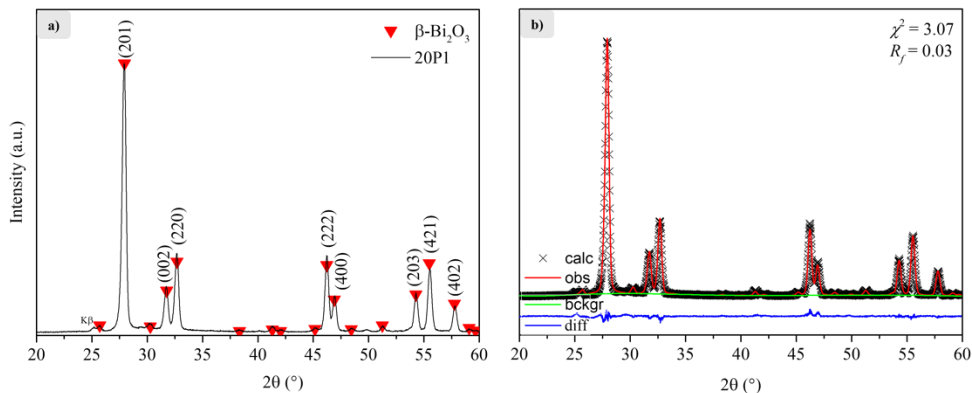


Figure 2.4 a) X-ray diffraction and b) Rietveld refined patterns of nanometric sized thermal sprayed $\beta\text{-Bi}_2\text{O}_3$ powder.

Rietveld refinement allowed us to calculate the structural parameters of as-synthesized powder. **Figure 2.4b** shows the refined pattern of *20P1* sample. The calculated lattice parameters are $a = b = 7.7405 \text{ \AA}$ and $c = 5.6328 \text{ \AA}$, which are in good agreement with theoretical values. The goodness coefficient (χ^2) and the structural factor (R_p) are 3.07 and 0.03, respectively, which represent the refinement quality (**Figure 2.4b**). The R_p -value suggests an excellent relationship between the calculated model and the experimental XRD pattern.

The optical absorption characteristics of the as-synthesized Bi_2O_3 measured respective to its band gap energy are shown in **Figure 2.5**. The band gap energy for a semiconductor can be measured by plotting $(F(R)hv)^{1/n}$ vs hv that corresponds to Tauc plot (Eq 2.1). As mentioned before, the function of reflectance $F(R)$ (**Figure 2.5a**) is determined by a method based on the Kubelka-Munk theory¹⁰⁵ (Eq 2.2). **Figure 2.5b** shows the

measured band gap energy of β - Bi_2O_3 by extrapolating the tangent of Tauc plot by a linear fit. For an indirect allowed transition $n = 2$, as obtained β - Bi_2O_3 powder possess a band gap energy of 2.26 eV. These results show that β - Bi_2O_3 can be excited in the visible range of the solar spectrum from 548 nm to the UV region and be applied as a visible light driven semiconductor for photocatalytic applications. Thus, flame spray oxidation allows obtaining a photoactive highly pure tetragonal bismuth oxide with a nanometric spherical morphology and a narrow band gap energy.

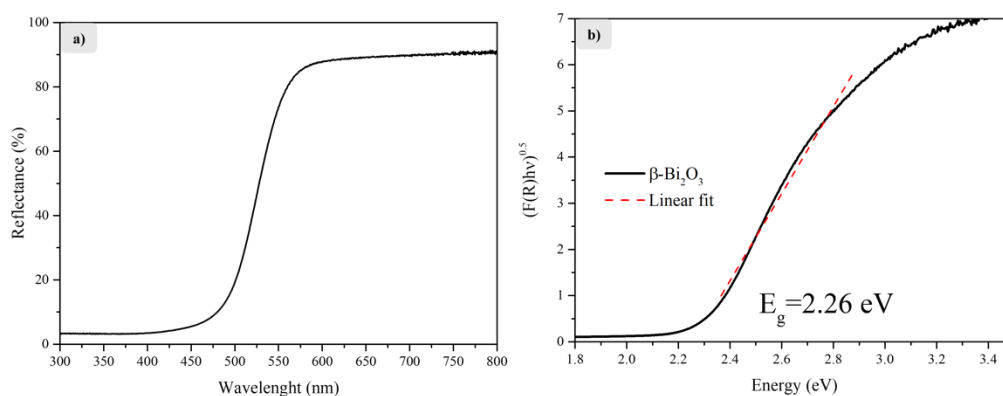


Figure 2.5 a) Reflectance spectra and b) Tauc plot to determine the indirect band gap energy of β - Bi_2O_3 .

2.3.4. Characterization of micrometric-sized bismuth oxidized powder

The quenched powder (collected in water) was labeled as “micrometric” and can be distinguished by a dark green color. The morphology of the micrometric sized oxidized powder recorded with a BSE detector is shown in [Figure 2.6](#). The micrometric powder showed particles with a rough surface and an approximately spherical morphology joined to the hemispheres of other smaller particles. Molten in-flight particles collided with each other leading to particular agglomeration features between few elements leading to the formation of the so-called “snowman-like” morphology^{107,108}. These particles show different colors, associated with at least two different phases. Clear zones Z_1 correspond to bismuth while the dark zones Z_2 are

Synthesis and characterization of photoactive β -bismuth oxide by flame spray

bismuth oxides (see arrows from Fig. 2.6c) according to their molecular weight. Samples 20P1 and 30P1 (Fig. 2.6a and 2.6b, respectively) present smaller particles < 50 μm compared to samples 20P2 and 30P2 > 50 μm (Fig. 2.6c and 2.6d, respectively).

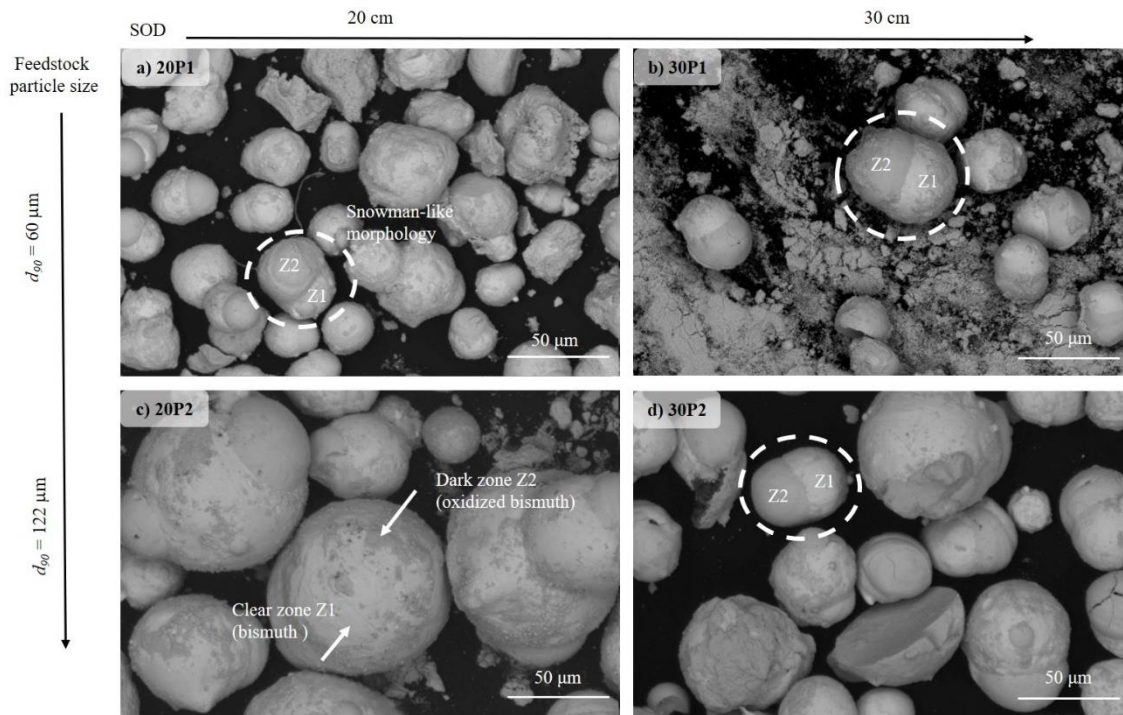


Figure 2.6 SEM micrographs of micrometric sized thermal sprayed β - Bi_2O_3 powder.

Table 2.1 shows the cumulative size distribution of the micrometric oxidized powder. The size of this powder decreases as the SOD distance increases. The d_{90} of this powder using fine P1 feedstock is 37 μm and 33 μm for SOD of 20 cm and 30 cm respectively. In the case of coarse P2 feedstock, the d_{90} size is 68 μm and 64 μm for SOD of 20 cm and 30 cm, respectively. Thus, the size of the obtained powder directly depends on the size of the feedstock material and is inversely proportional to the SOD distance, i.e., the size of the obtained micrometer powder decreases as the spray distance increases.

A change in the morphology and size of the feedstock powder is expected to take place interacting with the flame spray. It is well known, that the shape changes from irregular/angular morphology to a spherical shape (droplets formation) due to the flame process⁹⁷. The particles are subject to conductive heat transfer and become spherical after reaching their melting point (271 °C) while passing through the flame. All particles exhibit rough surfaces generated due to the quenching into cool water and in some cases address fractures because of the thermal shock. During the in-flight, the particles start evaporating (1564 °C) after reaching their melting point, where the amount of evaporated mass depends on the size, thermal conductivity, speed, and trajectory followed by each particle, leading to a decrease in size of the oxidized particles⁹⁷.

X-ray diffraction patterns of micrometric sized powder are shown in [Figure 2.7a](#). All samples present not oxidized bismuth identified with PDF 44-1246. The oxidized bismuth shows a tetragonal structure identified with PDF 27-0050. Moreover, samples *20P1* and *30P1* show a higher content of β -Bi₂O₃ according to the relative intensity of (201) plane at 27.9° of 2θ .

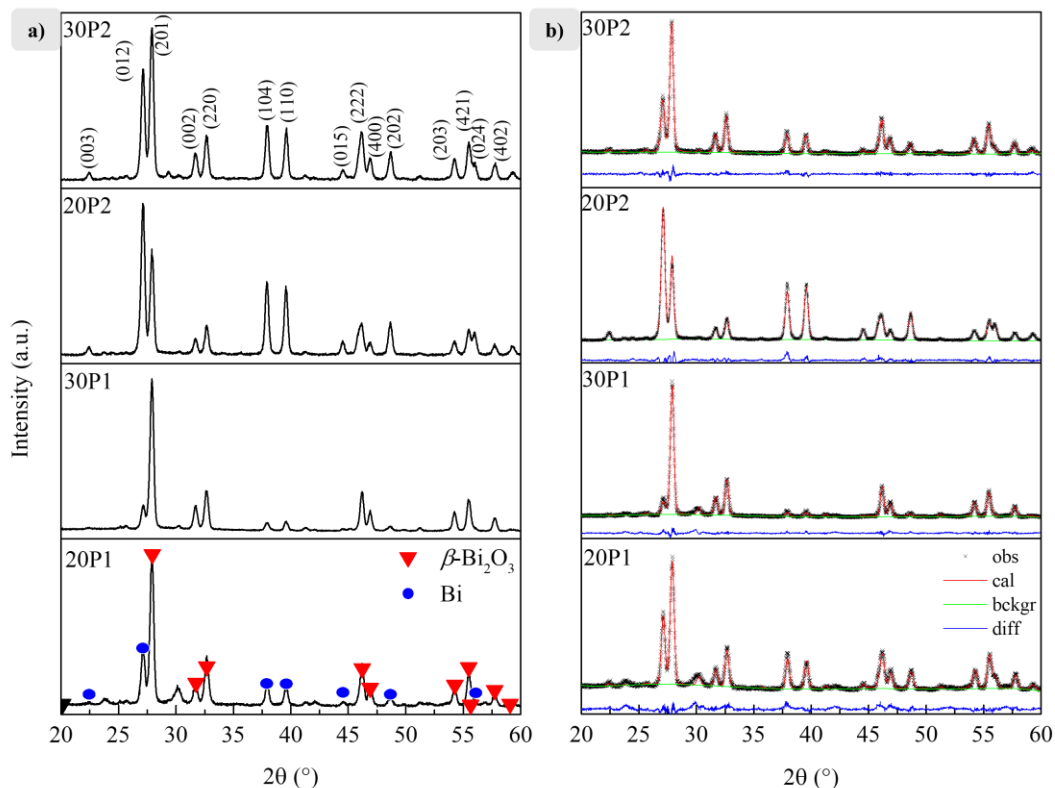


Figure 2.7 a) X-ray diffraction and b) Rietveld refined patterns of micrometric sized thermal sprayed bismuth oxidized powder.

Rietveld refinement was done to all X-ray patterns to quantify the phase content of samples and evaluate the effect of the flame spray process on the structure of bismuth oxide (Fig. 2.7b). Each refinement is composed by four curves: a) the experimental patterns (shown in black), b) the adjusted patterns (red), c) the adjusted background to calculate the phase content and lattice parameters (green) and d) the error line (blue) generated from the difference between the experimental and adjusted patterns. The obtained χ^2 and R_f were 3 and 0.1, respectively (Table 2.2). The quantification confirmed that samples prepared with fine feedstock powder (sample 20P1 and 30P1) exhibit a higher content of β -Bi₂O₃ 77% and 91%, respectively. The increase in SOD generates an increase in the amount of oxidized bismuth, which was consistently observed for fine and coarse feedstock powder.

In all samples, the lattice parameters a and c of β - Bi_2O_3 increased respectively to the theoretical value. Particularly, *30P1* sample presents the highest expansion of the crystal lattice generated due to the thermal spray process. β - Bi_2O_3 exhibits enhanced electron transport arising from its c -axis oriented tetragonal structure and its intrinsic polarizability. As mentioned before, the unique tunnel structure of β - Bi_2O_3 due to the special orientation of Bi LEPs has been reported to be associated with its excellent photocatalytic activity. These tunnels provide channels for the transfer of the photogenerated electrons and holes, preventing their excessive recombination and enabling more free charge carriers to participate in the photodecomposition process^{72,109}.

Table 2.2 Structural parameters of micrometric sized thermal sprayed powder obtained from Rietveld refinement.

Sample	Lattice parameters for		Phase fraction		GoF	Rf
	β - Bi_2O_3 (Å)		(wt.%)			
	$a=b$	c	β - Bi_2O_3	Bi		
<i>Theoretical</i>	7.743	5.631	100	0	—	—
<i>20P1</i>	7.739	5.635	77.9	22.1	3.22	0.12
<i>30P1</i>	7.751	5.642	91.07	8.92	1.98	0.04
<i>20P2</i>	7.747	5.640	41.44	58.55	2.33	0.04
<i>30P2</i>	7.744	5.636	71.64	28.35	2.36	0.10

It is worth mentioning that the physicochemical characteristics of this powder make it suitable to be used in spraying deposition processes, e.g., by cold spray.

2.3.5. Influence of flame spray parameters on oxidation characteristics of bismuth

The influence of thermal spray parameters is evidenced in the content of bismuth oxide. As mentioned before, a smaller feedstock size leads to a higher oxidation content. If the particle possesses a smaller diameter the heat transfer from the surface onto the core is favorable and the oxidation process is promoted. A similar effect is obtained with longer stand-off distances. The residence time of the in-flight particle in the flame increases by increasing the SOD. The particle is surrounded by oxidant gas for a longer time. Smaller particles have a higher surface area which maximizes the total content of formed bismuth oxide. Under these conditions, bismuth coarse powder does not completely oxidize due to its big size. The low surface area carries out poor contact with oxygen molecules. Moreover, the residence time of the in-flight particles in the heat zone of the flame is not enough to reach a melting state diminishing the conditions promoting oxidation^{97,102}.

For the sake of clarity, the effect of flame spray parameters, feedstock size, and SOD combinations on the oxidation of bismuth and the size of the micrometric as-synthesized powder is shown in [Figure 2.8](#). This figure provides a good summary of previously described effects, where the formation of β - Bi_2O_3 is promoted by using fine bismuth feedstock powder and small SOD ([Figure 2.8a](#)). The same effect is evidenced in the synthesis of small micrometric β - Bi_2O_3 particles ([Figure 2.8b](#)). This analysis agrees with the literature that establishes that oxidation of particles increases with the temperature, a higher residence time of in-flight particles in the flame by increasing SOD and with an adequate size of feedstock powder.

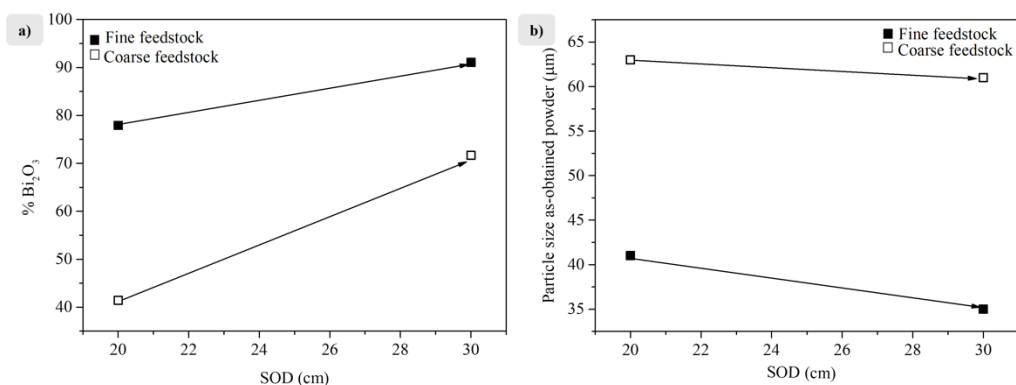


Figure 2.8 Effect of SOD and feedstock particle size on the a) phase content of β - Bi_2O_3 and b) particle size of micrometric sized thermal sprayed powder.

2.3.6. Oxidation mechanisms by electron microscopy

Figure 2.9 shows the oxidation characteristics of bismuth identified by EDS using an electron backscattering detector. The cross-sectional area of as-synthesized micrometric sized bismuth oxidized particles of 30P1 (Figure 2.9a) and 30P2 (Figure 2.9b) samples are shown. The oxidized powder shows a micrometric sized snowman-like morphology that possesses a heterointerface of two phases, similarly to that observed in Figure 2.6. Figure 2.9a shows a typical SEM micrograph of a 30P1 sample, where two micrometric dark and bright semi-spherical particles attached to each other are shown. The composite shows the coexistence of a flat interface between both particles. According to the atomic percentage measured from EDS analysis clear and dark colored zones correspond to bismuth and bismuth oxide, respectively.

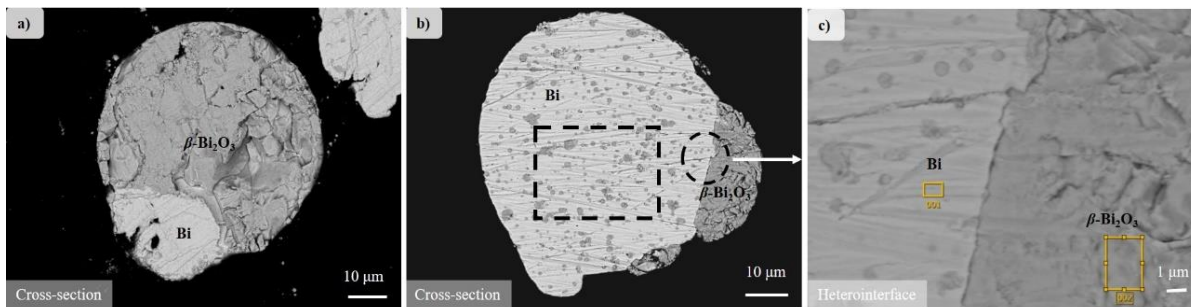


Figure 2.9 a, b) SEM micrographs of particle cross-sections for 30P1 and 30P2 samples respectively and c) heterointerface area between Bi/ β -Bi₂O₃.

Sample 30P2 (Figure 2.9b) shows a similar heterointerface between bismuth (clear zone) and bismuth oxide (dark zone). Whereas the oxidation mechanism is the opposite than 30P1 sample since the snowman-like particle possesses a higher content of bismuth than bismuth oxide. Although, the semi-sphere of bismuth is partially oxidized on its core.

Regarding the heterointerface between Bi and β -Bi₂O₃, the inset of Figure 2.9c shows a magnification of a 30P2 particle interface. This micrograph evidences the formation of a composite sharing different compositions in a heterogeneous interface between a metal and a metal oxide Bi/ β -Bi₂O₃.

These composites are usually classified as Janus particles and have a particular shape and surface chemistry showing different physical and chemical properties¹⁰⁸. Janus particles may show different magnetic, electrical, semiconductive, optical, optoelectronic, and catalytic properties¹⁰⁷. Due to the nature of as-synthesized snowman-like Bi/ β -Bi₂O₃ Janus particles, the photocatalytic properties of Bi₂O₃ are expected to be enhanced because of the interfacial interactions originated from electron transfer across the interface. It has been reported that Bi₂O₃ shows an enhancement in its photocatalytic activity by depositing metallic particles to serve as electron scavenger to decrease photorecombination of the electron-hole photogeneration and then induce charge separation to carry out redox reactions with pollutants^{22,110–112}. Electrodes of Bi/ β -Bi₂O₃ have shown stronger visible light absorption and high

photoactivity for hydrogen generation due to the electron transfer from Bi to β -Bi₂O₃⁴⁸. The current as-synthesized micrometric snowman-like Bi/ β -Bi₂O₃ Janus particles are a promising candidate for photocatalytic applications.

The obtained powder with 30P2 conditions kept the snowman morphology but showed as expected different oxidation characteristics. An internally partially oxidized big bismuth particle appears attached to a smaller one (Figure 2.9b). This behavior can be explained based on the heat transfer mechanism that takes place immediately after the particles interact with the hot gas, where they are heated from the surface to their nuclei. The kinetic of this process depends on several parameters, such as size and particle trajectory inside the flame, thermal conductivity, etc. Small particles (P1) get uniformly heated and reach faster conditions of fusion, vaporization, with the simultaneous oxidation process. On the opposite, bigger particles (P2) have intrinsically lower kinetics leading to an overall lower oxide content.

Heat and mass transfer play an important role in the definition of the oxidation characteristics of in-flight particles. The following expression (Eq 2.3) describes the net heat transfer between hot gas and particles and thus their reached temperature¹⁰²:

$$Q = h(\pi d_p^2)(T_\infty - T_s) - (\pi d_p^2)\varepsilon\sigma_s(T_s^4 - T_a^4) \quad (\text{Eq 2.3})$$

where d_p and T_s are the diameter and surface temperature (K) of the particle respectively, T_∞ and T_a are the temperature of hot gas and the environment (K), ε is the emissivity of the particle, σ_s is the Stefan-Boltzmann constant (5.67×10^{-8} W/m²K⁴), h is the heat transfer coefficient between the hot gas and the particle and expressed in terms of the Nusselt number (Nu) defined in Eq 2.4^{97,102}:

$$Nu = \frac{hd_p}{\kappa} \quad (\text{Eq 2.4})$$

where κ is the thermal conductivity of the gas.

For a particle to reach a uniform temperature it is required that its thermal conductivity K_p is higher than the K of the gas, described as the Biot number $Bi = \kappa/\kappa_p$ and should be $Bi < 0.01$ ^{97,102}.

A schematic representation of the oxidation mechanism that corresponds to an in-flight particle oxidized by combustion thermal spray as described elsewhere⁹⁷ can be adapted to the current results. In the referred figure, the oxidation mechanism of an in-flight particle interacting with hot gas depends on the heat transfer processes and the size of feedstock powder. Under melting and/or evaporation conditions, oxidation of the particles takes place and their diameter naturally decreases inside the flame plume, which is a time-dependent process influenced by their trajectory within the heat zone¹⁰².

2.4. Conclusion

Controlling flame spraying parameters (stand-off distance, flame temperature, Bi-powder morphology, and size) allows the synthesis of photoactive tetragonal bismuth oxide powder with nano- and micrometric sizes. Morphology of micrometric sized powder corresponds to Janus particles of a Bi/ β -Bi₂O₃ snowman-like morphology, where the heterostructure potentially allows the electron transfer between a semiconductor (β -Bi₂O₃) and an electron scavenger (Bi). This powder is ready to be used in spraying deposition processes, e.g., by cold spray. The obtained nanometric sized powder corresponds to highly pure β -Bi₂O₃, which is highly photoactive with a band gap energy $E_g = 2.26$ eV.

Chapter 3:Photocatalytic H₂ evolution and methanol photooxidation of visible-light driven bismuth-based heterojunctions synthesized by flame spray

3.1. Introduction

The properly designed semiconductor (SC) photocatalysts are promising materials for solving the current serious energy and environmental issues because of their ability of using sunlight to stimulate various photocatalytic reactions¹¹³. Especially, the constructed direct Z-scheme photocatalysts, mimicking the natural photosynthesis system, possess many merits, including increased light harvesting, spatially separated reductive and oxidative active sites, and well-preserved strong redox ability, which benefit the photocatalytic performance¹¹⁴.

The most effective approaches to enhance the photocatalytic activity of a catalyst and to carry on desired redox reactions is by semiconductor engineering coupling by a heterojunction assembles two or more catalyst¹¹⁵. The fate of heterojunctions relies on the efficient charge carrier separation, transfer, and reaction. As has been reported elsewhere, the energetic levels should be staggered and the catalyst with higher potential of the conduction band (E_{CB}), should be able to be a visible light driven semiconductor to inject electrons on the CB of the other semiconductor⁶⁰. Construction of heterojunction by combining two or more disparate functional materials in a hybrid structure offers an advanced strategy for enhanced solar energy utilization in photocatalysis and facilitate the charge separation due to the formation of an inner electric field between the composites of n-type and p-type semiconductors²⁷.

In the constructed heterojunctions, the Type-II photocatalytic mechanism usually takes place. The electrons in SC A with higher CB position can migrate to SC B with lower CB position (see [Figure 1.7](#)). Meanwhile, the photogenerated holes in these two semiconductors follow a reverse migration. The photoinduced electrons and holes are accumulated on SC B for a reduction reaction and SC A for an oxidation reaction, respectively²⁷. This promotes the spatial separation and suppresses recombination of charge

Photocatalytic H₂ evolution and methanol photooxidation of visible-light driven bismuth-based heterojunctions synthesized by flame spray

carriers, which significantly enhances the energy conversion efficiency of the designed heterojunction. However, these advantages are at the expense of redox abilities of charge carriers, which indicate a weakened driving force that may fail to drive a specific photocatalytic reaction. Therefore, manipulating the photogenerated electron–hole pairs in a Z-scheme mode is highly desirable for the constructed heterostructure because of its advantages over Type-II mode¹⁴.

In the direct Z-scheme mechanism, the relative band alignment is similar to type II heterojunction and resembles the natural photosynthesis mechanism. When excited by incident light, the photogenerated electrons in SC A and the photogenerated holes in SC B remain in their respective bands, preserving the strong reduction and oxidation activity of the components¹¹⁴. Meanwhile, the photogenerated electrons on SC B with a lower reduction potential than the electrons in SC A and holes on SC A with a lower oxidation potential than the holes in SC B recombine. As a result, the junction simultaneously has the strong redox capacity of both semiconductors and the reductive and oxidative sites are spatially separated, regarding direct Z-scheme composites for hydrogen production and organic compounds degradation, respectively¹⁴.

It is noteworthy that the close contact between SC A and SC B in the direct Z-scheme heterojunction system plays a crucial role because the interface has the same role as the electron mediators. Hence, the effective combination of SC A and SC B is essential for preparing efficient direct Z scheme heterojunction system. It is remarkable that the same materials can lead to different mechanisms depending on their synthesis procedure. Generally, it is necessary to investigate the charge transfer pathway for any heterojunction system because of the competition between Z-scheme and the type II heterojunction mechanisms¹¹⁶.

In this context, the construction of a heterojunction composed by metal oxide semiconductors is here presented for the photocatalytic generation of hydrogen and the photooxidation of methanol. Bismuth oxide-copper oxide multi-heterojunction was

Photocatalytic H₂ evolution and methanol photooxidation of visible-light driven bismuth-based heterojunctions synthesized by flame spray

synthesized by an alternative flame spray process reported for the first time and its physicochemical properties and photocatalytic performance was measured.

Bismuth oxide (Bi₂O₃) is a visible light driven semiconductor that has recently emerged as a multifunctional material applied in environmental remediation as a photocatalyst for degradation of hazardous compounds in aqueous and gas phase^{34,117–120}. Between its electrochemical properties, the positive valence band potential E_{VB} is suitable to undergo oxidative reactions of the photogenerated holes. Some of the major interesting functionalities of Bi₂O₃ is the different electronic, semiconducting, and photocatalytic properties depending on its structure phase¹²¹. Bi₂O₃ presents seven different polymorphs reported so far³³. The tetragonal structure β -phase has attracted attention in photocatalytic applications due to its tunable structure and the polarizability of its tetragonal unity due to the lone electron pair of Bi³⁺ which is attributed to an efficient separation of the photogenerated electron-hole pairs³⁷. However, Bi₂O₃ has a low conduction band potential $E_{CB} \sim +0.3$ V vs NHE that is disadvantageous for the photogenerated electrons to scavenge molecular oxygen O₂/O₂⁻ -0.33 V vs NHE⁷⁶.

Bi₂O₃ has proven to enhance its photocatalytic efficiency in the degradation of pollutants by coupling with other semiconductors in a heterojunction engineering^{31,122}. Cu₂O is a p-type visible active semiconductor with a narrow band gap energy of 2 eV and possess a remarkable photoconductivity and an advantageous potential of the conduction band (-1 V vs NHE) and the valence band (1 V vs NHE)^{123–125}. Therefore, it is demonstrated that coupling Cu₂O with Bi₂O₃ in a staggered band alignment could efficiently suppress the recombination of photogenerated electrons and holes inside Bi₂O₃, thus promoting the photocatalytic activity for organic pollutants degradation or water oxidation^{61–64}.

Most of the reported works available in the literature have proved that the physicochemical properties obtained in Bi₂O₃-Cu₂O heterojunctions and in the single catalyst, are directly dependent on the synthesis method and therefore relies on the photocatalytic performance. The synthesis of β -Bi₂O₃ presents many challenges for being a

Photocatalytic H₂ evolution and methanol photooxidation of visible-light driven bismuth-based heterojunctions synthesized by flame spray

metastable phase at room temperature. Recent studies reported the synthesis by several routes that include conventional chemical methods^{34,42,89–91} using bismuth nitrates and carbonates as precursors, and alternative physical methods based on the oxidation of granulated bismuth under air or vacuum atmospheres^{92–94}. Even these research groups reported the synthesis of bismuth oxide with a control on the processing parameters in the physicochemical properties and a remarkable photocatalytic activity, the necessity of a novel one-step synthesis route, low cost, sustainable and with high production efficiency is still needed. As has been reported in our previous studies¹²⁶, the synthesis of tetragonal β -Bi₂O₃ with nanometric spherical size (with narrow band gap energy) and micrometric Bi/ β -Bi₂O₃ Janus particles was achieved by flame spray process by collecting these two different powders from: i) in-flight particles evaporated and ii) quenching the as-sprayed powders in water, both of them collected in a home-made set-up powder collector.

Therefore, the synthesis of β -Bi₂O₃/Cu₂O by flame spray seems to be feasible based on our previous results for the successful synthesis of β -Bi₂O₃, from semi-metallic bismuth and metallic copper as precursor powder. The use of bismuth presents a potential use from its production as a byproduct from mineral refinement of silver, copper or lead mainly in China, Canada, Mexico, South America and USA¹⁰¹. Although bismuth and bismuth oxide are non-toxic and non-carcinogenic.

Further, based on the phase diagram and melting temperature of the precursors (bismuth has a melting point of 271 °C and a boiling point of 1560 °C, copper has a melting point of 1085 °C and a boiling point of 2595 °C)^{127,128}, the oxidation of both metals by the heat released due to the oxy-acetylene flame could be easily address. In this context, thermal spray process can be used for the synthesis of metal oxides in a one-step method to produce highly pure semiconductors with nanometric particle size or micrometric particles that are composed of a metal/metal oxide composition¹²⁶. The synthesis of Janus particles is one of the aims to achieve in bismuth-copper oxide heterojunctions since these particles share a heterointerface where the photocatalytic properties enhance because of the interfacial interactions originated from electron transfer across the interface¹⁰⁸.

Flame spray process is a thermal spray process in which the material to be sprayed can be fed in powder form and is the simplest and among the oldest spray processes usually used for the fabrication of coatings⁹⁷. FS uses the chemical energy of fuel gases to generate the high temperature flow. The combustion reaction involves a significant heat release. The powder is introduced axially through the rear of the nozzle into the flame burning at the nozzle exit. The powder is heated by the oxy-fuel flame and carried by the carrier gas and the hot gas to the work piece. A stream of compressed air, surrounding the flame, atomizes and generates material droplets in a continuous stream. The feedstock materials are melted and the particles or droplets accelerated toward the substrate surface (in this case a powder collector) by the expanding hot gas flow and air jets¹⁰².

Flame spraying requires the melting of the sprayed material. The flame temperature and enthalpy are determined by the fuel gas composition (C_xH_y) and flow rate and by the oxidizer (oxygen or air) flow rate. The mixture of acetylene (C₂H₂)–oxygen (O₂) at a stoichiometric ratio yields a temperature of 3,410 K at atmospheric pressure, which is the highest temperature of all combustible gases (C_xH_y) at this pressure (oxyacetylene torches are the most common ones)¹⁰².

If there is too much oxidizer, part of it will not be burned but will have to be heated to the combustion temperature without participating in it and thus the final temperature will be lower than that obtained with the stoichiometric mixture. Similarly, in a fuel-rich mixture, the excess of fuel will have to be heated by the reaction and the temperature will be lower than with the stoichiometric mixture.

Flame velocities depend on the combustible gas flow rates and are generally below 100 m/s. As the flame length is limited and the particle velocity is a few tens of m/s, the maximum temperature that particles can achieve (T_p) after their flight is about $T_p = 0.7T_g$ to $0.8T_g$, T_g being the gas temperature, i.e., about 2,300 K for T_p ¹⁰².

To the authors best knowledge, no previous reports on the synthesis of metal oxides, composites or heterojunctions in powder form by flame spray process has been reported so

far. There are several available reports on the thermal spray of metal oxides in powder form such as zirconia (ZrO₂), silica (SiO₂) or mullite where the only physical and chemical modification is a spheroidization process^{129,130}. Although the synthesis of different compounds (SiO₂, TiO₂, SnO₂, β-Bi₂O₃ among others) by flame spray pyrolysis is very common and has been widely studied where the feeding material is in liquid solution either water or organic solvent^{131,132}. In this work we part from metallic copper and semi-metallic bismuth in powder form to be feed in this granular form; by a one-step flame spray process we obtained a multi-heterojunction of bismuth oxide and copper oxide in powder form. The collection of the as-sprayed powder was achieved by a home set-up powder collector. The production efficiency, oxidation characteristic and different physical and chemical properties of the obtained powders is controlled based on the flame spray parameters and the design of the powder collector.

3.2. Materials and methods

3.2.1. Powder feeder calibration

The feeding rate of Bi and Bi-Cu powder was characterized using a PF50 powder feeder Spray Tech (Flame Spray Technologies, USA). The feeding process consist of a wheel speed displayed in revolution per minute. The feeder operates on a volumetric principle that directly controls the powder feed rate by the speed of the powder wheel. During operation the slots in the powder wheel fill with powder. Gravity, carrier gas (highly pure N₂), and rotation of the powder wheel deliver the powder to the powder hose. An inert carrier gas provides canister pressurization then transports the powder to the thermal spray torch. To set the wheel speed, the desired rpm into the controller is selected. The calibration was performed for 1, 2, 3, 4 and 5 rpm for each powder. The calibration curve obtained from a linear fit to obtain the feeding rate (g/min) is shown in [Figure S3.1](#).

3.2.2. Pulverization of bismuth pellets

The pulverization of bismuth pellets was performed by manual mechanical grinding using a ceramic mortar. After pulverization, the powder was sieved for 15 min in a Sieve shaker RO-Tap RX-94 (W.S. Tyler, USA) using sieving of 25, 53, 88, and 105 μm

Photocatalytic H₂ evolution and methanol photooxidation of visible-light driven bismuth-based heterojunctions synthesized by flame spray

aperture. The Bi pulverized powder used for flame spray were in the range from 25-53 μm. For the spraying of the heterojunctions, precursor feeding powders; pulverized bismuth powder and commercial copper powder (Praxair 99.9%) was mixed in an agate mortar in a 3:1 bismuth:copper ratio.

3.2.3. Thermal spray and collection

The choose flame spray conditions for Bi and Bi-Cu powder were chosen to study the different chemistry of the flame for the oxidation of the feeding powders and is shown in [Table 3.1](#). Highly pure nitrogen was used as carrying gas in the feeder and to carry out the particles to the torch. The feeding rate was chosen at 5 rpm that correspond to 88 g/min. Pressurized air was used to cool the torch. Oxygen and acetylene mixture was used as the combustion gases. Two oxidative and two reductive flames were studied varying the total gas flow according to the equivalence ratio ϕ described in [Eq 3.1](#):

$$\phi = \frac{F/A}{(F/A)_{stoich}} \quad (\text{Eq 3.1})$$

where F correspond to fuel and A correspond to the oxidizer. The mixture is called fuel rich if $\phi > 1$ and fuel lean if $\phi < 1$. The stoichiometric reaction ([Eq 3.2](#)) where $\phi = 1$ corresponds to the full transformation of C into CO₂ and H into H₂O, according to the global reaction¹⁰²:



The equivalence ratio for oxidative flames is $\phi = 0.8$, that according to theoretical data the temperature of the flame is approximately 3276 K. The reductive flames with a equivalence ratio $\phi = 1.7$ has a theoretical temperature of 3432 K¹⁰².

Table 3.1 Flame spray conditions and parameters.

<i>Feeding conditions</i>		<i>Oxygen fuel conditions</i>	<i>1</i>	<i>2</i>	<i>3</i>	<i>4</i>
Particle size (d_{50}) feeded Bi	8-45 μm	Oxygen flow (NLPM)	28	35.5	22	28
Particle size (d_{50}) feeded Cu	6-17 μm	Acetylene flow (NLPM)	9	11.5	15	19
Powder feeding rate	88 g/min	Total gas flow (NLPM)	37	47	37	47
Nitrogen pressure	15 psi (103.4 kPa)	Equivalence ratio f	0.8	0.8	1.7	1.7
Air pressure	20 psi (137.8 kPa)	Flame temperature (K)	3276	3276	3432	3432
Oxygen pressure	30 psi (206.8 kPa)					
Acetylene pressure	10 psi (68 kPa)					

3.2.4. Structural and optical characterization

The relative structural phases and structural parameters of the samples were determined by a XRD-6000 X-ray diffractometer Rigaku, SmartLab (Tokyo, Japan) coupled to a DTech lineal detector. The Cu-K α radiation (1.542 Å) was generated at 44 mA and 40 kV, recording the relative intensity in the scattering range of 2θ from 20° to 60° with a step size of $2\theta = 0.01^\circ$. Phase identification and quantification, structural parameters and crystallite size were analyze using Xpert High Score® and Rietveld refinement with GSAS®¹⁰³. The shape of the peaks in the experimental diffractions patterns was well described by an asymmetric pseudo-Voigt function. The procedure was adopted for the minimization of the difference between the observed (I_o) and the simulated (I_c) powder diffraction data. Refinements were carried out until convergence was reached and the value of GoF factor became close 1, which confirms the goodness of refinement.

Particle size distribution and morphology of precursor powders and as-synthesized heterojunction were characterized by field emission scanning electron microscopy (FESEM) with JEOL 7610F microscope (Tokyo, Japan) using a backscattered electron detector (BSE) at 15 kV electron acceleration voltage. EDS analysis was performed in the cross-sectional area of as-sprayed powders to observe the junction and assemble between

the different phases. The size distribution of feedstock powder and as-sprayed powder was measured using the laser diffractometer (HELOS/BR, Sympatec GmbH, Germany). The technique for measuring the dry powder was REDOS, where samples were placed in the powder feeder and air pressurized at 200 kPa.

Optical properties of Bi-based heterojunctions and precursor powders were measured to determine the band gap energy of as-prepared powders by diffused reflectance spectrophotometry (DRS) UV-Vis-NIR using a Cary Varian 100 spectrophotometer (Malvern, UK) in the range 200-900 nm.

From reflectance spectra, Kubelka Munk theory (Eq 3.3) was applied to measure band gap energies of semiconductors using Tauc method (Eq 3.4). For as-sprayed β -Bi₂O₃, an indirect optical transition¹³³ ($n = 2$) was used and for β -Bi₂O₃/Cu₂O heterojunction a direct optical transition ($n = 0.5$) based on the linear fit of Tauc plot¹³⁴.

$$F(R) = \frac{(1-R)^2}{2R} \quad (\text{Eq 3.3})$$

$$(F(R)hv)^{1/n} = C(hv - E_g) \quad (\text{Eq 3.4})$$

$F(R)$ is a function of reflectance, R is the reflectance measured by UV-Vis spectrophotometry, hv is the energy of the photons induced, n is the optical transition, C is a constant and E_g is the band gap energy of the bulk of semiconductor. The calculated band gap energies can be determined by a linear fit with x -axes that correspond to the intercept.

3.2.5. Photocatalytic activity

Methanol photooxidation was performed using a UV-light Xenon lamp of 75 W. In a typical procedure a flask of 100 mL was used. 80 mL 2.47 molL⁻¹ methanol (10% V) solution was used using ultrapure distilled water (18.2 M Ω cm). 1gL⁻¹ of catalyst was loaded to assure optical density. The solution was kept in the dark for equilibrium during 10 min under continuous stirring. After that, the solution was illuminated for 60 min. Aliquots of 1.5 mL were taken every 10 min to then keep it under dark in a freezer. Every single experiment was performed at least twice to assure the accuracy of the method and its

Photocatalytic H₂ evolution and methanol photooxidation of visible-light driven bismuth-based heterojunctions synthesized by flame spray

reproducibility. The photooxidation rate was determined by measuring the formaldehyde (HCHO) generated as a result of the methanol oxidation employing the Nash method¹³⁵. This method is based on the reaction of formaldehyde with Nash reagent (2 M ammonium acetate, 0.05 M acetic acid, 0.02 M acetylacetone) to form the yellow-colored 3:5-diacetyl-1:4-dihydrolutidine (DDL) with a maximum of absorbance at 412 nm. After irradiation, 1.5 mL aliquots of the anolyte were mixed with 1.5 mL of fresh Nash reagent and diluted in 1.5 mL of distilled water. After an overnight incubation, the yellow-colored (DDL) is formed. The absorbance of DDL was measured in the range from 200-800 nm in a quartz cuvette of 1 cm path length using a Varian Cary 100 Scan UV-vis spectrophotometer.

H₂ evolution experiments were carried out in septum-sealed 10 mL borosilicated glass reactors. The photocatalyst in a concentration of 1 gL⁻¹ was suspended in 6 mL of deionized water (18.2 MΩ) with 2.47 molL⁻¹ of methanol used as hole scavenger. Pt loaded in 1, 2, 3, 4 and 5 wt.% was photodeposited in situ by addition of the required amount of H₂PtCl₆. The system was purged with argon for 10 min and then irradiated with a 1000 W Xenon lamp (Hönle UV Technology, Sol 1200) under constant stirring. The temperature was maintained at 25 ± 1 °C using a water bath. The evolved gases were quantified by gas chromatography using a Shimadzu GC-8A (thermal conductivity detector).

3.3. Results and discussion

3.3.1. Characterization of precursor metallic powder

The particle size distribution of feeding powder is shown in [Figure 3.1](#). Bismuth pulverized powder shows a distribution of $d_{10} = 8.9 \mu\text{m}$, $d_{50} = 28.4 \mu\text{m}$ and $d_{90} = 45.5 \mu\text{m}$ while copper commercial powder presents a distribution of $d_{10} = 6.2 \mu\text{m}$, $d_{50} = 10.8 \mu\text{m}$ and $d_{90} = 17.03 \mu\text{m}$.

Photocatalytic H₂ evolution and methanol photooxidation of visible-light driven bismuth-based heterojunctions synthesized by flame spray

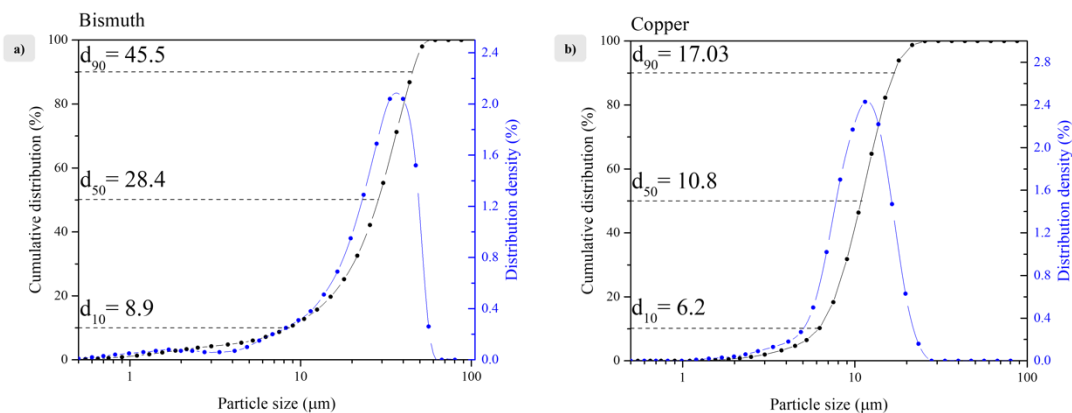


Figure 3.1 Particle size distribution for feeding powders a) bismuth pulverized and b) copper commercially available.

3.3.2. Experimental set-up and thermal spray conditions

The experimental set-up used for the collection of as-sprayed powders is shown in Figure 3.2. The torch is placed vertical to favor the collection of powder. Bi is a semimetal of low melting (271 °C) and boiling temperature (1564 °C) while for bismuth oxide the melting and boiling temperature are 817 °C and 1890 °C, respectively. In our previous studies¹²⁶, the volatilization of as oxidized bismuth oxide was one of the major problems while the retention of the collected powder is a major challenge. For this purpose, a powder feeder collector was designed and manufactured in the lab which consist of several steps that permits the cooling and carrying of the in-flight particles. The particles are first address to a hopper, this is connected to a series of steel tubes that carries the particles to a bucket and finally to a glass cyclone. The upper part of the cyclone is connected to a blower that suggest the gases evolved of the flame spray process. This generates that the in-flight particles address the pathway to be collected in the different chambers according to its particle size and oxidizing mechanism. All the set-up is inside a sealed cabin chamber.

Photocatalytic H₂ evolution and methanol photooxidation of visible-light driven bismuth-based heterojunctions synthesized by flame spray

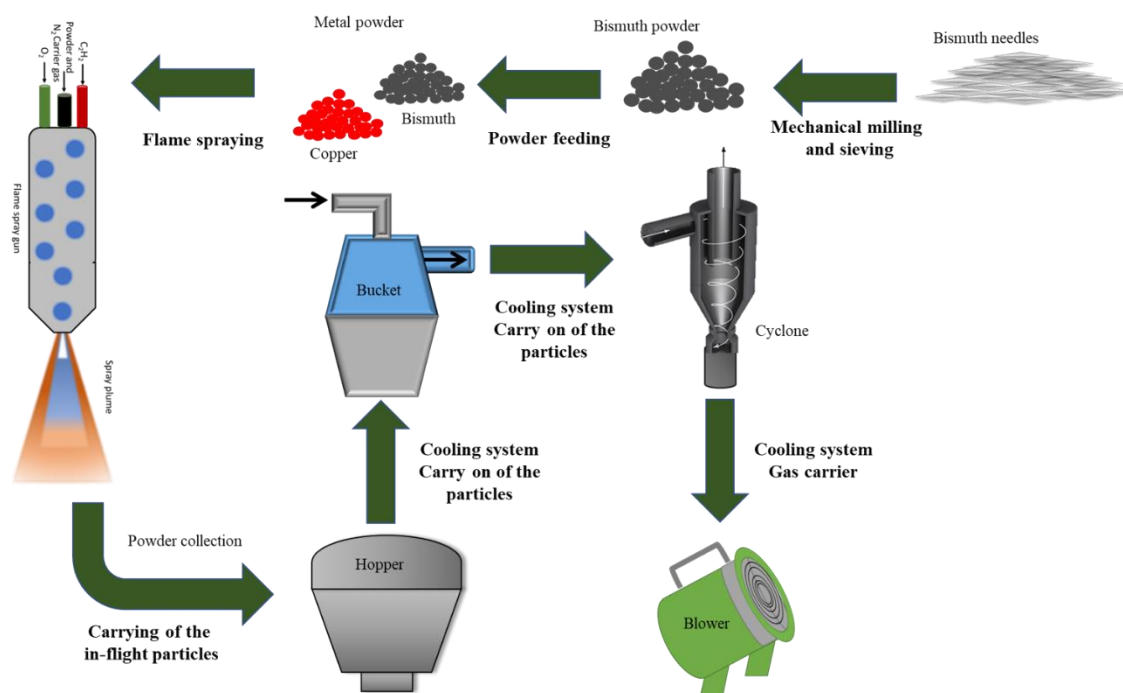


Figure 3.2 Flame spray cabin and experimental set-up for powder collection of in-flight particles.

3.3.3. Effect of flame sprayed parameters on the physicochemical properties of the obtained powder

The obtained bismuth and bismuth-copper as-sprayed powder was characterized dependent on the chemistry of the oxygen/acetylene flame and the stage of collection in the hopper, tubes, bucket and cyclone by X-ray diffraction and UV-vis spectrophotometry.

The X-ray patterns of as-sprayed bismuth powders are shown in [Figure 3.3](#) for a), b) oxidizing atmosphere ($\phi = 0.8$) and c), d) reductive atmosphere ($\phi = 1.7$) varying the total oxygen/acetylene gas flow, 37 NLPM (a and c) and 47 NLPM (b and d). The formation of tetragonal β -Bi₂O₃ was observed in all the samples indexed with $a = b = 7.7299 \text{ \AA}$, $c = 5.6587 \text{ \AA}$ unit cell parameters identified with PDF 27-0050 with a space group $P421-c$ (identified with \bullet). Remanent bismuth not oxidized was observed and indexed to PDF 44-1246 (identified with \bullet) with space group $R-3m$ and lattice parameters $a = b = 4.5392 \text{ \AA}$, $c = 11.8347 \text{ \AA}$. The presence of some traces of the room temperature stable phase α -Bi₂O₃

Photocatalytic H₂ evolution and methanol photooxidation of visible-light driven bismuth-based heterojunctions synthesized by flame spray

was observed for bismuth sprayed powders b), c) and d) (identified with ●). The α -phase was indexed to PDF 41-1449 with a space group $P21/c$ and $a = 5.83 \text{ \AA}$, $b = 8.14 \text{ \AA}$, $c = 7.48 \text{ \AA}$.

The effect of the chemistry of oxygen/acetylene gases and the mechanism of oxidation dependent on the collection stage is clearly evidenced. For powders collected in the hopper, tubes and bucket the formation of tetragonal β -Bi₂O₃ increase in the first stage of collection while the content of semi-metallic bismuth decreases. This can be clearly seen in the mean peak of β -Bi₂O₃(201) located at 27.93° and Bi(012) located at 27.16°. All as-sprayed powders collected in the cyclone shown a pure phase of β -Bi₂O₃.

As-sprayed powders in oxidizing atmosphere ($\phi = 0.8$) with lower gas flow (Figure 3.3a), present the higher content of semi metallic bismuth not oxidized that can be related due to the low temperature of the flame (3276 K). As it has been reported elsewhere¹⁰², the in-flight particles can only reach the 70% of the temperature of the flame and the velocities that reaches the particles are commonly in the range of 100 m/s. Although using a low gas flow there are less molecules of the mixture oxygen/acetylene that can oxidize bismuth.

Photocatalytic H₂ evolution and methanol photooxidation of visible-light driven bismuth-based heterojunctions synthesized by flame spray

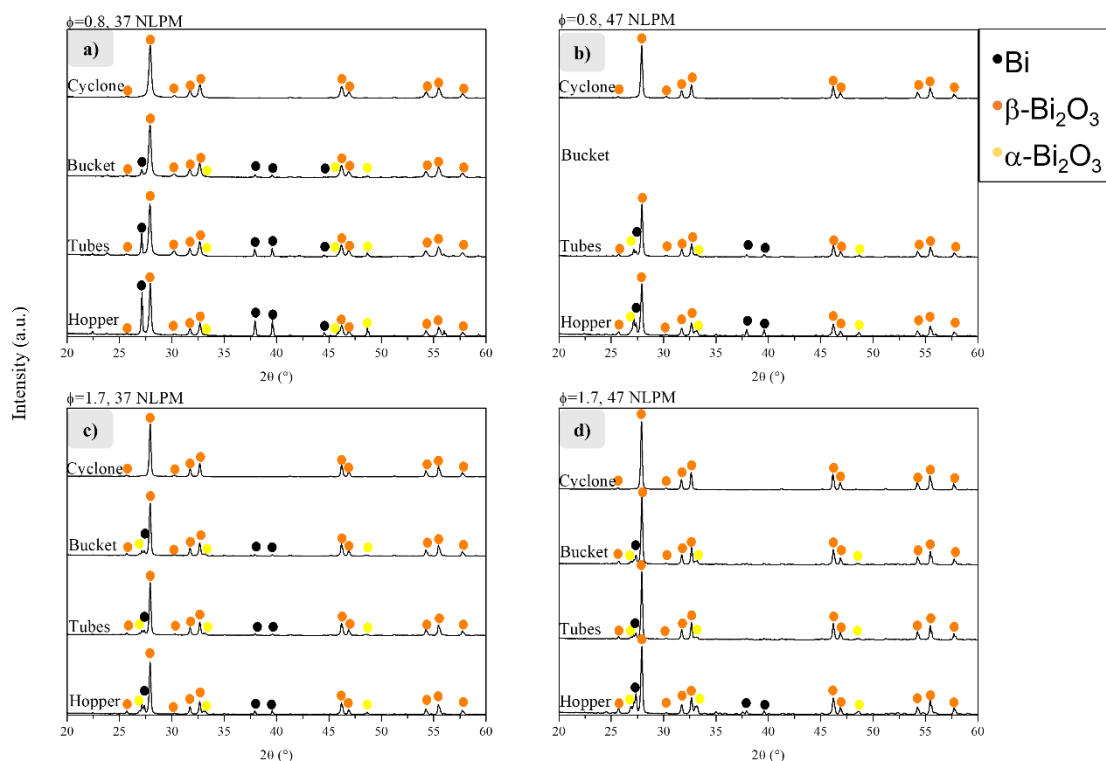


Figure 3.3 XRD patterns of bismuth flame sprayed powder for a) $\phi = 0.8$, 37 NLPM, b) $\phi = 0.8$, 47 NLPM, c) $\phi = 1.7$, 37 NLPM, and d) $\phi = 1.7$, 47 NLPM.

X-ray patterns of bismuth-copper as-sprayed powders are shown in Figure 3.4 for a), b) oxidizing atmosphere ($\phi = 0.8$) and c), d) reductive atmosphere ($\phi = 1.7$) varying the total oxygen/acetylene gas flow, 37 NLPM (a and c) and 47 NLPM (b and d), respectively. For powders collected in the hopper, tubes and bucket the formation of tetragonal β -Bi₂O₃ and cubic Cu₂O was identified and indexed to PDF 27-0050 and PDF 05-0667 (identified with \bullet) space group $Pm-3m$ (224) and $a = b = c = 4.2696 \text{ \AA}$, respectively. Semi-metallic bismuth (identified with \bullet) and metallic copper (identified with \bullet) not oxidized is observed and indexed to PDF 44-1246 and PDF 04-0836 space group $Fm-3m$ (225) and $a = b = c = 3.6153 \text{ \AA}$. Small traces of α -Bi₂O₃ are also observed. For powder collected in the cyclone a pure phase of β -Bi₂O₃ is observed, no traces of Bi, Cu or Cu₂O are observed.

Photocatalytic H₂ evolution and methanol photooxidation of visible-light driven bismuth-based heterojunctions synthesized by flame spray

These results evidence that the collection stage serves as a separator for the different chemistry of the powders obtained and is similar for flame spraying of bismuth. The amount of remanent metals not oxidized decreases from the hopper to the tubes and then to the bucket.

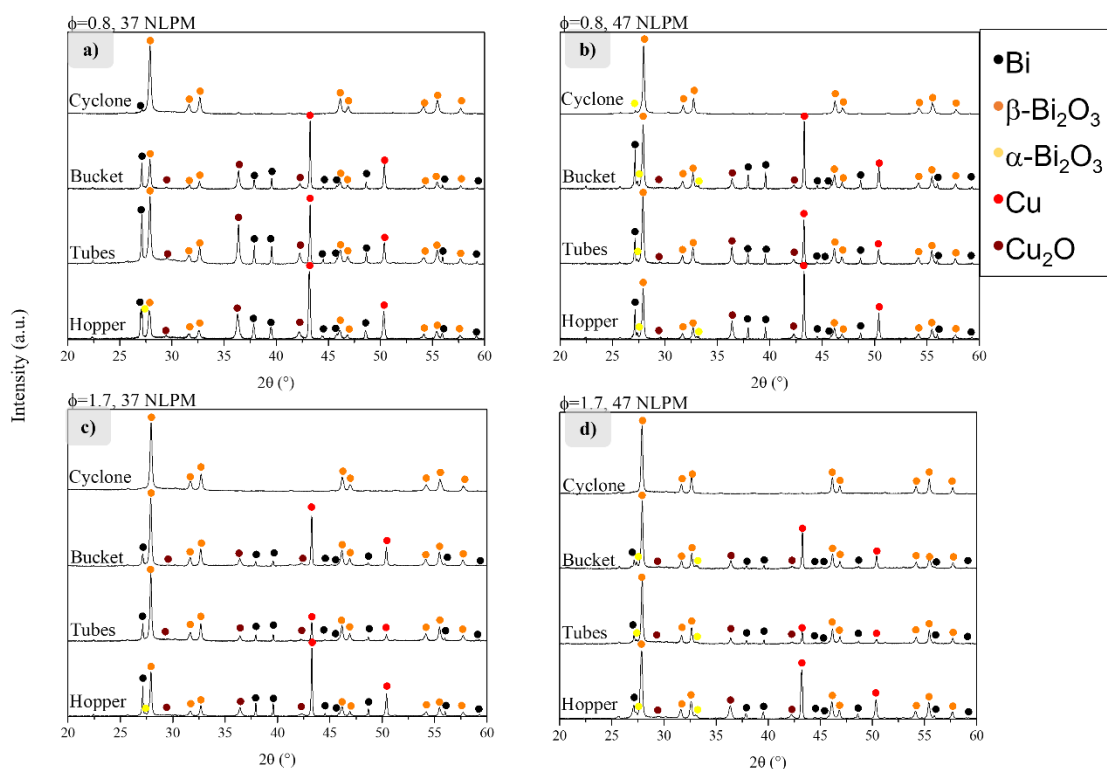


Figure 3.4 XRD patterns of bismuth-copper flame sprayed powder for a) $\phi = 0.8, 37$ NLPM, b) $\phi = 0.8, 47$ NLPM, c) $\phi = 1.7, 37$ NLPM, and d) $\phi = 1.7, 47$ NLPM.

The phase quantification of as-sprayed bismuth-copper powders obtained by Rietveld refinement using GSAS is shown in Table S3.1. The plot of the experimental patterns, the adjusted patterns, the adjusted background to calculate the phase content and lattice parameters, and the error line generated from the difference between the experimental and adjusted patterns is shown in Figure S3.2. The effect of the different amount of phases obtained by flame sprayed is shown in Figure 3.5 based on the stage of powder

Photocatalytic H₂ evolution and methanol photooxidation of visible-light driven bismuth-based heterojunctions synthesized by flame spray

collector (hopper, tubes, bucket and cyclone) according to the atmospheres used for the flame spraying.

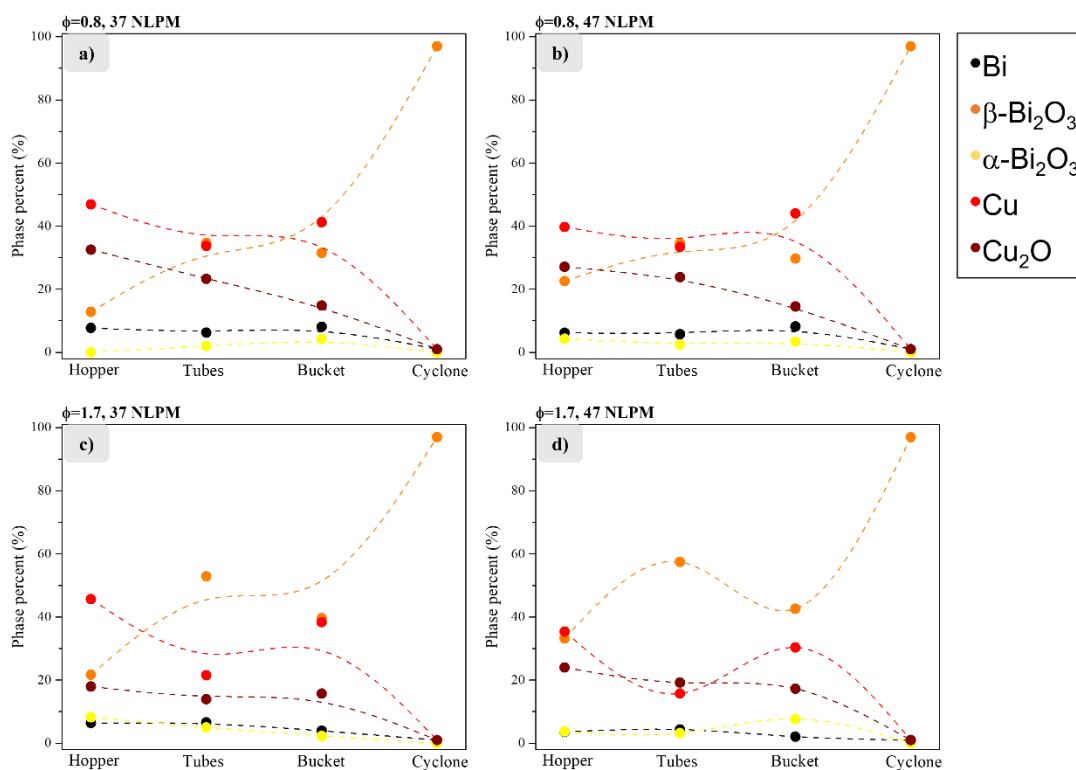


Figure 3.5 Phase quantification of as-sprayed heterojunctions as effect of powder collector stage and flame atmosphere.

The band gap energy of bismuth (Figure 3.6a and Figure 3.6b) and bismuth-copper (Figure 3.6c and Figure 3.6d) as-sprayed powder collected in the hopper and cyclone, respectively was determined using Kubelka-Munk function.

The heterojunction Bi/ β -Bi₂O₃ formed in the hopper (Figure 3.6a) exhibits a single absorption signal that is related to the efficient coupling between bismuth and bismuth oxide which generates the electron transfer from the semiconductor to the metal generating a red shifting to the visible range. The band gap energies determined are shown in Table 3.2. The E_g of the heterojunction tends to increase from oxidizing flame to reductive flame

Photocatalytic H₂ evolution and methanol photooxidation of visible-light driven bismuth-based heterojunctions synthesized by flame spray

and when the total gas flow increases. As it was observed in XRD, as-sprayed powders in oxidizing flame presents higher amount of bismuth which generate that, electrons are transferred to the metal serving as an electron scavenger. For β -Bi₂O₃ powders obtained in the cyclone, the E_g increases from 2.29 eV to 2.32 eV for oxidizing (light blue line) to reductive (wine line) flame (Figure 3.6b). This difference might be attributed to structural parameters of the tetragonal phase of β -Bi₂O₃ or the particle size of the powder.

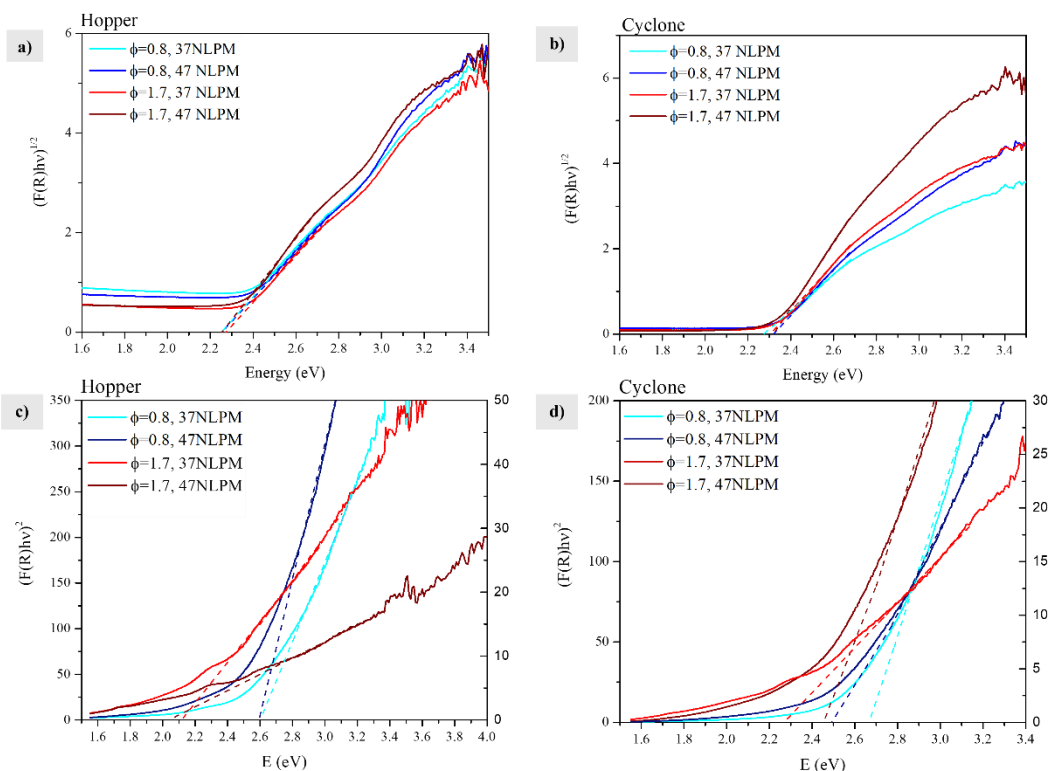


Figure 3.6 Tauc plot of as-sprayed recollected powder in hopper and cyclone for a), b) bismuth and c), d) bismuth-copper flame sprayed powder.

The band gap energies for bismuth-copper as-sprayed powders are shown in Figure 3.6c and 3.6d. The heterojunction Bi/ β -Bi₂O₃/Cu/Cu₂O formed in the hopper present a single absorption edge that refers to the formation of a heterojunction. The E_g of the compounds are presented in Table 3.2, as-sprayed powders in oxidizing flame present higher band gap energies compared to the compounds obtained with reductive flame. The

Photocatalytic H₂ evolution and methanol photooxidation of visible-light driven bismuth-based heterojunctions synthesized by flame spray

value decreases from 2.60 eV to 1.88 eV. For β -Bi₂O₃ powders obtained in the cyclone the band gap energies decrease from 2.67 eV to 2.24 eV for oxidizing to reductive atmosphere.

Table 3.2 Band gap energies (eV) determined from Tauc plot of as-sprayed powders.

Band gap energy E_g (eV)				
Flame sprayed	Bi flame sprayed n=2		Bi-Cu flame sprayed n=1/2	
Parameters	Bi/β-Bi₂O₃	β-Bi₂O₃	Cu/Cu₂O/Bi/β-Bi₂O₃	β-Bi₂O₃
	Hopper	Cyclone	Hopper	Cyclone
0.8 F1	2.2273	2.2947	2.6014	2.6712
0.8 F2	2.2427	2.3126	2.5639	2.5628
1.7 F1	2.2611	2.3198	2.1234	2.2470
1.7 F2	2.2618	2.3205	1.8891	2.4699

The particle size distribution density of bismuth (Figure 3.7a, b and c) and bismuth-copper (Figure 3.7d, e and f) flame sprayed are shown according to the stage of collection in hopper, tubes and bucket. The distribution d_{10} , d_{50} and d_{90} is shown in Table S3.2. The particle size of powder obtained in the cyclone is not shown since is composed of nanometric particles that cannot be analyzed with laser diffraction. For powder collected in the hopper and bucket the particles are composed of a bimodal mode of two populations. The clear tendency shows a majority of bigger particles in the powders as-sprayed with oxidizing atmosphere and it decreases in the powders obtained with reductive atmosphere. Although, the population of smaller particles is bigger for bismuth as-sprayed and it increases from oxidizing to reductive atmosphere.

Photocatalytic H₂ evolution and methanol photooxidation of visible-light driven bismuth-based heterojunctions synthesized by flame spray

In the case of powder collected in the tubes, the population of smaller particles increases that can be related to the mixing of particles collected in the hopper and the in-flight particles that carries to the cyclone generating a mixing of micrometric and nanometric particles.

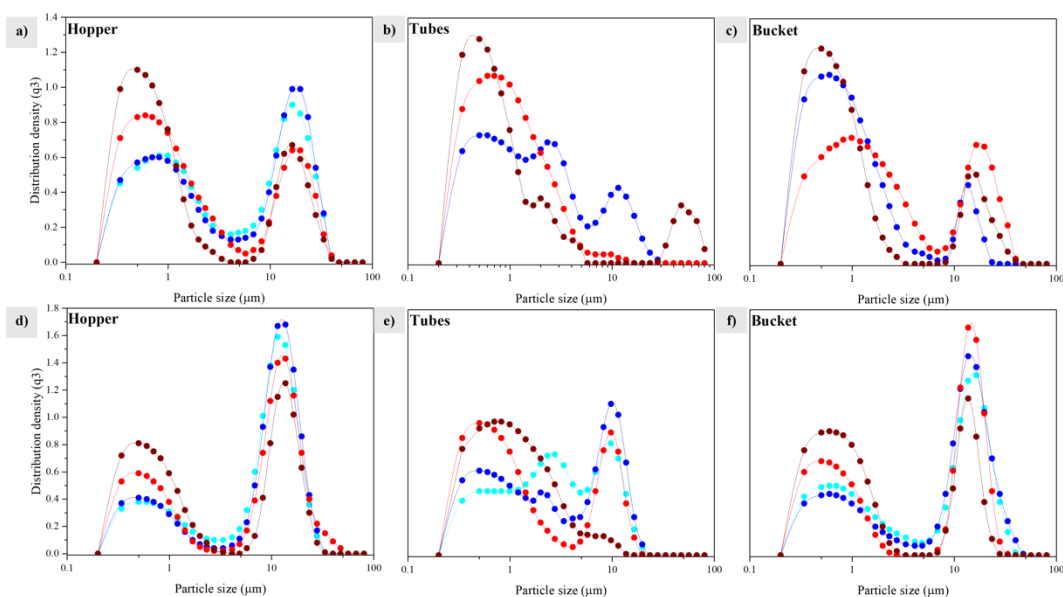


Figure 3.7 Particle size distribution density of a), b) and c) β - Bi_2O_3 and d), e) and f) β - $\text{Bi}_2\text{O}_3/\text{Cu}_2\text{O}$ flame sprayed at (•) $\phi = 0.8$, 37 NLPM, (◦) $\phi = 0.8$, 47 NLPM, (◐) $\phi = 1.7$, 37 NLPM, (◑) $\phi = 1.7$, 47 NLPM.

FESEM micrographs of as-sprayed bismuth-copper powder in oxidative ($\phi = 0.8$) and reductive ($\phi = 1.7$) flame using a gas flow of 37 NLPM is shown on Figure 3.8. The figure shows the powder collected in the hopper, tubes, bucket and cyclone. As it is clearly observed. The particle size decreases from the hopper to the cyclone from a micrometric size around 20 μm to nanometric size. The micrographs recollected in the hopper, tubes and bucket exhibits snowman and raspberry morphology.

Photocatalytic H₂ evolution and methanol photooxidation of visible-light driven bismuth-based heterojunctions synthesized by flame spray

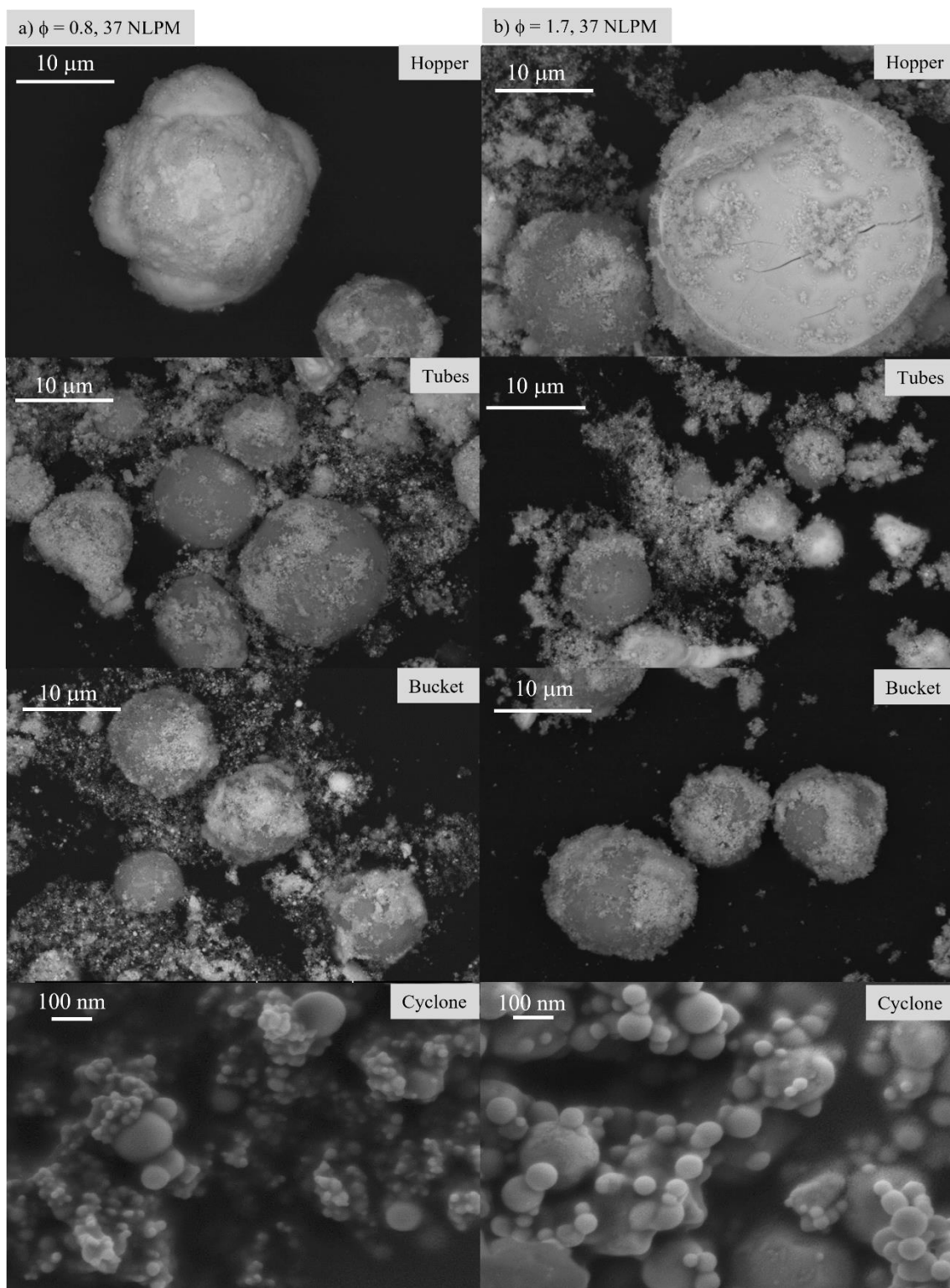


Figure 3.8 FESEM micrographs of bismuth-copper as-sprayed powder a) $\phi = 0.8$, 37 NLPM and b) $\phi = 1.7$, 37 NLPM at different collection stages.

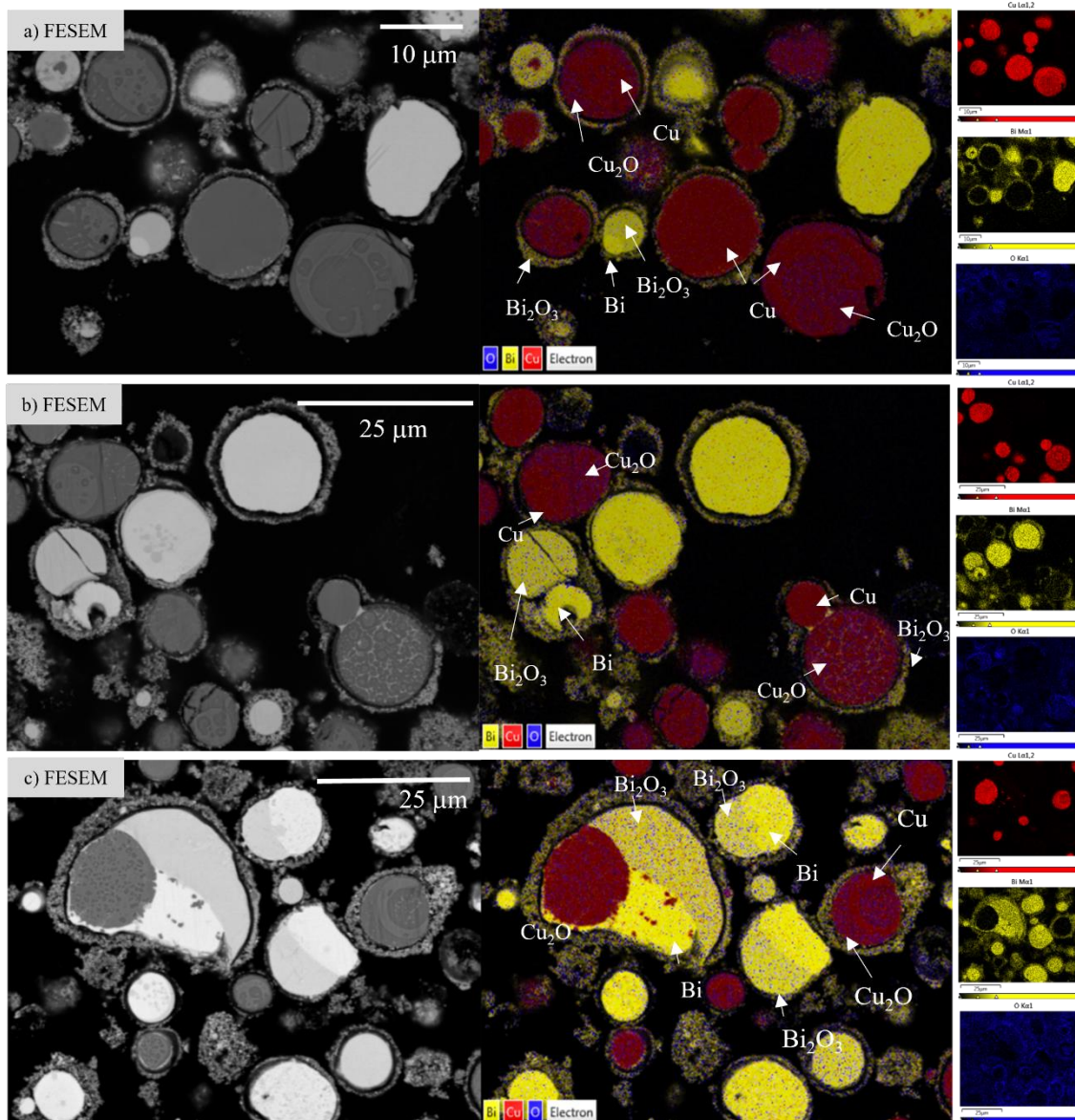


Figure 3.9 Oxidation mechanism of β - $\text{Bi}_2\text{O}_3/\text{Cu}_2\text{O}$ heterojunction obtained in the hopper analyzed in the cross-sectional area with EDS and EBSD.

EDS analysis on the cross-sectional area of β - $\text{Bi}_2\text{O}_3/\text{Cu}_2\text{O}$ flame sprayed heterojunctions collected in the hopper in oxidizing atmosphere ($\phi = 0.8$, 37 NLPM) is shown in Figure 3.9. The EDS mapping show the coexistence of different phases also identified by XRD. The zone of the particle that shows presence of oxygen is attributed to the oxide compounds of copper and bismuth respectively.

Photocatalytic H₂ evolution and methanol photooxidation of visible-light driven bismuth-based heterojunctions synthesized by flame spray

All the particles shown the junction of at least two phases a metal oxide join to its metal by a heterointerface, e.g., Cu/Cu₂O or Bi/ β -Bi₂O₃. Moreover, these particles are grafted on its surface by nanometric β -Bi₂O₃. This phenomenon could be explained since some bismuth as-sprayed particles are evaporated and oxidized according to the physical phenomena explained by Pawloski et. al⁹⁷ (Figure S3.3).

Although, EDS mapping of micrograph c) shows the coexistence of Bi/ β -Bi₂O₃/Cu₂O by sharing a heterointerface between semiconductors and metal that serves as an electron scavenger when the photocatalyst is irradiated with light. These results probe the formation of Janus particles that share different chemical composition with different semiconducting and optical properties to induce novel properties such as an efficient charge carrier transport to enhance the photocatalytic activity.

The mechanism of oxidation for bismuth and bismuth-copper sprayed powders is analyzed by electron microscopy and is shown in Figure 3.10. The heterojunctions formed in the hopper Bi/ β -Bi₂O₃ and Bi/ β -Bi₂O₃/Cu/Cu₂O present a micrometric particle size with Janus raspberry morphology^{136,137}. For bismuth flame sprayed powder the formation of a micrometric particle of ~10 μ m is formed and grafted on the surface is bismuth. For the heterojunction, Bi/ β -Bi₂O₃/Cu/Cu₂O is formed of a micrometric particle of Cu₂O (dark gray) and grafted of the surface is nanometric particles of β -Bi₂O₃.

The proposed oxidation mechanism is illustrated in the right side of the micrographs. For Bi/ β -Bi₂O₃ the oxidation starts in the surface and goes to the nuclei of the particle generating that some remanent semi-metallic bismuth remains not oxidized. For the oxidation of bismuth-copper the oxidation of every single particle starts in the surface and goes into the nuclei. In the process of oxidation, the particles are in a molten or semi-molten state which generated the fusion of both metals by a heterointerface generating a multi composite¹⁰⁷.

For the β -Bi₂O₃ powders collected in the cyclone all of them exhibits a nanometric particle size with spherical morphology. As it has been reported in our previous studies¹²⁶,

Photocatalytic H₂ evolution and methanol photooxidation of visible-light driven bismuth-based heterojunctions synthesized by flame spray

bismuth presents low fusion temperature which enhances the oxidation to form Bi₂O₃, the evaporation temperature of Bi₂O₃ is ~1500 °C much lower from the temperature of the flame which enhances the vaporization of the in-flight particles decreasing significantly its particle size (steps from 1 to 6). Pawlowski et al, reported the decrease in particle size and the oxidation mechanism for a particle with boiling point lower than the temperature of the flame (Figure S3.3).

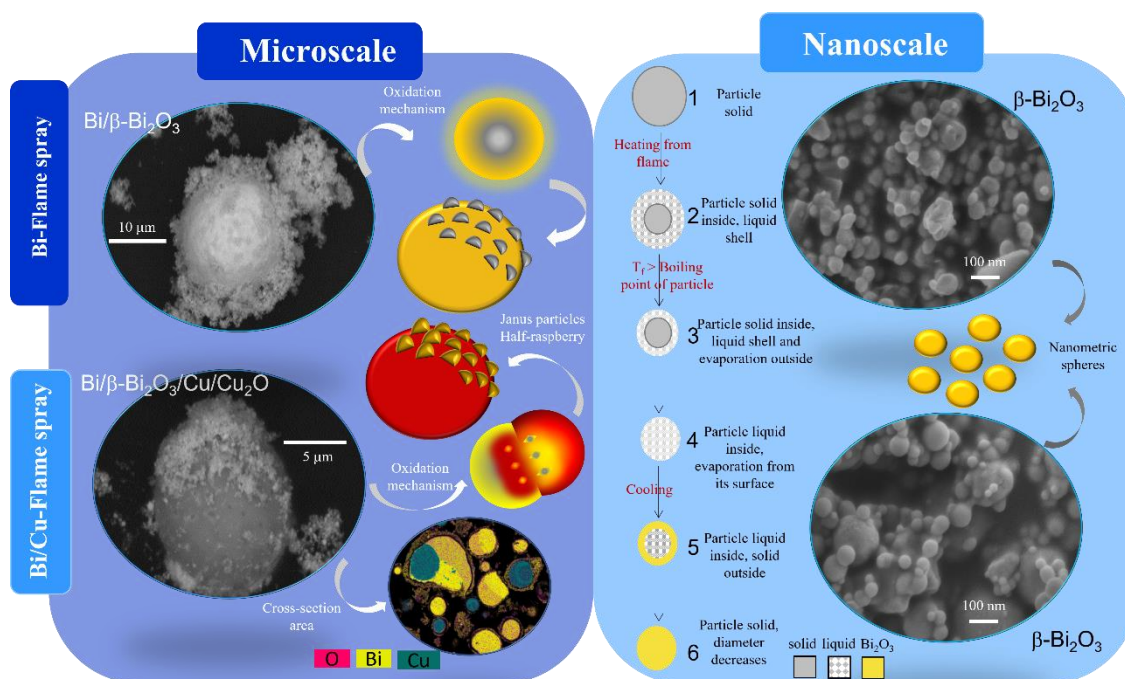


Figure 3.10 Proposed oxidation mechanism of bismuth and bismuth-copper flame sprayed in the hopper and in cyclone and the formation of Janus particles (obtained in the hopper) and nano-spherical particles (obtained in the cyclone).

3.3.4. Photocatalytic activity for methanol oxidation and hydrogen generation

The photocatalytic activity of micrometric heterojunctions Bi/ β -Bi₂O₃ and Bi/ β -Bi₂O₃/Cu/Cu₂O collected in the hopper (Figure 3.11a and 3.11d) and the respective β -Bi₂O₃ nanometric powder collected in the cyclone (Figure 3.11b and 3.11d) was measured for methanol photooxidation as the evolution in concentration of formaldehyde versus the

Photocatalytic H₂ evolution and methanol photooxidation of visible-light driven bismuth-based heterojunctions synthesized by flame spray

irradiation time using Nash method. Bi/ β -Bi₂O₃ (Figure 3.11a) shows higher activity than β -Bi₂O₃ (Figure 3.11b) and is higher in the powders sprayed in oxidizing atmosphere. This can be related since the content of Bi is higher and could serve as electron scavengers, then diminishing the electron-hole recombination and holes migrate to the surface of the particle and oxidize methanol. For the case of β -Bi₂O₃, the sample synthesized in oxidizing atmosphere and low gas flow present higher activity. These results might be referred due to the structural parameters of tetragonal bismuth oxide, the morphology and particle size.

Bi/ β -Bi₂O₃/Cu/Cu₂O heterojunctions also present higher activity than β -Bi₂O₃ (Figure 3.11c and 3.11d). The multi-heterojunction synthesized in oxidizing atmosphere shows higher activity which infers that a higher amount of metals in the surface promote the electron transfer from the semiconductor.

Photocatalytic H₂ evolution and methanol photooxidation of visible-light driven bismuth-based heterojunctions synthesized by flame spray

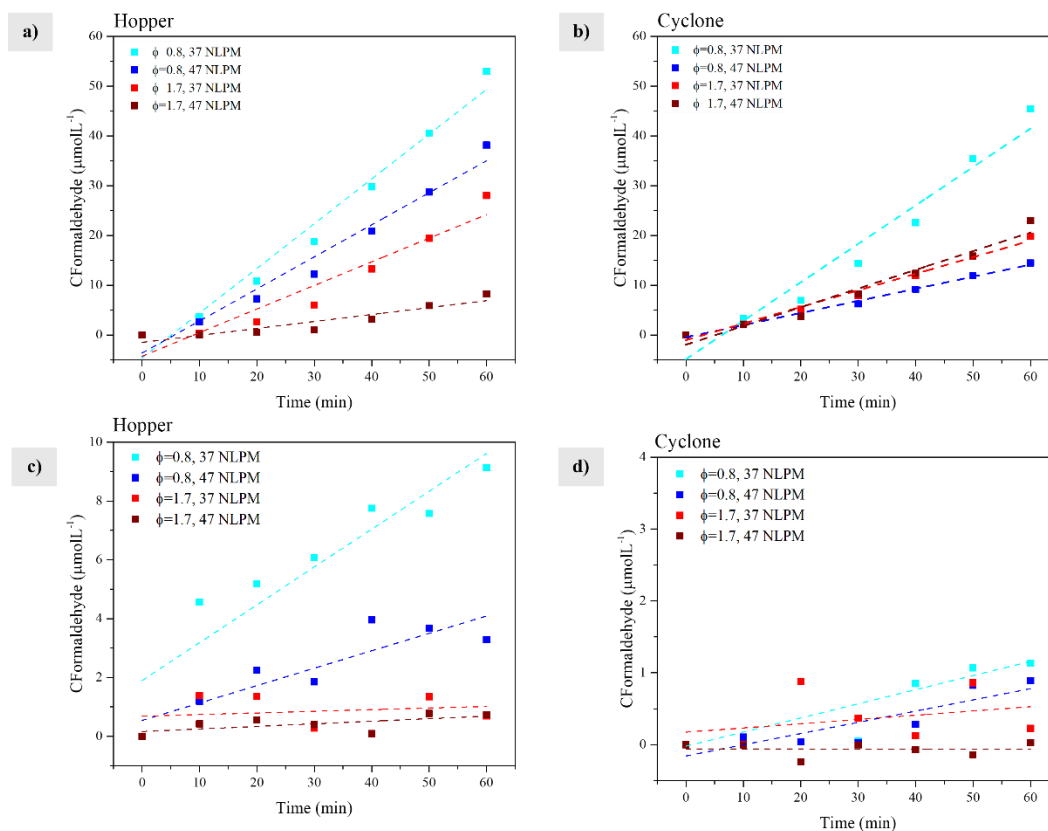


Figure 3.11 Formaldehyde formation over methanol photooxidation of as-sprayed recollected powder in hopper and cyclone for a), b) bismuth and c), d) bismuth-copper flame sprayed powder.

The measured reaction rates dC/dt for methanol oxidation was obtained from the slopes of the concentration-time plots and is shown in Table 3.3. Bismuth as-sprayed powder collected in the hopper present higher activity than the powder collected in the cyclone. The heterojunction between bismuth and bismuth oxide in micrometric particle size presents higher activity than pure nanometric bismuth oxide. In the case of bismuth-copper as-sprayed powder collected in the hopper shows higher activity than the powder collected in the cyclone. The multi-heterojunction between bismuth and copper and their respective oxide present higher activity than bismuth oxide recollected in the hopper.

Table 3.3 Reaction rate (dC/dt) for methanol photooxidation for bismuth and bismuth-copper as-sprayed powders collected in the hopper and in cyclone.

<i>Feedstock as-sprayed powder</i>	<i>Flame spray conditions</i>	<i>Reaction rate (dC/dt)</i>	
		$\mu\text{molL}^{-1}\text{min}^{-1}$	
		<i>Collection stage</i>	<i>Collection stage</i>
		<i>Hopper</i>	<i>Cyclone</i>
<i>Bismuth sprayed</i>	$\phi = 0.8, 37 \text{ NLMP}$	0.8986	0.7725
	$\phi = 0.8, 47 \text{ NLMP}$	0.6440	0.2432
	$\phi = 1.7, 37 \text{ NLMP}$	0.4745	0.3330
	$\phi = 1.7, 47 \text{ NLMP}$	0.1396	0.3761
<i>Bismuth-copper sprayed</i>	$\phi = 0.8, 37 \text{ NLMP}$	0.1286	0.0196
	$\phi = 0.8, 47 \text{ NLMP}$	0.0592	0.0156
	$\phi = 1.7, 37 \text{ NLMP}$	0.0055	0.0059
	$\phi = 1.7, 47 \text{ NLMP}$	0.0087	0.0006

The photocatalytic activity of heterojunctions evaluated for H₂ evolution over platinumized surface and in methanol aqueous solution using a solar simulator reactor with UV-visible light of 1000 W is shown in Figure 3.12. From the heterojunctions obtained in the hopper only Bi/ β -Bi₂O₃/Cu/Cu₂O shows activity for H₂ evolution, specifically the heterojunctions obtained in oxidizing atmosphere. However, β -Bi₂O₃ obtained in the cyclone do not show any activity even by platinumizing the surface with different wt.% or in methanol to work as a hole scavenger. The evolved H₂ of the heterojunctions sprayed in oxidizing atmosphere ($\phi = 0.8$) for an oxygen/acetylene gas flow of 37 NLPM (Figure

Photocatalytic H₂ evolution and methanol photooxidation of visible-light driven bismuth-based heterojunctions synthesized by flame spray

3.12a) and 47 NLPM (Figure 3.12a) is presented. For both heterojunctions, a higher amount of H₂ is evolved for 4 and 5 wt.% Pt and decreases gradually for 2 and 1 wt.% Pt.

The reaction mechanism to evolved H₂ in the heterojunction β -Bi₂O₃/Cu₂O infers that the charge carrier transfer corresponds to a direct Z-scheme where electrons are transferred from the CB of β -Bi₂O₃ to the VB of Cu₂O and then photoexcited to its CB, then holes remain in the VB of Bi₂O₃ creating a p-n junction barrier. Therefore, electrons in the CB of Cu₂O can reduce protons to form molecular hydrogen H⁺/H₂ and the holes in the VB of Bi₂O₃ can oxidize methanol •CHOOH, H⁺/CH₃OH.

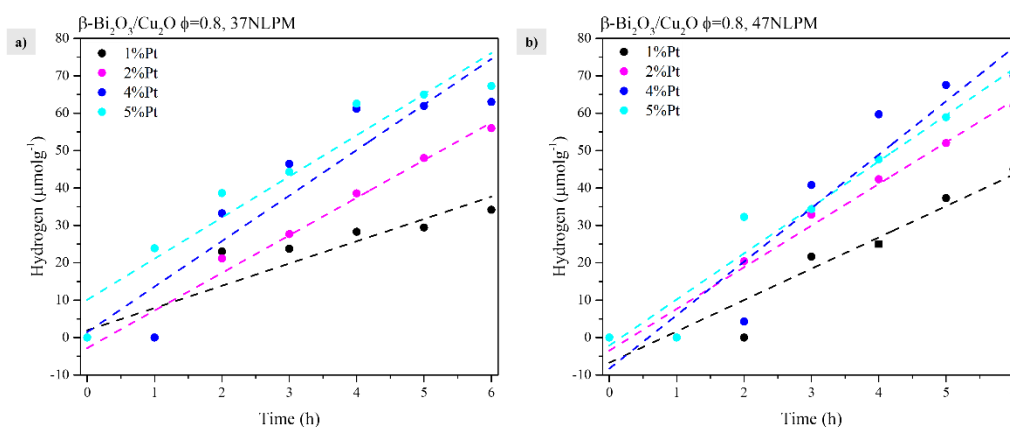


Figure 3.12 Photocatalytic H₂ evolution over flame sprayed β -Bi₂O₃/Cu₂O heterojunction obtained in the hopper for oxidizing atmosphere using a total gas flow of a) 37 NLPM and b) 47 NLPM. Catalyst concentration: 1gL^{-1} , methanol (hole scavenger) 2.47molL^{-1} , Pt (photodeposition H_2PtCl_6).

The platinumized surface serves as electron scavenger to enhance the charge carrier separation decreasing recombination. Although, metallic bismuth and copper grafted on the surface as effect of flame spray process serves as electron scavengers. A higher amount of these metals and Pt suggest that the photocatalytic activity of the heterojunctions enhance.

3.4. Conclusion

By the first time in the literature, the synthesis of a heterojunction in powder form was achieved by flame spray process. A family of bismuth based multi-heterojunctions and highly pure tetragonal β -Bi₂O₃ were synthesized by flame spray using metallic powder as feeding precursors. The chemistry of the oxygen/acetylene atmosphere and the total gas flow was varied to analyze the oxidation of the feeding powders. A powder collector set-up was designed and manufactured, and the powder collected in each step present different physicochemical properties indicating that two different materials can be synthesized:

- i) Metal/Semiconductor micrometric particles that present a Janus morphology which consists of a heterointerface between two different inorganic materials with different physicochemical properties. Bi/ β -Bi₂O₃ and Bi/ β -Bi₂O₃/Cu/Cu₂O heterojunctions were synthesized and collected in the hopper. These heterojunctions are formed of Janus particles with raspberry morphology.
- ii) A highly pure tetragonal phase β -Bi₂O₃ with nanometric particle size and spherical morphology is obtained in the cyclone as effect of the evaporation process due to high temperature of the flame.

The oxidation mechanism analyzed by X-ray diffraction and electron microscopy elucidate that as-sprayed powders synthesized in oxidation atmosphere present a higher content of metal not oxidized due to the low temperature of the flame. The heterojunctions synthesized in the oxidizing flame present higher photocatalytic activity for methanol oxidation and H₂ evolution. The high content of metal work as electron scavengers promoting the separation of electron-hole photogenerated.

3.5. Appendix

The calibration curve for bismuth powder fed using a flame spray technologies feeder is shown in Figure S3.1. The powder was fed for 1, 2, 3, 4 and 5 rpm. The amount of powder obtained after 1 min of feeding under N₂ gas as carrying gas was weight and is plot in y-axis. A fitting linear curve was done to obtain the equation for feeding rate at each rpm.

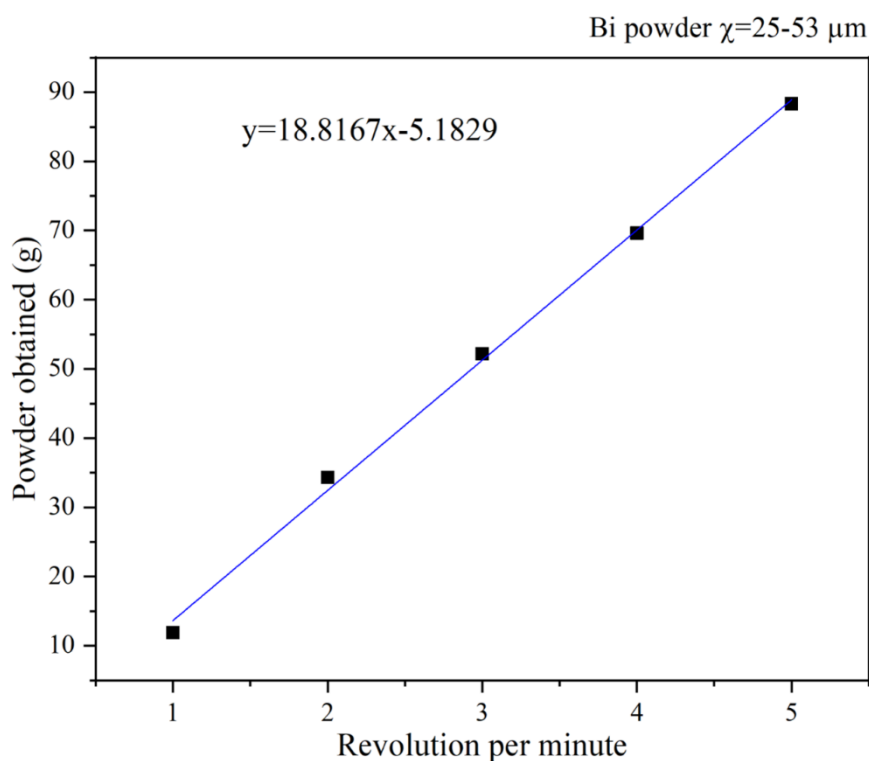


Figure S3.1 Calibration curve of powder feeder for bismuth powder.

Photocatalytic H₂ evolution and methanol photooxidation of visible-light driven bismuth-based heterojunctions synthesized by flame spray

Table S3.1 Phase quantification obtained from Rietveld refinement for bismuth-copper as-sprayed powder

Collected powder	Flame spray conditions	Phase composition (wt.%)					Chi ²	Radj
		Bi	β -Bi ₂ O ₃	α -Bi ₂ O ₃	Cu	Cu ₂ O		
Hopper	$\phi = 0.8$, 37NLMP	7.735	12.847	0	46.894	32.524	2.357	0.0225
	$\phi = 0.8$, 47NLMP	6.21	22.6	4.331	39.729	27.13	1.778	0.0462
	$\phi = 1.7$, 37NLMP	6.403	21.705	8.232	45.692	17.968	2.02	0.028
	$\phi = 1.7$, 47NLMP	3.598	33.25	3.754	35.39	24.007	1.786	0.0349
Tubes	$\phi = 0.8$, 37NLMP	6.237	34.701	2.033	33.724	23.304	1.918	0.0235
	$\phi = 0.8$, 47NLMP	5.742	34.594	2.446	33.4	23.818	1.73	1.73
	$\phi = 1.7$, 37NLMP	6.624	52.888	4.998	21.56	13.928	1.554	0.0117
	$\phi = 1.7$, 47NLMP	4.362	57.453	3.214	15.741	19.23	2.648	0.1222
Bucket	$\phi = 0.8$, 37NLMP	8.126	31.543	4.231	41.256	14.843	2.491	0.047
	$\phi = 0.8$, 47NLMP	8.223	29.746	3.433	44.064	14.533	2.572	0.0499
	$\phi = 1.7$, 37NLMP	3.974	39.642	2.273	38.38	15.73	1.415	0.0366
	$\phi = 1.7$, 47NLMP	2.08	42.626	7.682	30.351	17.263	2.158	0.0545

Photocatalytic H₂ evolution and methanol photooxidation of visible-light driven bismuth-based heterojunctions synthesized by flame spray

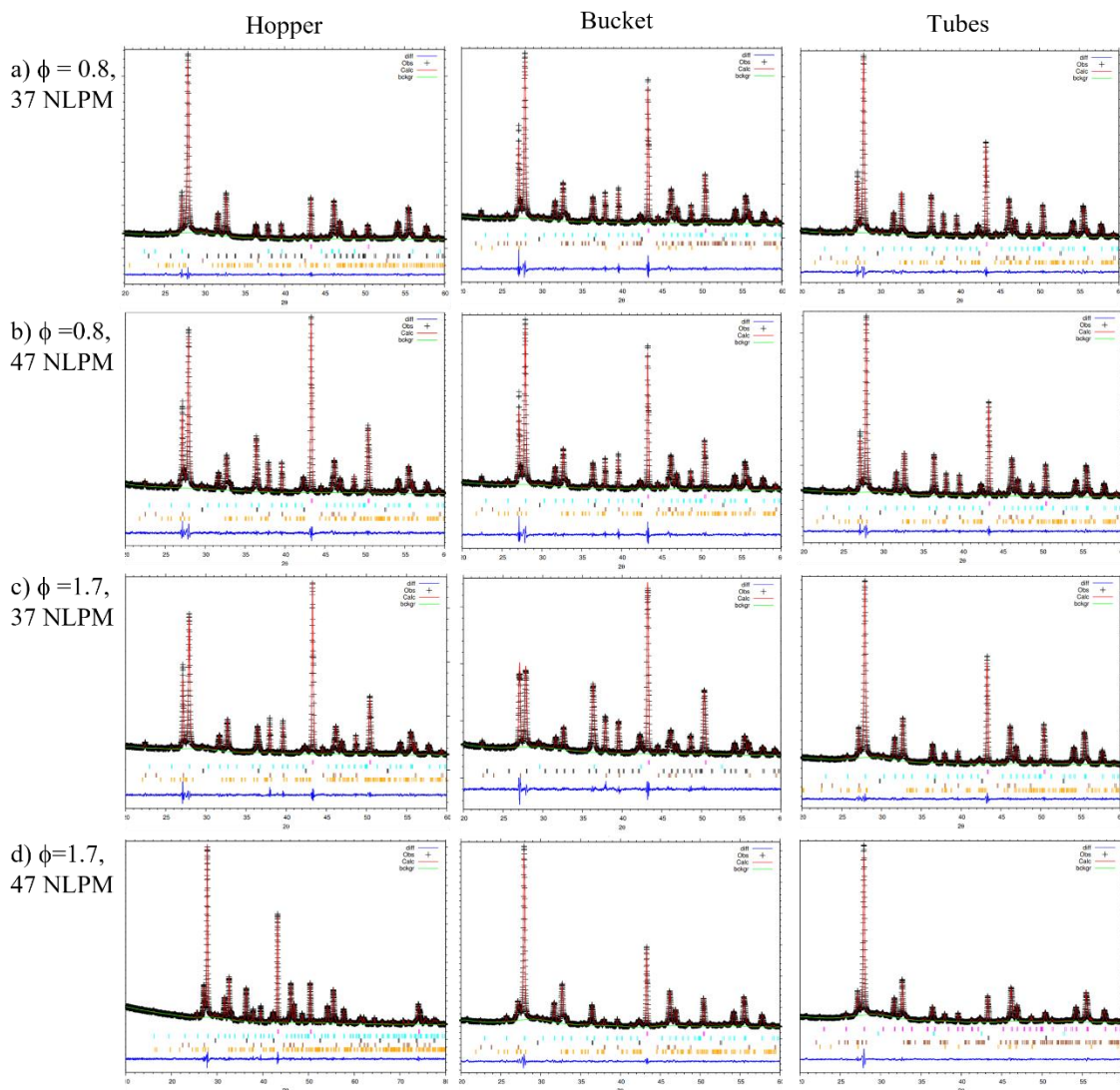


Figure S3.2 Rietveld refined patterns of bismuth-copper as-sprayed powder. Each refinement is composed by four curves: a) the experimental patterns (shown in black), b) the adjusted patterns (red), c) the adjusted background to calculate the phase content and lattice parameters (green) and d) the error line (blue) generated from the difference between the experimental and adjusted patterns.

Photocatalytic H₂ evolution and methanol photooxidation of visible-light driven bismuth-based heterojunctions synthesized by flame spray

Table S3.2 Particle size distribution density (μm) of as-sprayed bismuth and bismuth-copper in the powder collector at hopper, tubes, bucket and cyclone at different flame spray atmospheres.

Feedstock as-sprayed powder	Flame spray conditions	Hopper			Bucket			Tubes		
		d_{10}	d_{50}	d_{90}	d_{10}	d_{50}	d_{90}	d_{10}	d_{50}	d_{90}
Bismuth sprayed	$\phi = 0.8,$ 37NLMP	0.42	2.93	21.7	-	-	-	-	-	-
	$\phi = 0.8,$ 47NLMP	0.39	2.93	23.1	0.32	0.78	8.95	0.32	1.38	10.5
	$\phi = 1.7,$ 37NLMP	0.31	1.12	19.6	0.44	1.57	20.7	0.28	0.81	2.45
	$\phi = 1.7,$ 47NLMP	0.27	0.75	18.0	0.30	0.67	14.9	0.25	0.63	5.23
Bismuth- copper sprayed	$\phi = 0.8,$ 37NLMP	0.46	9.81	18.1	0.38	9.43	21.3	0.43	2.50	10.8
	$\phi = 0.8,$ 47NLMP	0.45	10.0	18.1	0.41	11.1	22.2	0.37	2.17	11.9
	$\phi = 1.7,$ 37NLMP	0.36	9.04	19.6	0.33	9.82	18.5	0.30	0.86	10.2
	$\phi = 1.7,$ 47NLMP	0.32	1.21	17.0	0.30	0.99	15.1	0.31	0.91	2.99

Table S3.3 Production efficiency from as-sprayed bismuth and bismuth-copper in the powder collector at hopper, tubes, bucket, and cyclone at different flame spray atmospheres.

<i>Feedstock powders</i>	<i>Flame sprayed parameters</i>	<i>Hopper</i>	<i>Tubes</i>	<i>Bucket</i>	<i>Cyclone</i>	<i>Total</i>
Bismuth flame spray	$\phi = 0.8$, 37NLMP	15.954	6.549	7.266	4.658	34.427
	$\phi = 0.8$, 47NLMP	16.997	7.552	7.799	3.288	35.636
	$\phi = 1.7$, 37NLMP	20.201	8.207	7.717	9.394	45.519
	$\phi = 1.7$, 47NLMP	16.565	5.626	7.963	5.597	35.751
Bismuth-copper flame spray	$\phi = 0.8$, 37NLMP	45.461	7.871	12.335	2.014	67.681
	$\phi = 0.8$, 47NLMP	26.251	7.196	17.698	3.023	54.168
	$\phi = 1.7$, 37NLMP	13.081	3.081	11.786	6.197	34.145
	$\phi = 1.7$, 47NLMP	24.308	2.874	10.833	5.241	43.256

Different situations that might occur during particle flight are depicted in [Figure S3.3](#). The figure shows a diagram of the associated physical phenomena. At stage 1, the particle is heated until its temperature reaches the melting point. A liquid shell develops around the particle in stage 2. At stage 3, the particle starts to cool down and the liquid shell becomes solidified. Then, the particle solidifies entirely at stage 4. In the thermal history of the

Photocatalytic H₂ evolution and methanol photooxidation of visible-light driven bismuth-based heterojunctions synthesized by flame spray

particle described by stages 1–4, the particle size is not changed. On the other hand, stage 5 initiates particle evaporation. The model of Knight (1979) for rapid surface vaporization with a back pressure can be used to investigate the particle evaporation. This model is based on the conservation of mass, momentum, and energy across a thin layer. At the stages 7 and 10, the particle has cooled down after evaporation from its surface and thus the outer diameter is $d'_p < d_p$.

Photocatalytic H₂ evolution and methanol photooxidation of visible-light driven bismuth-based heterojunctions synthesized by flame spray

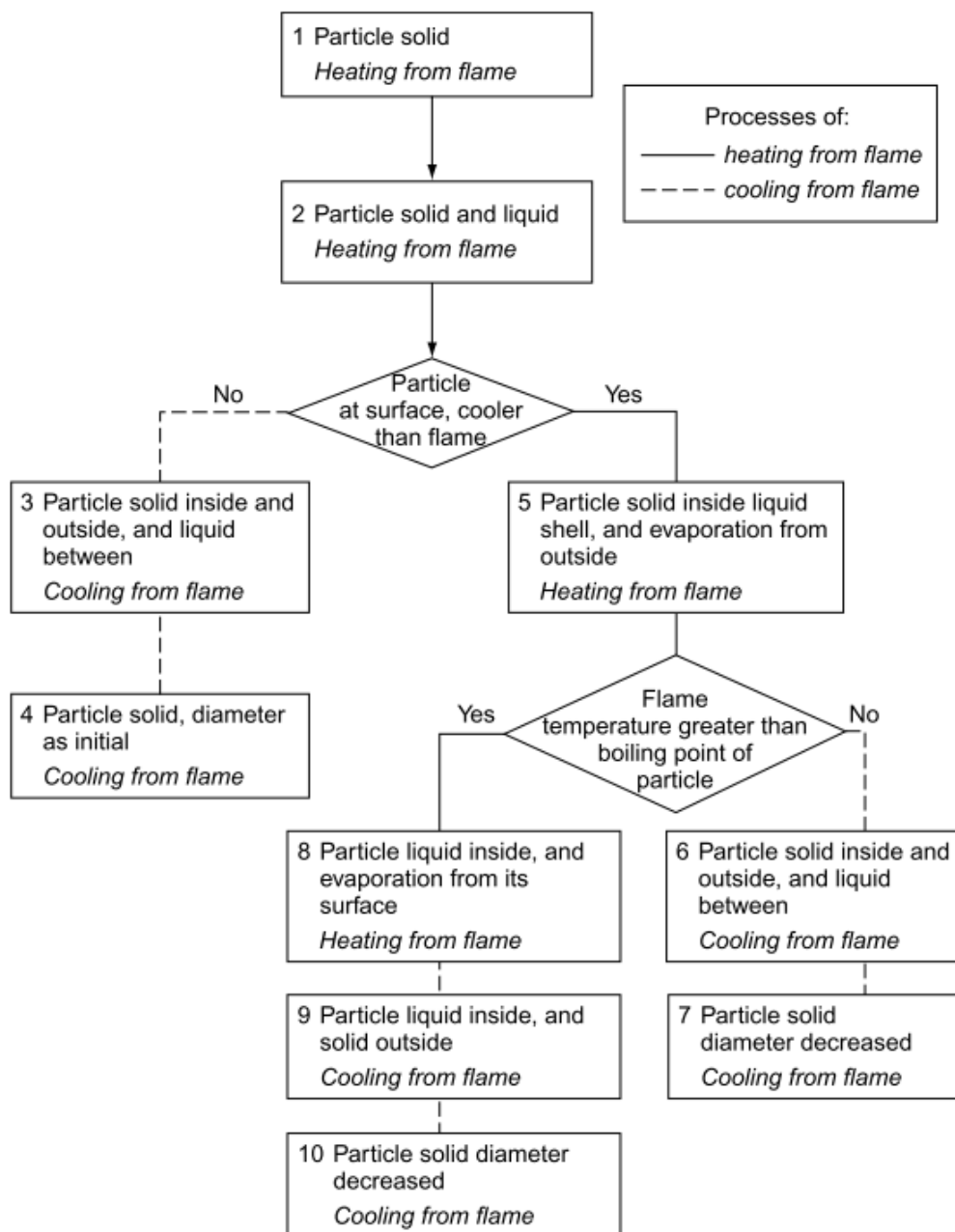


Figure S3.3 Diagram of possible physical phenomena occurring at flight in a plasma or flame.

Photocatalytic H₂ evolution and methanol photooxidation of visible-light driven bismuth-based heterojunctions synthesized by flame spray

Chapter 4:Bi-based heterojunctions synthesized by mechanical milling: Effect of the structural parameters in the optical properties

4.1. Introduction

Over the past few decades, bismuth oxide sesquioxide (Bi_2O_3) has become a promising candidate in photovoltaic¹³⁸ and fuel cells¹³⁹, optical coatings¹⁴⁰, oxygen sensors¹⁴¹, optoelectronics, supercapacitors^{142,143}, ferroelectric and multiferroic materials^{144,145}. Bismuth oxide is a highly active photocatalyst for the degradation of environmental pollutants^{26,30,150–153,39,45,51,96,146–149} and has been used as a photoanode for hydrogen generation under visible light irradiation^{47–49,109}. Its non-toxicity and its excellent properties such as narrow band gap energy^{121,133,154}, high photoconductivity, low photoluminescence^{65,96,109}, oxygen-ion conductivity^{155,156} and dielectric permittivity¹⁵⁷; has positioned Bi_2O_3 to be suitable in multiple applications reflecting the industrial, technologic and scientific importance of this compound^{29,31}.

Its high-performance efficiency is attributed to the anti-bonding states between the lone electron pairs of Bi^{3+} and electrons in O2p orbital that facilitates the photoinduced charge separation enhancing its photocatalytic properties^{76,158}. The electronic structure is composed of Bi6p orbitals in the conduction band minimum (CBM) and Bi6s and O2p orbitals in the valence band maximum (VBM). From the polymorphism of bismuth oxide, $\beta\text{-Bi}_2\text{O}_3$ exhibits enhanced electron transport arising from its *c*-axis oriented tetragonal structure. The high photoconductivity of $\beta\text{-Bi}_2\text{O}_3$ is attributed to its intrinsic polarizability and tetragonal structure, both of which favor the separation of photogenerated electron-hole pairs⁷⁶. The unequal bond lengths cause the formation of irregular BiO_4 tetrahedrons, which share corners to form large-size straight tunnels throughout the entire crystal. This unique crystal structure results in free charge and mass transportation and hence induces high photocatalytic activity³⁵. Since there exists displacement between the centers of bismuth and oxygen atoms, every BiO_4 tetrahedron causes the formation of electric dipole moments (EDM). EDM of the four BiO_4 tetrahedrons are offset along the *c*-axis, i.e., the tunnel direction. The components perpendicular to the *c*-axis oppositely point to the tunnel wall,

Bi-based heterojunctions synthesized by mechanical milling: Effect of the structural parameters in the optical properties

which will benefit the separation of the electron–hole pairs and induce the charge-carriers accumulation on the tunnel wall to react with the mass incoming from the environments³⁷.

β -Bi₂O₃ possess a deep valence band potential (E_{VB}) +2.83 V vs NHE¹⁵³ which offers a higher oxidation power of the holes in the valence band and a narrow band gap ~2.2 eV¹⁵⁹. However, the conduction band potential (E_{CB}) around +0.61 V vs NHE is not enough to achieve the reduction potential of water H⁺/H₂ at 0 V vs NHE for photocatalytic water splitting applications or to scavenge molecular oxygen O₂/O₂⁻ at a potential of -0.33 V vs NHE³⁷.

The construction of composites/heterojunctions is considered as the most viable method to improve the charge separation/transfer process and thereby increasing the overall photocatalysis efficiency²². Due to its appealing physico-chemical properties, many metal nanoparticles and semiconductors could easily be combined with Bi₂O₃ semiconductor. Coupling Bi₂O₃ and other semiconducting materials with different favorable properties induces the creation of band bending at the interface of the heterojunction with an inner electric field so that the transfer and the separation of free charges can be significantly improved¹⁶⁰. Type II heterojunction is commonly formed by the combination of two semiconductors (SC1 and SC2) possessing wide and small band gaps; among them one must has a more negative CB level. Upon light irradiation, when the CB and VB levels of SC1 are greater than the CB and VB positions of SC2, photogenerated holes (h⁺) migrate from the VB of SC2 to the VB of SC1. Meanwhile, photoexcited electrons (e⁻) migrates from the CB of SC1 to the CB of SC2¹¹⁶. In this way, the transfer of photoinduced e⁻ and h⁺ in opposite directions results in an efficient charge separation, which greatly enhance the photocatalytic efficiency. In this context, an efficiently approach to enhance the photocatalytic activity of Bi₂O₃ relays on the coupling with a semiconductor that possess a conduction band more negative than 0 V vs NHE, to entail the reduction reaction of O₂/O₂⁻ or H⁺/H₂ for hydrogen generation by water splitting¹².

Cu₂O is a non-toxic low cost visible light active catalyst with a direct band gap that possess high photocurrent and it has proven to be an active catalyst in visible light for H₂

generation by water splitting⁷¹. In reported studies coupling Bi₂O₃ with Cu₂O has shown to enhance the photocatalytic activity of the single oxides due to the efficient band alignment in a staggered engineering. Bi₂O₃-Cu₂O heterojunction has been synthesized by different routes and the photocatalytic activity was measured for water oxidation or dyes degradation. These studies shown the formation of a heterojunction with a narrow band gap energy around 2.12-2.7 eV. The enhanced in photocatalysis reactions is address due to the decrease of recombination of electron-hole pairs which promotes the transfer and reaction entailed in a type II heterojunction. Although most of the authors prove that the surface modification due to the coupling of both semiconductors promotes the photocatalytic activity⁶¹⁻⁶⁴. Few studies have been devoted to exploring the synergistic effects of crystal structure, structural parameters and optical properties in the charge carrier recombination, excitation, and separation aiming to realize efficient visible-light utilization and redox reaction for photocatalysis.

In this context, herein is presented the synthesis and characterization of β /Bi₂O₃-Cu₂O heterojunctions by a one-step method using high energy ball milling. We investigate the effect of Cu₂O concentration and milling parameters on the structural, microstructural, and optical properties of heterojunctions to enhance the photoresponse respect to single semiconductors and the mechanism of charge carrier recombination and transfer in a p-n heterojunction.

4.2. Materials and methods

4.2.1. Synthesis of heterojunctions

Precursor powders Bi₂O₃ and Cu₂O were used as reagent grade from Sigma Aldrich (99.99 %) without further purification. Heterojunctions (1- χ) β /Bi₂O₃- χ Cu₂O with χ = 25, 50, 75 wt.% were synthesize by high energy ball milling using SPEX SamplePrep mill (Metuchen, EE. UU.). In a typical procedure a ratio of 10:1 ball-to-powder ratio were used with Si₃N₄ balls of 5 mm and 10 mm diameter as milling media, 200 μ L of methanol were used as surfactant and then were sealed and milled for 5, 10-, 20-, 30- and 60 min. Samples were collected and dried for 30 min at 100 °C in an oven.

4.2.2. Structural and microstructural characterization

The relative structural phases and structural parameters of the samples were determined by an XRD-6000 X-ray diffractometer Rigaku, SmartLab (Tokyo, Japan) coupled to a DTech lineal detector. The Cu-K α radiation (1.542 Å) was generated at 44 mA and 40 kV, recording the relative intensity in the scattering range of 2θ from 20° to 60° with a step size of $2\theta = 0.01^\circ$. Phase quantification, structural parameters and crystallite size were analyze using the Rietveld refinement with Full Prof®¹⁶¹. The shape of the peaks in the experimental diffractions patterns was well described by an asymmetric pseudo-Voigt function. The background of each pattern was fitted by a polynomial function of degree 5. To simulate the theoretical X-ray powder diffraction patterns the initial structure refinement for Bi₂O₃ and Cu₂O was based on the structural parameters of Blower & Greaves¹⁶², space group $P-42_1C$ and Kirfel & Eichhorn¹⁶³, space group $Pn-3m$, respectively.

The procedure was adopted for the minimization of the difference between the observed (I_o) and the simulated (I_c) powder diffraction data. The progress of minimization has been monitored using the reliability index parameters, such as the weighted residual error (R_{wb}) (Eq 4.1) and the expected error (R_{exp}) (Eq 4.2) defined as:

$$R_{wp} = \left[\frac{\sum_i w_i (I_o - I_c)^2}{\sum_i w_i (I_o)^2} \right]^{1/2} \quad (\text{Eq 4.1})$$

$$R_{exp} = \left[\frac{N-P}{\sum_i w_i (I_o)^2} \right]^{1/2} \quad (\text{Eq 4.2})$$

where w_i are weight factors, N is the number of experimental observations and P is the number of refined parameters. Also, we used the goodness of fit factor (GoF) (Eq 4.3):

$$GoF = \frac{R_{wp}}{R_{exp}} \quad (\text{Eq 4.3})$$

Refinements were carried out until convergence was reached and the value of GoF factor became close 1, which confirms the goodness of refinement.

Particle size distribution and morphology of precursor powders and as-synthesized heterojunction were characterized by field emission scanning electron microscopy (FESEM) with JEOL 7610F microscope (Tokyo, Japan) using a backscattered electron (BSE) detector at 15 kV electron acceleration voltage. Particle size were measured by image analysis using ImageJ®¹⁰⁴. The specific surface area of the photocatalysts was determined by a single-point Brunauer–Emmett–Teller (BET) measurement through physisorption of nitrogen at liquid nitrogen temperature (−196 °C) using a Chemisorb 2700 apparatus from Micromeritics Instrument Company (Norcross, EE. UU.). The heterojunction Bi₂O₃-Cu₂O synthesized at 60 min milling were characterized by transmission electron microscopy (TEM) analysis using a JEM-2200FS microscope (Tokyo, Japan).

4.2.3. Optical properties

Optical properties of Bi-based heterojunctions and precursor powders were measured to determine the band gap energy of as-prepared powders by diffused reflectance spectrophotometry (DRS) UV-Vis-NIR using a Cary Varian 5000 spectrophotometer (Malvern, UK) with an integrated sphere recovered of PTFE in the range 200-900 nm.

From reflectance spectra, Kubelka Munk theory (Eq 4.4) was applied to measure band gap energies of semiconductors using Tauc method (Eq 4.5). For β -Bi₂O₃, an indirect optical transition¹³³ ($n = 2$) was used and for Cu₂O a direct optical transition¹²³ ($n = 0.5$).

$$F(R) = \frac{(1-R)^2}{2R} \quad (\text{Eq 4.4})$$

$$(F(R)hv)^{1/n} = C(hv - E_g) \quad (\text{Eq 4.5})$$

$F(R)$ is a function of reflectance, R is the reflectance measured by UV-Vis spectrophotometry, hv is the energy of the photons induced, n is the optical transition, C is a constant and E_g is the band gap energy of the bulk of semiconductor. The calculated band gap energies can be determined by a linear fit with x -axes that correspond to the intercept.

Photoluminescence spectra were performed with a microRaman LabRam HR Evolution, Horiba (Villeneuve d'Ascq, France) under ambient conditions at 22 °C with a blue laser of 488 nm. The oxidation states were characterized in an X-ray photoelectron spectroscopy (XPS) instrument assembled by Intercovamex (Morelos, Mexico) with a monochromatic X-ray aluminum $K\alpha_1$ ($h\nu = 1486.7$ eV) source (XR5, from ThermoFisher, East Grinstead, UK) and a 7-channeltron hemispherical spectrometer Alpha110, also from ThermoFisher (Massachusetts, USA). XPS measurements were done at a base pressure of 9×10^{-11} Torr. The energy was calibrated by setting the adventitious C1s binding energy to 284.8 eV. The deconvolution of the XPS signals was performed using a Voigt function and Tougaard background.

4.2.4. Electrochemical measurements

The electrochemical measurements were performed in a three-electrode electrochemical cell consisting of a working electrode, a Pt wire counter electrode and an Ag/AgCl/NaCl (3 molL^{-1}) reference electrode. A pH 6 0.1 molL^{-1} KCl solution was used as the electrolyte. The working electrodes were prepared by using a spray coating technique. For this purpose, 50 mL of 2-propanol solutions containing 20 gL^{-1} of powder was sprayed on top of fluoride-doped tin oxide (FTO) conductive glasses heated to 100 °C for 3 h as reported in our group³⁴. The solution was forced through the nozzle using pressurized air at 1 bar (100 kPa) pressure. A solar simulator (LOT-Quantum Design GmbH) with a 300 W Xe lamp and an AM (air mass) 1.5-global filter was employed as the light source and a Zennium potentiostat (Fa. Zahner-Elektrik GmbH & Co. KG, Germany). Cyclic light voltammetry (CLV) measurements were performed in an aqueous solution with 10 vol-% methanol (2.47 molL^{-1}) in a potential regime between -0.2 V and 1.6 V at a scan rate of 10 mVs^{-1} . The flat band potentials (E_{FB}) were determined according to the Mott-Schottky equation (Eq 4.6)¹⁶⁴.

$$\frac{1}{C_{SC}^2} = \frac{2}{\epsilon \epsilon_0 q N_D} \left(E_{appl} - E_{FB} - \frac{kT}{q} \right) \quad (\text{Eq 4.6})$$

C_{SC} is the capacitance of the space charge layer, ϵ is the dielectric constant of the semiconductor, ϵ_0 is the permittivity of the vacuum, A is the interfacial area, N_D the donor density, E_{FB} the flat band potential, k_B the Boltzmann constant, T the temperature and q the

electronic charge. By plotting C_{SC}^{-2} against E_{appl} , the flat band potential can be derived from the abscissa intercept. The E_{FB} at pH 7 is measured from (Eq 4.7), X is the pH of the electrolyte used in the electrochemical cell.

$$E_{FB}(pH = 7) = E_{FB}(pH = X) + 0.059(pH = X) \quad (\text{Eq 4.7})$$

The measurements were performed in the dark in an aqueous solution in a potential area between -1V to -0.6V for Bi_2O_3 and 0V to 0.6 V for Cu_2O at a frequency of 10 Hz.

4.3. Results and discussion

4.3.1. Characterization of precursor catalyst powders

X-ray diffraction patterns of precursor powder are shown in Figure S4.1. Bismuth oxide shows a tetragonal phase (β -phase) identified with PDF 27-0050 that possess a spatial group $P-42_1c$ and lattice parameter $a = b = 7.742 \text{ \AA}$ $c = 5.631 \text{ \AA}$. Cu_2O powder presents a single cubic phase identified with PDF 05-0667 with the spatial group $Pn-3m$ and lattice parameter $a = 4.2696 \text{ \AA}$. Mathematical Rietveld refinement were used to calculate the lattice parameters, cell volume and crystallite size using Fullprof® (Figure S4.1b). The calculated data is shown on Table S4.1. The refinement shows that the adjustment (GoF) less than or equal to 1 ensures the accuracy of the calculation.

Microstructural characteristics of as-received Cu_2O and $\beta\text{-Bi}_2\text{O}_3$ commercial powders evaluated by SEM microscopy is shown in Figure 4.1a and 4.1b, respectively. $\beta\text{-Bi}_2\text{O}_3$ shows a homogeneous distribution of sub-micrometric spherical particles. Cu_2O presents angular morphology with flat faces and micrometric heterogeneous distribution. Particle size distribution was calculated using image analysis in at least 5 micrographs for each sample with ImageJ®. The cumulative distribution for $\beta\text{-Bi}_2\text{O}_3$ and Cu_2O is $d_{50} = 0.047 \text{ \mu m}$ and $d_{50} = 1.6 \text{ \mu m}$, respectively. According to this result, the particle size of $\beta\text{-Bi}_2\text{O}_3$ powder is approximately one order of magnitude smaller than Cu_2O . The BET surface area measured is $4.13 \text{ m}^2/\text{g}$ for $\beta\text{-Bi}_2\text{O}_3$ and $0.45 \text{ m}^2/\text{g}$ for Cu_2O . As it has been reported elsewhere, low-dimensional $\beta\text{-Bi}_2\text{O}_3$ could provide more advantages for photocatalytic reaction, for example, fast carrier mobility and slow recombination for enhanced charge

Bi-based heterojunctions synthesized by mechanical milling: Effect of the structural parameters in the optical properties

separation in the plane direction⁶³. The particle size and morphological characteristics of a catalyst are of great significance to promote a high contact heterointerface between both semiconductors forming a composite.

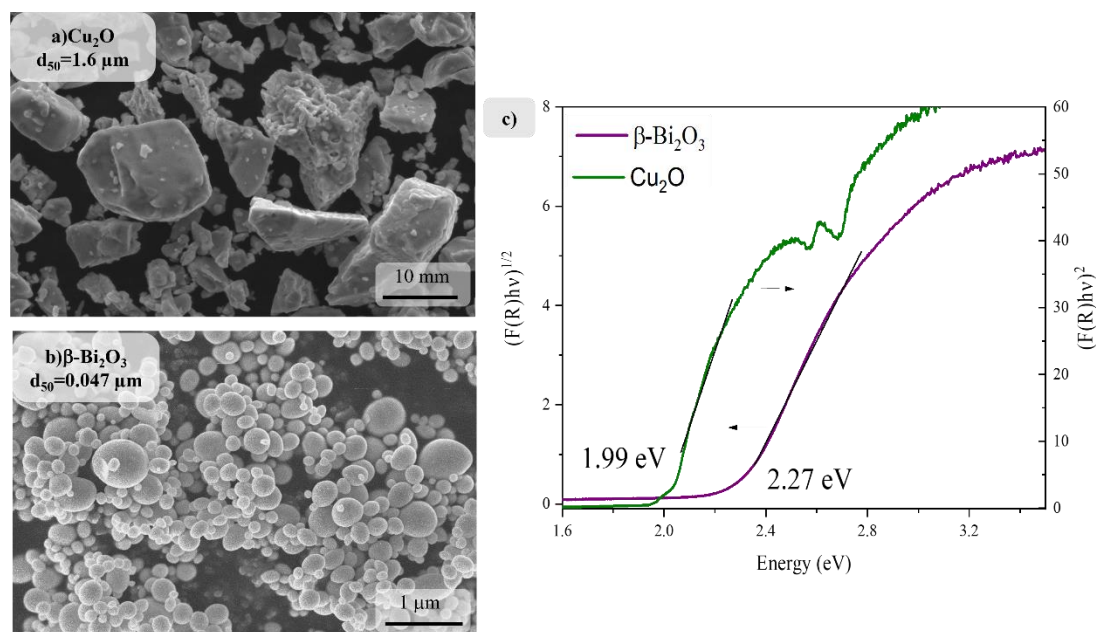


Figure 4.1 SEM micrographs and particle size distribution of a) Cu_2O and b) $\beta\text{-Bi}_2\text{O}_3$, respectively and c) Tauc plot with the band gap energy of the catalysts.

Figure 4.1c shows the Tauc plot for $\beta\text{-Bi}_2\text{O}_3$ with an indirect band gap of 2.27 eV and for Cu_2O with a direct gap of 1.99 eV. $\beta\text{-Bi}_2\text{O}_3$ absorbs in the UV and near-visible range from 546 nm while Cu_2O absorbs from 620 nm which indicates strong responses to the visible light. Both catalyst are visible light active semiconductors able to be activated under solar light irradiance¹⁶⁵.

Photoluminescence spectra were measured for both catalysts to compare the electron-hole recombination when light is irradiated to the semiconductor. PL emission spectra can be used to investigate the efficiency of charge carrier trapping, immigration, and transfer, and to understand the fate of electron-hole pairs in semiconductors, as PL emissions result from recombination of free carriers either directly (band-band) or indirectly (via a band gap

state)¹⁶⁶. Figure 4.2 shows the PL spectra and the deconvolution to show the signal of the electronic transitions present in β -Bi₂O₃ (a) and Cu₂O (b). β -Bi₂O₃ shows a lower intensity of PL signals compared to Cu₂O which represents the lower recombination of electron-holes pair.

β -Bi₂O₃ shows a broad signal center at 647 nm that is the contribution of three PL signals at 2.05 eV, 1.87 eV and 1.56 eV. The emission at 2.05 eV can be related to the direct transitions between the conduction and valence band, since the band-gap energy of β -Bi₂O₃ is 2.27 eV. Trivalent Bi ions in inorganic compounds exhibit PL properties related to their 6s² levels. The luminescence of Bi³⁺ ions appear in the blue-green region (400-600 nm) of the spectrum and is attributed to the ³P₁-¹S₀ transitions or charge transfer between the bonding oxygen and Bi³⁺ ions¹⁶⁷. The PL emissions at 1.87 and 1.56 eV correspond to lower energies in the red region (600-800 nm). Recent research associated emissions in the low-energy spectral range to structural defects of oxygen (oxygen vacancies)¹⁶⁸. The higher the emission intensity at this spectral range, the greater the vacancy density. Moreover, the luminescence in the low-energy spectral range is normally attributed to the ²P_{3/2}-²P_{1/2} transition of Bi²⁺ ions¹⁶⁷. In order to determine the cause for the PL emission at this spectral range, it is necessary to verify the existence of Bi²⁺ ions on the material surface.

For Cu₂O several peaks are detected at 634 nm (1.96 eV) and 910 nm (1.36 eV). These PL emissions are attributed to exciton luminescence around 1.96 eV which is in good agreement with the UV-vis measurements. The PL peak at 1.36 eV correspond to the luminescence signal V_{Cu} that is due to the recombination of bound excitons at copper vacancies¹⁶⁹. This luminescence signal is usually assigned from signal resulting defect states¹⁷⁰.

Bi-based heterojunctions synthesized by mechanical milling: Effect of the structural parameters in the optical properties

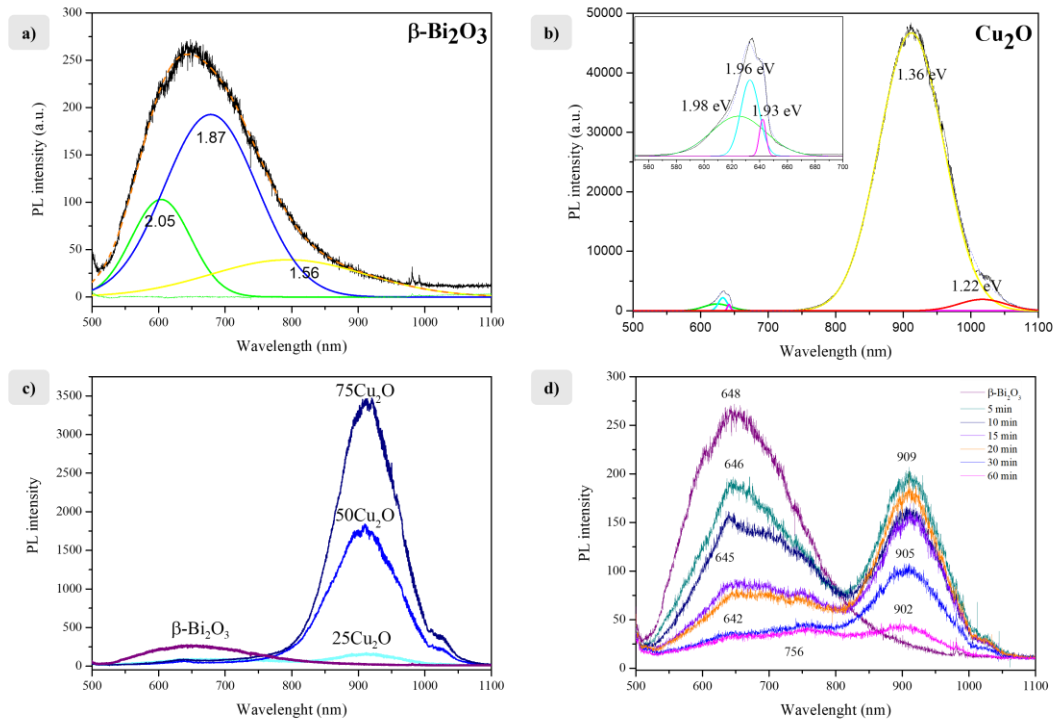


Figure 4.2 Photoluminescence spectra of a) $\beta\text{-Bi}_2\text{O}_3$, b) Cu_2O and c) $(1-\chi)\beta\text{-Bi}_2\text{O}_3/\chi\text{Cu}_2\text{O}$ for $\chi=25, 50, 75$ (w/w) at 15 min of milling and d) $75\beta\text{-Bi}_2\text{O}_3/25\text{Cu}_2\text{O}$ heterojunction as function of milling time.

4.3.2. Optical properties of heterojunctions

The optical properties were evaluated to study the effect of synthesis procedure on the coupling between both catalyst by PL characteristics. **Figure 4.2c** shows the PL spectra of $(1-\chi)\beta\text{-Bi}_2\text{O}_3/\chi\text{Cu}_2\text{O}$ heterojunctions in different amounts $\chi = 25, 50, 75\%$ (w/w). As the content of Cu_2O decreases the PL emission of the compound diminishes until it is lower than the intensity of $\beta\text{-Bi}_2\text{O}_3$ for $\chi = 25\%$ of Cu_2O . These results indicate that a certain amount of Cu_2O is necessary to enhance the charge carrier transfer between both semiconductors. **Figure 4.2d** shows the effect of milling time of $75\beta\text{-Bi}_2\text{O}_3/25\text{Cu}_2\text{O}$ heterojunction on the PL intensity. By increasing the time from 5 to 60 min, the decrease of PL emission is evidenced and in all cases is lower than the intensity of $\beta\text{-Bi}_2\text{O}_3$. This effect evidence that milling plays an important role on the physical coupling of both powders as is

evidenced a decrease on the counts of recombination of electron hole pairs that are observed in PL spectra as effect of photon release.

Figure 4.3a shows the UV-vis diffused reflectance spectra of 75 β -Bi₂O₃/25Cu₂O heterojunction as function of milling time. As milling time increases up to 60 min the material shows stronger absorption which infers that the absorption of the catalyst shifts to narrow visible light. From DRS of 5 min, it is seen two absorption signals that might correspond to Cu₂O that starts at 640 nm (2 eV) and a second signal around 560 nm (2.21 eV) that is attributed to β -Bi₂O₃, as time increases up to 60 min the signal become one in the absorbance emission which can be seen as an effect of coupling of both semiconductors. Figure 4.3b shows Tauc plot to determine band gap energy for an indirect transition $n = 2$ in accordance with the band structure of β -Bi₂O₃ since is the majority semiconductor in the heterojunction. The band gap energy of the composite decreases from 2.13 eV at 5 min to 1.84 eV at 60 min. This effect can be explained as an efficient coupling between both materials that now can absorb in lower energies in the visible region due to efficient charge transfer.

Bi-based heterojunctions synthesized by mechanical milling: Effect of the structural parameters in the optical properties

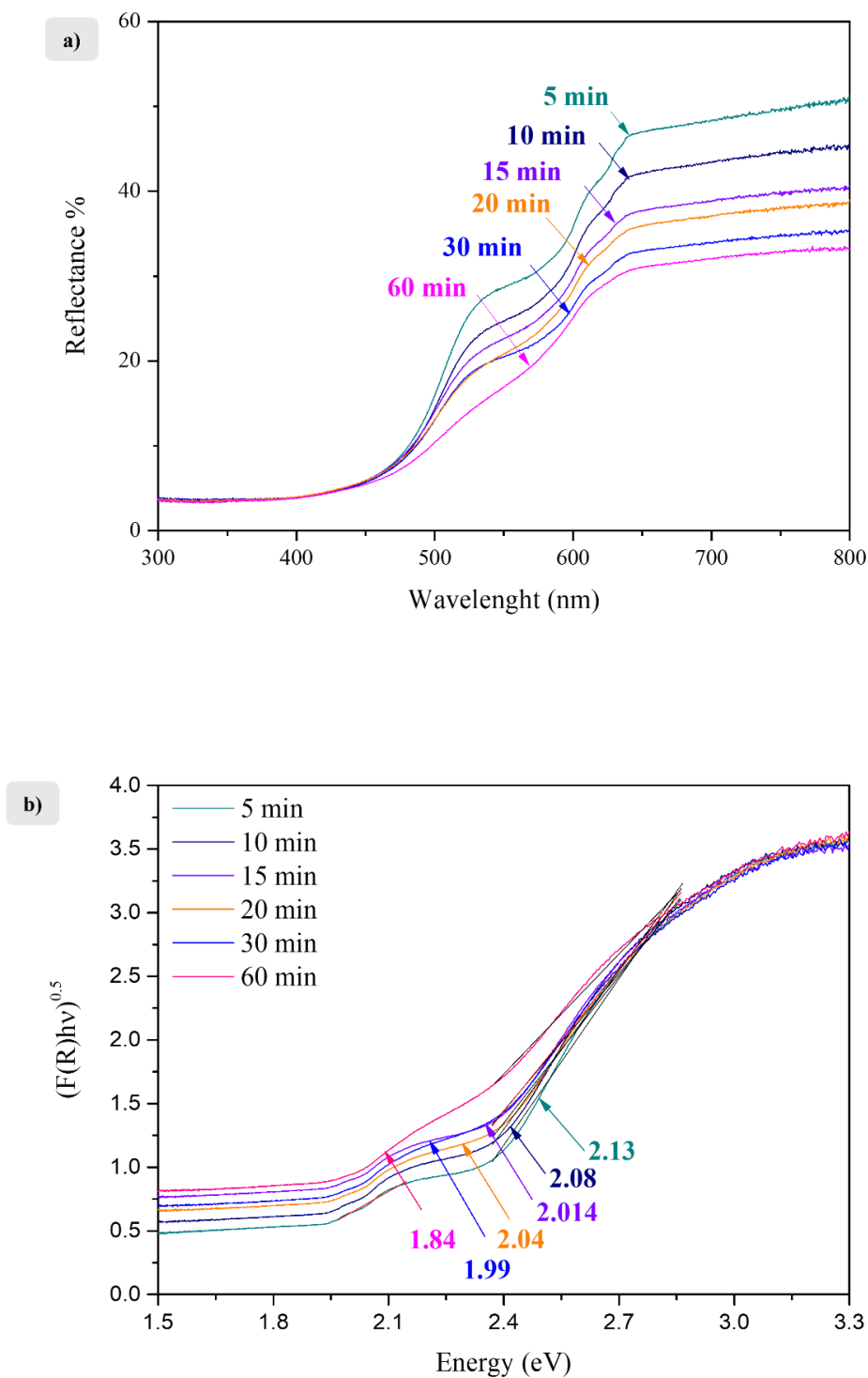


Figure 4.3 a) Reflectance spectra and b) Tauc plot of band gap energies of $75\beta\text{-Bi}_2\text{O}_3/25\text{Cu}_2\text{O}$ heterojunction as function of milling time.

4.3.3. Structural and microstructural properties of heterojunctions

XRD patterns of 75 β -Bi₂O₃/25Cu₂O heterojunction powders after high energy ball milling process, at 5, 10, 15, 20, 30 and 60 minutes is shown in [Figure 4.4a](#). All the pattern peaks were indexed with the Cu₂O and β -Bi₂O₃ phases, PDF 05-0667 and PDF 27-0050 respectively, the same reported for the starting powders. They are readily identified as none of the phase peaks are overlapped and no other peaks of additional phases are observed. From these results it is assumed that there is no solid solution formation or changes in the starting materials phases, promoted by the milling conditions. Additionally, there are no peaks related to impurities introduced from the Si₃N₄ balls milling media, for they are highly stable. In [Figure 4.4b](#) and [4.4c](#) are presented a shorter range of the patterns in 2θ , where are observed the main peaks of the two identified phases, the (201) of β -Bi₂O₃ (27.5-28.4°) and (111) of Cu₂O (35.6-37.4°) respectively, for all the milled conditions. In both plots was observed that with the increment of the milling time, the peak positions did not show a significant change, but the widths and intensities showed differences, which are related to changes in the crystallite size. [Figure S4.2](#) shows the Rietveld refinement. The lattice parameters and crystallite size of the heterojunction determined by Rietveld refinement is shown in [Table S4.1](#). The goodness of fit (*GoF*) was close to 1 for all these patterns indicates the quality of the fitting is quite good.

Bi-based heterojunctions synthesized by mechanical milling: Effect of the structural parameters in the optical properties

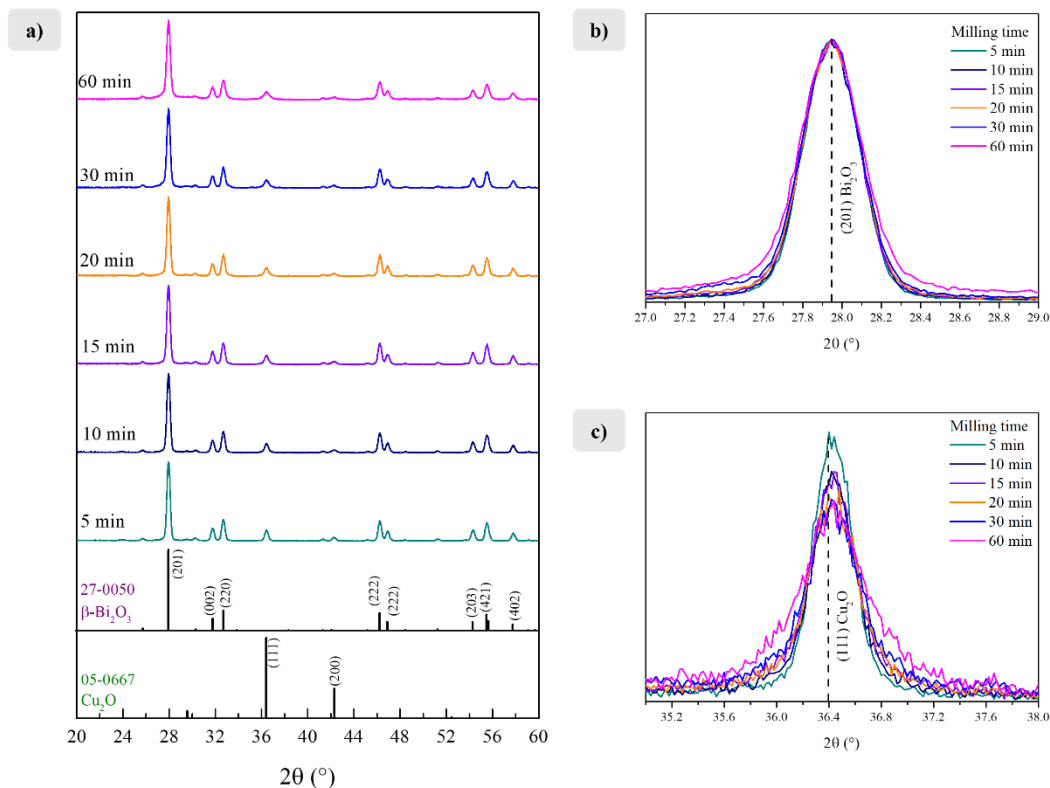


Figure 4.4 a) XRD patterns of as prepared 75 β -Bi₂O₃/25Cu₂O heterojunctions by solid state reaction, b) and c) effect of milling time on the lattice distortion of (201) β -Bi₂O₃ and (111) Cu₂O plane respectively.

Figure 4.5 shows the crystallite size of β -Bi₂O₃ in its single form and in the heterojunction as a function of the milling time (blue line). Crystallite size generally corresponds to the coherent volume in the material for the respective diffraction peak. In simple terms is the smallest single crystal in powder form. For both catalysts, crystallite size decreases as the milling time increases. The crystallite size dropped from about 504 nm to 279 nm for β -Bi₂O₃ and from 382 nm to 137.45 nm for Cu₂O. The variation of lattice parameter c for β -Bi₂O₃ with increasing the milling time is also shown (purple line). An increase in the lattice parameter was observed respect to the time; probably caused by the grain expansion due to the increase in the density of dislocations with their characteristic

fields. The band gap energy obtained from Figure 4.3 is also shown in Figure 4.5 (black line) showing a decrease respect to the milling time.

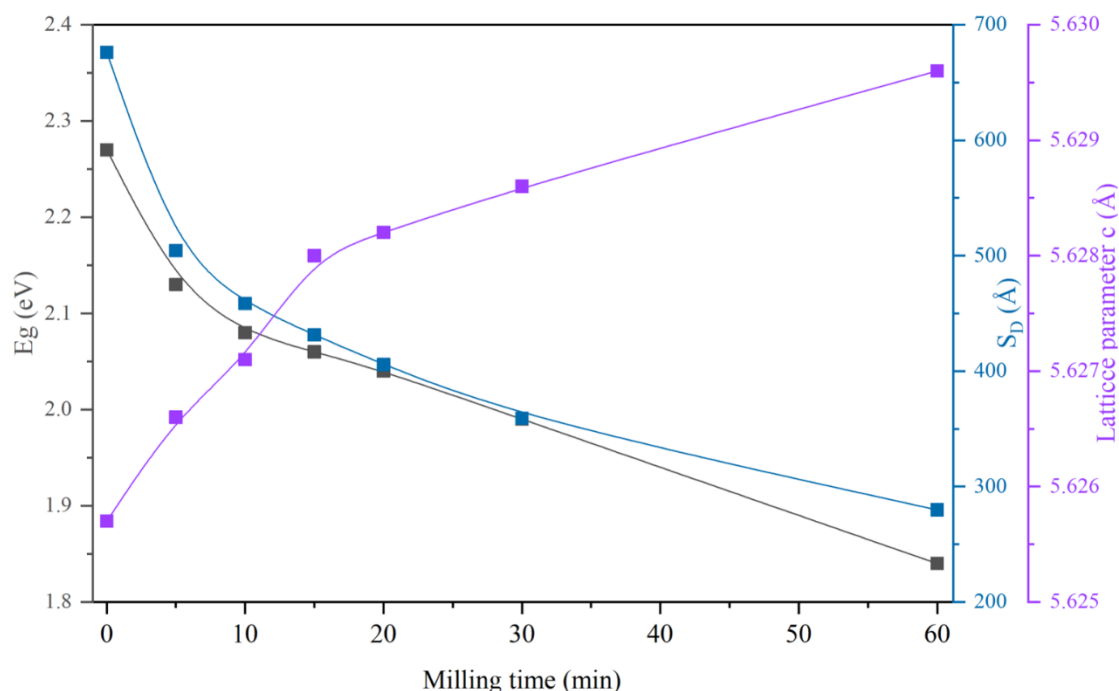


Figure 4.5 Effect of milling time in the band gap energy (dark line), lattice parameter c (purple line) and crystallite size (blue line) of $75\beta\text{-Bi}_2\text{O}_3/25\text{Cu}_2\text{O}$ heterojunction. The values at $t=0$ correspond to single $\beta\text{-Bi}_2\text{O}_3$.

In the mechanical milling process homogenization and reduction of particle size occur, not necessarily with mechanically induced transformations or material transfer. Mechanical deformation is introduced into the powder, particle and crystallite refinement occurs and the lattice strain increases, leading to the X-ray diffraction peak broadening and heights decreasing¹⁷¹. Ball milling produces much finer particles with larger surface area and also activates them mechanically via the introduction of high concentration defects.

The crystal refinement, the increase of tetragonality (increase of lattice parameter c) of β - Bi_2O_3 , and the high absorbance of the heterojunction in the visible region are well related to the diminish of PL signal that is a direct analysis of the low recombination of electron-hole pairs. The tunnels structure in β - Bi_2O_3 sample can provide the channels for the charge carriers transfer and separation. The formation of vacancies functioned as trapping sites to induce the delocalized photogenerated carriers to be converged and then accelerate the separation efficiency. The introduction of defects could induce the localization of charge carriers, which can not only facilitate the adsorption and activation of reactants but also accelerate the separation of photogenerated carriers³⁵.

In [Figure 4.6](#) are shown the SEM micrographs recorded with backscattering detector, of the 75 β - Bi_2O_3 /25 Cu_2O heterojunction powder milled at 5, 10, 15, 20, 30 and 60 min. From the previous microstructural analysis of the precursor powder ([Fig. 4.1](#)), in the milled powder micrographs showed irregular shape particles with different contrasts, these observations suggests that the darker gray shade microstructures correspond to the Cu_2O particles, whereas the smaller spherical particles of a lighter gray shade, to the β - Bi_2O_3 powder. On the SEM images of the powder milled at 5 and 10 min, the β - Bi_2O_3 and Cu_2O particles are mixed, however the microstructures of both compounds can be distinguished since the precursor powder morphology and size characteristics did not show significant changes. With higher milling times (20 – 60 min) is observed a progression of the powder mixing process, particle fragmentation is more evident, especially on the Cu_2O particles of larger sizes. In the micrograph of the powder milled for 60 min is observed that a good assemble of the two compounds is achieved, in the present work this would be considered as the optimal milling time. Since the milled compounds are not of ductile nature, the product of the mechanical milling process of the samples is not expected to be an alloy, additionally, the use of a process control agent (surface active agent), in this case methanol, inhibits agglomeration and reduces the effect of cold welding¹⁷¹.

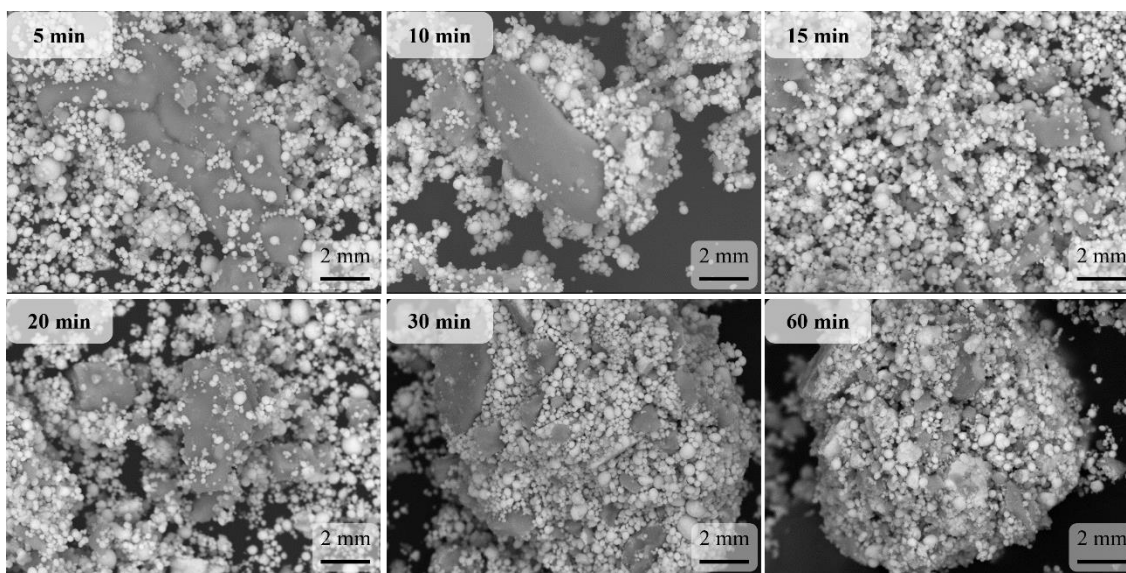


Figure 4.6 SEM micrographs of powder mixtures showing the evolution of the heterojunction assemble as a function of by milling time.

In order to get more details about the structure of β - $\text{Bi}_2\text{O}_3/\text{Cu}_2\text{O}$ TEM, high resolution transmission electron microscopy (HRTEM) and selected area electron diffraction (SAED) of the sample 75 β - Bi_2O_3 /25 Cu_2O milled 60 min was investigated to give an intuitionistic image for the formation of chemically bonded interfaces between β - Bi_2O_3 and Cu_2O particles. Based on the areas selected in the yellow and red circle in Figure 4.7a and 4.7b, the average thickness of lattice fringes of Cu_2O and β - Bi_2O_3 have been found. The lattice spacing was estimated to be approximately 0.135 nm and 0.127 nm, which matched well with the (310) plane of Cu_2O and (610) crystal plane of β - Bi_2O_3 , respectively suggesting that both compounds exist in the heterojunction. Figure 4.7c, shows the clear boundary and transition area between Cu_2O and β - Bi_2O_3 . Figure 4.7d and 4.7e shows the SAED patterns obtained in two different particles (Z1 and Z2). The SAED of zone 1 (Z1) (Figure 4.7d) was indexed as (4 -2 5) axis zone, the diffraction spots corresponding to the tetragonal β - Bi_2O_3 and zone 2 (Z2) (Figure 7e) was indexed as (-2 2 0) axis zone, the diffraction rings corresponding to the (1 1 1), (2 2 0) and (3 1 1) planes indicate that the particle Z2 is a Cu_2O crystal with a cubic structure. All results clearly demonstrate that β - Bi_2O_3 and cubic

Bi-based heterojunctions synthesized by mechanical milling: Effect of the structural parameters in the optical properties

Cu₂O coexist in heterojunction. [Figure 4.7f](#) and [4.7g](#) shows a mapping of EDS that shows the zones of β -Bi₂O₃ and Cu₂O in a heterojunction assemble.

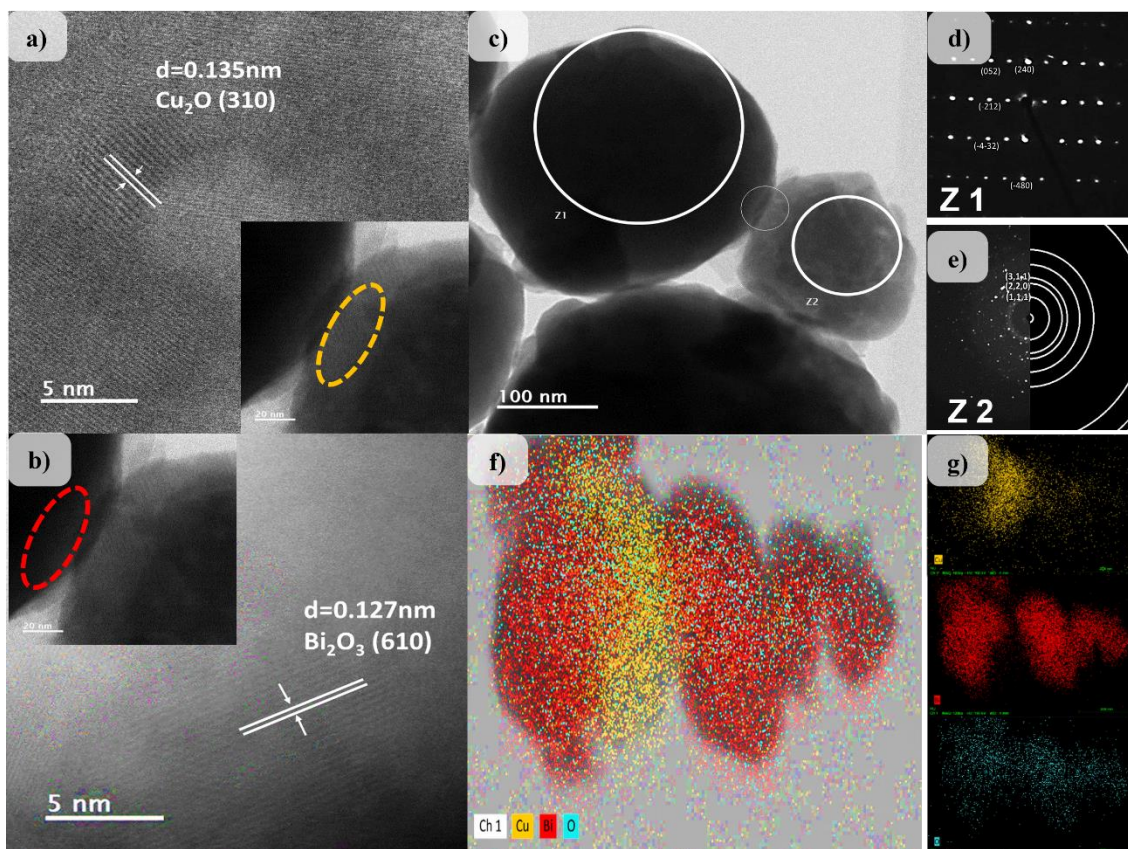


Figure 4.7 a), b) HRTEM of 75 β -Bi₂O₃/25Cu₂O (60 min) showing the heterojunction phase of both catalyst and the index planes of Cu₂O and β -Bi₂O₃ respectively, c) TEM, d), e) XRD patterns of Bi₂O₃ (Z1) and Cu₂O (Z2), f) EDS map of the heterojunction zone.

XPS analysis was performed to identify the chemical states of β -Bi₂O₃ and Cu₂O before and after the heterojunction. [Figure 4.8](#) shows the deconvolution fitting of XPS signals to evaluate the chemical states of Bi4f level in β -Bi₂O₃ ([Fig. 4.8a](#)) and ([Fig. 4.8b](#)) in the heterojunction. Two peaks located at 158.82 eV and 164.03 eV correspond to Bi4f_{5/2} and Bi4f_{7/2}, a small peak is located at 156.53 eV related to the presence of α -Bi₂O₃. The binding energy difference of 5.3 eV confirms that Bi exists in the Bi³⁺ oxidation state. In the heterojunction the peaks are shifted to smaller energy 156.8 eV and 162.1 eV for Bi4f_{5/2}

and $\text{Bi}4f_{7/2}$, respectively. The shift of the peaks of Bi^{3+} indicated that the surfaces of Bi_2O_3 nanospheres were successfully modified by Cu_2O , and there is a strong interaction between them^{63,109}.

XPS analysis of Cu2p level of Cu_2O in single form (Fig. 4.8c) and in heterojunction (Fig. 4.8d) is shown for $\text{Cu}2p_{1/2}$ and $\text{Cu}2p_{3/2}$ located at 935.8 eV and 955.7 eV which are characteristic peaks for Cu^{+1} . The satellite peaks located at 947.1 eV are attributed to Cu^{2+} . This observation suggested that a small portion of Cu_2O on the surface of the particle was oxidized to CuO , which may be attributed to the exposure to the air. After the milling of the powders to form the heterojunction, Cu_2O shows a shifting of the peaks to 930.6 eV and 950.1 eV for $\text{Cu}2p_{1/2}$ and $\text{Cu}2p_{3/2}$, respectively. The satellite peak shift to lower energy to 939 eV and the intensity increases which can be related to higher oxidation of Cu_2O to CuO due to the high energy released in the milling process.

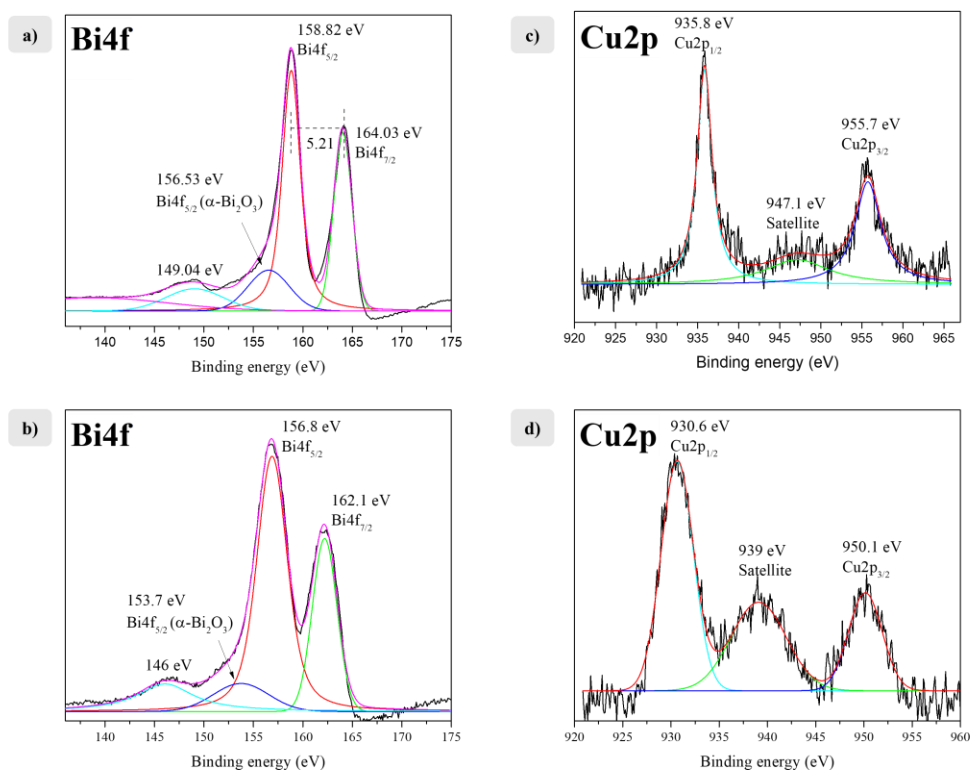


Figure 4.8 XPS spectra of $\text{Bi}4f$ in a) $\beta\text{-Bi}_2\text{O}_3$ as single catalyst and b) in heterojunction and $\text{Cu}2p$ in c) Cu_2O as single catalyst and d) in heterojunction.

4.3.4. Electrochemical measurements of heterojunctions

Figure 4.9 shows Mott-Schottky plots for β -Bi₂O₃ (Fig. 4.9a) as a n-type semiconductor and Cu₂O (Fig. 4.9b) as a p-type semiconductor. The plot shows the relation between C^{-2} (interfacial capacitance) and E the applied potential (Eq. 4.6). For β -Bi₂O₃ the flat band potential E_{FB} is -0.28 V and for Cu₂O is +0.51 V. In the case of β -Bi₂O₃ E_{FB} correspond to the potential of its conduction band (E_{CB}) and for Cu₂O the value of E_{FB} correspond to the valence band (E_{VB}). The position of the VB of β -Bi₂O₃ is determined by subtracting the band gap energy value to the E_{CB} . The same procedure is used to determine the value of the E_{CB} for Cu₂O. The potential of the valence and conduction band potential for both semiconductors are shown on Figure 4.9c. The graph shows the reduction potential of protons and oxygen and the oxidation potential of water and methanol. β -Bi₂O₃ is a promising photocatalyst for water and methanol photooxidation due to its positive potential of its VB. However, the electrons on its CB do not have the potential to carry out reduction of H⁺ or O₂. In the case of Cu₂O, its negative potential of the CV is able to produce H₂ and reduce O₂. The holes photogenerated on the VB will be able to photooxidize water but not methanol as it requires more positive potential.

Bi-based heterojunctions synthesized by mechanical milling: Effect of the structural parameters in the optical properties

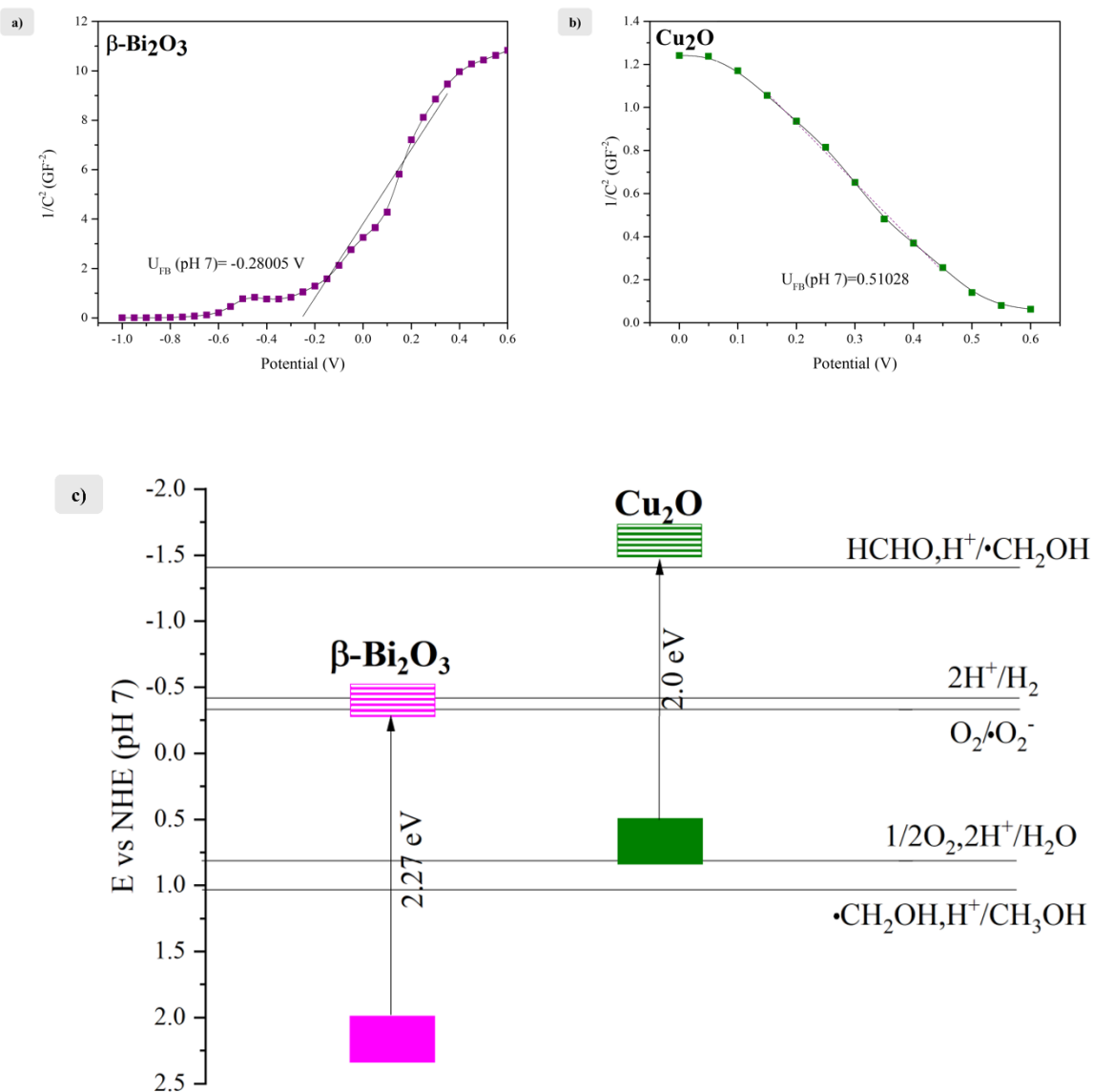


Figure 4.9 Mott-Schottky plot of a) $\beta\text{-Bi}_2\text{O}_3$ and b) Cu_2O and c) the band edge potential of both catalyst at pH 7 and oxidation of water and methanol and reduction of oxygen.

The band alignment of the heterojunction is presented in Figure 4.10. The configuration is a staggered engineering that correspond to a type II heterojunction (Fig. 4.10a) where photogenerated electrons are accumulated in the CB of $\beta\text{-Bi}_2\text{O}_3$ and holes

Bi-based heterojunctions synthesized by mechanical milling: Effect of the structural parameters in the optical properties

remain in the VB of Cu_2O . These two semiconductors are p-type and n-type, respectively, a p–n heterojunction can be obtained. Before light irradiation, a space-charge region can be formed at the interface due to the diffusion of majority carriers, resulting in a built-in electric field that can direct the photogenerated electrons and holes to flow in the opposite direction. Compared with type-II heterojunction, the charge separation of p–n heterojunction is faster due to the synergy between the internal field and the band alignment²⁷. In the case of a Z-scheme (Fig. 4.10b) the mechanistic pathway on charge carrier transfer will induce an electron injection from $\text{CB}_{\beta\text{-Bi}_2\text{O}_3}$ to $\text{VB}_{\text{Cu}_2\text{O}}$. Electrons then will be photoexcited to $\text{CB}_{\text{Cu}_2\text{O}}$ to carry out hydrogen production and $\beta\text{-Bi}_2\text{O}_3$ will have a saturation of holes on its VB to oxidize water or methanol (usually used as hole scavenger).

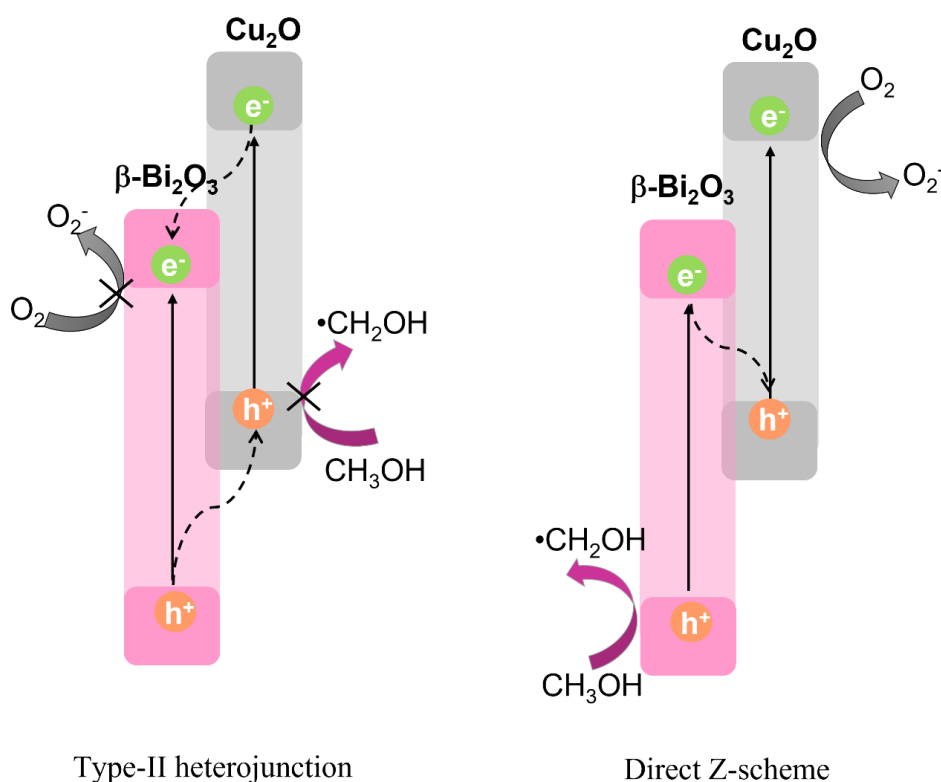


Figure 4.10 Possible mechanism of charge carrier transfer and reaction in the $\beta\text{-Bi}_2\text{O}_3/\text{Cu}_2\text{O}$.

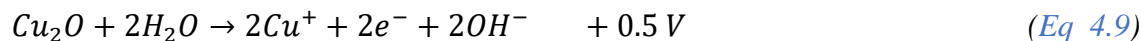
To obtain a general idea of the ability of the electrodes to generate currents from its photoelectrochemical oxidation we performed CLV measurements under polychromatic irradiation (Figure 4.10). The photoelectrochemical activity of the electrodes was analyzed

via the oxidation of methanol in a 0.1 M KCl and 10 vol-% methanol electrolyte. Methanol is a typical model compound for the determination of the photocatalytic or photoelectrochemical activity of a material, since it is a small molecule, readily available, and colorless.

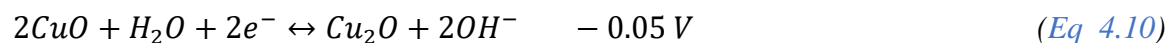
Cyclic voltammetry curves were performed in the dark and in polychromatic illumination using a solar simulator. [Figure 4.10a](#) shows CV curves of Cu₂O as-prepared electrodes as a measure of the photocurrent density vs the applied potential. Cu₂O is a p-type semiconductor that works as a photocathode and is able to reduce molecular oxygen or protons for water splitting. Cu₂O shows an increase in photocurrent as the potential applied is increased to positive values. The maximum anodic photocurrent recorded at 1.6 V was 171.4 μAcm⁻². This demonstrates that Cu₂O is able to carry out oxidation reactions. One cathodic peak and two anodic peaks are observed in the potential range from -0.2 to 0.6 V. As it has been reported elsewhere, Cu₂O suffers from oxidation and reduction induced by photogenerated electrons and the photocorrosion of Cu₂O has been recognized as a cause for the degradation of its photocatalytic properties. The first anodic peak (1) at about 0.17 V correspond to the oxidation of Cu₂O to CuO^{170,172}.



The second anodic peak (2) at 0.5 V correspond to the dissolution of Cu₂O to Cu²⁺



The cathodic peak (3) at -0.05 V correspond to the reduction of CuO to Cu₂O



A clear and consistent trend in the electrochemical behavior of Cu₂O films with repeated CV cycling was observed in all Cu₂O samples.

Examining the band structure of Cu₂O in [Figure 4.9](#) it can be concluded that the redox potentials for H₂ evolution, O₂ reduction and water oxidation as well the oxidation of

Bi-based heterojunctions synthesized by mechanical milling: Effect of the structural parameters in the optical properties

Cu₂O to CuO are all within the band gap and therefore, all these processes are possible, in principle. However, the driving force for water oxidation is minimal, while the oxidation of Cu₂O is thermodynamically favorable.

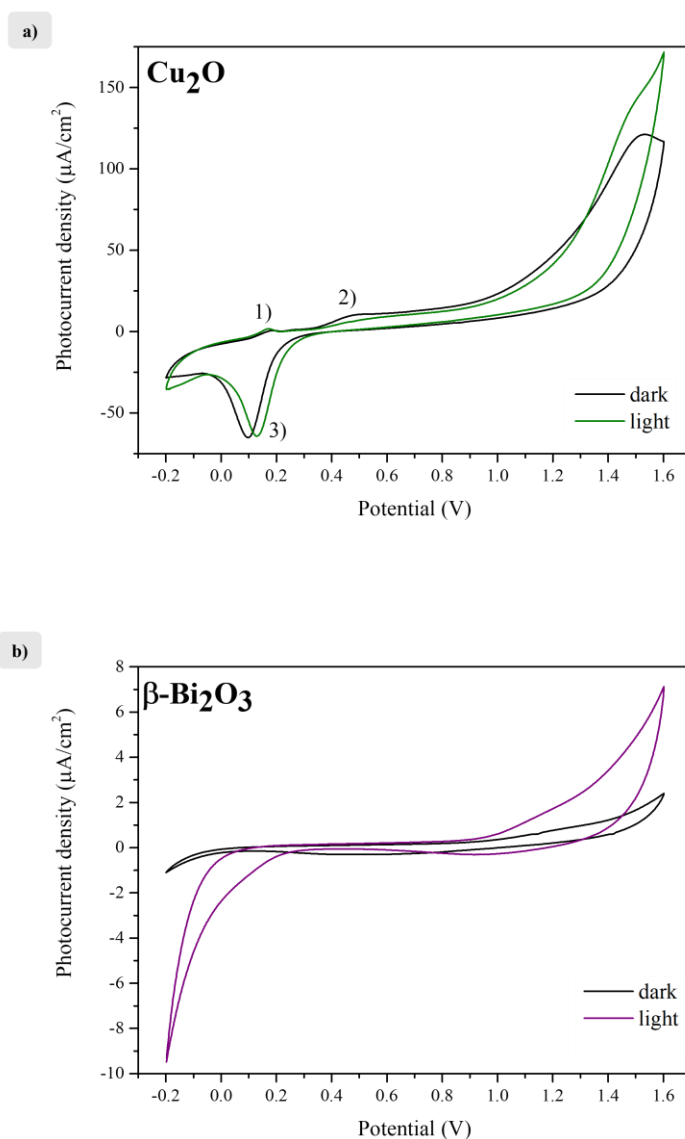


Figure 4.11 Cyclic voltammetry of Cu₂O and Bi₂O₃ electrodes synthesized by spray coating (100 mg of powder, 80 µL of nafion and 1 mL of 2-propanol) dispersed on FTO glass and heated at 100 °C for 3h. The measurement was carried out in aqueous solution of 0.1M KCl+10vol% methanol recorded at a scan rate of 10 mVs⁻¹.

CLV curves of β - Bi_2O_3 electrode is shown in [Figure 4.11b](#). The electrode β - Bi_2O_3 of n-type semiconductivity function as a photoanode. The maximum anodic photocurrent recorded at 1.6 V was $7 \mu\text{Acm}^{-2}$ which it refers to the oxidation of methanol and in cathodic potential the maximum photocurrent recorded at -0.2 V was $-9.28 \mu\text{Acm}^{-2}$. This reduction peak could be related to dissolution of Bi_2O_3 into the ionic species BiO_2^- which has been reported in alkaline media¹⁷³. The reduction of the dissolved species is shown in [Eq 4.11](#) to [Eq 4.13](#).



In this context, the photocurrent density of β - Bi_2O_3 shows faster charge transfer and efficient electron-hole pair separation with a slow recombination rate than Cu_2O at the surface as is evidenced from the signal under light illumination vs the dark. The increased visible-light harvesting by β - Bi_2O_3 is attributed to its lower band gap and tetragonal structure, which facilitates fast hole transport. The heterojunction β - $\text{Bi}_2\text{O}_3/\text{Cu}_2\text{O}$ composed of a photoanode, and a photocathode can then address oxidation of water or methanol and reduction of molecular oxygen or protons for H_2 evolution.

4.4. Conclusion

A p-n β - $\text{Bi}_2\text{O}_3/\text{Cu}_2\text{O}$ junction was synthesized by a one-step mechanical milling process. The synthesis procedure was analyzed on the optical and structural properties. The increase of milling time generates an increase of the lattice parameter c of β - Bi_2O_3 in the heterojunction and a decrease of crystallite size. Although the increase of milling time enhances the coupling between both semiconductor as it was proved by photoluminescence and UV-vis spectrophotometry. The heterojunction synthesized at 60 min present a low PL intensity which refers the low electron-hole recombination and a band gap of 1.88 eV. The increase of tetragonality of the β - Bi_2O_3 phase promotes the charge separation as it was

observed in PL intensity. The decrease of the crystallite size generated by mechanical milling induce the presence of structural defects that generates a decrease of band gap energy.

Mott-Schottky plots and cyclic voltammetry prove the presence of a p-n junction between Bi₂O₃ (n-type semiconductor) and Cu₂O (p-type semiconductor). The band edge potentials elucidate the possible charge carrier transfer where electrons remain in the CB of Cu₂O and holes remain in the VB of Bi₂O₃ via direct Z-scheme. The heterojunction synthesized can be used for H₂ evolution by water or methanol oxidation as was demonstrated in the photocurrent density.

4.5. Appendix

The X-ray patterns of Cu₂O and β-Bi₂O₃ as-received commercially powders are shown in [Figure S4.1a](#). Both powders did not show impurity or secondary phases. β-Bi₂O₃ presents a tetragonal phase indexed with PDF 27-0050 with lattice parameters $a = b = 7.742 \text{ \AA}$ $c = 5.631 \text{ \AA}$ and spatial group $P-42_1c$. Cu₂O powder presents a single cubic phase identified with PDF 05-0667 with the spatial group $Pn-3m$ and lattice parameter $a = 4.2696 \text{ \AA}$. Mathematical Rietveld refinement were used to calculate the lattice parameters, cell volume and crystallite size using Fullprof® ([Figure S4.1b](#)). The calculated data is shown on [Table S4.1](#). The refinement shows that the adjustment (GoF) less than or equal to 1 ensures the accuracy of the calculation.

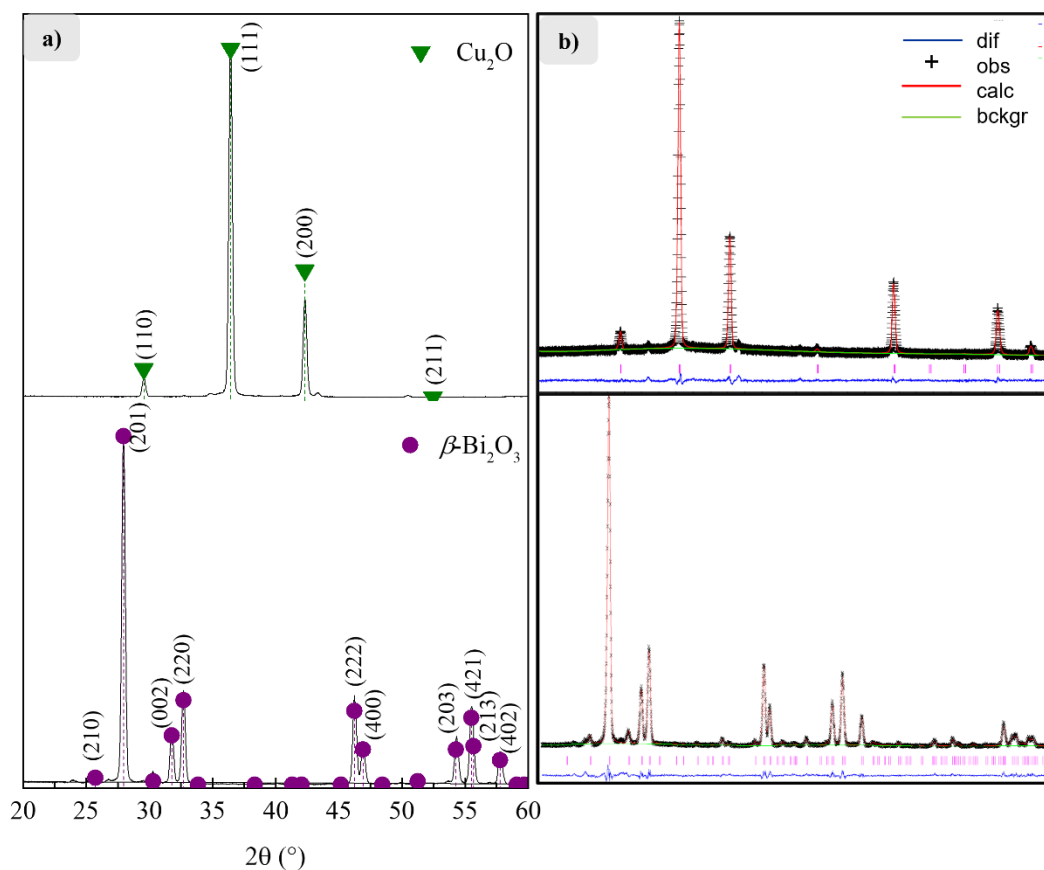


Figure S4.1 a) XRD and b) Rietveld refined patterns of $\beta\text{-Bi}_2\text{O}_3$ and Cu_2O precursor powders.

Rietveld refinement patterns of XRD 75 $\beta\text{-Bi}_2\text{O}_3$ /25 Cu_2O heterojunction synthesized at different milling time is shown in Figure S4.2. The red points correspond to the signal obtained from the X-ray patterns, the black line is the fitting between the theoretical and the experimental signal, the green line is the residual of the fitting and the blue lines correspond to the crystallographic information file (CIF) of the crystal phases ($\beta\text{-Bi}_2\text{O}_3$ and Cu_2O).

Bi-based heterojunctions synthesized by mechanical milling: Effect of the structural parameters in the optical properties

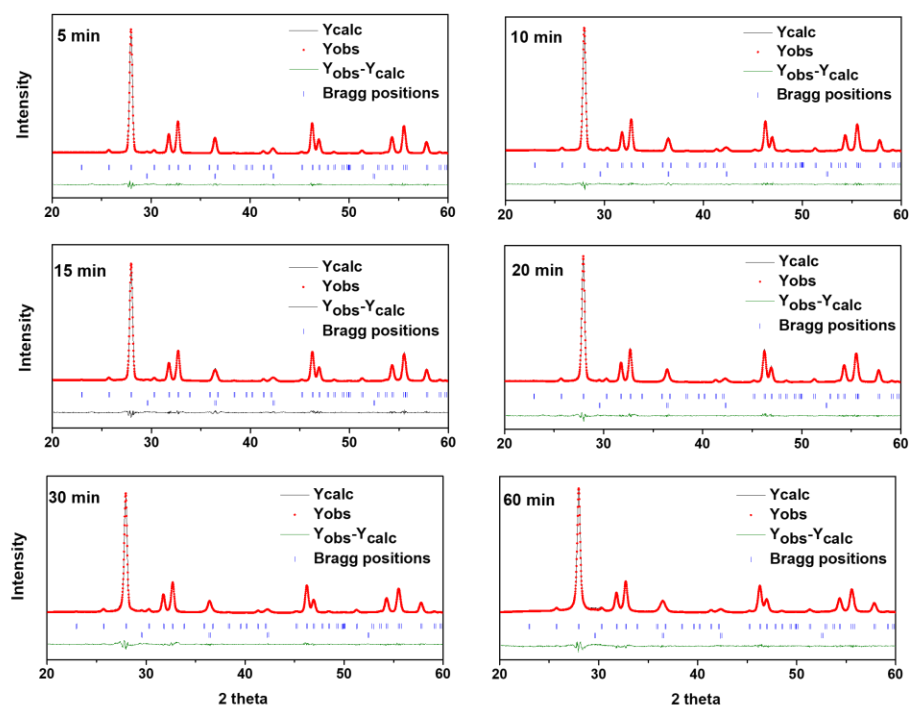


Figure S4.2 Rietveld refinement of X-ray patterns of β - $\text{Bi}_2\text{O}_3/\text{Cu}_2\text{O}$ heterojunctions as function of milling time.

The calculated structural parameters from the Rietveld refinements of heterojunction are shown in [Table S4.1](#). The phase percent and crystallite size are shown for Cu_2O and β - Bi_2O_3 as individual powders and in the heterojunction as function of milling time. Although, the lattice parameter a and c of β - Bi_2O_3 is shown as single catalyst and in the heterojunction. The BET surface area is only shown for β - Bi_2O_3 and Cu_2O , and 75 β - $\text{Bi}_2\text{O}_3/25\text{Cu}_2\text{O}$ heterojunction milled at 60 min.

Table S 4.1 Structural parameters, phase content, crystallite size, BET Surface area and refined parameters of precursor powders and 75 β -Bi₂O₃/25Cu₂O heterojunction obtained from XRD and Rietveld refinement.

Sample	Phase content (%)		Lattice parameter β -Bi ₂ O ₃ (Å)		Crystallite size	Crystallite size	GoF	BET surface area m ² /g	
	β -Bi ₂ O ₃	Cu ₂ O	a (Å)	c (Å)	β -Bi ₂ O ₃	Cu ₂ O			
β -Bi ₂ O	100	–	7.7383	5.6257	676	–		4.135	
Cu ₂ O	–	100	4.271	4.271	–	574		0.454	
75 β -Bi ₂ O ₃ /25Cu ₂ O	5 min	74.81	25.19	7.7383	5.6257	504.26	382	1.47	–
	10 min	76.03	23.97	7.7387	5.6266	458.54	265.42	1.43	–
	15 min	75.46	24.54	7.7389	5.6271	431.23	238.51	1.36	–
	20 min	76.01	23.99	7.7398	5.6280	405.46	209.37	1.33	–
	30 min	72.34	27.66	7.7399	5.6282	359.11	181.43	1.64	–
	60 min	72.89	27.11	7.7400	5.6295	279.73	137.45	1.55	3.136

Bi-based heterojunctions synthesized by mechanical milling: Effect of the structural parameters in the optical properties

Chapter 5:Photocatalytic activity of Bi-based heterojunction for methanol oxidation using a black-body like reactor

5.1. Introduction

Semiconductor photocatalysis has emerged as one of the potential methods for fuel production and environmental remediation by utilize solar energy¹⁷⁴. Heterogeneous photocatalysis in solid–liquid systems is an effective method to harvest photons for the oxidative degradation of organic water pollutants, the generation of molecular hydrogen by water splitting or reforming of organic compounds, the fixation of carbon dioxide or molecular nitrogen, and the synthesis of organic compounds¹¹³.

In photocatalytic reactions, reaction rates are usually reported to compare the activities of the catalyst. In addition to the reaction rate, the number of absorbed photons should be measured to obtain the quantum yield. The quantum yield of a photochemical reaction is defined as Φ = the number of events, e.g. molecules changed, formed or destroyed, divided by the number of absorbed photons of that particular wavelength in the same period of time¹⁷⁵. However, in heterogeneous systems the measure of absorbed photons implicates some struggles due to scattering and reflection of the light by solid particles of the photocatalyst which generates a loss of photons¹⁷⁶.

In photocatalytic reactions that uses photoreactors with external illumination source, the photons enter to the fluid phase throw a window and inevitably some of them are reflected. In photoreactors that have a positive irradiation geometry, reflection at the interfaces of the window and scattering of the suspension takes place. The portion of photons that are transmitted through the windows enter the fluid phase and interact with the photocatalyst and could be absorbed or transmitted by them. The photons transmittance through the suspension generates a decrease on the efficiency of the photocatalytic reaction. However, this can be avoided using an appropriate reactor geometry and by choosing a sufficiently high catalyst concentration along the optical path of sufficient length^{177,178}.

Photocatalytic activity of Bi-based heterojunction for methanol oxidation using a black-body like reactor

The concept of a black body reactor (BBR) was firstly named by Emeline and coauthors¹⁷⁷. Herein, the fraction of reflected and transmitted light is approximately zero due to the negative irradiation geometry of the reactor and the high optical density of the system. The light entrance is surrounded by the suspension containing the catalyst in all three spatial directions. It can be assumed that all photons of suitable wavelengths emitted by the light source and entering the suspension are absorbed by the photocatalyst. The reaction rate determined in a photoreactor having positive irradiation geometry and the resulting photonic efficiency is then influenced by the optical properties of the suspension and is, therefore, not a measure of the intrinsic activity of the photocatalyst under consideration. The suspension optically dense for all photons with appropriate energy emitted by the light source, photons that have an energy greater than the band gap energy of the photocatalyst, are absorbed by the photocatalyst (no photons are transmitted through the reactor).

Thus employing a BBR to carry on photocatalytic reactions, it is assumed that the reaction rate (dn/dt) is just only diminished by the recombination of the photogenerated charge carriers and is independent from the scattering properties of the photocatalyst¹⁷⁸. Therefore, reaction rates can be easily compared for different photocatalytic systems¹⁷⁹. To measure the amount of photons emitted by the light source and entering to the BBR, chemical actinometry was employed¹⁸⁰. When using a monochromatic light source, a quantum yield as is usual for homogeneous photochemical reactions can thus be calculated for heterogeneous systems¹⁷⁶. Although. It must be considered that a measurement of quantum yield will only be meaningful if the photocatalyst is the only species that absorbs the photons entering the suspension. By means, the probe compound must therefore be optically transparent, and additionally the photocatalytic conversion of the probe compound must not yield intermediates and products capable to absorb the incoming light.

Further, Megatiff and coauthors apply this black body reactor for the degradation of dichloroacetic acid in UV light. At sufficiently high concentrations of the probe compound and the photocatalyst, the rate of conversion was found to be impartial by the initial

concentration of the probe compound, the mass concentration of the photocatalyst, and the suspension volume^{178,181}. This work is based on them results.

The photocatalytic activity of aqueous semiconductor suspension using a black body reactor is measured for methanol photooxidation. Nowadays, water splitting is one of the most attractive applications of semiconductor photocatalysis¹⁰. Although it presents some limitations, in the process employing pure water is usually rather inefficient or is not even operative at all. This is related to the fact that the simultaneous reduction and oxidation of water is a complex multistep reaction involving four electrons^{5,182}. Using sacrificial molecules as electron donors is one of the easiest and feasible approaches to remarkably improve the H₂ production. The photogenerated holes are scavenged by these molecules thus reducing significantly the charge carrier recombination⁴. Furthermore, since O₂ is not produced, the back reaction to produce water is suppressed thus increasing the H₂ yield and avoiding a subsequent gas separation stage. Some common and widely used hole scavengers (electron donors) for photocatalytic H₂ generation are inorganic compounds such as alcohols, organic acids, and hydrocarbons⁴. Methanol has been and is being used as a model compound for sacrificial reagent. The addition of methanol as an electron donor in water splitting reactions generates an irreversible reaction with the photogenerated valence band holes thus enhancing the photocatalytic electron-hole separation efficiency, resulting in higher quantum yields¹⁹.

Two possible mechanisms for methanol photooxidation have been proposed, the first one is the direct oxidation by photogenerated holes (Eq 5.1) and the second is the indirect oxidation via interfacially formed •OH radicals (Eq 5.2). These radicals are products of the trapping of VB holes by surface –OH groups or adsorbed water molecules^{15,183}. It has been reported that the oxidation by •OH radicals is the mechanism when water is the dominant surface specie¹⁸⁴. In the presence of molecular oxygen, formaldehyde is formed as the dominant stable product in a quantitative reaction¹⁸³ (Eq 5.3).



Photocatalytic activity of Bi-based heterojunction for methanol oxidation using a black-body like reactor



Thus, to envisage the photocatalytic methanol oxidation in a liquid-solid system, the formation of formaldehyde (HCHO) as the first stable oxidation product is measured by the Nash method¹³⁵.

For methanol photooxidation four different catalysts and its heterojunctions were evaluated. β -Bi₂O₃ is a visible light active photocatalyst that possess a deep valence band potential E_{VB} (+2.4 V vs NHE) which has probe to possess high photocatalytic performance for organic pollutants degradation due to the high oxidative power of its photogenerated holes. However, the electrons have a positive conduction band edge potential E_{CB} (+0.4 V vs NHE) which are not suitable for oxygen reduction or hydrogen generation¹⁵⁹. A heterojunction composite with β -Bi₂O₃ has proven to present an enhanced performance for photocatalytic reactions due to charge carrier transport between both semiconductors and also to generate reduction reaction in the cocatalyst that possess a more negative conduction band potential^{59,60,64}. Three different heterojunctions and the single catalysts were evaluated for methanol photooxidation Cu₂O/ β -Bi₂O₃, ZnO/ β -Bi₂O₃ and Bi_{0.5}Na_{0.5}TiO₃/ β -Bi₂O₃. The photon flux and the quantum yield were evaluated by chemical actinometry. The mechanism of charge transfer process of photocatalytic methanol oxidation is discussed based on the band alignment of the catalyst and the heterojunctions.

5.2. Materials and methods

5.2.1. Synthesis of photocatalyst

Four different photocatalyst (β -Bi₂O₃, Cu₂O, ZnO and Bi_{0.5}Na_{0.5}TiO₃) and its heterojunctions (Cu₂O/ β -Bi₂O₃, ZnO/ β -Bi₂O₃ and BNT/ β -Bi₂O₃,) were probed for the photocatalytic methanol oxidation. β -Bi₂O₃, Cu₂O and ZnO were commercially available powders (99.95%, Sigma Aldrich). Bi_{0.5}Na_{0.5}TiO₃ were prepared by a solid-state reaction⁷⁸ from the precursors β -Bi₂O₃ (99.95%, Sigma Aldrich), Na₂CO₃ (99.95%, Meyer) and TiO₂ (99.95%, Sigma Aldrich). All the precursors were mill in a planetary mill Retsch (Haan, Germany) for 2 h in a ball:powder ratio 10:1 in weight percent. For milling media, Si₃N₄

balls of 10 mm and 5 mm diameter were used. 1 mL of methanol (99.8%, J.T. Baker) was added per gram of powder as surfactant¹⁷¹. The calcination was performed 2 times at 920 °C for 5 h with a heating rate of 5 °C/min in a Thermolyne Furnace, TermoFischer Scientific (Massachusetts, USA). The heterojunctions were synthesized by high energy ball milling using a SPEX 8000D mill SPEX SamplePrep (Metuchen, USA). The milling time were chosen at 1 h using Si₃N₄ as milling media of diameter of 10 mm and 5 mm, 200 µL of methanol was added as surfactant.

5.2.2. Catalysts characterization

Optical properties of photocatalysts and the heterojunctions were measured to determine the band gap energy of as-prepared powders by diffused reflectance UV-Vis-NIR spectrophotometry (DRS) using a Cary Varian 100 spectrophotometer (Malvern, UK) in the range 200-900 nm.

From reflectance spectra, Kubelka Munk theory (Eq 5.4) was applied to measure band gap energies of semiconductors using the Tauc method (Eq 5.5). For β-Bi₂O₃ and BNT^{133,185} an indirect optical transition ($n = 2$) was used and for Cu₂O and ZnO^{123,186} a direct optical transition ($n = 1/2$).

$$F(R) = \frac{(1-R)^2}{2R} \quad (\text{Eq 5.4})$$

$$((F(R)hv)^{\frac{1}{n}} = C(hv - E_g) \quad (\text{Eq 5.5})$$

$F(R)$ is a function of reflectance, R is the reflectance measured by UV-Vis spectrophotometry, hv is the energy of the photons induced, n is the electronic transition, C is a constant and E_g is the band gap energy of the bulk of semiconductor. The calculated band gap energies can be determined by a linear fit of the plot and extrapolate $(F(R)hv)^{1/n} = 0$ to obtained E_g .

The electrochemical measurements were performed in a three-electrode electrochemical cell consisting of a working electrode, a Pt wire counter electrode and an Ag/AgCl/NaCl (3 molL⁻¹) reference electrode. A pH 6 0.1 molL⁻¹ KCl (>99%, Fluka)

Photocatalytic activity of Bi-based heterojunction for methanol oxidation using a black-body like reactor

solution was used as the electrolyte. The working electrodes were prepared by using a spray coating technique. For this purpose, 50 mL of 2-propanol (>99.7%, J.T. Baker) solutions containing 20 gL⁻¹ of powder was sprayed on top of fluoride-doped tin oxide (FTO) conductive glasses (7 Ω/sq, Sigma-Aldrich) heated to 100 °C for 3 h as reported in our group¹⁵⁹. The solution was forced through the nozzle using pressurized air at 1 bar pressure (100 kPa). A solar simulator (LOT-Quantum Design GmbH) with a 300 W Xe lamp and an AM 1.5-global filter was employed as the light source and a Zennium potentiostat (Fa. Zahner-Elektrik GmbH & Co. KG, Germany). The flat band potentials (E_{FB}) were determined under the dark at a frequency of 10 Hz according to the Mott-Schottky equation (Eq 5.6)¹⁶⁴.

$$\frac{1}{C_{SC}^2} = \frac{2}{\epsilon\epsilon_0qN_D} \left(E_{appl} - E_{FB} - \frac{k_B T}{q} \right) \quad (\text{Eq 5.6})$$

C_{SC} is the capacitance of the space charge layer, ϵ is the dielectric constant of the semiconductor, ϵ_0 is the permittivity of the vacuum, A is the interfacial area, N_D the donor density, E_{FB} the flat band potential, k_B the Boltzmann constant, T the temperature and q the electronic charge. By plotting C_{SC}^{-2} against E , the flat band potential can be derived from the abscissa intercept. The E_{FB} at pH 7 is measured from Nernstian pH dependence equation (Eq 5.7), which shifts negative 59 mV per pH unit at room temperature¹⁶⁴. X is the pH of the electrolyte used in the electrochemical cell.

$$E_{FB}(pH\ 7) = E_{FB}(pH\ X) + 0.059(X - 7) \quad (\text{Eq 5.7})$$

5.2.3. Photocatalytic methanol oxidation

Methanol photooxidation was performed in a black body like reactor shown in Figure 5.1. A 250 mL volumetric glass flask is used, on the top of the flask a glass tube is fixed to place the optical fiber. The monochromatic LED lamp is directed to the optical fiber (to work as a waveguide) and placed on the center of the suspension, and then connected to the power supply of 1.2 A. The light inlet was thus surrounded by the suspension in all spatial directions. Therefore, it can be assumed that the condition for a blackbody reactor, all incident photons are absorbed in the suspension, is satisfied. The suspension that contains

Photocatalytic activity of Bi-based heterojunction for methanol oxidation using a black-body like reactor

the methanol solution with the catalyst is added to the flask and is kept under stirring in a mixing plate maintained at room temperature.

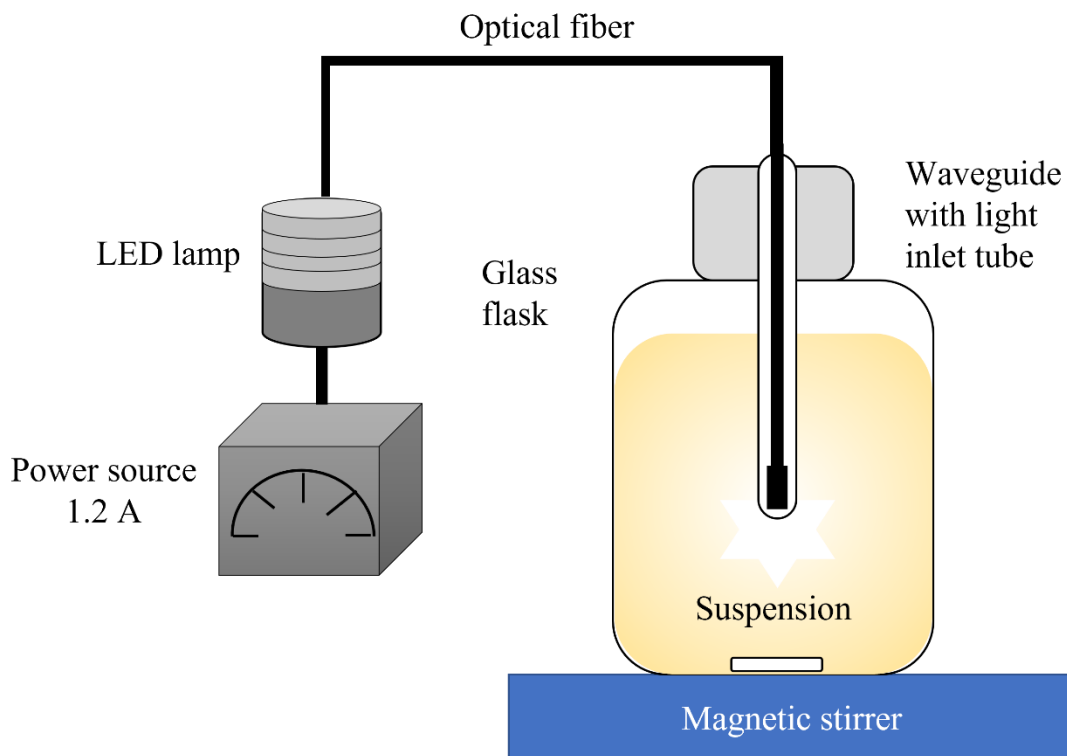


Figure 5.1 Experimental set-up of the black body like reactor for methanol photooxidation¹⁷⁷.

In a typical procedure a flask of 250 mL was used. A solution of 2.47 molL⁻¹ methanol ($\geq 99\%$, Carl Rot) was used using ultrapure distilled water (18.2 M Ω cm). 5gL⁻¹ of catalyst was loaded to assure an optical density allowing the absorption of all photons entering in the suspension. The solution was kept in the dark for equilibrium during 30 min with continuous stirring. After that, the solution was illuminated at ambient temperature with monochromatic light using an LED lamp (ThorLabs, Germany) emitting either UV ($\lambda = 365$ nm, irradiance 21 μ W/mm²) or visible light ($\lambda = 455$ nm light, irradiance = 31.2 μ W/mm²). Aliquots of 750 μ L were taken every 30 min for 6 hours and then kept in the dark in a freezer. Every single experiment was performed at least twice to assure the accuracy of the method and its reproducibility. The photooxidation rate was determined by measuring the formaldehyde (HCHO) generated as a result of the methanol oxidation

Photocatalytic activity of Bi-based heterojunction for methanol oxidation using a black-body like reactor

employing the Nash method¹³⁵. This method is based on the reaction of formaldehyde with Nash reagent; 2 M ammonium acetate ($\geq 97\%$, Carl Roth), 0.05 M acetic acid (100%, Carl Roth), 0.02 M acetylacetone ($\geq 98\%$, Carl Roth), to form the yellow-colored 3:5-diacetyl-1:4-dihydrolutidine (DDL) with a maximum of absorbance at 412 nm. After irradiation, 750 μL aliquots of the anolyte were mixed with 750 μL of fresh Nash reagent and diluted in 750 μL of distilled water. After an overnight incubation, the yellow-colored (DDL) is formed. The absorbance of DDL was measured in the range from 200-800 nm in a quartz cuvette of 1 cm path length using a Varian Cary 100 Scan UV-vis spectrophotometer.

5.2.4. Determination of quantum yields

The determination of the incident photon flux was performed by chemical actinometry using ferrioxalate $[\text{Fe}(\text{C}_2\text{O}_4)_3]^{3-}$ as an actinometer. All the experimental data is shown in Supporting Information.

The catalyst's efficiency in utilizing the absorbed photons, known as the quantum yield (Φ), needs to be determined accurately. The quantum yield of heterogeneous photochemical systems is described exactly following to the quantum yield definition in homogenous systems, as the number of defined events divided by the number of photons absorbed by the catalyst at a specific wavelength. Φ can also be expressed in a kinetic definition (Eq 5.8) as the ratio of the rate of conversion of molecules relative to the absorbed photon flux at one specific wavelength¹⁷⁵.

$$\Phi = \frac{\text{rate of conversion}}{\text{rate of photons absorbed}} \quad (\text{Eq } 5.8)$$

5.3. Results and discussion

The photocatalytic oxidation of methanol in aqueous suspensions containing bismuth-based heterojunctions and its catalysts employing a black body photoreactor is shown respect to the quantum yields measured. The quantum yield is calculated from Eq. 5.9 according to the reported data for photochemical reactions¹⁷⁵.

Photocatalytic activity of Bi-based heterojunction for methanol oxidation using a black-body like reactor

$$\Phi = \frac{\text{rate of conversion}}{\text{rate of photons absorbed}} = \frac{\frac{d\xi(i)}{dt}}{\frac{dn_p}{dt}} \quad (\text{Eq 5.9})$$

where $d\xi(i)/dt$ is the evolved species (formaldehyde formed from oxidation of methanol) and dn_p/dt is the photons absorbed measured by chemical actinometry. For UV light, the number of photons absorbed per time is $2.11 \mu\text{mol s}^{-1}$ and for visible light is $4.36 \mu\text{mol s}^{-1}$, as it is shown in the plots of Figure S5.1.

The obtained quantum yields are shown in Figure 5.2 for each catalyst and heterojunction, the left bars correspond to $\Phi_{365\text{nm}}$ for UV light and the right bars for $\Phi_{455\text{nm}}$ in visible light. As it is obvious, all the photocatalysts present higher quantum yield in UV than in visible light.

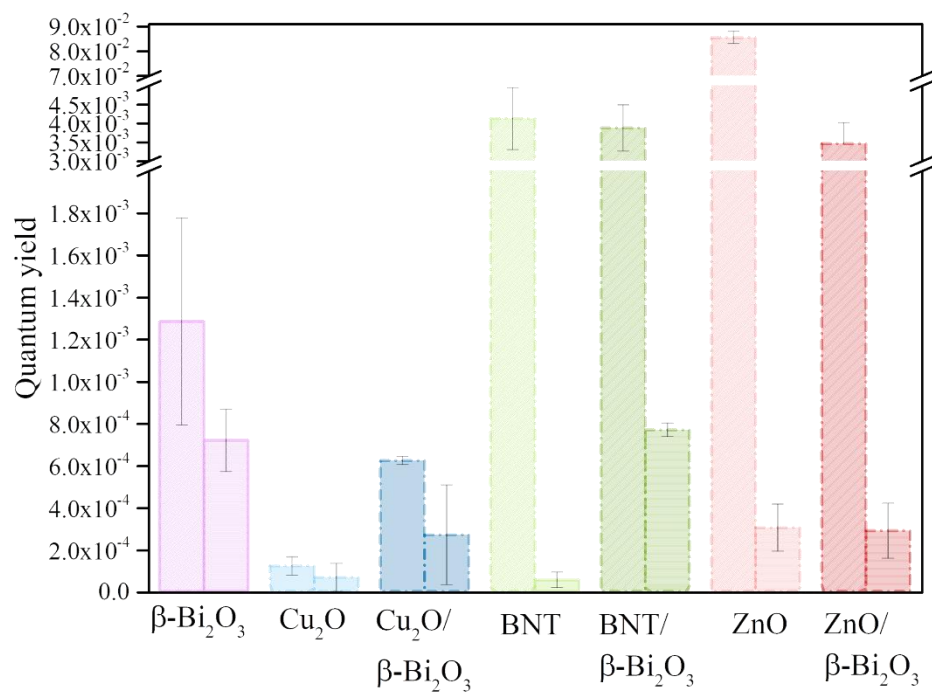


Figure 5.2 Quantum yield of methanol photooxidation for the formation of formaldehyde in UV (right bars) and visible light (left bars).

Photocatalytic activity of Bi-based heterojunction for methanol oxidation using a black-body like reactor

The comparison of quantum yields for methanol photooxidation on bismuth-based heterojunctions and its catalysts then must be studied as the effect of $\beta\text{-Bi}_2\text{O}_3$ in the activity of the cocatalyst. For UV light the quantum yields of each set of heterojunctions are: $\text{ZnO} > \text{ZnO}/\beta\text{-Bi}_2\text{O}_3 > \beta\text{-Bi}_2\text{O}_3$, $\text{BNT} \geq \text{BNT}/\beta\text{-Bi}_2\text{O}_3 > \beta\text{-Bi}_2\text{O}_3$, and $\beta\text{-Bi}_2\text{O}_3 > \text{Cu}_2\text{O}/\beta\text{-Bi}_2\text{O}_3 > \text{Cu}_2\text{O}$. From this point of view, $\beta\text{-Bi}_2\text{O}_3$ diminishes the $\Phi_{365\text{nm}}$ in the coupling of ZnO but the quantum yield of the heterojunction $\text{ZnO}/\beta\text{-Bi}_2\text{O}_3$ is higher than $\beta\text{-Bi}_2\text{O}_3$. On the other hand, BNT and $\text{BNT}/\beta\text{-Bi}_2\text{O}_3$ shows almost the same $\Phi_{365\text{nm}}$, here it can be suggested that the contribution of $\beta\text{-Bi}_2\text{O}_3$ in the heterojunction does not significantly modifies the efficiency of the compound. An interesting case is that $\beta\text{-Bi}_2\text{O}_3$ shows higher efficiency than $\text{Cu}_2\text{O}/\beta\text{-Bi}_2\text{O}_3$ heterojunction and Cu_2O .

In visible light experiments, the $\Phi_{455\text{nm}}$ respect to the heterojunction effectivity are $\text{BNT}/\beta\text{-Bi}_2\text{O}_3 \geq \beta\text{-Bi}_2\text{O}_3 > \text{BNT}$, $\beta\text{-Bi}_2\text{O}_3 > \text{ZnO}/\beta\text{-Bi}_2\text{O}_3 \geq \text{ZnO}$ and $\beta\text{-Bi}_2\text{O}_3 > \text{Cu}_2\text{O}/\beta\text{-Bi}_2\text{O}_3 > \text{Cu}_2\text{O}$. For the case of $\text{BNT}/\beta\text{-Bi}_2\text{O}_3$, the $\Phi_{455\text{nm}}$ is similar as $\beta\text{-Bi}_2\text{O}_3$, this might be attributed to the wide band gap of BNT which are not able to be activated under visible light (455 nm). The same behavior is observed for $\text{ZnO}/\beta\text{-Bi}_2\text{O}_3$, the $\Phi_{455\text{nm}}$ is lower than $\beta\text{-Bi}_2\text{O}_3$ since ZnO presents a wide band gap and it cannot be excited in visible light, the charge carrier transfer between both catalyst is suppressed decreasing the activity of the heterojunction. An interesting case is $\text{Cu}_2\text{O}/\beta\text{-Bi}_2\text{O}_3$, both catalysts are visible light driven semiconductors with advantageous E_{CB} and E_{VB} potentials for methanol oxidation, (i.e., from holes photogenerated in $E_{VB}(\text{Bi}_2\text{O}_3)$) and oxygen reduction (i.e., from electrons photogenerated $E_{CB}(\text{Cu}_2\text{O})$), respectively. However, the heterojunction shows a diminishing of the Φ compared with single $\beta\text{-Bi}_2\text{O}_3$. This behavior might be attributed to the mechanism of charge transfer process between the conduction band and valence band of the charge carriers photogenerated that will be discussed below.

The photocatalytic activity of Bi-based heterojunctions and the single catalysts for methanol photooxidation is presented as the evolution in concentration of formaldehyde versus the irradiation time using Nash method and is shown in [Figure 5.3](#) for UV (a) and

visible light (b). The concentration of formaldehyde was determined by Beer-Lambert Law (Eq 5.10).

$$A = \epsilon lc \quad (\text{Eq 5.10})$$

where c is the concentration of the formed yellow-colored DDL, A is the absorbance (412 nm), ϵ is the extinction coefficient for DDL ($8000 \text{ M}^{-1}\text{cm}^{-1}$)¹³⁵, l is the path of the light (1 cm).

Photocatalytic activity of Bi-based heterojunction for methanol oxidation using a black-body like reactor

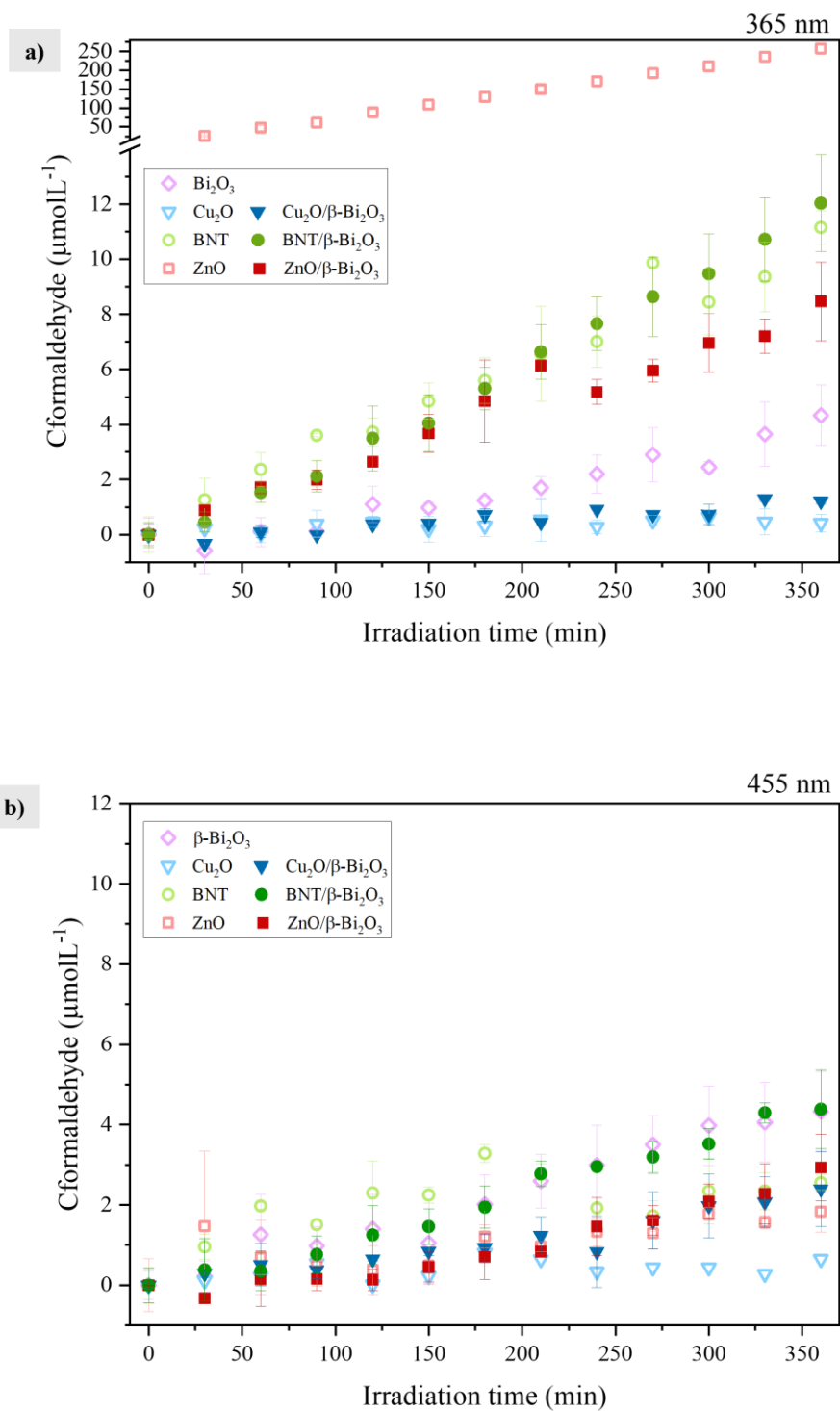


Figure 5.3 Formaldehyde formation from the methanol photooxidation with different photocatalysts in a) UV (365nm) and b) visible (455 nm) light.

All the experimental runs shown linear concentration-time plots obtained from at least two replicates per each catalyst. The photocatalytic activity for single catalysts in UV light (Figure 5.3a) presents the tendency $\text{ZnO} > \text{BNT} > \beta\text{-Bi}_2\text{O}_3 > \text{Cu}_2\text{O}$. In the case of bismuth-based heterojunctions the photocatalytic activity is as $\text{BNT}/\beta\text{-Bi}_2\text{O}_3 > \text{ZnO}/\beta\text{-Bi}_2\text{O}_3 > \text{Cu}_2\text{O}/\beta\text{-Bi}_2\text{O}_3$. Comparing the effect of coupling $\beta\text{-Bi}_2\text{O}_3$ with the different catalysts, it can be clearly seen that $\text{BNT}/\beta\text{-Bi}_2\text{O}_3$ show a similar activity as BNT but higher than $\beta\text{-Bi}_2\text{O}_3$. $\text{ZnO}/\beta\text{-Bi}_2\text{O}_3$ shows higher activity than $\beta\text{-Bi}_2\text{O}_3$ but lower than ZnO. In the heterojunction $\text{Cu}_2\text{O}/\beta\text{-Bi}_2\text{O}_3$, the activity is higher than Cu_2O but lower than $\beta\text{-Bi}_2\text{O}_3$. For visible light, the activity of the photocatalysts is shown in Figure 5.3b. By comparing the single photocatalysts the activity is as $\beta\text{-Bi}_2\text{O}_3 > \text{BNT} > \text{ZnO} > \text{Cu}_2\text{O}$ and for the heterojunctions the activity behaves the same as in UV light $\text{BNT}/\beta\text{-Bi}_2\text{O}_3 > \text{ZnO}/\beta\text{-Bi}_2\text{O}_3 > \text{Cu}_2\text{O}/\beta\text{-Bi}_2\text{O}_3$. In visible light all the heterojunctions present higher activity than the single cocatalyst. Although, $\beta\text{-Bi}_2\text{O}_3$ presents a similar activity than $\text{BNT}/\beta\text{-Bi}_2\text{O}_3$ but higher than $\text{ZnO}/\beta\text{-Bi}_2\text{O}_3$ and $\text{Cu}_2\text{O}/\beta\text{-Bi}_2\text{O}_3$.

For comparative studies of the photocatalytic activities of methanol photooxidation the reaction rates are measured. Reaction rates are usually reported on a volume basis (converted amount of the probe compound per unit time and unit suspension volume)¹⁷⁸. For the direct comparison of the rates obtained by the measurements of these analytes, the rates of conversion as defined by the IUPAC are used¹⁷⁵. The rate of conversion of a species i is defined as the time derivative of the extent of reaction $\xi(i)$ (Eq 5.11).

$$\frac{d\xi(i)}{dt} = \frac{V}{\nu(i)} \frac{dC(i)}{dt} = \frac{1}{\nu(i)} \frac{dn(i)}{dt} \quad (\text{Eq 5.11})$$

where $n(i)$ and $C(i)$ are the amount and the amount concentration (molarity), respectively, of this species at any time t , $\nu(i)$ is its stoichiometric coefficient, and V is the volume of the suspension. Then the reaction rates defined as the time derivative of the amount concentration (dC/dt) are directly obtained from the slope of the formation of formaldehyde over the time.

Photocatalytic activity of Bi-based heterojunction for methanol oxidation using a black-body like reactor

The reaction rate dn/dt was obtained from the slopes of [Figure 5.3](#) and multiplied by the volume of the suspension used in the BBR and are shown in [Table S5.1](#). The table shows the comparison of single catalyst for UV (left) and visible (right) light. ZnO and BNT presents high reaction rates for methanol photooxidation in UV light. The reaction rate of β - Bi_2O_3 for methanol photooxidation in UV light, increases by coupling the catalyst in the heterojunction composites BNT/ β - Bi_2O_3 and ZnO/ β - Bi_2O_3 . Moreover, β - Bi_2O_3 and BNT/ β - Bi_2O_3 presents the higher reaction rate in methanol photooxidation under visible light.

To understand the behavior of quantum yields and reaction rates of Bi-based heterojunctions and its single catalyst. The structural characteristics, the band gap energies and the potential of the conduction band and valence band were determined.

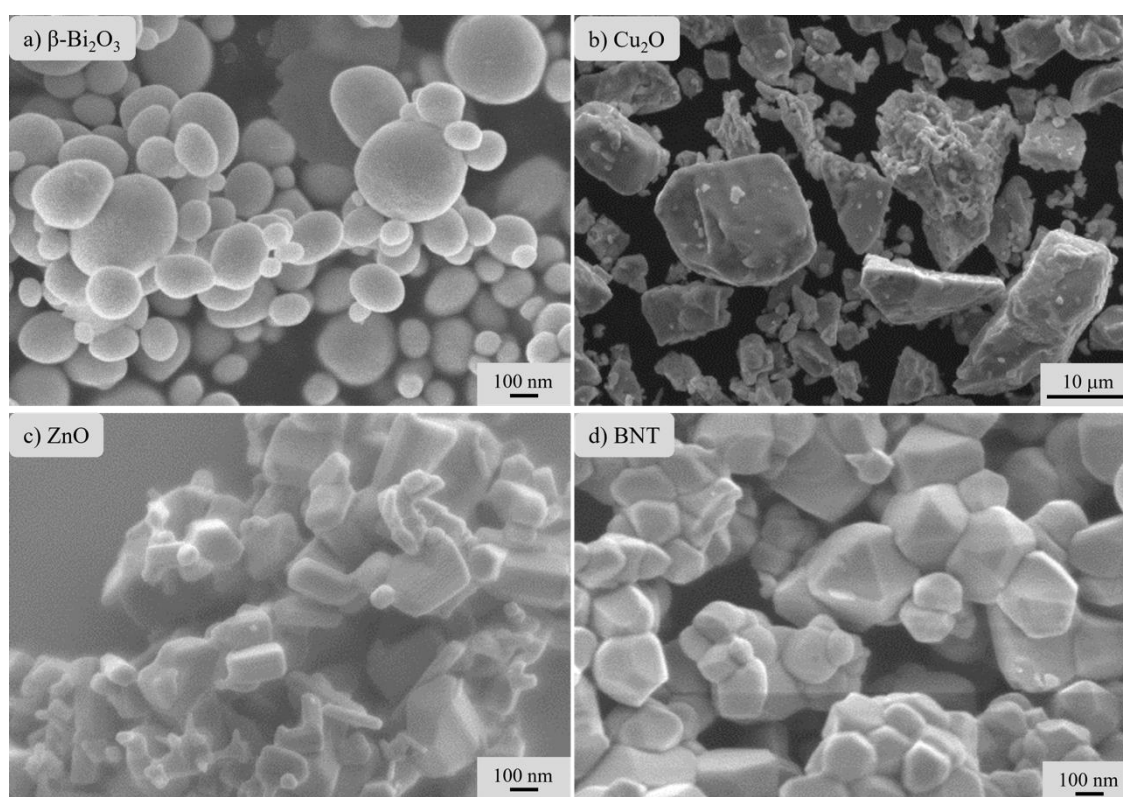


Figure 5.4 FESEM micrographs of a) β - Bi_2O_3 , b) Cu_2O , c) ZnO , and d) BNT photocatalysts. a), c) and d) are nanometric sized powder, whereas b) is micrometric sized.

The SEM micrographs of the catalyst are shown in [Figure 5.4](#). β - Bi_2O_3 presents a nanometric particle size of spherical morphology. BNT and ZnO also shows nanometric particles with rhombohedral and cubic morphology, respectively. On the other hand, Cu_2O present irregular morphology of bigger particles. The mean cumulative size distribution measured by ImageJ® in at least five micrographs per catalyst is $d_{50} = 0.047 \mu\text{m}$ for β - Bi_2O_3 , $d_{50} = 1.40 \mu\text{m}$ for Cu_2O , $d_{50} = 0.175 \mu\text{m}$ for ZnO and $d_{50} = 0.44 \mu\text{m}$ for BNT ([Figure S5.2](#)).

The coupling between β - Bi_2O_3 and the cocatalyst is shown in [Figure 5.5](#). [Figure 5.5a](#) shows the coupling of the heterojunction $\text{Cu}_2\text{O}/\beta$ - Bi_2O_3 , the micrographs exhibit that both catalysts are well attached, the bigger dark particles correspond to Cu_2O and in the surface there is grafted smaller spherical particles that correspond to β - Bi_2O_3 . For BNT/ β - Bi_2O_3 ([Figure 5.5b](#)) and ZnO/ β - Bi_2O_3 ([Figure 5.5c](#)) the same catalyst coupling is observed, β - Bi_2O_3 is deposited on the surface of the cocatalyst as it is clearly evidenced by the difference in color detected by back scattering electrons. These results shows that as-synthesized bismuth-based heterojunctions by mechanical milling exhibits an efficient coupling between both catalysts to induce a good contact in the heterointerface to promote the charge carrier transfer, separation, and migration.

Photocatalytic activity of Bi-based heterojunction for methanol oxidation using a black-body like reactor

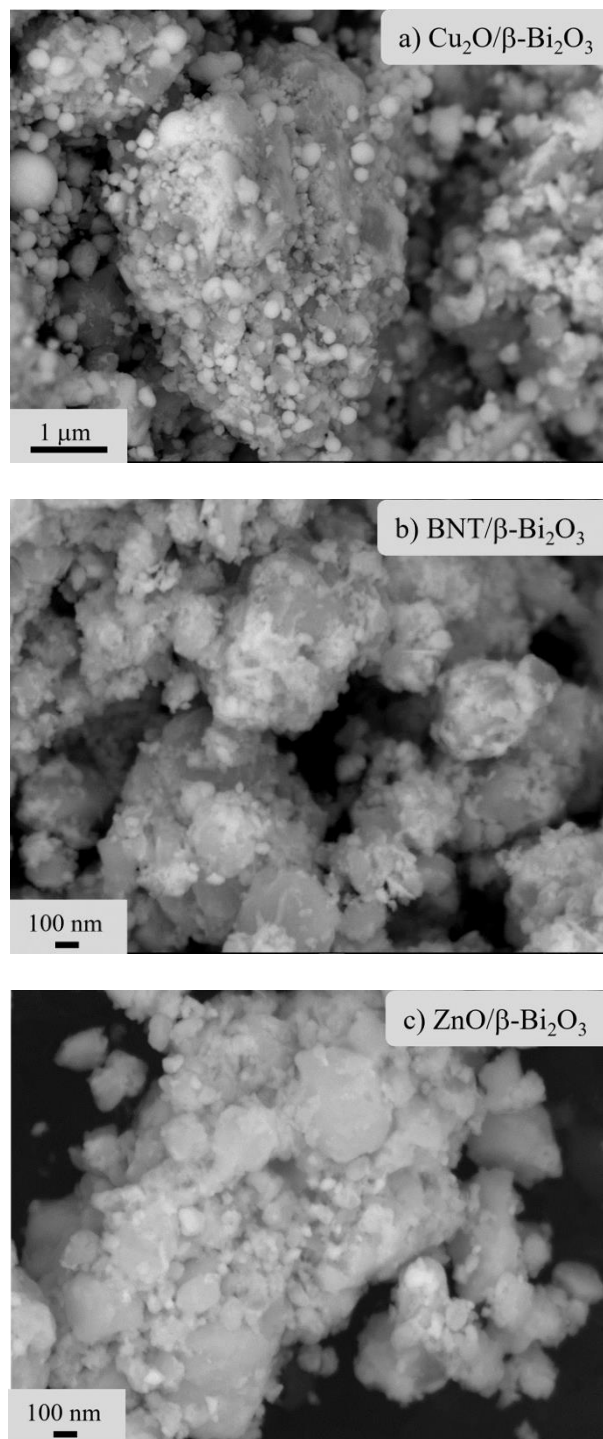


Figure 5.5 FESEM micrographs of heterojunctions a) $\text{Cu}_2\text{O}/\beta\text{-Bi}_2\text{O}_3$, b) $\text{BNT}/\beta\text{-Bi}_2\text{O}_3$ and c) $\text{ZnO}/\beta\text{-Bi}_2\text{O}_3$ synthesized by high energy ball milling at 60 min.

The band gap energy of single photocatalysts and its heterojunction assembles is shown in [Figure 5.6](#). β - Bi_2O_3 and Cu_2O shows an indirect band gap of 2.2 eV and 2 eV respectively, while BNT and ZnO shows a direct band gap of 3.05 eV and 3.2 eV respectively ([Figure 5.6a](#)), these values are in good agreement with reported data^{126,187–189}. β - Bi_2O_3 and Cu_2O are photoactive semiconductors that absorb light in a wide range of the UV and visible region while BNT and ZnO only absorbs in the UV region.

The light absorption properties of the heterojunctions can also be measured by Kubelka-Munk theory and is shown in [Figure 5.6b](#) for a direct band gap and in [Figure 5.6c](#) for an indirect band gap. Direct band gap energies show a best linear fit than indirect transition, two absorption edges for all heterojunctions are observed suggesting the contribution of both catalysts for each case. All as-synthesized bismuth-based heterojunctions present a bright yellow color which infers that can be photoactivated in visible light. For direct optical transition ([Figure 5.6b](#)) ZnO/ β - Bi_2O_3 and BNT/ β - Bi_2O_3 heterojunctions shows a red shift i.e., lower band gap energies than ZnO and BNT, respectively. However, $\text{Cu}_2\text{O}/\beta$ - Bi_2O_3 presents a higher band gap energy than Cu_2O due to the contribution of β - Bi_2O_3 .

Photocatalytic activity of Bi-based heterojunction for methanol oxidation using a black-body like reactor

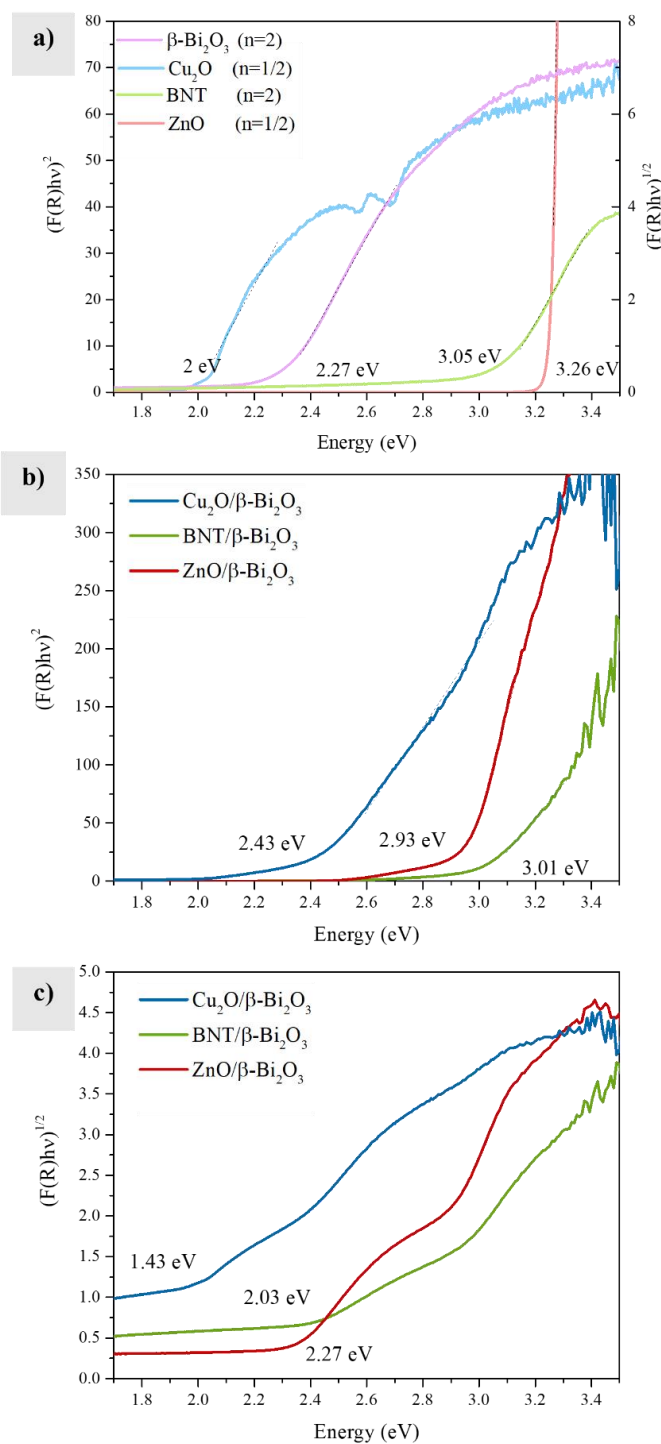


Figure 5.6 Band gap energies determined from Tauc plots of a) photocatalysts and bismuth-based heterojunctions for b) direct and c) indirect transitions.

For indirect transition (Figure 5.6c), all the heterojunctions present lower band gap energies than its respective co-catalyst. These results indicate that the band structure of the photocatalyst might be modified. As has been reported before, the efficient electronic transfer between two semiconductor approaches when there is an efficient assemble formed by a heterointerface²². The idea of coupling of two semiconductors to overcome the disadvantages of their pure phases appears to be challenging and promising since it can improve the light absorption and charge carrier separation efficiency. Considering that the shown data are a contribution of the E_g of both photocatalysts, this value reflects the light absorption characteristics as an effect of charge carrier excitation, mobility, and transfer between both photocatalysts. Band gap energy matching between two semiconductors is one of the most important parameters in designing and fabricating composite photocatalysts because band gap energy matching can efficiently separate electron-hole pairs¹¹⁴.

The semiconducting type of the photocatalysts was identified in a photoelectrochemical set-up using a potentiostat where the electrodes were placed inside a PEC cell immersed in an electrolyte. A solar simulator lamp was used for these measurements, the measured negative or positive potential as effect of the charge carrier's mobility after equilibrium under light irradiation indicates an n-type or p-type semiconductivity, respectively. Capacitance–voltage measurements are widely used to determine the flat band potential and doping density of semiconductors. Plots of $1/C_{sc}^2$ versus electrode potential are expected to be straight lines with slopes that are inversely proportional to the doping density¹⁶⁴. The positive slope of β - Bi_2O_3 and ZnO of Mott-Schottky plots in the depletion region show that the catalysts are n-type semiconductor. BNT and Cu_2O shown the opposite behavior with negative slopes, indicating that are p-type semiconductors (Figure S5.3). From this point of view β - $\text{Bi}_2\text{O}_3/\text{Cu}_2\text{O}$ and β - $\text{Bi}_2\text{O}_3/\text{BNT}$ heterojunctions correspond to a n-p type junction while β - $\text{Bi}_2\text{O}_3/\text{ZnO}$ is a n-n type junction.

For n-type semiconductors the Fermi level which is the energetic level of 0.5 probable occupancy is positioned lower than the conduction band while for p-type semiconductors the Fermi level is higher than the energetic level of the valence band. In the

Photocatalytic activity of Bi-based heterojunction for methanol oxidation using a black-body like reactor

energetic situation of a semiconductor/electrolyte, after equilibrium the Fermi level can be estimated in the measurement of the flat band potential respective to Mott-Schottky equation¹⁹⁰. The flat band potential E_{FB} from Mott-Schottky plots were determined by the slope of the lineal part of the curve for n-type or p-type semiconductors. The E_{FB} was determined at pH 7 according to Eq 5.7. The E_{FB} is a direct information of the position of the potential of conduction band E_{CB} for n-type semiconductor. To determine the value of the potential of the valence band E_{VB} for n-type semiconductors, the band gap energy is added to the E_{CB} . For p-type semiconductors, the E_{FB} correspond to the valence band potential (E_{VB}) and to determine the conduction band potential, the band gap energy is subtracted to this value. The valence band and conduction band potential respective to the normal hydrogen electrode (NHE) of photocatalysts are shown in Figure 5.7. The potential for water oxidation and hydrogen evolution for $2e^-$ reaction are shown in the graph according to reported data. The potential of methanol oxidation and the reduction of oxygen as well the redox couples relevant for the mechanisms of HCHO formation from methanol photooxidation are also presented^{191–193}.

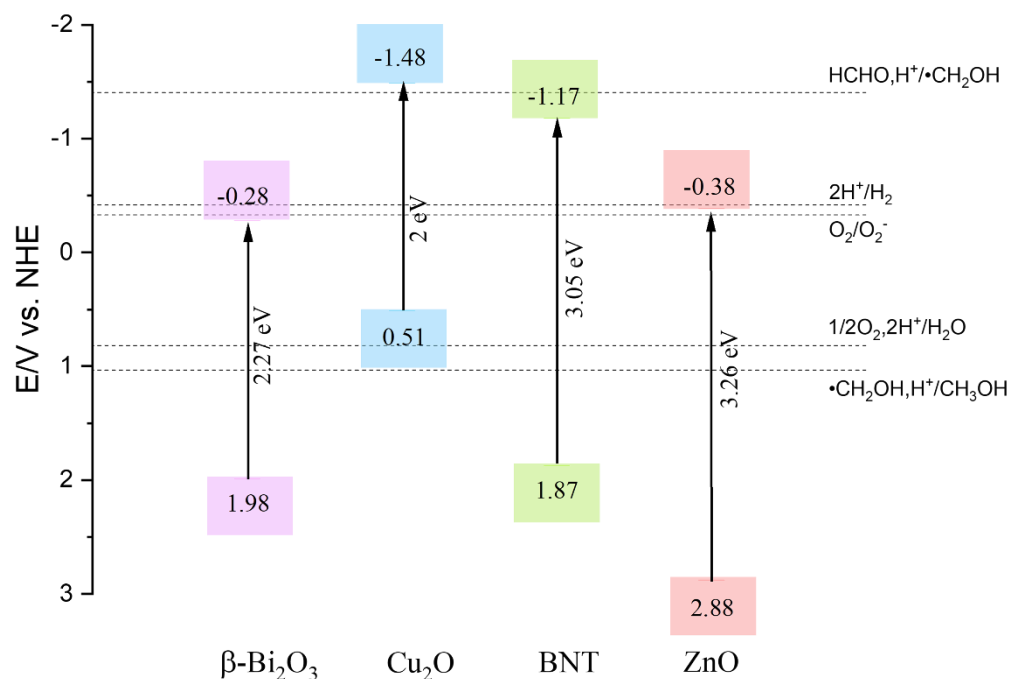


Figure 5.7 Conduction and valence bands edge positions of photocatalysts determined at pH 7. The potentials for methanol and water oxidation reactions and proton and oxygen reduction are also shown.

The potential of conduction and valence band of photocatalyst elucidate the mechanism for methanol photooxidation and the subsequent reactions in aerobic conditions. From the plotted potentials, β -Bi₂O₃, ZnO and BNT present high oxidative power of the holes in the valence band suitable for methanol and water oxidation. Cu₂O is the only photocatalyst that is not able to oxidize methanol, the E_{VB} is more negative than the redox reaction •CH₂OH, H⁺/CH₃OH (Eq 5.1). ZnO, BNT and Cu₂O present a favorable E_{CB} able to reduce H⁺ by electrons photogenerated to produce H₂ or to form the superoxide radical O₂^{•-} by the scavenging of e⁻ to molecular O₂. However, the E_{CB} of β -Bi₂O₃ (-0.28 V) is less negative than the reduction potential of 2H⁺/H₂ (-0.21 V) and O₂/O₂^{•-} (-0.33V). The inability of the conduction band electrons to scavenge surface oxygen molecules result in fast recombination of the photoexcited electrons and holes.

Photocatalytic activity of Bi-based heterojunction for methanol oxidation using a black-body like reactor

These results exemplify that the heterojunction assemble between β - Bi_2O_3 with the cocatalyst Cu_2O , ZnO and BNT could efficiently enhance the electron transfer and separation due to the band energy alignment, since the cocatalysts are able to reduce molecular oxygen and β - Bi_2O_3 is capable to carry on methanol photooxidation. The construction of heterojunctions by coupling two semiconductors with staggered band structure configuration results in an efficient way to realize the spatial separation of photoexcited electron-hole pairs. The formation of the built-in electric field at the heterojunction interface and photoexcited carrier transfer behavior depend on many factors, such as semiconductivity (n-type or p-type) and E_{CB}/E_{VB} potentials of semiconductors¹⁶⁰. The type of heterojunction formed by coupling the semiconductors and the mechanism of electronic excitation, mobility and transfer will be proposed based on these results and the photocatalytic activity for methanol oxidation.

To elucidate the mechanism of charge transfer process for methanol oxidation in UV light, the scheme of heterojunctions assemble is shown in [Figure 5.8](#). The potential of the valence band and conduction band of the catalyst is plotted according to Mott-Schottky measurements and the band gap energies. The redox couples relevant for the photooxidation of methanol are also plotted. According to the comparison of the photocatalytic activity as concentration-time plots, the reaction rates (dn/dt) and the quantum yields the mechanism of charge transfer process in the photocatalytic oxidation of methanol in UV light of the Bi-based heterojunctions is here presented.

Photocatalytic activity of Bi-based heterojunction for methanol oxidation using a black-body like reactor

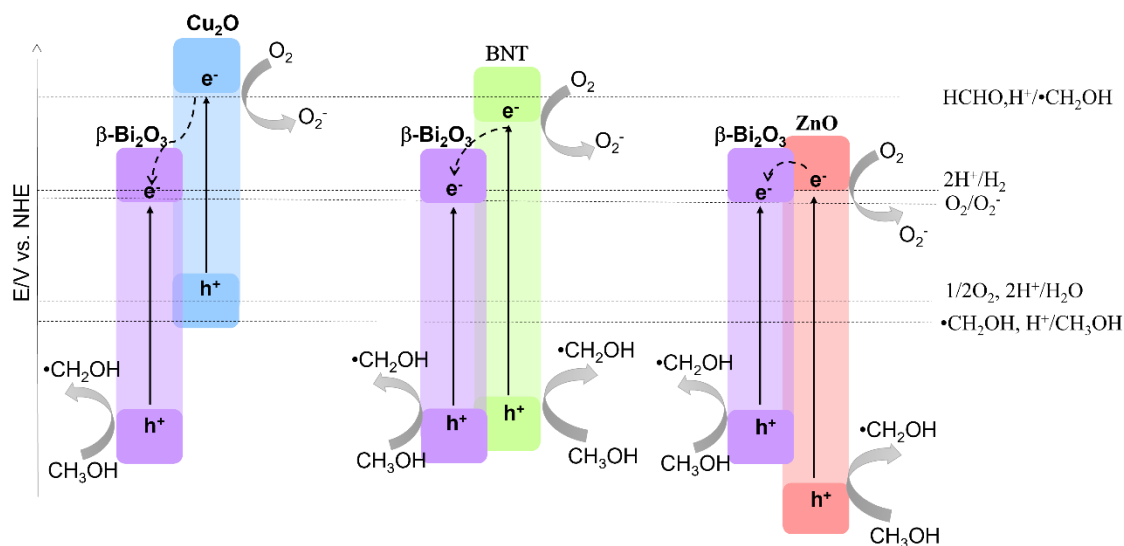


Figure 5.8 Mechanism of charge carrier transfer in photocatalytic process for methanol oxidation in bismuth-based heterojunctions at pH 7.

$\beta\text{-Bi}_2\text{O}_3/\text{Cu}_2\text{O}$ is a p-n heterojunction that shows the lower activity for methanol photooxidation. After irradiation of the heterojunction the electrons and holes photogenerated can migrate to the surface of the catalyst. In Cu_2O , some of the electrons can scavenge molecular oxygen while other electrons can migrate to the conduction band of $\beta\text{-Bi}_2\text{O}_3$. These e^- are not able to react with any absorbed specie and thus the photorecombination process happens. Even when $\beta\text{-Bi}_2\text{O}_3$ is capable to oxidize methanol the photocatalytic reactions suppressed for the recombination of e^- and the inability of holes in the valence band of Cu_2O to oxidize methanol.

$\text{BNT}/\beta\text{-Bi}_2\text{O}_3$ is a p-n type heterojunction with high photocatalytic activity for methanol oxidation. After excitation of the heterojunction under UV light, the photogenerated electrons in the CB of BNT are capable to scavenge molecular oxygen and some others are transferred to the CB of $\beta\text{-Bi}_2\text{O}_3$. Even than the e^- in the CB of $\beta\text{-Bi}_2\text{O}_3$ recombine, both catalyst presents a high positive potential of its valence band to promote methanol photooxidation. Further, the staggered alignment in $\text{BNT}/\beta\text{-Bi}_2\text{O}_3$ promotes a better charge carrier separation and mobility.

Photocatalytic activity of Bi-based heterojunction for methanol oxidation using a black-body like reactor

ZnO/ β -Bi₂O₃ is an n-n type heterojunction, the band alignment between the catalysts is not favorable for electron separation as it is corroborated by the photocatalytic activity since it decreases compared to single ZnO. After photoexcitation of the heterojunction in UV light, the photogenerated e⁻ in the CB of ZnO can scavenge molecular oxygen or migrate to the CB of β -Bi₂O₃. Both catalysts are able to photooxidize methanol, the activity diminishes due to the inability of β -Bi₂O₃ electrons to scavenge O₂, and thus decreasing the activity.

5.4. Conclusion

A new family of visible-light active bismuth-based photocatalytic heterojunctions shows to present an efficient activity for photooxidation of methanol in aqueous semiconductor suspension. BNT/ β -Bi₂O₃, β -Bi₂O₃ and BNT show high quantum yields for methanol photooxidation in UV and visible light. These compounds are non-toxic⁸⁰ and low-cost materials that can be synthesized by a simple solid-state solution⁷⁸ or thermal spray process¹²⁶ making them a promising candidate for different photocatalytic applications.

A black body reactor was employed to measure reaction rates and quantum yields for methanol photooxidation with good accuracy and high reproducibility thanks to i) the reactor geometry that allows to measure the absorbed photons emitted by the light source (photon flux), ii) the high optical density of the catalyst to assure that all photons can be absorbed and iii) the probe compound does not absorb light, the catalyst is the only light absorbing species. The quantum yields measure are an intrinsic measurement of the catalyst properties.

5.5. Appendix

The determination of the incident photon flux was performed by chemical actinometry using ferrioxalate [Fe(C₂O₄)₃]³⁻ as an actinometer. All the experimental data is shown in Supporting Information.

Photocatalytic activity of Bi-based heterojunction for methanol oxidation using a black-body like reactor

A chemical actinometer is a chemical system that undergoes a light-induced reaction (at a certain wavelength, λ) for which the quantum yield, $\Phi(\lambda)$, is accurately known¹⁹⁴. Determination of conversion to the products affords the total number of photons absorbed by the liquid or gas volume or solid surface, which may have any form or geometry¹⁹⁴. Potassium ferrioxalate undergoes degradation by photolysis to form ferrous iron Fe^{2+} . For the spectrophotometric determination of the ferrous iron formed in this reaction, 1,10-phenanthroline suggests itself as a suitable reagent. Under suitable conditions it forms a compound with ferrous iron which is very stable and has a strong absorption band with peak intensity at a wavelength of 510 nm where the absorption by the ferrioxalate ion is very low.

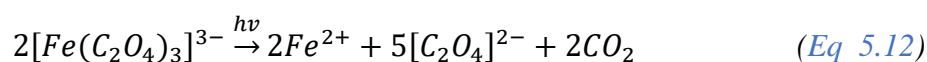
This potassium ferrioxalate was prepared by mixing a solution of 1.5M $\text{K}_2\text{C}_2\text{O}_4$ ($\geq 98.5\%$, Carl Roth) with a solution of 1.5M FeCl_3 (98%, Sigma Aldrich) in the ratio of 3 to 1. The mixed solution was stirred in a dark flask during 30 min at 40 °C and dried for 24 h in a desiccator. The solution was filtered in a kitosato flask with a funnel using a vacuum pump to obtain the crystals. The formed crystals were dried in a desiccator for 24 h. Crystals were washed with distilled water under stirring at 65 °C for 30 min and let it cool at room temperature inside a desiccator. The recrystallization process was repeated 2 times. The obtained $\text{K}_3\text{Fe}(\text{C}_2\text{O}_4)_3 \cdot 3\text{H}_2\text{O}$ green crystals were placed in a dark bottle and dried overnight in 45 °C in a hot plate. It should be mentioned that all the procedure was done in a dark room under red light.

The photolysis experiments were done by preparing 30 mM ferrioxalate solution in 0.1 N H_2SO_4 (96%, Carl Roth). The solution was placed in the glass flask used as the black body reactor (250 mL) and illuminated for 60 min. Samples were taken in 10 min time intervals. For analysis, the samples were mixed in a ratio 2 to 1 with a buffer solution of 0.105 molL⁻¹ sodium acetate and 0.199 molL⁻¹ acetic acid (100%, Carl Roth). In a typical procedure 2 mL of buffer were mixed with 1 mL of illuminated solution and 2 mL 0.1 wt.% 1,10-phenanthroline in a flask and made up to 15 mL by adding water. Exactly after 60 min for each sample, the concentration of the complex of ferrous iron and 1,10-phenanthroline $[\text{Fe}(\text{phen})_3]^{2+}$ was measured with a UV-vis spectrophotometer at 510 nm. In order to

Photocatalytic activity of Bi-based heterojunction for methanol oxidation using a black-body like reactor

interpret the obtained results, a standard curve was prepared. For this purpose, a solution of ferrous iron in 0.1 N H₂SO₄ was mixed with a buffer solution and 0.1 wt. % 1,10-phenanthroline and left for 60 min so that the complex of ferrous iron and 1,10-phenanthroline could fully develop.

The photon flux determined by actinometry is measured by the absorbance of potassium ferrioxalate in the black body reactor under the same conditions of the geometry of the reactor. On exposure to light of wavelength less than about 490 nm solutions of the ferrioxalate ion undergo decomposition according to [Eq. 5.12](#)¹⁸⁰:



The number of photons absorbed by the iron complex can easily be calculated by measuring the rate of the light-induced reduction of Fe³⁺ for which the quantum yield is known. The concentration of Fe²⁺ is measured through monitoring the colored complex of this ion with 1,10-phenanthroline at 510 nm wavelength by means of a UV-vis spectrophotometer.

The absorbance spectra are shown in [Figure S5.1a](#) and [S5.1c](#) for UV and visible light, respectively. The concentration of the complex over the time measured from Beer-Lambert equation is shown in [Figure S5.1b](#) and [S5.1d](#). The reaction rate (dn_p/dt) can be determined from the slope of the fitting of concentration-time plots multiplied by the volume of the probe suspension. This value is then the rate of photons absorbed, i.e., mols of photons per unit time (μmols^{-1}) ([Eq. 5.13](#))¹⁷⁵ that is defined as the photon flux in amount basis for a photoelectrochemical reaction.

$$I_0 = \frac{dn_p}{dt} \quad (\text{Eq. 5.13})$$

Photocatalytic activity of Bi-based heterojunction for methanol oxidation using a black-body like reactor

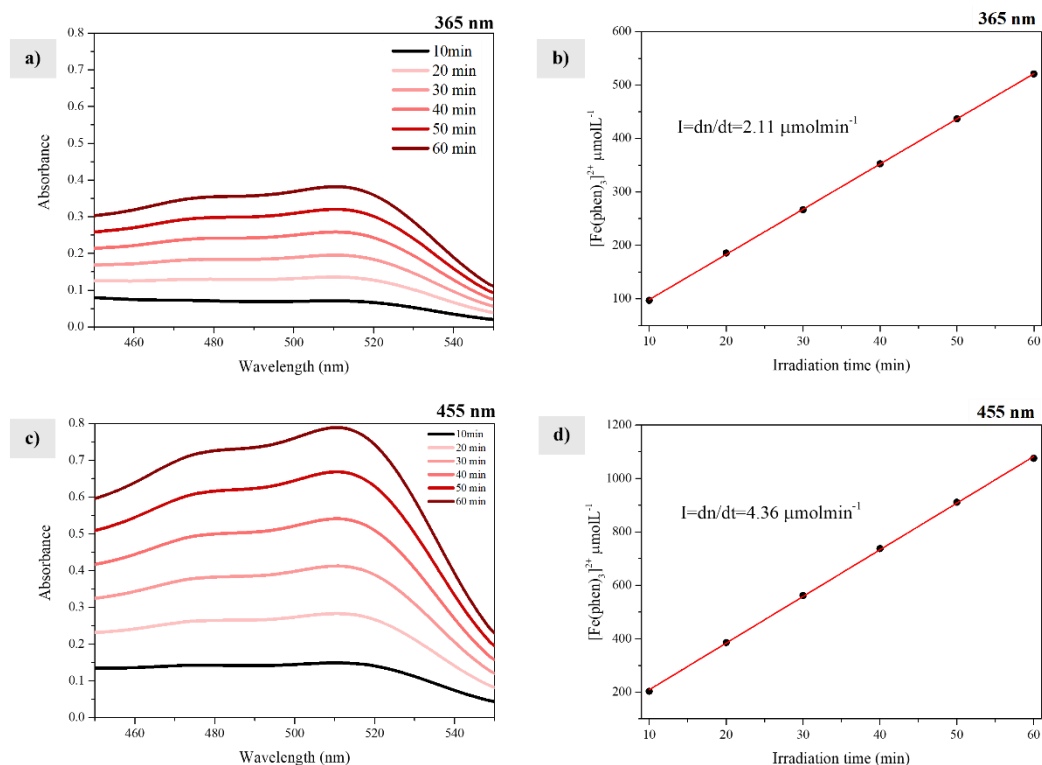


Figure S5.1 a) and c) UV-vis absorbance spectra and b) and d) concentration-time plots of ferrioxalate photolysis to determine the photon flux in UV and visible light.

For UV light, the number of photons absorbed per time is $2.11 \mu\text{mol s}^{-1}$ and $4.36 \mu\text{mol s}^{-1}$ for visible light as it is shown in the plots of [Figure S5.1b](#) and [S5.1d](#), respectively.

The determination of photon flux for monochromatic light using chemical actinometers are usually measured employing [Eq. 5.14](#)^{195,196}.

$$I_0 = \frac{n_a}{\Phi_a t (1 - 10^{-\epsilon [act] l})} \quad (\text{Eq. 5.14})$$

where I_0 is the photon flux (einstein s^{-1}), Φ_a is the quantum yield of oxalate at a certain wavelength ($\Phi_{365\text{nm}} = 1.21$ and $\Phi_{455\text{nm}} = 0.92$)¹⁸⁰, t is the irradiation time, ϵ is the extinction coefficient of ferrioxalate ($1.10\text{E}4 \text{ mol}^{-1}\text{cm}^{-1}\text{L}$), $[act]$ is the concentration of the ferrioxalate measured from Beer-Lambert equation, l is the path of the light and n_a correspond to [Eq. 5.15](#):

Photocatalytic activity of Bi-based heterojunction for methanol oxidation using a black-body like reactor

$$n_a = \frac{NV_1V_3A_{510}}{\varepsilon V_2l} \quad (\text{Eq 5.15})$$

where N is the Avogadro number, V_1 , V_2 and V_3 correspond to the volume of the solution irradiated in the reactor, the aliquots, and the volume of the mixture, A_{510} is the maximum absorbance of ferrioxalate at 510 nm, ε is the extinction coefficient ($1.104\text{E}4 \text{ mol}^{-1}\text{cm}^{-1}\text{L}$) and l is the path of the light (1 cm). The obtained photon flux for UV light is $1.90\text{E}16 \text{ einsteins}^{-1}$ and for visible light is $5.14\text{E}16 \text{ einsteins}^{-1}$.

Figure S5.2 shows the particle size distribution obtained from image analysis of the micrographs per each catalyst using ImageJ®. The analysis was performed in at least five micrographs in each catalyst and the size distribution can be measured from the cumulative frequency. The graph shows the distribution for the 10% (d_{10}), 50% (d_{50}) and 90% (d_{90}) of the density of particles. $\beta\text{-Bi}_2\text{O}_3$ shows a nanometric particle size while ZnO and BNT exhibits submicrometric size distribution and Cu_2O presents the biggest particle size.

Photocatalytic activity of Bi-based heterojunction for methanol oxidation using a black-body like reactor

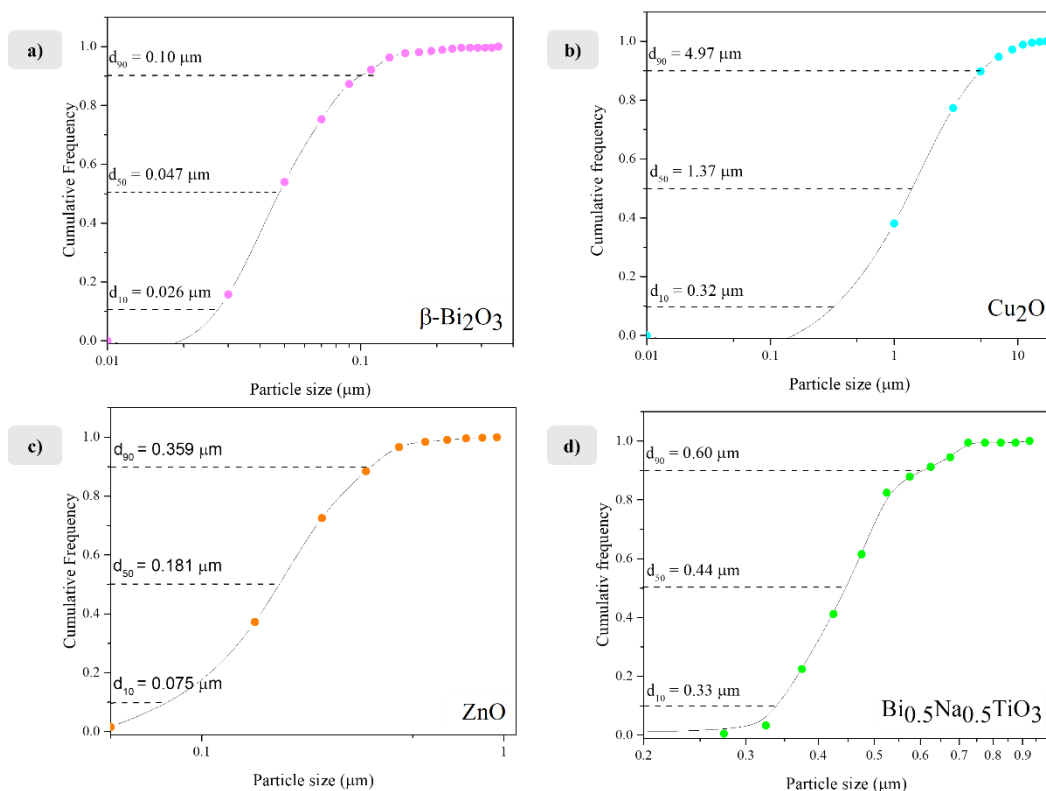


Figure S5.2 Cumulative particle size distribution of single catalyst obtained from image analysis.

Figure S5.3 shows the Mott-Schottky plots obtained from the electrodes in a potentiostat using a 0.1 M KCl electrolyte (pH 6) recorded at 10 Hz. $\beta\text{-Bi}_2\text{O}_3$ and ZnO shows a positive slope of the capacitance vs potential curve which indicates an n-type semiconductivity. Cu_2O and BNT shows negative slopes that indicates the p-type semiconductivity. The flat band potential is measured by a linear fit and then measured at pH 7 using Nernstian equation.

Photocatalytic activity of Bi-based heterojunction for methanol oxidation using a black-body like reactor

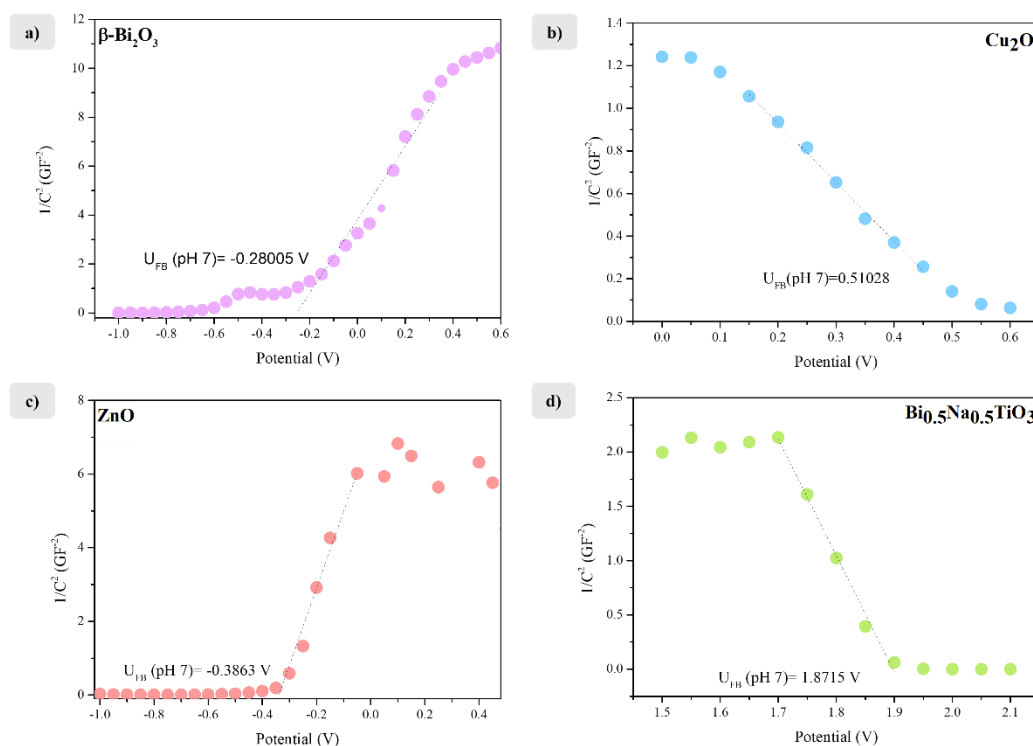


Figure S5.3 Mott-Schottky plots of electrodes synthesized by spray coating. The measurement was carried out in aqueous solution of 0.1M KCl recorded at a frequency of 10Hz.

Table S5.1 shows the reaction rate (dn/dt) obtained from the slopes of concentration-time plots for formaldehyde evolution over photocatalytic methanol oxidation in UV and visible light as a comparative between the single catalyst studied. Besides, the band gap energy, flat band potential the band edge potential of the valence band and conduction band as well the surface energy and the particle size distribution (d_{50}) is shown.

Table S5.1 Band gap energies, band edge potential, surface area and particle size of photocatalysts. The reaction rates (dn/dt) for methanol photooxidation in UV and visible light is also shown.

<i>Catalyst</i>	E_g (eV)	E_{FB} (pH 7)	E_{CB} (pH 7)	E_{VB} (pH 7)	S_A (m^2g^{-1})	d_{50} (mm)	$(\frac{dn}{dt})_{365nm}$ $\mu molmin^{-1}$	$(\frac{dn}{dt})_{455nm}$ $\mu molmin^{-1}$
$\beta-Bi_2O_3$	2.27	-0.28 V	-0.28	1.98	2.77	0.047	0.002712 ± 0.0007	0.003135 ± 0.0004
Cu_2O	2	0.51 V	-1.48	0.51	1.07	1.40	0.000255 ± 0.00006	0.0002925 ± 0.00001
ZnO	3.26	-0.38 V	-0.38	2.78	6.5	0.175	0.1806 ± 0.0036	0.0013225 ± 0.0003
BNT	3.05	1.87 V	-1.17	1.87	2	0.44	0.008715 ± 0.0012	0.00023925 ± 0.0001

Photocatalytic activity of Bi-based heterojunction for methanol oxidation using a black-body like reactor

Chapter 6: Photoinduced H₂ evolution of Bi-based heterojunctions: Fate of photogenerated charge carriers

6.1. Introduction

Photocatalytic water splitting as a source for hydrogen (H₂) is one of the most promising technologies for solar energy conversion and storage. As a clean, inexhaustible, and renewable natural resource, solar energy emerges as the main option to overcome the dwindling energy resources and environmental deterioration³. Contrarily to fossil fuels, the photocatalytic production of hydrogen over semiconductor nanomaterials leads to a minimal environmental impact, with no atmospheric pollutants or particulates emitted during the production itself or the subsequent combustion of hydrogen¹².

Nowadays, water splitting is one of the most attractive applications of semiconductor photocatalysis¹⁰. Although it presents some limitations, in the process employing pure water is usually rather inefficient or is not even operative at all. This is related to the fact that the simultaneous reduction and oxidation of water is a complex multistep reaction involving four electrons^{5,182}.

Numerous strategies have been considered to improve photocatalytic performance of a semiconductor. Surface decoration with metals (especially Pt, Au, Ag, Cu) can simultaneously enhance charge carrier separation and reduce the overpotential for H₂ evolution, which is known to greatly improve the H₂ production efficiency¹⁹⁷. Amongst the metals that facilitate electron capture, Pt has been extensively reported as the most effective¹¹². Using sacrificial molecules as electron donors is one of the easiest and feasible approaches to remarkably improve the H₂ production¹⁵. The photogenerated holes are scavenged by these molecules thus reducing significantly the charge carrier recombination⁴. Furthermore, since O₂ is not produced, the back reaction to produce water is suppressed thus increasing the H₂ yield and avoiding a subsequent gas separation stage. Some common and widely used hole scavengers (electron donors) for photocatalytic H₂ generation are inorganic compounds such as alcohols, organic acids, and hydrocarbons⁴. Methanol has been and is being used as a model compound for sacrificial reagent. The addition of

methanol as an electron donor in water splitting reactions generates an irreversible reaction with the photogenerated valence band holes thus enhancing the photocatalytic electron-hole separation efficiency, resulting in higher quantum yields¹⁹.

Exploring the charge carrier kinetics is essential for understanding the photocatalytic mechanism occurring at semiconductor surface. Electron paramagnetic resonance (EPR) (also called electron spin resonance (ESR)) spectroscopy is a powerful and sensitive technique to study radicals formed upon illumination¹⁹⁸. EPR spectroscopy has been developed to reveal the underlying photocatalytic pathways based on interfacial charge transfer and radical reactions. EPR is especially useful to elucidate the mechanism for the degradation of organic compounds, herewith, the interactions between radical oxygen species (OH•, HO₂•, O₂•-) and organic radicals are characterized¹⁹⁹. The roles of isolated oxygen species in the complete photocatalytic reaction is further clarified by using proper scavengers for holes or electrons²⁰⁰.

Every electron has a magnetic moment and spin quantum number $s = 1/2$ with magnetic components $m_s = 1/2$ or $m_s = -1/2$. In the presence of an external magnetic field with strength B_0 , the electron's magnetic moment aligns itself either antiparallel ($m_s = -1/2$) or parallel ($m_s = 1/2$) to the field, each alignment having a specific energy (Eq. 6.1) due to the Zeeman effect²⁰¹.

$$E = m_s g_e \mu_B B_0 \quad (\text{Eq. 6.1})$$

Where g_e is the electron's so-called g -factor $g_e = 2.0023$ for the free electron and μ_B is the Bohr magneton ($5.7883\text{E}-5 \text{ eVT}^{-1}$). Therefore, the separation between the lower and the upper state is (Eq. 6.2):

$$\Delta E = g_e \mu_B B_0 \quad (\text{Eq. 6.2})$$

for unpaired free electrons. This equation implies (since both g_e and μ_B are constant) that the splitting of the energy levels is directly proportional to the magnetic field's strength. An unpaired electron can change its electron spin by either absorbing or emitting a photon

of energy $h\nu$ such that the resonance condition, $h\nu = \Delta E$, is obeyed. This leads to the fundamental equation of EPR spectroscopy (Eq. 6.3):

$$h\nu = g_e \mu_B B_0 \quad (\text{Eq. 6.3})$$

The photocatalytic activity for H₂ evolution and methanol oxidation was evaluated for different bismuth-based heterojunctions using Pt as electron scavenger grafted on the surface by photodeposition and methanol as hole scavenger. The fate of photogenerated charge carriers was evaluated by electron paramagnetic resonance in solid phase to study the reactions evolved from the photogenerated charge carriers and in liquid phase for detection of free radicals that participate in the photocatalytic reactions in oxygen and anoxic conditions.

6.2. Materials and methods

EPR measurements were performed by a MiniScope X-band spectrometer (MS400 Magnettech GmbH) operating at about 9.42–9.44 GHz field frequency as described before. For samples in suspension, 0.5 mL of 1 gL⁻¹ of the photocatalyst in water was purged with argon or oxygen and 2 μL of DMPO (5,5-Dimethyl-1-pyrroline N-oxide) was added. The center field was 335 mT and sweep time was 15 s. For powder samples, liquid N₂ was used to maintain the temperature at 77 K, with the center field at 335 mT and sweep time of 60 s. Sample irradiation during EPR measurements was provided by a built-in optical fiber connected to a Hamamatsu LC8 light source (200 W Hg–Xe lamp).

Pt was grafted on the surface of the catalyst by photodeposition which is the most commonly used technique for the deposition of co-catalyst nanoparticles²⁰². Although one reason is that it tends to result in the most active materials, other beneficial features include the possibility of creating well-defined co-catalyst nanoparticles, with control over their geometrical distribution, size, and oxidation state, without the need for elevated temperatures or applied bias as other methods require.

H₂ evolution was performed in a solar simulator reactor. In a typical procedure 10 mL borosilicate glass vials are used. The photocatalyst in a concentration of 1 gL⁻¹ is suspended in 6 mL of deionized water with 10 % methanol used as hole scavenger. H₂PtCl₆ (0.01 M) is used as Pt⁰ noble metal loaded by in situ photodeposition during the reaction. Before irradiation vials were sealed and purge with Ar (> 99.999%) during 10 min. Then, the vials were horizontally fixed inside an orbital shaker placed at 30 cm distance below a 1000 W Xenon lamp (Hönle UV Technology, Sol 1200) as a simulated solar light equipped with a filter to mimic the emission profile of sunlight.

The photocatalytically evolved molecular hydrogen was quantitatively determined by means gas chromatography using a Shimadzu GC-8A (thermal conductivity detector). For this purpose, a 50 µL gas sample was periodically taken from the head space over the suspension using a Valco gas tight sampling syringe equipped with a push-button valve. The gas sample was then injected into the injection port of the GC.

The photonic efficiencies ξ was calculated based on Eq. 6.4, where dC/dt is the formation of hydrogen rate in units of mols⁻¹, A is the illuminated area (4.2×10^{-4} m²), I_0 the photon flux density and V is the suspension volume (0.006 L)

$$\xi(\%) = \frac{\text{formation initial rate (mols}^{-1}\text{)}}{\text{photon flux (mols}^{-1}\text{)}} = \frac{dC}{dt} \frac{V}{I_0 A} \times 100 \quad (\text{Eq 6.4})$$

The photon flux density I_0 was determined from Eq. 6.2, where I is the light intensity (Wm⁻²), λ is the corresponding wavelength (m), N_A is Avogadro's constant (6.022×10^{23} mol⁻¹), h is Planck's constant (6.636×10^{-34} Ws²) and c is the speed of light (3×10^8 ms⁻¹).

$$I_0 = \frac{I\lambda}{N_A h c} \quad (\text{Eq 6.5})$$

6.3. Results and discussion

Photocatalytic activity of bismuth oxide and bismuth-based heterojunctions was initially evaluated for 0.1% Pt loading as electron scavenger in methanol solution (hole

scavenger) in UV-vis excitation using a solar simulation light irradiance in argon atmosphere. The evolved H₂ over the time for single catalyst and its heterojunctions is shown in [Figure 6.1](#).

From single semiconductors only Bi_{0.5}Na_{0.5}TiO₃ and ZnO shows activity while β-Bi₂O₃ and Cu₂O do not shows activity at all. The inactivity of β-Bi₂O₃ is excepted based on the potential of its conduction band E_{CB} that is not negative enough (-0.28 V vs NHE, pH 7) for the reduction of protons to produce molecular hydrogen H⁺/H₂ (-0.413 V vs NHE, pH 7). Although, the holes in the valence band have the sufficient potential for oxidize methanol, the inactivity of electrons to reduce H⁺ generates a fast recombination of photogenerated charge carriers, decreasing the activity of the semiconductor.

In the case of Cu₂O, the E_{CB} is negative enough to reduce H⁺ and the E_{VB} is positive enough to oxidize water. Nevertheless, as it was evidenced in [Chapter 4](#), Cu₂O suffers photocorrosion in the oxidation to form CuO. Moreover, the oxidation potential of CuO by photogenerated holes is more favorable than the oxidation of water. This generates that Cu₂O is unstable under light irradiation and is not favorable to produce H₂.

In the case of ZnO, the catalyst shows the higher activity of the single catalyst as is in accordance to a vast research that can be found on the literature²⁰³ based on the physical and chemical properties of ZnO such as a wide band gap, the negative potential of the conduction band, the strong oxidation ability and the large free-exciton binding energy. Otherwise, Bi_{0.5}Na_{0.5}TiO₃ shows a comparable activity very similar than ZnO for H₂ evolution as is shown in [Figure 6.1](#).

BNT is a bismuth-based perovskite and has not been widely studied for photocatalytic applications. Some of the reported research has proved to be a high active potential catalyst for H₂ evolution^{158,187}. These studies evaluated the activity of BNT under UV and visible light in the presence of sacrificial agents and electron scavengers and show a remarkable stability of the catalyst in repeated cycles. The structures of bismuth-based titanates are constructed from layers built up by edge and/or corner-sharing of TiO₆

Photoinduced H₂ evolution of Bi-based heterojunctions: Fate of photogenerated charge carriers

octahedral, which forms a zigzag ribbon or a tunnel structure. Further, the anti-bonding states between the lone electron pairs of Bi³⁺ and electrons in O2p orbital generates a promotion in the separation of the electron-holes photogenerated¹⁵⁸.

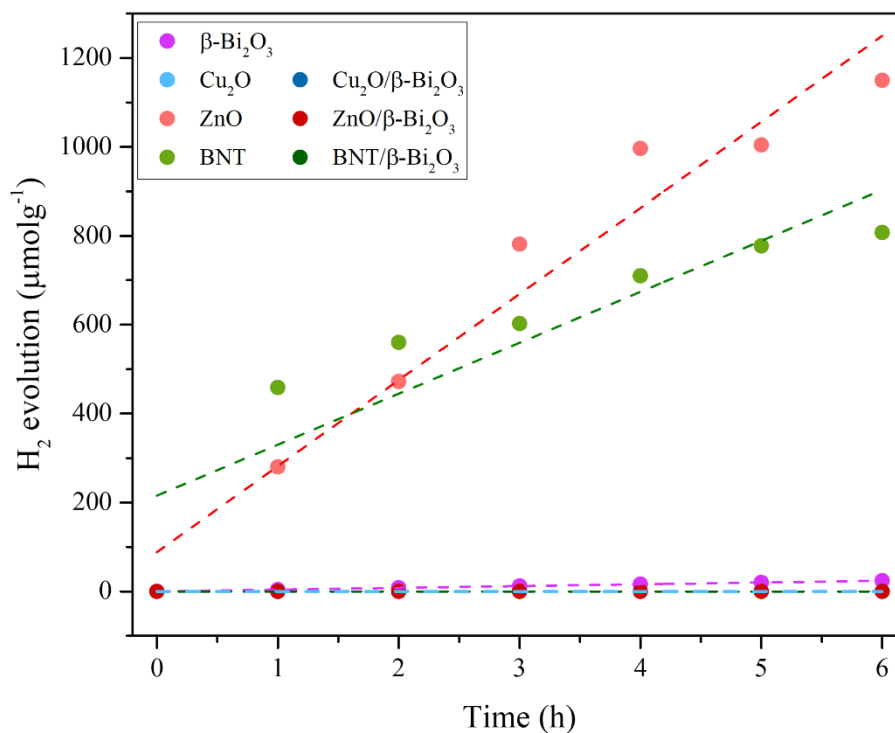


Figure 6.1 Photocatalytic H₂ evolution over different Bi-based heterojunctions in a 1000 W Xenon lamp UV-vis solar simulator. Catalyst concentration: 1 gL⁻¹, methanol (hole scavenger) 2.47 molL⁻¹, 0.1 wt% Pt (electron scavenger) photodeposition using a 0.1 M solution (H₂PtCl₆).

The Bi-based heterojunctions β -Bi₂O₃/Cu₂O, β -Bi₂O₃/ZnO and β -Bi₂O₃/BNT do not show any activity for H₂ evolution in the presence of sacrificial agents. Also, different amounts (wt.%) of Pt loaded on the surface of the catalyst was evaluated (not shown here) and the heterojunctions are not photocatalytic active. This can be explained based on the band alignment of each heterojunction shown in Chapter 5. The photogenerated electrons

migrate from the conduction band of the catalyst with higher E_{CB} (Cu₂O, BNT or ZnO) to the conduction band of β -Bi₂O₃ according to a type II heterojunction mechanism of charge carriers. Besides, the experiments performed show a change in color for Bi-based heterojunctions and β -Bi₂O₃ from yellow to dark which can be inferred as a photocorrosion behavior. Methanol was used as a sacrificial agent in all the H₂ evolution experiments, methanol is an electron donor that injects electrons into the CB of the catalyst¹⁵. If these electrons are injected into the CB of β -Bi₂O₃, they cannot reduce protons to form H₂ and then photocorrode β -Bi₂O₃ as it was explained in [Chapter 4](#).

A simple experiment to bear out this phenomenon was performed by a sample preparation of β -Bi₂O₃ in four different conditions: 1 gL⁻¹ of catalyst was loaded in 6 mL of i) 10 vol% methanol and purged in Ar atmosphere, ii) distilled water and purged in Ar atmosphere, iii) 10 vol% methanol solution and sealed in air atmosphere and iv) distilled water and sealed in air atmosphere. The samples were placed in the solar simulator reactor and illuminated for 3 h under continuous stirring in the same conditions as the experiments for photocatalytic H₂ evolution. The samples are shown in [Figure 6.2](#).

As it can be clearly seen, in air atmosphere β -Bi₂O₃ does not show a difference in color under 3 h of light irradiation in water or in methanol solution. The photogenerated electrons of the catalyst or the electrons injected from the oxidation of methanol can scavenge molecular oxygen. Otherwise, the catalyst in Ar atmosphere and methanol solution shows a difference in color from yellow (characteristic color of β -Bi₂O₃) to black. This was evidenced in the first hour of illumination. The catalyst in Ar atmosphere and in water solution, does not show a difference in color. These results might be attributed due to photocorrosion caused by electron injection from methanol oxidation reaction (electron donor) into the conduction band of the catalyst. The electrons accumulated on the CB of β -Bi₂O₃ cannot reduce H⁺ to produce H₂ (higher redox potential) or scavenge molecular oxygen (anoxic conditions). For Bi-based heterojunctions under Ar atmosphere and in methanol aqueous solution (conditions for H₂ evolution experiments) the same change in color was observed indicating that these heterojunctions also exhibit photocorrosion from β -Bi₂O₃.

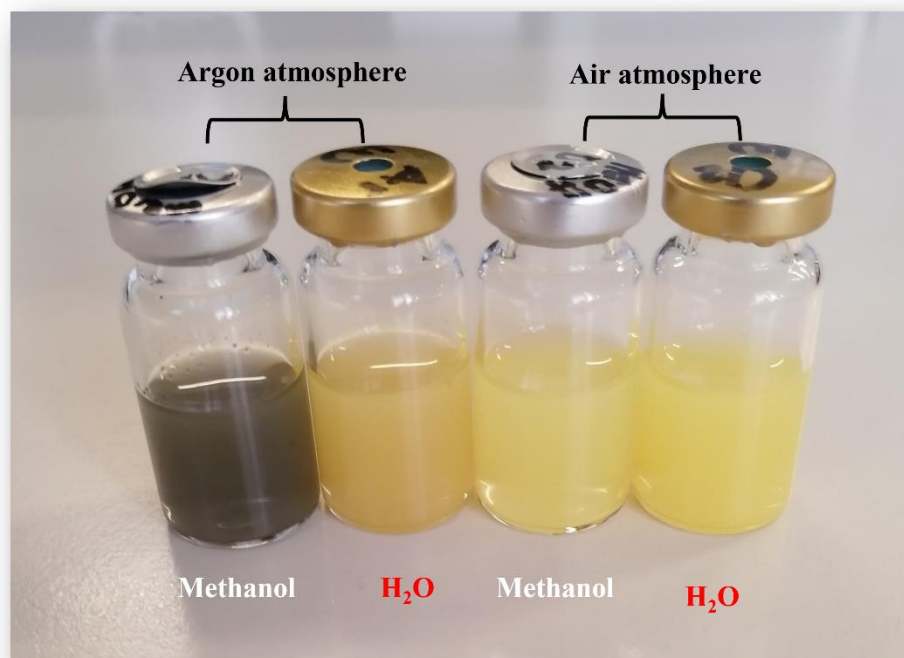


Figure 6.2 Solar simulator light irradiation in β -Bi₂O₃ under argon and air atmosphere in a suspension of 10 vol% methanol or distilled water to envisage the instability of the catalyst.

In this context, Bi-based heterojunctions are not able to be applied as H₂ evolution photocatalysts. We then focus our attention in Bi_{0.5}Na_{0.5}TiO₃, the photocatalytic activity for H₂ generation was evaluated for different amount of Pt grafted on the surface (Figure 6.3) at 0.1, 0.5, 1, 2 and 5 wt.%. 0.1% Pt shows the higher amount of H₂ evolved while for 0.5% Pt H₂ shows a decrease and for 1, 2 and 5% poorly shows activity. As the content of Pt increases the H₂ tends to decrease. This tendency can be explained since a higher amount of deposited Pt could obstruct the active surface sites of the catalyst and inhibits the redox reactions decreasing then the photocatalytic activity.

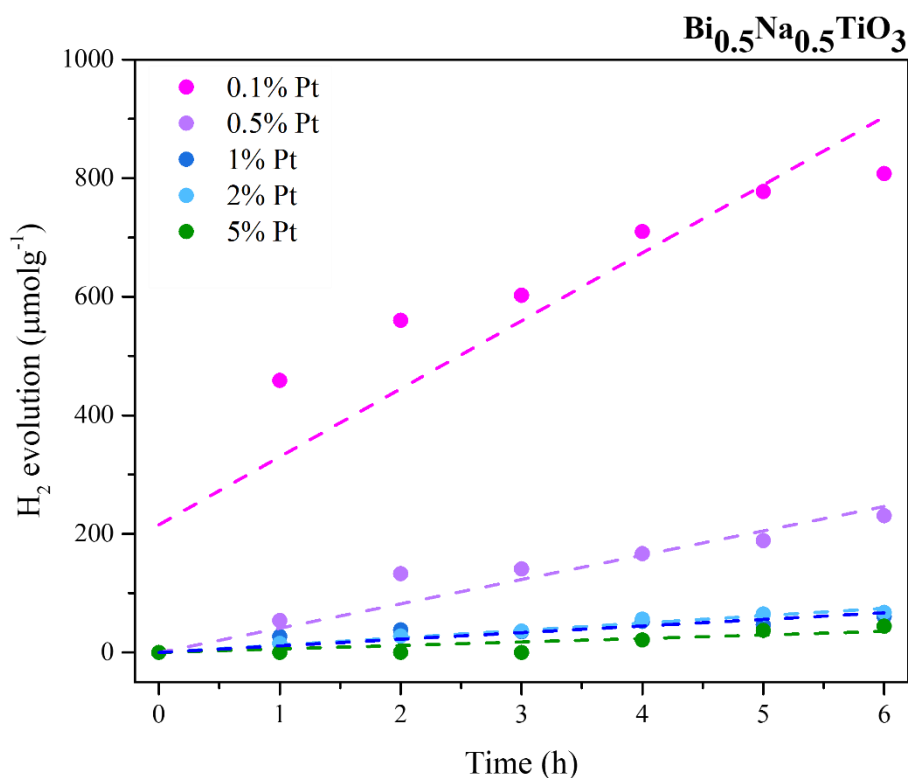


Figure 6.3 Photocatalytic H₂ evolution over Bi_{0.5}Na_{0.5}TiO₃ with Platinized surface in a 1000 W Xenon lamp UV-vis solar simulator. Catalyst concentration: 1 gL⁻¹, methanol (hole scavenger) 2.47 molL⁻¹, Pt (electron scavenger) photodeposition using a 0.1 M solution (H₂PtCl₆).

Table 6.1 Reaction rates and photonic efficiency for H₂ evolution under solar simulator light irradiance.

Sample	H ₂ evolved (μmolg ⁻¹ h ⁻¹)	Photonic efficiency ξ %
BNT 0.1%Pt	114.63	1.92
BNT 0.5%Pt	35.52	0.55
BNT 1%Pt	12.40	0.22
BNT 2%Pt	12.01	0.20
BNT 5%Pt	8.14	0.13
ZnO 0.1%	193.64	3.33

The comparison of reaction rates and photonic efficiencies is summarized in [Table 6.1](#). From previous studies in our research group the photon flux measured of the spectral irradiance in the wavelength range between 350 nm and 380 nm at the irradiated area, the photon flux was found to be $I_0 = 383 \times 10^{-6} \text{ molm}^{-2}\text{s}^{-1}$. Ignoring losses of light due to reflecting and scattering out, 1.42×10^{-7} mole of photons is entering the irradiated suspension per second²⁰⁴. The photonic efficiencies are calculated using this photon flux and multiplied by the formation rate of hydrogen, the volume of the irradiated sample and the area of illumination. The values for photocatalytic H₂ evolution in aqueous suspension using methanol as hole scavenger and loaded different amount of wt.% Pt is shown in [Table 6.1](#). Also, the photonic efficiency of 1% Pt ZnO is presented.

The fate of photogenerated charge carriers and the mechanism transfer and reactions can be evaluated by electron paramagnetic resonance. To evaluate the non-activity of Bi-based heterojunctions, EPR measurements was performed for $\beta\text{-Bi}_2\text{O}_3$, $\text{Bi}_{0.5}\text{Na}_{0.5}\text{TiO}_3$ and $\beta\text{-Bi}_2\text{O}_3/\text{BNT}$. From the previous studies for methanol oxidation, the heterojunction shows a remarkable photocatalytic activity for methanol oxidation and higher than $\beta\text{-Bi}_2\text{O}_3$. Moreover, the non-activity of this heterojunction for H₂ evolution could be understood by determining the fate of photogenerated charge carriers. EPR spectra of the powder samples at 77 K in air without any radical scavenger are presented in [Figure 6.4](#).

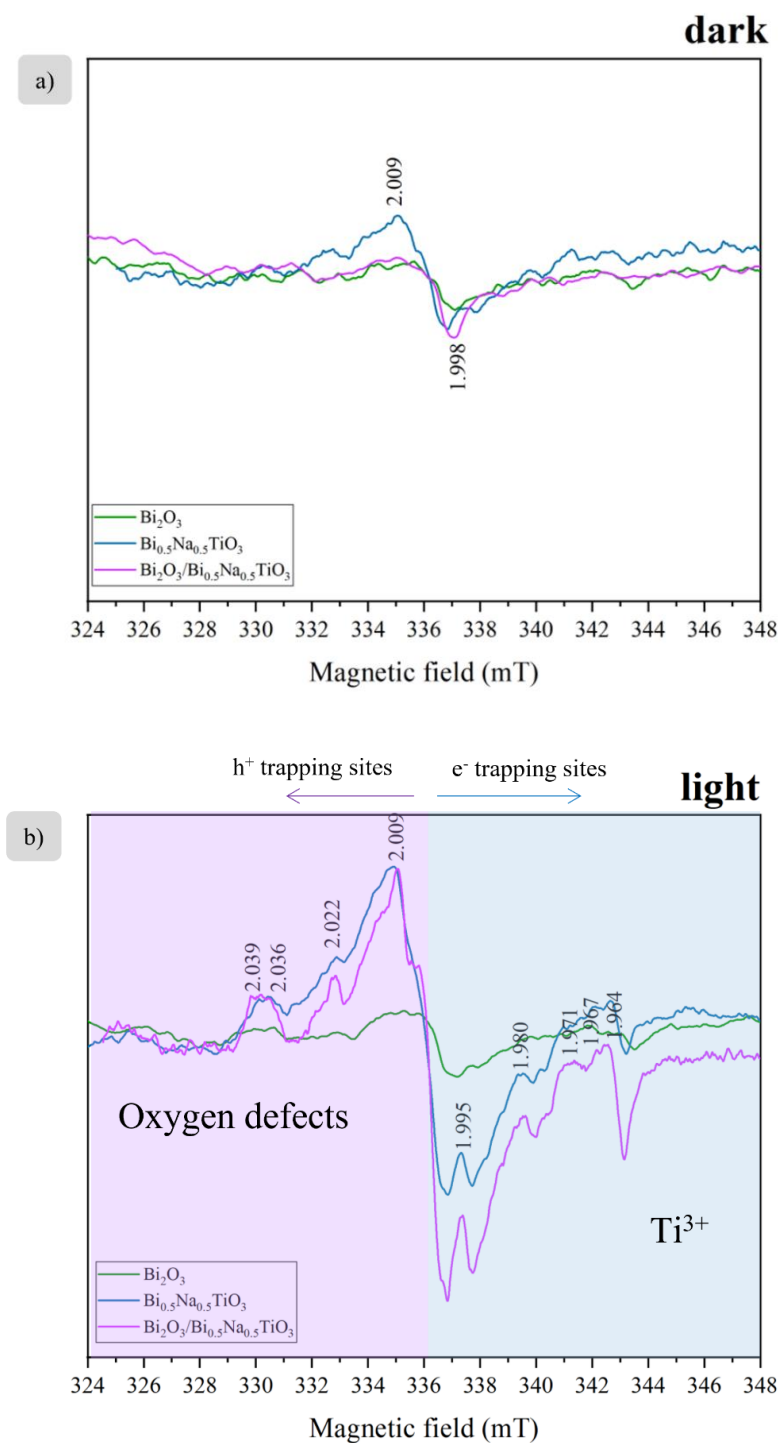


Figure 6.4 EPR spectra of solid samples recorded at 77 K (liquid N₂) in air atmosphere a) in the dark and b) before UV illumination for 7 min.

Photoinduced H₂ evolution of Bi-based heterojunctions: Fate of photogenerated charge carriers

EPR spectra of powder samples in air and at 77 K were obtained in the dark (Figure 6.3a) and compared with those under UV irradiation (Figure 6.3b). Under dark conditions, there is no signal for the β -Bi₂O₃ spectrum, but a small one for BNT at $g = 2.009$ and at $g = 1.998$ which can be related to free unpaired electrons trapped on oxygen-vacancy sites. Additionally, for the heterojunction β -Bi₂O₃/BNT a small signal at $g = 1.998$ is shown.

Under UV light irradiation, β -Bi₂O₃ do not show a significant increase of the signal compared with BNT and the heterojunction β -Bi₂O₃/BNT. These both catalysts show a signal at $g = 2.039$, $g = 2.036$, $g = 2.022$ and $g = 2.009$ that correspond to oxygen defects due to the trapping sites of photogenerated holes ($g > 2$). On the other hand, the signal detected at $g = 1.995$, $g = 1.980$, $g = 1.971$, $g = 1.967$ and $g = 1.964$ is attributed to the formation of Ti³⁺ from the electrons in trapping sites ($g < 2$). As it is clearly evidenced, BNT show a higher signal than the heterojunction. the substitution of A-site or B-site in BNT perovskite structure can create oxygen vacancy to compensate charge and retain overall crystal charge neutrality in the crystal²⁰⁵.

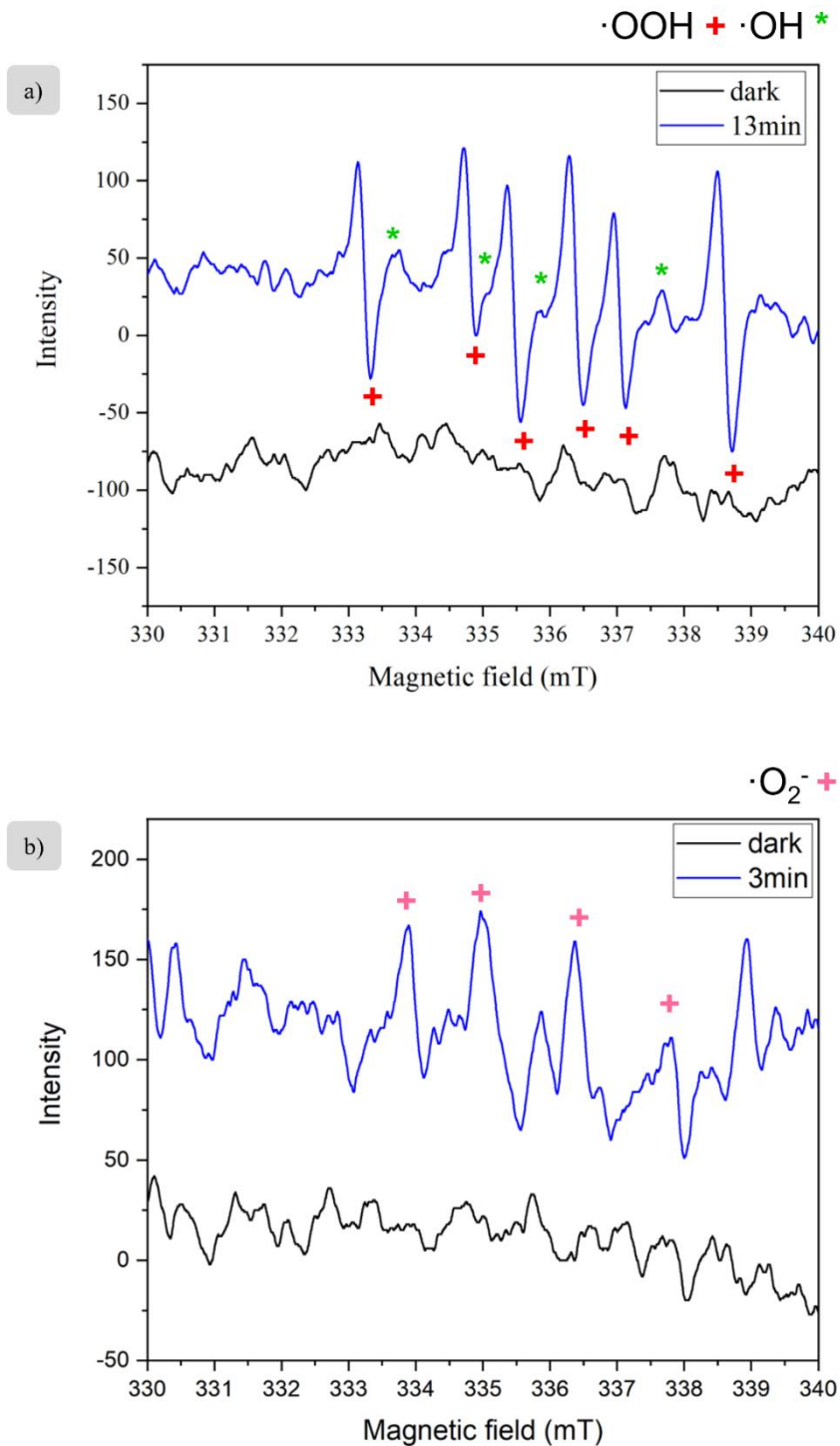


Figure 6.5 EPR spectra at 298 K of aqueous suspensions of 0.1% Pt Bi_{0.5}Na_{0.5}TiO₃ with DMPO (spin trapping agent) in a) argon and b) oxygen atmospheres before and under UV irradiation (200 W Hg-Xe lamp). 1 gL⁻¹ of catalyst in 2.47 molL⁻¹ methanol solution.

To determine the evolved radicals of BNT in aqueous phase, EPR measurements under argon (Figure 6.5a) and oxygen (Figure 6.5b) atmosphere using DMPO (5,5-dimethyl-1-pyrroline N -oxide) is shown. BNT in a liquid solution of methanol in argon atmosphere shows the formation of •OH radicals and •OOH radicals. These radicals are usually formed in the oxidation of water or methanol. Under oxygen atmosphere, the signal of superoxide radical was detected O₂^{•-}. The signal in both atmospheres (argon and oxygen) is produced immediately after illumination is started (1 min) and presented a saturation level before 13 min for Ar and 3 min for O₂. After this time, the signal decreases until keeping a stable evolution rate until the source is switched off.

Simultaneously, upon the generation, separation, and transport of charge carriers in BNT, e⁻/h⁺ pairs might participate in redox reactions via interfacial charge carrier transfer. In aqueous media, water layers adsorb, physically and chemically, on the BNT surface creating a BNT/H₂O interface. The photogenerated holes can react on the surface either with hydroxyl groups or with H₂O resulting in the formation of hydroxyl radicals, OH•. Therefore, not only h⁺ is produced by the photoexcitation of BNT but also hydroxyl radicals can be formed on hydrated BNT surfaces²⁰⁶.

6.4. Conclusion

Bi-based heterojunctions synthesized by high-energy ball milling do not show activity for H₂ evolution in the presence of sacrificial agents or electron scavengers. The charge carrier transfer and separation mechanism in these heterojunctions correspond to a type II heterojunction while the photogenerated electrons remain in the CB of β-Bi₂O₃. The potential of its conduction band $E_{CB} = -0.28$ V vs NHE (pH 7) is not negative enough for H₂ production H⁺/H₂ $E = -0.413$ V vs NHE (pH 7). The electrons do not react with any surface specie and the recombination of e⁻/h⁺ pairs increase generating the diminishing of photocatalytic activity. Moreover, the bismuth-based perovskite shows high photocatalytic performance for H₂ evolution with a small amount of Pt grafted on its surface to work as an electron scavenger. The EPR measurements elucidate the fate of photogenerated charge carriers and mechanism of the photocatalytic reactions. Bi_{0.5}Na_{0.5}TiO₃ is a potential catalyst to be applied in a wide variety of scenarios for environmental remediation.

Chapter 7: Summary and outlook

β - Bi_2O_3 with nanometric particle size, spherical morphology and narrow band gap energy was synthesized by a novel route using flame spray process. Semi-metallic bismuth in powder form was used as feedstock powder. A home-made set up powder collector was used to collect this sample that evaporates as an effect of the high temperature of the oxy-acetylene flame and the low boiling point of Bi_2O_3 . The semiconductor exhibits good photocatalytic activity for methanol oxidation, a model compound. The activity of the material is attributed to the high oxidative power of the holes in the valence band capable to oxidize water or methanol in presence of oxygen atmosphere.

A heterojunction of a metal/metal-oxide composition between Bi and β - Bi_2O_3 joined by a heterointerface was obtained in the first three stages of powder collection in the set-up device. The structural and microstructural analysis elucidate the formation of Janus particles with snowman-like and raspberry-like morphology composed of micrometric particles of β - Bi_2O_3 and deposited on the surface Bi smaller particles. The mechanism of oxidation remains in the high velocities obtained in flame spray and the temperature that reaches the in-flight particles as well the high cooling rates obtained in the as-sprayed powders due to the geometry and design of the powder collector. The heterojunction Bi/ β - Bi_2O_3 exhibits high photocatalytic performance for methanol oxidation compared with nanometric β - Bi_2O_3 . The heterointerface formed in these heterojunctions between a metal and a semiconductor generated an efficient charge carrier transfer and separation so bismuth work as an electron scavenger and the photogenerated holes remain in β - Bi_2O_3 to generated oxidation reactions (methanol oxidation).

The new synthesis route developed serve to synthesize a wide variety of metal oxides, composites, heterojunctions and other semiconductors by flame spray based on the oxidation reaction mechanism. The synthesis of a multi-heterojunction by flame spraying was achieved by using as feedstock powder a combination of semi-metallic bismuth and metallic copper to study the effect of the chemistry of the oxy-acetylene flame and evaluate the production efficiency of the process. The synthesis of Bi/ β - Bi_2O_3 /Cu/ Cu_2O was

Summary and outlook

obtained by flame spray and collected in the set-up powder collector. The phase composition of these heterojunction was obtained in the first three stages of the powder collector while in the last stage the formation of a highly pure nanometric β - Bi_2O_3 powder was obtained. $\text{Bi}/\beta\text{-Bi}_2\text{O}_3/\text{Cu}/\text{Cu}_2\text{O}$ heterojunction shows an enhanced activity for methanol photocatalytic oxidation compared to $\beta\text{-Bi}_2\text{O}_3$; besides, it was the only heterojunction that shows activity for H_2 evolution in presence of Pt as an electron scavenger and methanol as a hole scavenger. The morphology and chemical composition of the heterojunction is based on Janus particles with raspberry morphology that address that Bi and Cu are grafted on the surface and serve as electron scavenger which are assigned to the enhance of photocatalytic efficiency.

As a comparative study, different bismuth-based heterojunctions were synthesized by high energy ball milling route a simple, one-step and non-expensive process. $\beta\text{-Bi}_2\text{O}_3/\text{Cu}_2\text{O}$ heterojunction synthesized by high energy ball milling was characterized to study the effect of its structural, microstructural, and optical properties. Mechanical milling time and the amount of Cu_2O coupled to $\beta\text{-Bi}_2\text{O}_3$, generated structural defects, refinement of crystallite size and increase in tetragonality of $\beta\text{-Bi}_2\text{O}_3$ that generates a decrease on the band gap energy of the heterojunction to lower values and a decrease in the photorecombination in electron-hole pairs. These results and the characterization on the microstructural properties elucidate an efficient coupling between both semiconductors. Besides, this p-n semiconductor heterojunction shows high photocurrent density for water and methanol oxidation and oxygen reduction. The band edge potentials elucidate the possible charge carrier transfer where electrons remain in the CB of Cu_2O , and holes remain in the VB of Bi_2O_3 via direct Z-scheme.

Based on these results, three different Bi-based heterojunction was measure for the photocatalytic activity for methanol photooxidation in a black body reactor; $\beta\text{-Bi}_2\text{O}_3/\text{Cu}_2\text{O}$, $\beta\text{-Bi}_2\text{O}_3/\text{Bi}_{0.5}\text{Na}_{0.5}\text{TiO}_3$ and $\beta\text{-Bi}_2\text{O}_3/\text{ZnO}$. The determination of reaction rates (dn/dt) and quantum yields by chemical actinometry shows that $\beta\text{-Bi}_2\text{O}_3/\text{Bi}_{0.5}\text{Na}_{0.5}\text{TiO}_3$ present the higher activity for methanol oxidation under UV and visible light compared to $\beta\text{-Bi}_2\text{O}_3$. The staggered band alignment of the heterojunction between an n-type and p-type

semiconductors as well the chemical stability of both catalysts as well the position of the valence band and conduction band of both catalysts promotes the efficient charge carrier transfer and separation to promote the photocatalytic oxidation of methanol.

For the photocatalytic activity for H₂ evolution it was concluded that as-synthesized heterojunctions are not able to reduce protons since all electrons are transferred to the conduction band of β -Bi₂O₃. However, the bismuth-based perovskite Bi_{0.5}Na_{0.5}TiO₃ shows a remarkable activity in presence of sacrificial agents to work as electron and hole scavengers.

The research performed in this doctoral project elucidates the synthesis of a new family of bismuth-based heterojunctions with high photocatalytic activity for the oxidation of model compounds. The synthesis procedure plays a crucial role on the performance of the heterojunction. The efficient coupling between the semiconductor is one of the most relevant characteristics to promote the charge carrier transfer and separation in order to study the possible mechanisms of reactions.

Summary and outlook

Chapter 8:References

- (1) Barbir, F.; Veziroglu, T. N.; Plass, H. J. *Environmental Damage Due to Fossil Fuels Use*; 1990; Vol. 15.
- (2) Liu, L.; Cheng, S. Y.; Li, J. B.; Huang, Y. F. Mitigating Environmental Pollution and Impacts from Fossil Fuels: The Role of Alternative Fuels. *Energy Sources, Part A Recover. Util. Environ. Eff.* **2007**, *29* (12), 1069–1080. <https://doi.org/10.1080/15567030601003627>.
- (3) Rievaj, V.; Gaňa, J.; Synák, F. Is Hydrogen the Fuel of the Future? In *Transportation Research Procedia*; Elsevier B.V., 2019; Vol. 40, pp 469–474. <https://doi.org/10.1016/j.trpro.2019.07.068>.
- (4) Chen, X.; Shen, S.; Guo, L.; Mao, S. S. Semiconductor-Based Photocatalytic Hydrogen Generation. *Chem. Rev.* **2010**, *110* (11), 6503–6570. <https://doi.org/10.1021/cr1001645>.
- (5) Lee, J. S. Photocatalytic Water Splitting under Visible Light with Particulate Semiconductor Catalysts. *Catal. Surv. from Asia* **2005**, *9* (4), 217–227. <https://doi.org/10.1007/s10563-005-9157-0>.
- (6) Ahmad, H.; Kamarudin, S. K.; Minggu, L. J.; Kassim, M. Hydrogen from Photocatalytic Water Splitting Process: A Review. *Renew. Sustain. Energy Rev.* **2015**, *43*, 599–610. <https://doi.org/10.1016/j.rser.2014.10.101>.
- (7) Fujishima, A.; Honda, K. Electrochemical Photolysis of Water at a Semiconductor Electrode. *Nature* **1972**, *238* (5358), 37–38. <https://doi.org/10.1038/238037a0>.
- (8) Reddy, K. H.; Martha, S.; Parida, K. M. Facile Fabrication of Bi₂O₃/Bi–NaTaO₃ Photocatalysts for Hydrogen Generation under Visible Light Irradiation. *RSC Adv.* **2012**, *2* (25), 9423. <https://doi.org/10.1039/c2ra21083e>.
- (9) Walter, M. G.; Warren, E. L.; McKone, J. R.; Boettcher, S. W.; Mi, Q.; Santori, E. A.; Lewis, N. S. Solar Water Splitting Cells. *Chem. Rev.* **2010**, *110* (11), 6446–6473. <https://doi.org/10.1021/cr1002326>.
- (10) Maeda, K.; Domen, K. Photocatalytic Water Splitting: Recent Progress and Future Challenges. *J. Phys. Chem. Lett.* **2010**, *1* (18), 2655–2661. <https://doi.org/10.1021/jz1007966>.
- (11) Ismail, A. A.; Bahnemann, D. W. Photochemical Splitting of Water for Hydrogen Production by Photocatalysis: A Review. *Sol. Energy Mater. Sol. Cells* **2014**, *128*, 85–101. <https://doi.org/10.1016/j.solmat.2014.04.037>.
- (12) Pan, J.; Shen, S.; Zhou, W.; Tang, J.; Ding, H.; Wang, J.; Chen, L.; Au, C. T.; Yin, S. F. Recent Progress in Photocatalytic Hydrogen Evolution. *Wuli Huaxue Xuebao/Acta Phys. - Chim. Sin.* **2020**, *36* (3). <https://doi.org/10.3866/PKU.WHXB201905068>.
- (13) Lin, Y.; Yuan, G.; Liu, R.; Zhou, S.; Sheehan, S. W.; Wang, D. Semiconductor

References

- Nanostructure-Based Photoelectrochemical Water Splitting: A Brief Review. *Chem. Phys. Lett.* **2011**, *507* (4–6), 209–215. <https://doi.org/10.1016/j.cplett.2011.03.074>.
- (14) Martín, S. S.; Rivero, M. J.; Ortiz, I. Unravelling the Mechanisms That Drive the Performance of Photocatalytic Hydrogen Production. *Catalysts* **2020**, *10* (8), 1–27. <https://doi.org/10.3390/catal10080901>.
- (15) Schneider, J.; Bahnemann, D. W. Undesired Role of Sacrificial Reagents in Photocatalysis. *J. Phys. Chem. Lett.* **2013**, *4*, 3479–3483.
- (16) Kudo, A.; Miseki, Y. Heterogeneous Photocatalyst Materials for Water Splitting. *Chem. Soc. Rev.* **2009**, *38* (1), 253–278. <https://doi.org/10.1039/b800489g>.
- (17) Ni, M.; Leung, M. K. H.; Leung, D. Y. C.; Sumathy, K. A Review and Recent Developments in Photocatalytic Water-Splitting Using TiO₂ for Hydrogen Production. *Renew. Sustain. Energy Rev.* **2007**, *11* (3), 401–425. <https://doi.org/10.1016/j.rser.2005.01.009>.
- (18) Abe, R. Recent Progress on Photocatalytic and Photoelectrochemical Water Splitting under Visible Light Irradiation. *J. Photochem. Photobiol. C Photochem. Rev.* **2010**, *11* (4), 179–209. <https://doi.org/10.1016/j.jphotochemrev.2011.02.003>.
- (19) Ismail, A. A.; Bahnemann, D. W. Photochemical Splitting of Water for Hydrogen Production by Photocatalysis: A Review. *Sol. Energy Mater. Sol. Cells* **2014**, *128*, 85–101. <https://doi.org/10.1016/j.solmat.2014.04.037>.
- (20) Sayama, K.; Mukasa, K.; Abe, R.; Abe, Y.; Arakawa, H. Stoichiometric Water Splitting into H₂ and O₂ Using a Mixture of Two Different Photocatalysts and an IO₃⁻/I⁻ Shuttle Redox Mediator under Visible Light Irradiation. *Chem. Commun.* **2001**, *1* (23), 2416–2417. <https://doi.org/10.1039/b107673f>.
- (21) Abe, R.; Sayama, K.; Domen, K.; Arakawa, H. A New Type of Water Splitting System Composed of Two Different TiO. *Chem. Phys. Lett.* **2001**, *344* (August), 339–344.
- (22) Moniz, S. J. A.; Shevlin, S. A.; Martin, D. J.; Guo, Z. X.; Tang, J. Visible-Light Driven Heterojunction Photocatalysts for Water Splitting—a Critical Review. *Energy Environ. Sci.* **2015**, *8* (3), 731–759.
- (23) Schneider, J.; Matsuoka, M.; Takeuchi, M.; Zhang, J.; Horiuchi, Y.; Anpo, M.; Bahnemann, D. W. Understanding TiO₂ photocatalysis: Mechanisms and Materials. *Chem. Rev.* **2014**, *114* (19), 9919–9986. <https://doi.org/10.1021/cr5001892>.
- (24) Linsebigler, A. L.; Lu, G.; Yates, J. T. Photocatalysis on TiO₂ Surfaces: Principles, Mechanisms, and Selected Results. *Chem. Rev.* **1995**, *95* (3), 735–758. <https://doi.org/10.1021/cr00035a013>.
- (25) Jalalah, M.; Faisal, M.; Bouzid, H.; Park, J. G.; Al-Sayari, S. A.; Ismail, A. A. Comparative Study on Photocatalytic Performances of Crystalline α - and β -Bi₂O₃ Nanoparticles under Visible Light. *J. Ind. Eng. Chem.* **2015**, *30*, 183–189. <https://doi.org/10.1016/j.jiec.2015.05.020>.

- (26) Yang, K.; Li, J.; Peng, Y.; Lin, J. Enhanced Visible Light Photocatalysis over Pt-Loaded Separation, Transfer and Capture †. *Phys. Chem. Chem. Phys.* **2016**, *19*, 251–257. <https://doi.org/10.1039/C6CP06755G>.
- (27) Su, Q.; Li, Y.; Hu, R.; Song, F.; Liu, S.; Guo, C.; Zhu, S.; Liu, W.; Pan, J. Heterojunction Photocatalysts Based on 2D Materials: The Role of Configuration. *Adv. Sustain. Syst.* **2020**, *4* (9), 1–19. <https://doi.org/10.1002/adsu.202000130>.
- (28) Kudo, A.; Hiji, S. H₂ or O₂ Evolution from Aqueous Solutions on Layered Oxide Photocatalysts Consisting of Bi³⁺ with 6s² Configuration and D⁰ Transition Metal Ions. *Chemistry Letters*. 1999, pp 1103–1104. <https://doi.org/10.1246/cl.1999.1103>.
- (29) Zhao, H.; Tian, F.; Wang, R.; Chen, R. A Review on Bismuth-Related Nanomaterials for Photocatalysis. *Rev. Adv. Sci. Eng.* **2014**, *3* (1), 3–27.
- (30) Mehring, M. From Molecules to Bismuth Oxide-Based Materials: Potential Homo- and Heterometallic Precursors and Model Compounds. *Coord. Chem. Rev.* **2007**, *251* (7–8), 974–1006.
- (31) Fang, W.; Shangguan, W. A Review on Bismuth-Based Composite Oxides for Photocatalytic Hydrogen Generation. *Int. J. Hydrogen Energy* **2019**, *44* (2), 895–912. <https://doi.org/10.1016/j.ijhydene.2018.11.063>.
- (32) Lee, G.-J.; Zheng, Y.-C.; Wu, J. J. Fabrication of Hierarchical Bismuth Oxyhalides (BiOX, X = Cl, Br, I) Materials and Application of Photocatalytic Hydrogen Production from Water Splitting. *Catal. Today* **2018**, *307* (January 2017), 197–204. <https://doi.org/10.1016/j.cattod.2017.04.044>.
- (33) Deng, H. Y.; Hao, W. C.; Xu, H. Z. A Transition Phase in the Transformation from α -, β - And ϵ - to δ -Bismuth Oxide. *Chinese Phys. Lett.* **2011**, *28* (5), 3–6.
- (34) Selvamani, T.; Anandan, S.; Granone, L.; Bahnemann, D. W.; Ashokkumar, M. Phase-Controlled Synthesis of Bismuth Oxide Polymorphs for Photocatalytic Applications. *Mater. Chem. Front.* **2018**, *2* (9), 1664–1673. <https://doi.org/10.1039/c8qm00221e>.
- (35) Lei, B.; Cui, W.; Sheng, J.; Wang, H.; Chen, P.; Li, J.; Sun, Y.; Dong, F. Synergistic Effects of Crystal Structure and Oxygen Vacancy on Bi₂O₃ Polymorphs: Intermediates Activation, Photocatalytic Reaction Efficiency, and Conversion Pathway. *Sci. Bull.* **2020**, *65* (6), 467–476. <https://doi.org/10.1016/j.scib.2020.01.007>.
- (36) Pereira, A. L. J.; Gomis, O.; Sans, J. A.; Contreras-García, J.; Manjón, F. J.; Rodríguez-Hernández, P.; Muñoz, A.; Beltrán, A. β -Bi₂O₃ under Compression: Optical and Elastic Properties and Electron Density Topology Analysis. *Phys. Rev. B* **2016**, *93* (22), 1–13.
- (37) Zhang, J.; Dang, W.; Yan, X.; Li, M.; Gao, H.; Ao, Z. Doping Indium in β -Bi₂O₃ to Tune the Electronic Structure and Improve the Photocatalytic Activities: First-Principles Calculations and Experimental Investigation. *Phys. Chem. Chem. Phys.* **2014**, *16* (42), 23476–23482. <https://doi.org/10.1039/c4cp02656j>.

References

- (38) Diez, E.; Monnereau, O.; Tortet, L.; Vacquier, G.; Llewellyn, P.; Rouquerol, F. Synthesis of Bismuth (III) Oxide From Oxalate: A Study By Controlled Transformation Rate Thermal Analysis (Crta). *J. Optoelectronics Adv. Mater.* **2000**, *2* (5), 552–556.
- (39) Wang, C.; Shao, C.; Wang, L.; Zhang, L.; Li, X.; Liu, Y. Electrospinning Preparation, Characterization and Photocatalytic Properties of Bi₂O₃ Nanofibers. *J. Colloid Interface Sci.* **2009**, *333* (1), 242–248. <https://doi.org/10.1016/j.jcis.2008.12.077>.
- (40) Brezesinski, K.; Ostermann, R.; Hartmann, P.; Perlich, J.; Brezesinski, T. Exceptional Photocatalytic Activity of Ordered Mesoporous β -Bi₂O₃ Thin Films and Electrospun Nanofiber Mats. **2010**, No. 5, 3079–3085. <https://doi.org/10.1021/cm903780m>.
- (41) Ayekoe, P. Y.; Robert, D.; Lancine, D. Preparation of Effective TiO₂ / Bi₂O₃ Photocatalysts for Water Treatment. **2016**, 387–393. <https://doi.org/10.1007/s10311-016-0565-3>.
- (42) Jiang, H.-Y.; Li, P.; liu, G.; Ye, J.; Lin, J. Synthesis and Photocatalytic Properties of Metastable β -Bi₂O₃ Stabilized by Surface-Coordination Effects. *J. Mater. Chem. A* **2015**, *3* (9), 5119–5125. <https://doi.org/10.1039/C4TA06235C>.
- (43) Sun, Y.; Wang, W.; Zhang, L.; Zhang, Z. Design and Controllable Synthesis of a - / c -Bi₂O₃ Homojunction with Synergetic Effect on Photocatalytic Activity. *Chem. Eng. J.* **2012**, *211–212*, 161–167. <https://doi.org/10.1016/j.cej.2012.09.084>.
- (44) Sun, N.; Qu, Y.; Chen, S.; Yan, R.; Humayun, M.; Liu, Y.; Bai, L.; Jing, L.; Fu, H. Environmental Science Nano. *Environ. Sci. Nano* **2017**, *4*, 1147–1154. <https://doi.org/10.1039/C7EN00188F>.
- (45) Huang, Y.; Wang, W.; Zhang, Q.; Cao, J.; Huang, R.; Ho, W. In Situ Fabrication of α - Heterojunctions with Tunable Optical Property and Photocatalytic Activity. *Nat. Publ. Gr.* **2016**, No. November 2015, 1–9. <https://doi.org/10.1038/srep23435>.
- (46) Lakshmana Reddy, N.; Emin, S.; Valant, M.; Shankar, M. V. Nanostructured Bi₂O₃@TiO₂ photocatalyst for Enhanced Hydrogen Production. *Int. J. Hydrogen Energy* **2017**, *42* (10), 6627–6636. <https://doi.org/10.1016/j.ijhydene.2016.12.154>.
- (47) Xu, D.; Hai, Y.; Zhang, X.; Zhang, S.; He, R. Bi₂O₃ Cocatalyst Improving Photocatalytic Hydrogen Evolution Performance of TiO₂. *Appl. Surf. Sci.* **2017**, *400*, 530–536. <https://doi.org/10.1016/j.apsusc.2016.12.171>.
- (48) Li, C.; Zhang, J.; Liu, K. A New Method of Enhancing Photoelectrochemical Characteristics of Bi/Bi₂O₃ Electrode for Hydrogen Generation via Water Splitting. *Int. J. Electrochem. Sci.* **2012**, *7*, 5028–5034.
- (49) Hashimoto, T.; Ohta, H.; Nasu, H.; Ishihara, A. Preparation and Photocatalytic Activity of Porous Bi₂O₃ Polymorphisms. *Int. J. Hydrogen Energy* **2016**, *41* (18), 7388–7392. <https://doi.org/10.1016/j.ijhydene.2016.03.109>.
- (50) Shi, Y.; Luo, L.; Zhang, Y.; Chen, Y.; Wang, S.; Li, L.; Long, Y. Synthesis and

- Characterization of α / β -Bi₂O₃ with Enhanced Photocatalytic Activity for 17 α -Ethinylestradiol. *Ceram. Int.* **2017**, *43* (10), 7627–7635. <https://doi.org/10.1016/j.ceramint.2017.03.057>.
- (51) Li, R.; Chen, W.; Kobayashi, H.; Ma, C. Platinum-Nanoparticle-Loaded Bismuth Oxide: An Efficient Plasmonic Photocatalyst Active under Visible Light. *Green Chem.* **2010**, *12* (2), 212. <https://doi.org/10.1039/b917233e>.
- (52) Wang, Y.; Jiang, L.; Chen, J.; Liu, F.; Lai, Y. Realization of Nanostructured N-Doped p-Type Bi₂O₃ Thin Films. *Mater. Lett.* **2017**, *193*, 228–231. <https://doi.org/10.1016/j.matlet.2017.01.115>.
- (53) Han, M.; Sun, T.; Tan, P. Y.; Chen, X.; Tan, O. K.; Tse, M. S. M-BiVO₄@ γ -Bi₂O₃ Core–Shell p–n Heterogeneous Nanostructure for Enhanced Visible-Light Photocatalytic Performance. *RSC Adv.* **2013**, *3* (47), 24964. <https://doi.org/10.1039/c3ra42870b>.
- (54) Fan, H.; Li, H.; Liu, B.; Lu, Y.; Xie, T.; Wang, D. Photoinduced Charge Transfer Properties and Photocatalytic Activity in Bi₂O₃/BaTiO₃ Composite Photocatalyst. *ACS Appl. Mater. Interfaces* **2012**, *4* (9), 4853–4857. <https://doi.org/10.1021/am301199v>.
- (55) Ayekoe, P. Y.; Robert, D.; Goné, D. L. TiO₂/Bi₂O₃ Photocatalysts for Elimination of Water Contaminants. Part 1: Synthesis of α - and β -Bi₂O₃ Nanoparticles. *Environ. Chem. Lett.* **2015**, *13* (3), 327–332. <https://doi.org/10.1007/s10311-015-0505-7>.
- (56) Yi, S.; Yue, X.; Xu, D.; Liu, Z.; Zhao, F.; Wang, D.; Lin, Y. Properties and Enhanced Visible-Light. *New J. Chem.* **2015**, *39*, 2917–2924. <https://doi.org/10.1039/C4NJ01738B>.
- (57) Huang, T. J.; Huang, M. C.; Huang, M. S. Novel Methane Steam-Reforming Catalyst of Ni-Bi₂O₃/GDC to Reduce CO for Hydrogen Production. *Appl. Catal. A Gen.* **2009**, *354* (1–2), 127–131. <https://doi.org/10.1016/j.apcata.2008.11.020>.
- (58) Peng, Y.; Yan, M.; Chen, Q.-G.; Fan, C.-M.; Zhou, H.-Y.; Xu, A.-W. Novel One-Dimensional Bi₂O₃–Bi₂WO₆ p–n Hierarchical Heterojunction with Enhanced Photocatalytic Activity. *J. Mater. Chem. A* **2014**, *2* (22), 8517–8524. <https://doi.org/10.1039/C4TA00274A>.
- (59) Ayekoe, P. Y.; Robert, D.; Goné, D. L. Preparation of Effective TiO₂/Bi₂O₃ Photocatalysts for Water Treatment. *Environ. Chem. Lett.* **2016**, *14* (3), 387–393. <https://doi.org/10.1007/s10311-016-0565-3>.
- (60) Yi, S.; Yue, X.; Xu, D.; Liu, Z.; Zhao, F.; Wang, D.; Lin, Y. Study on Photogenerated Charge Transfer Properties and Enhanced Visible-Light Photocatalytic Activity of p-Type Bi₂O₃/n-Type ZnO Heterojunctions. *New J. Chem.* **2015**, *39* (4), 2917–2924. <https://doi.org/10.1039/c4nj01738b>.
- (61) Li, L.; Jiang, J.; Luan, X.; Feng, C.; Yang, Q.; Chen, M.; Zhang, M. One-Step Solid-State Synthesis of Cu₂O/Bi₂O₃ Nanocomposite at Room Temperature and Its Enhanced Photocatalytic Activity under Visible Light Irradiation. *J. Optoelectron.*

References

- Adv. Mater.* **2015**, *17* (3–4), 372–376.
- (62) Luo, Y.; Huang, Q.; Li, B.; Dong, L.; Fan, M.; Zhang, F. Synthesis and Characterization of Cu₂O-Modified Bi₂O₃ Nanospheres with Enhanced Visible Light Photocatalytic Activity. *Appl. Surf. Sci.* **2015**, *357*, 1072–1079. <https://doi.org/10.1016/j.apsusc.2015.09.126>.
- (63) Ke, J.; Zhao, C.; Zhou, H.; Duan, X.; Wang, S. Enhanced Solar Light Driven Activity of P-n Heterojunction for Water Oxidation Induced by Deposition of Cu₂O on Bi₂O₃ Microplates. *Sustain. Mater. Technol.* **2019**, *19*. <https://doi.org/10.1016/j.susmat.2018.e00088>.
- (64) Abdulkarem, A. M.; Aref, A. A.; Abdulhabeeb, A.; Li, Y. F.; Yu, Y. Synthesis of Bi₂O₃/Cu₂O Nanoflowers by Hydrothermal Method and Its Photocatalytic Activity Enhancement under Simulated Sunlight. *J. Alloys Compd.* **2013**, *560*, 132–141. <https://doi.org/10.1016/j.jallcom.2013.01.134>.
- (65) Kumar, A.; Police, R.; Vattikuti, S. V. P.; Kumar, K.; Chennaiahgari, M.; V, P. S. M.; Kumari, D.; Byon, C. Bismuth Oxide Cocatalyst and Copper Oxide Sensitizer in Cu₂O/TiO₂/Bi₂O₃ Ternary Photocatalyst for Efficient Hydrogen Production under Solar Light Irradiation. *Ceram. Int.* **2018**, *44* (10), 11783–11791. <https://doi.org/10.1016/j.ceramint.2018.03.262>.
- (66) Priya, B.; Raizada, P.; Singh, N.; Thakur, P.; Singh, P. Adsorptional Photocatalytic Mineralization of Oxytetracycline and Ampicillin Antibiotics Using Bi₂O₃/BiOCl Supported on Graphene Sand Composite and Chitosan. *J. Colloid Interface Sci.* **2016**, *479*, 271–283. <https://doi.org/10.1016/j.jcis.2016.06.067>.
- (67) Chu, L.; Zhang, J.; Wu, Z.; Wang, C.; Sun, Y.; Dong, S.; Sun, J. Solar-Driven Photocatalytic Removal of Organic Pollutants over Direct Z-Scheme Coral-Branch Shape Bi₂O₃/SnO₂ Composites. *Mater. Charact.* **2020**, *159* (November 2019), 110036. <https://doi.org/10.1016/j.matchar.2019.110036>.
- (68) Yan, Q.; Xie, X.; Liu, Y.; Wang, S.; Zhang, M.; Chen, Y.; Si, Y. Constructing a New Z-Scheme Multi-Heterojunction Photocatalysts Ag-AgI/BiOI-Bi₂O₃ with Enhanced Photocatalytic Activity. *J. Hazard. Mater.* **2019**, *371* (January), 304–315. <https://doi.org/10.1016/j.jhazmat.2019.03.031>.
- (69) Han, A.; Sun, J.; Chuah, G. K.; Jaenicke, S. Enhanced P-Cresol Photodegradation over BiOBr/Bi₂O₃ in the Presence of Rhodamine B. *RSC Adv.* **2017**, *7* (1), 145–152. <https://doi.org/10.1039/c6ra24852g>.
- (70) Ge, M.; Li, Y.; Liu, L.; Zhou, Z.; Chen, W. Bi₂O₃-Bi₂WO₆ Composite Microspheres: Hydrothermal Synthesis and Photocatalytic Performances. *J. Phys. Chem. C* **2011**, *115* (13), 5220–5225. <https://doi.org/10.1021/jp108414e>.
- (71) Komoda, M.; Shinohara, K.; Kondo, J. N.; Kondo, T.; Ikeda, S.; Tanaka, A.; Domen, K.; Hara, M. Cu₂O as a Photocatalyst for Overall Water Splitting under Visible Light Irradiation. *ChemInform* **2010**, *29* (25), no-no. <https://doi.org/10.1002/chin.199825027>.

- (72) Salomão, P. E. A.; Gomes, D. S.; Ferreira, E. J. C.; Moura, F.; Nascimento, L. L.; Patrocínio, A. O. T.; Pereira, M. C. Photoelectrochemical Hydrogen Production from Water Splitting Using Heterostructured Nanowire Arrays of Bi₂O₃/BiAl Oxides as a Photocathode. *Sol. Energy Mater. Sol. Cells* **2019**, *194*, 276–284.
- (73) Maruthamuthu, P.; Gurunathan, K.; Subramanian, E.; Sastri, M. V. C. Visible Light Induced Hydrogen Production with Cu(II) Bi₂O₃ and Pt/Bi₂O₃/RuO₂ from Aqueous Methyl Viologen Solution. **1993**, *18* (1), 9–13.
- (74) Žerjav, G.; Teržan, J.; Djinović, P.; Barbieriková, Z.; Hajdu, T.; Brezová, V.; Zavašnik, J.; Kovač, J.; Pintar, A. TiO₂-β-Bi₂O₃ Junction as a Leverage for the Visible-Light Activity of TiO₂ Based Catalyst Used for Environmental Applications. *Catal. Today* **2021**, *361* (August 2019), 165–175. <https://doi.org/10.1016/j.cattod.2020.03.053>.
- (75) Naik, B.; Martha, S.; Parida, K. M. Facile Fabrication of Bi₂O₃/TiO₂-XN_xnanocomposites for Excellent Visible Light Driven Photocatalytic Hydrogen Evolution. *Int. J. Hydrogen Energy* **2011**, *36* (4), 2794–2802. <https://doi.org/10.1016/j.ijhydene.2010.11.104>.
- (76) Li, M.; Li, F.; Yin, P. G. Tailoring the Band Structure of β-Bi₂O₃ by Co-Doping for Realized Photocatalytic Hydrogen Generation. *Chem. Phys. Lett.* **2014**, *601*, 92–97. <https://doi.org/10.1016/j.cplett.2014.03.091>.
- (77) Gurunathan, K. Photocatalytic Hydrogen Production Using Transition Metal Ions-Doped γ-Bi₂O₃ Semiconductor Particles. *Int. J. Hydrogen Energy* **2004**, *29* (9), 933–940. <https://doi.org/10.1016/j.ijhydene.2003.04.001>.
- (78) Fernandez-Benavides, D. A.; Gutierrez-Perez, A. I.; Benitez-Castro, A. M.; Ayala-Ayala, M. T.; Moreno-Murguía, B.; Muñoz-Saldaña, J. Comparative Study of Ferroelectric and Piezoelectric Properties of BNT-BKT-BT Ceramics near the Phase Transition Zone. *Materials (Basel)*. **2018**, *11* (3), 2–16.
- (79) Fernández-Benavides, D. A.; Cervera-Chiner, L.; Jiménez, Y.; de Fuentes, O. A.; Montoya, A.; Muñoz-Saldaña, J. A Novel Bismuth-Based Lead-Free Piezoelectric Transducer Immunosensor for Carbaryl Quantification. *Sensors Actuators, B Chem.* **2019**, *285* (January), 423–430.
- (80) Esquivel-Gaon, M.; Anguissola, S.; Garry, D.; Del, A.; Gallegos-Melgar, C.; Muñoz-Saldaña, J.; Dawson, K. A.; De Vizcaya-Ruiz, A.; Razo, L. M. Del. Bismuth-Based Nanoparticles as the Environmentally Friendly Replacement for Lead- Based Piezoelectrics. *R. Soc. Chem. Adv.* **2015**, *5*, 27295–27304. <https://doi.org/10.1039/c5ra02151k>.
- (81) Jardiel T.; Caballero, A. C.; Villegas, M. Aurivillius Ceramics: Bi₄Ti₃O₁₂-Based Piezoelectrics. *J. Ceram. Soc. Japan* **2008**, *116*, 511–518.
- (82) Malmros, G.; Fernholt, L.; Ballhausen, C. J.; Ragnarsson, U.; Rasmussen, S. E.; Sunde, E.; Sørensen, N. A. The Crystal Structure of Alpha-Bi₂O₂. *Acta Chemica Scandinavica*. 1970, pp 384–396. <https://doi.org/10.3891/acta.chem.scand.24-0384>.

References

- (83) H.A. Harwig. On the Structure of Bismuthsesquioxide: The Alpha, Beta, Gamma and Delta-Phase. *Z. anorg, allg. Chem.* **1978**, *444*, 151–166.
- (84) Cornei, N.; Tancret, N.; Abraham, F.; Mentré, O. New ε -Bi₂O₃ Metastable Polymorph. *Inorg. Chem.* **2006**, *45* (13), 4886–4888.
- (85) Gualtieri, A. F.; Immovilli, S.; Prudenziati, M. Powder X-Ray Diffraction Data for the New Polymorphic Compound ω -Bi₂O₃. *Powder Diffr.* **1997**, *12* (2), 90–92.
- (86) Ghedia, S.; Locherer, T.; Dinnebier, R.; Prasad, D. L. V. K.; Wedig, U.; Jansen, M. High-Pressure and High-Temperature Multianvil Synthesis of Metastable Polymorphs of Bi₂O₃: Crystal Structure and Electronic Properties. *Phys. Rev. B* **2010**, *82*, 1–12.
- (87) Pereira, A. L. J.; Sans, J. A.; Vilaplana, R.; Gomis, O.; Manjón, F. J.; Rodríguez-Hernández, P.; Muñoz, A.; Popescu, C.; Beltrán, A. Isostructural Second-Order Phase Transition of β -Bi₂O₃ at High Pressures: An Experimental and Theoretical Study. *J. Phys. Chem. C* **2014**, *118* (40), 23189–23201.
- (88) Meng, X.; Zhang, Z. Bismuth-Based Photocatalytic Semiconductors: Introduction, Challenges and Possible Approaches. *Journal Mol. Catal. A, Chem.* **2016**, *423*, 533–549.
- (89) Schlesinger, M.; Schulze, S.; Hietschold, M.; Mehring, M. Metastable β -Bi₂O₃ Nanoparticles with High Photocatalytic Activity from Polynuclear Bismuth Oxide Clusters. *Dalt. Trans.* **2013**, *42* (4), 1047–1056.
- (90) Liu, L.; Jiang, J.; Jin, S.; Xia, Z.; Tang, M. Hydrothermal Synthesis of β -Bismuth Oxide Nanowires from Particles. *CrystEngComm* **2011**, *13* (7), 2529–2532.
- (91) Wang, J.; Yang, X.; Zhao, K.; Xu, P.; Zong, L.; Yu, R.; Wang, D.; Deng, J.; Chen, J.; Xing, X. Precursor-Induced Fabrication of β -Bi₂O₃ Microspheres and Their Performance as Visible-Light-Driven Photocatalysts. *J. Mater. Chem. A* **2013**, *1* (32), 9069–9074.
- (92) Hu, H. X.; Qiu, K. Q.; Xu, G. F. Preparation of Nanometer δ - and β -Bismuth Trioxide by Vacuum Vapor-Phase Oxidation. *Trans. Nonferrous Met. Soc. China (English Ed.)* **2006**, *16* (1), 173–177.
- (93) Kumari, L.; Lin, J. H.; Ma, Y. R. Synthesis of Bismuth Oxide Nanostructures by an Oxidative Metal Vapour Phase Deposition Technique. *Nanotechnology* **2007**, *18* (29), 7pp.
- (94) Diez, E.; Monnereau, O.; Tortet, L.; Vacquier, G.; Llewellyn, P.; Rouquerol, F. Synthesis of Bismuth (III) Oxide from Oxalate: A Study by Controlled Transformation Rate Thermal Analysis (CRTA). *J. Optoelectron. Adv. Mater.* **2000**, *2* (5), 552–556.
- (95) Huang, Q.; Zhang, S.; Cai, C.; Zhou, B. β - and α -Bi₂O₃ Nanoparticles Synthesized via Microwave-Assisted Method and Their Photocatalytic Activity towards the Degradation of Rhodamine B. *Mater. Lett.* **2011**, *65* (6), 988–990. <https://doi.org/10.1016/j.matlet.2010.12.055>.

- (96) Hou, J.; Yang, C.; Wang, Z.; Zhou, W.; Jiao, S.; Zhu, H. In Situ Synthesis of α - β Phase Heterojunction on Bi₂O₃ Nanowires with Exceptional Visible-Light Photocatalytic Performance. *Appl. Catal. B Environ.* **2013**, *142–143*, 504–511. <https://doi.org/10.1016/j.apcatb.2013.05.050>.
- (97) Pawlowski, L. *The Science and Engineering of Thermal Spray Coatings*, John Wiley.; Sussex, England, 2008. <https://doi.org/10.1002/9780470754085>.
- (98) Fanicchia, F.; Axinte, D. A.; Kell, J.; McIntyre, R.; Brewster, G.; Norton, A. D. Combustion Flame Spray of CoNiCrAlY & YSZ Coatings. *Surf. Coatings Technol.* **2017**, *315*, 546–557. <https://doi.org/10.1016/j.surfcoat.2017.01.070>.
- (99) Harwig, H. A.; Gerards, A. G. The Polymorphism of Bismuth Sesquioxide. *Thermochim. Acta* **1979**, *28* (1), 121–131.
- (100) Harwig, H. A.; Weenk, J. W. Phase Relations in Bismuthsesquioxide. *ZAAC - J. Inorg. Gen. Chem.* **1978**, *444* (1), 167–177.
- (101) Naumov, A. V. World Market of Bismuth : A Review. *Metall. rare noble Met.* **2007**, *48* (1), 13–19.
- (102) Fauchais, P. L.; Heberlein, J. V. R.; Boulos, M. I. *Thermal Spray Fundamentals: From Powder to Part*, Springer.; New York, 2014. <https://doi.org/10.1007/978-0-387-68991-3>.
- (103) Toby, B. H.; Von Dreele, R. B. GSAS-II: The Genesis of a Modern Open-Source All Purpose Crystallography Software Package. *J. Appl. Crystallogr.* **2013**, *46* (2), 544–549.
- (104) Schneider, C. A.; Rasband, W. S.; Eliceiri, K. W. NIH Image to ImageJ: 25 Years of Image Analysis. *Nat. Methods* **2012**, *9* (7), 671–675.
- (105) Murphy, A. B. Band-Gap Determination from Diffuse Reflectance Measurements of Semiconductor Films, and Application to Photoelectrochemical Water-Splitting. *Sol. Energy Mater. Sol. Cells* **2007**, *91* (14), 1326–1337.
- (106) U. I. Gaya. *Heterogeneous Photocatalysis Using Inorganic Semiconductor Solids*; Springer, Ed.; Dordrecht, 2013.
- (107) Mou, F.; Chen, C.; Guan, J.; Chen, D. R.; Jing, H. Oppositely Charged Twin-Head Electropray: A General Strategy for Building Janus Particles with Controlled Structures. *Nanoscale* **2013**, *5* (5), 2055–2064.
- (108) Hu, J.; Zhou, S.; Sun, Y.; Fang, X.; Wu, L. Fabrication, Properties and Applications of Janus Particles. *Chem. Soc. Rev.* **2012**, *41* (11), 4356–4378.
- (109) Kim, M. W.; Joshi, B.; Samuel, E.; Kim, K.; Kim, Y. II; Kim, T. G.; Swihart, M. T.; Yoon, S. S. Highly Nanotextured β -Bi₂O₃ Pillars by Electrostatic Spray Deposition as Photoanodes for Solar Water Splitting. *J. Alloys Compd.* **2018**, *764*, 881–889.
- (110) Jiang, H. Y.; Cheng, K.; Lin, J. Crystalline Metallic Au Nanoparticle-Loaded α -Bi₂O₃ Microrods for Improved Photocatalysis. *Phys. Chem. Chem. Phys.* **2012**, *14* (35), 12114–12121.

References

- (111) Zhu, G.; Que, W.; Zhang, J. Synthesis and Photocatalytic Performance of Ag-Loaded β -Bi₂O₃ Microspheres under Visible Light Irradiation. *J. Alloys Compd.* **2011**, *509* (39), 9479–9486.
- (112) Yang, K.; Li, J.; Peng, Y.; Lin, J. Enhanced Visible Light Photocatalysis over Pt-Loaded Bi₂O₃: An Insight into Its Photogenerated Charge Separation, Transfer and Capture. *Phys. Chem. Chem. Phys.* **2017**, *19* (1), 251–257.
- (113) Ibhaddon, A. O.; Fitzpatrick, P. Heterogeneous Photocatalysis: Recent Advances and Applications. *Catalysts* **2013**, *3* (1), 189–218. <https://doi.org/10.3390/catal3010189>.
- (114) Xu, Q.; Zhang, L.; Yu, J.; Wageh, S.; Al-Ghamdi, A. A.; Jaroniec, M. Direct Z-Scheme Photocatalysts: Principles, Synthesis, and Applications. *Mater. Today* **2018**, *21* (10), 1042–1063. <https://doi.org/10.1016/j.mattod.2018.04.008>.
- (115) Marschall, R. Semiconductor Composites: Strategies for Enhancing Charge Carrier Separation to Improve Photocatalytic Activity. *Adv. Funct. Mater.* **2014**, *24* (17), 2421–2440. <https://doi.org/10.1002/adfm.201303214>.
- (116) Rhimi, B.; Wang, C.; Bahnemann, D. W. Latest Progress in G-C₃N₄ Based Heterojunctions for Hydrogen Production via Photocatalytic Water Splitting: A Mini Review. *J. Phys. Energy* **2021**, 0–25.
- (117) Qiu, Y.; Yang, M.; Fan, H.; Zuo, Y.; Shao, Y.; Xu, Y.; Yang, X.; Yang, S. Nanowires of α - And β -Bi₂O₃: Phase-Selective Synthesis and Application in Photocatalysis. *CrystEngComm* **2011**, *13* (6), 1843–1850. <https://doi.org/10.1039/c0ce00508h>.
- (118) Wang, J.; Yang, X.; Zhao, K.; Xu, P.; Zong, L.; Yu, R.; Wang, D.; Deng, J.; Chen, J.; Xing, X. Precursor-Induced Fabrication of β -Bi₂O₃ Microspheres and Their Performance as Visible-Light-Driven Photocatalysts. *J. Mater. Chem. A* **2013**, *1* (32), 9069–9074. <https://doi.org/10.1039/c3ta11652b>.
- (119) Xiao, X.; Hu, R.; Liu, C.; Xing, C.; Qian, C.; Zuo, X.; Nan, J.; Wang, L. Facile Large-Scale Synthesis of β -Bi₂O₃ Nanospheres as a Highly Efficient Photocatalyst for the Degradation of Acetaminophen under Visible Light Irradiation. *Appl. Catal. B Environ.* **2013**, *140–141*, 433–443. <https://doi.org/10.1016/j.apcatb.2013.04.037>.
- (120) Luévano-Hipólito, E.; Torres-Martínez, L. M.; Cantú-Castro, L. V. F. Self-Cleaning Coatings Based on Fly Ash and Bismuth-Photocatalysts: Bi₂O₃, Bi₂O₂CO₃, BiOI, BiVO₄, BiPO₄. *Constr. Build. Mater.* **2019**, *220*, 206–213. <https://doi.org/10.1016/j.conbuildmat.2019.06.030>.
- (121) Wang, F.; Cao, K.; Zhang, Q.; Gong, X.; Zhou, Y. A Computational Study on the Photoelectric Properties of Various Bi₂O₃ Polymorphs as Visible-Light Driven Photocatalysts. *J. Mol. Model.* **2014**, *20* (11), 1–6. <https://doi.org/10.1007/s00894-014-2506-z>.
- (122) Chen, L.; He, J.; Liu, Y.; Chen, P.; Au, C. T.; Yin, S. F. Recent Advances in Bismuth-Containing Photocatalysts with Heterojunctions. *Cuihua Xuebao/Chinese J. Catal.* **2016**, *37* (6), 780–791. [https://doi.org/10.1016/S1872-2067\(15\)61061-0](https://doi.org/10.1016/S1872-2067(15)61061-0).

- (123) French, M.; Schwartz, R.; Stolz, H.; Redmer, R. Electronic Band Structure of Cu₂O by Spindensity Functional Theory. *J. Phys. Condens. Matter* **2009**, *21* (1), 19–23. <https://doi.org/10.1088/0953-8984/21/1/015502>.
- (124) Tachibana, Y.; Muramoto, R. Photoelectrochemistry of P-Type Cu₂O Semiconductor. **2006**, *32* (5), 575–583.
- (125) Ho, W. C. J.; Tay, Q.; Qi, H.; Huang, Z.; Li, J.; Chen, Z. Photocatalytic and Adsorption Performances of Faceted Cuprous Oxide (Cu₂O) Particles for the Removal of Methyl Orange (MO) from Aqueous Media. *Molecules* **2017**, *22* (4). <https://doi.org/10.3390/molecules22040677>.
- (126) Ayala-Ayala, M. T.; Ferrer-Pacheco, M. Y.; Muñoz-Saldaña, J. Manufacturing of Photoactive β-Bismuth Oxide by Flame Spray Oxidation. *J. Therm. Spray Technol.* **2021**, *30* (4), 1107–1119. <https://doi.org/10.1007/s11666-021-01182-2>.
- (127) Peppiaatt, S. J. The Melting of Small Particles. II. Bismuth. *Proc. R. Soc. London. A. Math. Phys. Sci.* **1975**, *345* (1642), 401–412. <https://doi.org/10.1098/rspa.1975.0145>.
- (128) Brand, H.; Dobson, D. P.; Voadlo, L.; Wood, I. G. Melting Curve of Copper Measured to 16 GPa Using a Multi-Anvil Press. *High Press. Res.* **2006**, *26* (3), 185–191. <https://doi.org/10.1080/08957950600873089>.
- (129) Károly, Z.; Szépvölgyi, J.; Trichet, A.; Lemoigne, A. Behavior of Silica Particles of Different Microstructure on RF Thermal Plasma Treatment. *J. Mater. Sci. Lett.* **2002**, *21* (24), 1943–1945.
- (130) Hossain, K. M. Z.; Patel, U.; Ahmed, I. Development of Microspheres for Biomedical Applications: A Review. *Prog. Biomater.* **2015**, *4* (1), 1–19. <https://doi.org/10.1007/s40204-014-0033-8>.
- (131) Grass, R. N.; Stark, W. J. Flame Spray Synthesis under a Non-Oxidizing Atmosphere: Preparation of Metallic Bismuth Nanoparticles and Nanocrystalline Bulk Bismuth Metal. *J. Nanoparticle Res.* **2006**, *8* (5), 729–736. <https://doi.org/10.1007/s11051-006-9097-2>.
- (132) Mädler, L.; Pratsinis, S. E. Bismuth Oxide Nanoparticles by Flame Spray Pyrolysis. *J. Am. Ceram. Soc.* **2002**, *85* (7), 1713–1718. <https://doi.org/10.1111/j.1151-2916.2002.tb00340.x>.
- (133) Azhar, N. S.; Taib, M. F. M.; Hassan, O. H.; Yahya, M. Z. A.; Ali, A. M. M. Structural, Electronic and Optical Properties of Bi₂O₃ Polymorphs by First-Principles Calculations for Photocatalytic Water Splitting. *Mater. Res. Express* **2017**, *4* (3), 034002. <https://doi.org/10.1088/2053-1591/aa5f67>.
- (134) Tauc, J.; Grigorovivi, R.; Vancu, A. Optical Properties and Electronic Structure of CaO. *Phys. Stat. Sol.* **1966**, *15*, 627–637. <https://doi.org/10.1007/s10812-016-0329-7>.
- (135) Nash, T. The Colorimetric Estimation of Formaldehyde by Means of the Hantzsch Reaction. *Biochem. J.* **1953**, *55* (3), 416–421. <https://doi.org/10.1042/bj0550416>.

References

- (136) Chauhan, A.; Rastogi, M.; Scheier, P.; Bowen, C.; Kumar, R. V.; Vaish, R. Janus Nanostructures for Heterogeneous Photocatalysis. *Appl. Phys. Rev.* **2018**, *5* (4). <https://doi.org/10.1063/1.5039926>.
- (137) Perro, A.; Reculosa, S.; Ravaine, S.; Bourgeat-Lami, E.; Duguet, E. Design and Synthesis of Janus Micro- and Nanoparticles. *J. Mater. Chem.* **2005**, *15* (35–36), 3745–3760. <https://doi.org/10.1039/b505099e>.
- (138) Soga, T. Applied Sciences Study of Annealing Temperature Effect on the Photovoltaic Performance of BiOI-Based Materials. **2019**.
- (139) Ayhan, Y. S.; Buyukaksoy, A. Impact of Fabrication Temperature on the Stability of Yttria Doped Bismuth Oxide Ceramics. *Solid State Ionics* **2019**, *338* (December 2018), 66–73. <https://doi.org/10.1016/j.ssi.2019.05.013>.
- (140) Zou, J.; Yu, Z. Solar Energy Materials and Solar Cells Yellow β -Bi₂O₃/BaCO₃ Complex Pigments with Impressive near Infrared Reflectance and Excellent Color Performance. *Sol. Energy Mater. Sol. Cells* **2019**, *199* (April), 99–107. <https://doi.org/10.1016/j.solmat.2019.04.031>.
- (141) Zheng, H.; Nian, H.; Xia, J.; Zhou, G.; Jiang, D.; Li, Q. Bi/Bi₂O₃ Sensor for Quantitation of Dissolved Oxygen in Molten Salts. *J. Adv. Ceram.* **2018**, *7* (1), 1–4. <https://doi.org/10.1007/s40145-017-0250-4>.
- (142) Zhao, J.; Li, Z.; Shen, T.; Yuan, X.; Qiu, G.; Jiang, Q.; Lin, Y.; Song, G.; Meng, A.; Li, Q. Immobilized on N-Doped Graphene Nanotubes as Robust Electrode Materials for High-Energy. **2019**, 7918–7931. <https://doi.org/10.1039/c8ta11953h>.
- (143) Xavier, F. F. S.; Bruziquesi, C. G. O.; Fagundes, W. S.; Matsubara, E. Y.; Rosolen, J. M.; Silva, A. C.; Canobre, S. C.; Amaral, F. A. New Synthesis Method for a Core-Shell Composite Banded on Alpha-Bi₂O₃@PPy and Its Electrochemical Behavior as Supercapacitor Electrode. **2019**, *30* (4), 727–735.
- (144) Yu, D.; Zhao, M.; Wang, C.; Wang, L.; Gai, Z.; Wang, C.; Zhang, J.; Li, J. Amorphous Phases and Composition Dependence of Piezoelectricity in BaTiO₃-Bi₂O₃ Polar Amorphous Ceramics. *Ceram. Int.* **2016**, *42* (1), 1777–1781. <https://doi.org/10.1016/j.ceramint.2015.09.140>.
- (145) Reyes, L.; Kassab, P.; Eiji, M.; Silverio, D.; Alexandre, T.; Assumpção, A. De; Fedorchuk, A. O.; Plucinski, K. J. Laser Stimulated Piezoelectricity in Er³⁺ Doped GeO₂-Bi₂O₃ Glasses Containing Silicon Nanocrystals. *Opt. Mater. (Amst.)* **2014**, *38*, 28–32. <https://doi.org/10.1016/j.optmat.2014.09.025>.
- (146) Wu, Y.; Huang, Y.; Yang, H. Performance of Vanadium-Modified Bismuth Oxide. *CrystEngComm* **2016**, *18*, 6881–6888. <https://doi.org/10.1039/C6CE00954A>.
- (147) Wang, Y.; Wen, Y.; Ding, H. Improved Structural Stability of Titanium-Doped β -Bi₂O₃ during Visible-Light-Activated Photocatalytic Processes. **2010**, 1385–1392. <https://doi.org/10.1007/s10853-009-4096-1>.
- (148) Hameed, A.; Montini, T.; Gombac, V.; Fornasiero, P. Surface Phases and Photocatalytic Activity Correlation of Bi₂O₃/Bi₂O_{4-x} Nanocomposite. *J. Am.*

- Chem. Soc.* **2008**, *130* (30), 9658–9659. <https://doi.org/10.1021/ja803603y>.
- (149) Protasova, L. N.; de Croon, M. H. J. M.; Hessel, V. Review of Patent Publications from 1990 to 2010 on Catalytic Coatings on Different Substrates, Including Microstructured Channels: Preparation, Deposition Techniques, Applications. *Recent Patents Chem. Eng.* **2012**, *5* (1), 28–44. <https://doi.org/10.2174/1874478811205010028>.
- (150) Saison, T.; Chemin, N.; Chanéac, C.; Durupthy, O.; Ruaux, V.; Mariey, L.; Maugé, F.; Beaunier, P.; Jolivet, J.-P. Bi₂O₃, BiVO₄, and Bi₂WO₆: Impact of Surface Properties on Photocatalytic Activity under Visible Light. *J. Phys. Chem. C* **2011**, *115* (13), 5657–5666. <https://doi.org/10.1021/jp109134z>.
- (151) Shi, Y.; Luo, L.; Zhang, Y.; Chen, Y.; Wang, S.; Li, L.; Long, Y.; Jiang, F. Synthesis and Characterization of α/β -Bi₂O₃ with Enhanced Photocatalytic Activity for 17 α -Ethinylestradiol. *Ceram. Int.* **2017**, *43* (10), 7627–7635. <https://doi.org/10.1016/j.ceramint.2017.03.057>.
- (152) Sun, Y.; Wang, W.; Zhang, L.; Zhang, Z. Design and Controllable Synthesis of α/γ -Bi₂O₃ homojunction with Synergetic Effect on Photocatalytic Activity. *Chem. Eng. J.* **2012**, *211–212*, 161–167. <https://doi.org/10.1016/j.cej.2012.09.084>.
- (153) Selvamani, T.; Anandan, S.; Granone, L. MATERIALS CHEMISTRY FRONTIERS Phase-Controlled Synthesis of Bismuth Oxide Polymorphs for Photocatalytic Applications †. **2018**, 1664–1673. <https://doi.org/10.1039/c8qm00221e>.
- (154) Walsh, A.; Watson, G. W.; Payne, D. J.; Edgell, R. G.; Guo, J.; Glans, P. A.; Learmonth, T.; Smith, K. E. Electronic Structure of the α and δ Phases of Bi₂O₃: A Combined Ab Initio and x-Ray Spectroscopy Study. *Phys. Rev. B - Condens. Matter Mater. Phys.* **2006**, *73* (23), 1–13. <https://doi.org/10.1103/PhysRevB.73.235104>.
- (155) Punn, R.; Feteira, A. M.; Sinclair, D. C.; Greaves, C. Enhanced Oxide Ion Conductivity in Stabilized δ -Bi₂O₃. *J. Am. Chem. Soc.* **2006**, *128* (48), 15386–15387. <https://doi.org/10.1021/ja065961d>.
- (156) Boyapati, S.; Wachsman, E. D.; Jiang, N. Effect of Oxygen Sublattice Ordering on Interstitial Transport Mechanism and Conductivity Activation Energies in Phase-Stabilized Cubic Bismuth Oxides. *Solid State Ionics* **2001**, *140* (1–2), 149–160. [https://doi.org/10.1016/S0167-2738\(01\)00698-1](https://doi.org/10.1016/S0167-2738(01)00698-1).
- (157) Du, H.; Liu, D.; Tang, F.; Zhu, D.; Zhou, W.; Qu, S. Microstructure, Piezoelectric, and Ferroelectric Properties of Bi₂O₃-Added (K_{0.5}Na_{0.5})NbO₃ Lead-Free Ceramics. *J. Am. Ceram. Soc.* **2007**, *90* (9), 2824–2829. <https://doi.org/10.1111/j.1551-2916.2007.01846.x>.
- (158) Wang, L.; Wang, W. Photocatalytic Hydrogen Production from Aqueous Solutions over Novel Bi_{0.5}Na_{0.5}TiO₃ microspheres. *Int. J. Hydrogen Energy* **2012**, *37* (4), 3041–3047. <https://doi.org/10.1016/j.ijhydene.2011.10.105>.
- (159) Selvamani, T.; Anandan, S.; Granone, L.; Bahnemann, D. W.; Ashokkumar, M. Phase-Controlled Synthesis of Bismuth Oxide Polymorphs for Photocatalytic

References

- Applications. *Mater. Chem. Front.* **2018**, 2 (9), 1664–1673.
- (160) Yang, H. A Short Review on Heterojunction Photocatalysts: Carrier Transfer Behavior and Photocatalytic Mechanisms. *Mater. Res. Bull.* **2021**, 142 (May), 111406. <https://doi.org/10.1016/j.materresbull.2021.111406>.
- (161) Rodríguez-Carvajal, J. Recent Advances in Magnetic Structure Determination by Neutron Powder Diffraction. *Phys. B Phys. Condens. Matter* **1993**, 192 (1–2), 55–69. [https://doi.org/10.1016/0921-4526\(93\)90108-I](https://doi.org/10.1016/0921-4526(93)90108-I).
- (162) Blower, S. K.; Greaves, C. The Structure of $\beta\text{-Bi}_2\text{O}_3$ from Powder Neutron Diffraction Data. *Acta Crystallogr. Sect. C* **1988**, 44 (4), 587–589. <https://doi.org/10.1107/S0108270187011661>.
- (163) Kirfel, A.; Eichhorn, K. Accurate Structure Analysis with Synchrotron Radiation. The Electron Density in Al_2O_3 and Cu_2O . *Acta Crystallogr. Sect. A* **1990**, 46 (4), 271–284. <https://doi.org/10.1107/S0108767389012596>.
- (164) Peter, L. M. Photoelectrochemistry: From Basic Principles to Photocatalysis. In *Photocatalysis: Fundamentals and perspectives*; 2016; pp 1–28. <https://doi.org/10.1039/9781782620419-00001>.
- (165) Ismail, A. A.; Bahnemann, D. W. Solar Energy Materials & Solar Cells Photochemical Splitting of Water for Hydrogen Production by Photocatalysis: A Review. *Sol. Energy Mater. Sol. Cells* **2014**, 128, 85–101. <https://doi.org/10.1016/j.solmat.2014.04.037>.
- (166) Bebb, H. B.; Williams, E. W. Photoluminescence I: Theory. *Semicond. Semimetals* **1972**, 8 (C), 181–320. [https://doi.org/10.1016/S0080-8784\(08\)62345-5](https://doi.org/10.1016/S0080-8784(08)62345-5).
- (167) Schmidt, S.; Kubaski, E. T.; Volanti, D. P.; Sequinel, T.; Bezzon, V. D. N.; Beltrán, A.; Tebcherani, S. M.; Varela, J. A. Effect of Pressure-Assisted Heat Treatment on Photoluminescence Emission of $\alpha\text{-Bi}_2\text{O}_3$ Needles. *Inorg. Chem.* **2015**, 54 (21), 10184–10191. <https://doi.org/10.1021/acs.inorgchem.5b01237>.
- (168) Schmidt, S.; Kubaski, E. T.; Li, M. S.; Bezzon, V. D. N.; Sequinel, T.; Tebcherani, S. M. Blue or Red Photoluminescence Emission in $\alpha\text{-Bi}_2\text{O}_3$ Needles: Effect of Synthesis Method. *Luminescence* **2018**, 33 (7), 1281–1287. <https://doi.org/10.1002/bio.3547>.
- (169) Solache-Carranco, H.; Juárez-Díaz, G.; Esparza-García, A.; Briseño-García, M.; Galván-Arellano, M.; Martínez-Juárez, J.; Romero-Paredes, G.; Peña-Sierra, R. Photoluminescence and X-Ray Diffraction Studies on Cu_2O . *J. Lumin.* **2009**, 129 (12), 1483–1487. <https://doi.org/10.1016/j.jlumin.2009.02.033>.
- (170) Luo, J.; Steier, L.; Son, M. K.; Schreier, M.; Mayer, M. T.; Grätzel, M. Cu_2O Nanowire Photocathodes for Efficient and Durable Solar Water Splitting. *Nano Lett.* **2016**, 16 (3), 1848–1857. <https://doi.org/10.1021/acs.nanolett.5b04929>.
- (171) Suryanarayana, C. Mechanical Alloying and Milling. *Prog. Mater. Sci.* **2001**, 46, 1–184. <https://doi.org/10.4150/kpmi.2006.13.5.371>.

- (172) Wu, L.; Tsui, L. K.; Swami, N.; Zangari, G. Photoelectrochemical Stability of Electrodeposited Cu₂O Films. *J. Phys. Chem. C* **2010**, *114* (26), 11551–11556. <https://doi.org/10.1021/jp103437y>.
- (173) Vivier, V.; Régis, A.; Sagon, G.; Nedelec, J. Y.; Yu, L. T.; Cachet-Vivier, C. Cyclic Voltammetry Study of Bismuth Oxide Bi₂O₃ Powder by Means of a Cavity Microelectrode Coupled with Raman Microspectrometry. *Electrochim. Acta* **2001**, *46* (6), 907–914. [https://doi.org/10.1016/S0013-4686\(00\)00677-0](https://doi.org/10.1016/S0013-4686(00)00677-0).
- (174) Hoffmann, M. R.; Martin, S. T.; Choi, W.; Bahnemann, D. W. Environmental Applications of Semiconductor Photocatalysis. *Chem. Rev.* **1995**, *95* (1), 69–96. <https://doi.org/10.1021/cr00033a004>.
- (175) Laidler, K. J. A Glossary of Terms Used in Chemical Kinetics, Including Reaction Dynamics (IUPAC Recommendations 1996). *Pure Appl. Chem.* **1996**, *68* (1), 149–192. <https://doi.org/10.1351/pac199668010149>.
- (176) Kisch, H.; Bahnemann, D. Best Practice in Photocatalysis: Comparing Rates or Apparent Quantum Yields? *J. Phys. Chem. Lett.* **2015**, *6* (10), 1907–1910. <https://doi.org/10.1021/acs.jpcclett.5b00521>.
- (177) Emeline, A. V.; Zhang, X.; Jin, M.; Murakami, T.; Fujishima, A. Application of a “Black Body” like Reactor for Measurements of Quantum Yields of Photochemical Reactions in Heterogeneous Systems. *J. Phys. Chem. B* **2006**, *110* (14), 7409–7413. <https://doi.org/10.1021/jp057115f>.
- (178) Megatiff, L.; Dillert, R.; Bahnemann, D. W. Reaction Rate Study of the Photocatalytic Degradation of Dichloroacetic Acid in a Black Body Reactor. *Catalysts* **2019**, *9* (8), 1–17. <https://doi.org/10.3390/catal9080635>.
- (179) Megatiff, L.; Dillert, R.; Bahnemann, D. W. A Method to Compare the Activities of Semiconductor Photocatalysts in Liquid–Solid Systems. *ChemPhotoChem* **2018**, *2* (11), 948–951. <https://doi.org/10.1002/cptc.201800134>.
- (180) Hatchard, C. G.; Parker, C. A. A New Sensitive Chemical Actinometer II. Potassium Ferrioxalate as a Standard Chemical Actinometer. *Proc. R. Soc. London. Ser. A. Math. Phys. Sci.* **1956**, *235* (1203), 518–536. <https://doi.org/10.1098/rspa.1956.0102>.
- (181) Megatiff, L.; Dillert, R.; Bahnemann, D. W. Determination of the Quantum Yield of a Heterogeneous Photocatalytic Reaction Employing a Black Body Photoreactor. *Catal. Today* **2020**, *355* (June), 698–703. <https://doi.org/10.1016/j.cattod.2019.06.008>.
- (182) Maeda, K. New Materials for Water Splitting. In *Photocatalysis: Fundamentals and perspectives*; The Royal Society of Chemistry, 2016; pp 295–317. <https://doi.org/10.1039/9781782620419-00295>.
- (183) Ahmed, A. Y.; Kandiel, T. A.; Oekermann, T.; Günnemann, C.; Bahnemann, D. Mechanistic Investigations of Photoelectrochemical Water and Methanol Oxidation on Well-Defined TiO₂ Anatase (101) and Rutile (110) Surfaces. *ACS Appl. Energy Mater.* **2019**, *2* (7), 5308–5318. <https://doi.org/10.1021/acsaem.9b01163>.

References

- (184) Wang, C.; Groenzin, H.; Shultz, M. J. Direct Observation of Competitive Adsorption between Methanol and Water on TiO₂: An in Situ Sum-Frequency Generation Study. *JACS Commun.* **2004**, *126*, 8094–8095.
- (185) Bousquet, M.; Duclère, J. R.; Orhan, E.; Boule, A.; Bachelet, C.; Champeaux, C. Optical Properties of an Epitaxial Na_{0.5}Bi_{0.5}TiO₃ Thin Film Grown by Laser Ablation: Experimental Approach and Density Functional Theory Calculations. *J. Appl. Phys.* **2010**, *107* (10), 1–13. <https://doi.org/10.1063/1.3400095>.
- (186) M, S. S.; Bose, L.; Kc, G. Optical Properties of ZnO Nanoparticles. **2009**, *XVI* (1), 57–65.
- (187) Zhao, Z.; Wei, L.; Li, S.; Zhu, L.; Su, Y.; Liu, Y.; Bu, Y.; Lin, Y.; Liu, W.; Zhang, Z. Exclusive Enhancement of Catalytic Activity in Bi_{0.5}Na_{0.5}TiO₃ nanostructures: New Insights into the Design of Efficient Piezocatalysts and Piezo-Photocatalysts. *J. Mater. Chem. A* **2020**, *8* (32), 16238–16245. <https://doi.org/10.1039/c9ta14007g>.
- (188) Ramírez-Ortega, D.; Meléndez, A. M.; Acevedo-Peña, P.; González, I.; Arroyo, R. Semiconducting Properties of ZnO/TiO₂ Composites by Electrochemical Measurements and Their Relationship with Photocatalytic Activity. *Electrochim. Acta* **2014**, *140*, 541–549. <https://doi.org/10.1016/j.electacta.2014.06.060>.
- (189) Minami, T.; Miyata, T.; Nishi, Y. Cu₂O-Based Heterojunction Solar Cells with an Al-Doped ZnO/Oxide Semiconductor/Thermally Oxidized Cu₂O Sheet Structure. *Sol. Energy* **2014**, *105*, 206–217. <https://doi.org/10.1016/j.solener.2014.03.036>.
- (190) Beranek, R. (Photo)Electrochemical Methods for the Determination of the Band Edge Positions of TiO₂-Based Nanomaterials. *Adv. Phys. Chem.* **2011**, *2011* (Iv), 80–83. <https://doi.org/10.1155/2011/786759>.
- (191) Wang, C. Y.; Pagel, R.; Bahnemann, D. W.; Dohrmann, J. K. Quantum Yield of Formaldehyde Formation in the Presence of Colloidal TiO₂-Based Photocatalysts: Effect of Intermittent Illumination, Platinization, and Deoxygenation. *J. Phys. Chem. B* **2004**, *108* (37), 14082–14092. <https://doi.org/10.1021/jp048046s>.
- (192) Ilan, Y. A.; Czapski, G.; Meisel, D. The One-Electron Transfer Redox Potentials of Free Radicals. I. The Oxygen/Superoxide System. *Biochim. Biophys. Acta* **1976**, *430* (2), 209–224. [https://doi.org/10.1016/0005-2728\(76\)90080-3](https://doi.org/10.1016/0005-2728(76)90080-3).
- (193) Can, E.; Yildirim, R. Data Mining in Photocatalytic Water Splitting over Perovskites Literature for Higher Hydrogen Production. *Appl. Catal. B Environ.* **2019**, *242* (August 2018), 267–283. <https://doi.org/10.1016/j.apcatb.2018.09.104>.
- (194) Kuhn, H. J.; Braslavsky, S. E.; Schmidt, R. Chemical Actinometry (IUPAC Technical Report). *Pure Appl. Chem.* **2004**, *76* (12), 2105–2146. <https://doi.org/10.1351/pac200476122105>.
- (195) Roibu, A.; Fransen, S.; Leblebici, M. E.; Meir, G.; Van Gerven, T.; Kuhn, S. An Accessible Visible-Light Actinometer for the Determination of Photon Flux and Optical Pathlength in Flow Photo Microreactors. *Sci. Rep.* **2018**, *8* (1), 1–10. <https://doi.org/10.1038/s41598-018-23735-2>.

- (196) Serpone, N.; Salinaro, A. Terminology, Relative Photonic Efficiencies and Quantum Yields in Heterogeneous Photocatalysis. Part I: Suggested Protocol (Technical Report). *Pure Appl. Chem.* **1999**, *71* (2), 303–320. <https://doi.org/10.1351/pac199971020303>.
- (197) Sakthivel, S.; Shankar, M. V.; Palanichamy, M.; Arabindoo, B.; Bahnemann, D. W.; Murugesan, V. Enhancement of Photocatalytic Activity by Metal Deposition: Characterisation and Photonic Efficiency of Pt, Au and Pd Deposited on TiO₂ Catalyst. *Water Res.* **2004**, *38* (13), 3001–3008. <https://doi.org/10.1016/j.watres.2004.04.046>.
- (198) Polliotto, V.; Livraghi, S.; Giamello, E. Electron Magnetic Resonance as a Tool to Monitor Charge Separation and Reactivity in Photocatalytic Materials. *Res. Chem. Intermed.* **2018**, *44* (7), 3905–3921. <https://doi.org/10.1007/s11164-018-3467-0>.
- (199) Qian, R.; Zong, H.; Schneider, J.; Zhou, G.; Zhao, T.; Li, Y.; Yang, J.; Bahnemann, D. W.; Pan, J. H. Charge Carrier Trapping, Recombination and Transfer during TiO₂ Photocatalysis: An Overview. *Catal. Today* **2019**, *335* (September 2018), 78–90. <https://doi.org/10.1016/j.cattod.2018.10.053>.
- (200) Balayeva, N. O.; Zheng, N.; Dillert, R.; Bahnemann, D. W. Visible-Light-Mediated Photocatalytic Aerobic Dehydrogenation of N-Heterocycles by Surface-Grafted TiO₂ and 4-Amino-TEMPO. *ACS Catal.* **2019**, 10694–10704. <https://doi.org/10.1021/acscatal.9b03322>.
- (201) Reusch, W. Spectroscopy.
- (202) Wenderich, K.; Mul, G. Methods, Mechanism, and Applications of Photodeposition in Photocatalysis: A Review. *Chem. Rev.* **2016**, *116* (23), 14587–14619. <https://doi.org/10.1021/acs.chemrev.6b00327>.
- (203) Di Mauro, A.; Fragalà, M. E.; Privitera, V.; Impellizzeri, G. ZnO for Application in Photocatalysis: From Thin Films to Nanostructures. *Materials Science in Semiconductor Processing*. Elsevier Ltd October 1, 2017, pp 44–51. <https://doi.org/10.1016/j.mssp.2017.03.029>.
- (204) AlSalka, Y.; Hakki, A.; Schneider, J.; Bahnemann, D. W. Co-Catalyst-Free Photocatalytic Hydrogen Evolution on TiO₂: Synthesis of Optimized Photocatalyst through Statistical Material Science. *Appl. Catal. B Environ.* **2018**, *238*, 422–433. <https://doi.org/10.1016/j.apcatb.2018.07.045>.
- (205) Zhu, K.; Song, B.; Ge, G.; Lin, J. F.; Yan, F.; Xu, L.; Yan, H.; Shen, B.; Zhai, J.; Chou, X. Construction of Multi-Domain Coexistence Enhanced Piezoelectric Properties of Bi_{0.5}Na_{0.5}TiO₃-Based Thin Films. *J. Eur. Ceram. Soc.* **2021**, *41* (13), 6456–6464. <https://doi.org/10.1016/j.jeurceramsoc.2021.05.050>.
- (206) Al-Madanat, O.; AlSalka, Y.; Ramadan, W.; Bahnemann, D. W. TiO₂ Photocatalysis for the Transformation of Aromatic Water Pollutants into Fuels. *Catalysts* **2021**, *11* (3), 1–45. <https://doi.org/10.3390/catal11030317>.

Curriculum vitae

Personal data

Name	María Teresa Ayala Ayala
Address	Queretaro Mexico
Email	ayala@iftc.uni-hannover.de , maría.ayala@cinvestav.mx
Date of birth	13.04.1992
Place of birth	Morelia, Mexico
Nationality	Mexican
Marital status	Married

Education

01.2018-05-2022	PhD student at the Leibniz University of Hannover, Institute of Technical Chemistry, Hannover, Germany and Center of Research and Advanced Studies (Cinvestav) at IPN, National Laboratory of Thermal Spray Queretaro, Mexico. PhD thesis: “Fabrication of bismuth-based photocatalytic heterojunctions for hydrogen generation”
08.2015-12.2017	Master of Science in Materials Science at Center of Research and Advanced Studies (Cinvestav) at IPN, Queretaro, Mexico. Master thesis: “Synthesis and characterization of bismuth oxide for photocatalytic applications.”
08.2010-05-2015	Bachelor of Materials Engineering at National Technological of Mexico, Morelia Mexico. Specialty: Welding and steel manufacturing of iron and steel. Bachelor thesis: “Study of the tetragonal system BNT-BKT-BT ferroelectric ceramics by experimental design in thermal treatment stage.”

Work experience

Assistant Professor of “Mechanical properties of materials” in the master program of Materials Science 2018 at CINVESTAV, Queretaro.

Languages

English	Course of English language from basic to advanced level. Baden-Powell English Institute. 2010-2012. Final grade: approved Course of Teaching Methods for English language Instituto Tecnologico de Morelia 2013-2014 Final grade: approved Toefl PBT test for English language November 2017 Final grade 520/660.
German	A1 level course in Bildungsverein from the Leibniz University of Hannover.

Publications

Journal publications

- **Ayala-Ayala M.T. (50%)**, Ferrer-Pacheco M.Y. (15%), Munoz-Saldana J. (35%), Manufacturing of photoactive β -bismuth oxide by flame spray oxidation, Journal of thermal spray technologies, 2021. <https://doi.org/10.1007/s11666-021-01182-2>
Conceptualization; **M.T.A.A.** and J.M.S., Formal analysis; **M.T.A.A.** and M.Y.F.P., Investigation; **M.T.A.A.**, Supervision; J.M.S., Visualization; **M.T.A.A.** and J.M.S., Writing-original draft; **M.T.A.A.**, Writing-review and editing; **M.T.A.A.**, M.Y.F.P., and J.M.S. The manuscript was written through contributions of all authors.
- Gutierrez-Perez A.I. (35%), **Ayala-Ayala M.T. (15%)**, Mora-García A.G. (15%), Moreno-Murguía B. (10%), Ruiz-Luna H. (10%), Munoz-Saldana J. (15%), Visible-light photoactive thermally sprayed coatings deposited from spray-dried $(\text{Na}_{0.5}\text{Bi}_{0.5})\text{TiO}_3$ microspheres, Surface and coatings technology, 2021. <https://doi.org/10.1016/j.surfcoat.2021.127851>
Conceptualization; A.I.G.P. and A.G.M.G., Formal analysis; A.I.G.P, **M.T.A.A.** and A.G.M.G., Investigation; A.I.G.P. and A.G.M.G., Supervision; J.M.S., Visualization; A.I.G.P. and J.M.S., Writing-original draft; A.I.G.P., A.G.M.G. and **M.T.A.A.**, Writing-review and editing; A.I.G.P., A.G.M.G., **M.T.A.A.**, B.M.M., H.R.L., and J.M.S. The manuscript was written through contributions of all authors.
- Cardenas-Terrazas P. S. (35%), **Ayala-Ayala M. T. (15%)**, Muñoz-Saldaña J. (20%), Fuentes A. F. (5%), Leal-Chavez D. A. (5%), Ledezma-Sillas J. E. (5%), Carreño-Gallardo C. (5%) and Herrera-Ramirez J. M. (20%), High ionic conductivity dysprosium and tantalum Co-doped bismuth oxide electrolyte for low-temperature SOFCs, Ionics, 2020. <https://doi.org/10.1007/s11581-020-03572-y>
Conceptualization; P.S.C.T., J.M.S. and J.M.H.R., Formal analysis; P.S.C.T., J.M.S. and **M.T.A.A.**, Investigation; P.S.C.T., A.F.F., D.A.L.C., J.E.L.S., C.C.G., Supervision; J.M.S. and J.M.H.R., Visualization; P.S.C.T., J.M.S. and J.M.H.R., Writing-original draft;

P.S.C.T., J.M.S. and **M.T.A.A.**, Writing-review and editing; P.S.C.T., **M.T.A.A.**, J.M.S., J.M.H.R. The manuscript was written through contributions of all authors.

- Fernandez-Benavides D.A. (30%), Gutierrez-Perez A.I. (20%), Benitez-Castro A.M. (10%), **Ayala-Ayala M.T. (10%)**, Moreno-Murguia B. (10%) and Muñoz-Saldaña J. (20%), Comparative Study of Ferroelectric and Piezoelectric Properties of BNT-BKT-BT Ceramics near the Phase Transition Zone, *Materials*, 2018. <https://doi.org/10.3390/ma11030361>

Conceptualization; D.A.F.B. and A.I.G.P., Formal analysis; D.A.F.B., A.I.G.P., **M.T.A.A.**, A.M.B.C., B.M.M. and J.M.S., Investigation; D.A.F.B., A.I.G.P., **M.T.A.A.**, A.M.B.C., B.M.M., Supervision; J.M.S., Visualization; D.A.F.B. and J.M.S., Writing-original draft; D.A.F.B., A.I.G.P., **M.T.A.A.**, A.M.B.C. and B.M.M., Writing-review and editing; D.A.F.B., A.I.G.P., **M.T.A.A.**, A.M.B.C., B.M.M. and J.M.S. The manuscript was written through contributions of all authors.

Oral presentations

Ayala-Ayala M.T., “Thermal spray manufacturing of coatings and powders with multifunctional properties,” 36th Circle of studies of Materials Engineering developed in the National Technologic of Mexico, November 11th, 2021, Morelia Mexico.

Ayala-Ayala M.T., Ferrer-Pacheco M.Y., Muñoz-Saldana J., “Manufacturing of photoactive β -bismuth oxide by flame spray oxidation,” International Meeting for researchers in Materials and Plasma Technology 5+IIMRMPT. On-site and remote conference, June 2-4, 2021, Medellin, Colombia.

Ayala-Ayala M.T., “Multifunctional bismuth-based ceramics: Energy generation and harvesting”, 21th National Conferences on Materials Engineering at Technologic Institute of Morelia, March 29th, 2019, Morelia Mexico.

Publications

Poster presentations

Ayala-Ayala M.T., Gutierrez-Perez A.I., Hernandez-Navarro C., Patiño-García J., Munoz-Saldana J., “Visible-light photocatalytic multi-heterojunction synthesized by flame spray” #Env076 poster, #LatinXChem Twitter Conference, September 20, 2021.

Courses

Participation in the “Certified: Business Development and Technology-Based Entrepreneurship” in charge of the MSc Jaime Acevedo with the project: “Visible-light active photocatalytic materials and coatings for environmental remediation” Maria Teresa Ayala Ayala, Aixa Iveth Gutierrez Perez, Angelica Maria Benitez Castro, Juan Muñoz Saldaña. September 2020-March 2021.